



저작자표시-비영리-변경금지 2.0 대한민국

이용자는 아래의 조건을 따르는 경우에 한하여 자유롭게

- 이 저작물을 복제, 배포, 전송, 전시, 공연 및 방송할 수 있습니다.

다음과 같은 조건을 따라야 합니다:



저작자표시. 귀하는 원저작자를 표시하여야 합니다.



비영리. 귀하는 이 저작물을 영리 목적으로 이용할 수 없습니다.



변경금지. 귀하는 이 저작물을 개작, 변형 또는 가공할 수 없습니다.

- 귀하는, 이 저작물의 재이용이나 배포의 경우, 이 저작물에 적용된 이용허락조건을 명확하게 나타내어야 합니다.
- 저작권자로부터 별도의 허가를 받으면 이러한 조건들은 적용되지 않습니다.

저작권법에 따른 이용자의 권리는 위의 내용에 의하여 영향을 받지 않습니다.

이것은 [이용허락규약\(Legal Code\)](#)을 이해하기 쉽게 요약한 것입니다.

[Disclaimer](#)

이학박사 학위논문

Arrays of Ordered Nanostructures  
Synthesized from Diblock Copolymers and  
Their Micelles for  
Large-Area Graphene Nanopatterning

이중블록공중합체와 마이셀로부터 합성한  
정렬된 나노구조 배열의  
대면적 그래핀 나노패터닝 응용

2015년 8월

서울대학교 대학원

화학부 고분자화학 전공

김 성 수

## **Abstract**

# Arrays of Ordered Nanostructures Synthesized from Diblock Copolymers and Their Micelles for Large-Area Graphene Nanopatterning

Sung-Soo Kim  
Department of Chemistry  
The Graduate School  
Seoul National University

Controlling or optimizing the chemical and physical properties of graphene, a flat monolayer of  $sp^2$ -bonded carbon atoms in a two-dimensional honeycomb lattice, has been of great importance for a variety of applications such as novel electronic, chemical, and membrane devices. Numerous results obtained by theoretical calculations and experimental observations have indicated that patterning graphene into nanometer-sized structures is useful for altering the physicochemical properties of graphene-based devices. Therefore, the use of modern nanofabrication and nanopatterning technologies with graphene materials has garnered much interest. Because the two-dimensional geometry of graphene is directly compatible with existing processing techniques used in the silicon-based semiconductor industry, a diversity of conventional top-down approaches including electron and focused ion beam lithography have been utilized for graphene nanopatterning. Top-down lithographic methods afford a precise means of controlling the feature sizes of

nanoscaled patterns, resulting in the clear observation of various extraordinary properties of nanopatterned graphene as well as a deeper and more accurate understanding of the relationships between those properties and the pattern dimensions of graphene. However, the expensive, time-consuming, and sophisticated techniques associated with top-down approaches are major causes of the lack of flexibility and scalability of the graphene patterning process. In contrast, bottom-up approaches involving the use of molecular self-assembly processes, offer a wide range of opportunities to generate nanopatterned graphene through a low-cost, simple, and facile method, as these approaches effectively enable the fabrication of nanostructures and nanomaterials in large areas. The diblock copolymer approach, one of various bottom-up approaches, is a promising technique when used to generate nanostructures and nanopatterns of various materials. It can be used effectively to create nanopatterned graphenes. Diblock copolymers composed of two different polymers spontaneously assemble into periodic nanostructures, of which the size and morphology can be controlled by the molecular weight and composition of copolymers. In addition, when diblock copolymers are dissolved in a selective solvent for one of the blocks, spherical micelles with a soluble corona and an insoluble core can be obtained. The diblock copolymers and their micelles can be coated onto solid substrates to form nanostructured thin films, and they can be used as nanoscale lithographic masks for etching processes and nanotemplates to generate ordered arrays of inorganic nanomaterials. Because graphene is a two-dimensional, atomically flat material, a thin film of diblock copolymers and their micelles can be readily coated onto graphene which it is deposited onto any solid substrate, therefore guaranteeing further nanopatterning processes of the type used with substrates without graphene.

This dissertation proposes the preparation, characterization and application of nanopatterned large-area graphene using the diblock copolymer approach. After introducing the background and objectives of this study in chapter I, the method used to fabricate diverse arrays of ordered inorganic nanostructures including nanoparticles (NPs), nanowires (NWs), and nanorings (NRs) from a thin film of diblock copolymers and their micelles is demonstrated in chapter II. Prepared nanostructures were used to prepare nanopatterned graphene as a nanotemplate, an etching mask, and a catalytic etcher, of which the feature sizes and spacings were effectively and accurately controlled at the nanoscale by adjusting the molecular weight of the copolymers. Chapter III presents the experimental results and the characterization of nanopatterned reduced graphene oxides (rGOs) and graphene, in this case rGOs decorated with nanoparticles, rGO nanodots, nanoribbons, and anti-NRs as well as nanoperforated graphene. This large-area nanopatterning technique using diblock copolymers provides a relatively facile and effective means of preparing various forms of nanostructured graphene in a controlled manner. Therefore, this methodology has immense potential when used with numerous electronic, chemical, biological, and environmental applications.

**Keywords: diblock copolymer, micelle, graphene, nanopatterning**

*Student number: 2009-20290*

# Table of Contents

Abstract .....	i
Table of Contents .....	iv
List of Figures .....	vi
List of Tables .....	xxi
List of Equations .....	xxii
Glossary .....	xxiii

## Chapter

### I. Introduction

1. Graphene nanopatterning .....	1
2. Diblock copolymers and their micelles .....	6
3. Aims and objectives .....	10

### II. Fabrication of arrayed inorganic nanostructures

1. Arrayed TiO <sub>2</sub> nanostructures .....	11
2. Arrayed nanoparticles .....	21
3. Arrayed nanowires .....	34
4. Arrayed nanorings .....	48
5. Ordered complex arrays .....	69

### III. Fabrication of nanopatterned graphene

1. Graphene decorated with arrayed nanoparticles .....	87
2. Graphene nanodot arrays .....	115

3. Graphene tailored by Pt nanostructures .....	131
IV. Summary and outlook .....	160
References .....	163
Appendices	
A. Electrochemical analysis .....	172
B. Photoluminescence from ZnO nanorods .....	175
C. Correlation analysis of nanoporated graphene .....	177
Abstract in Korean .....	181
Curriculum Vitae .....	184

# List of Figures

## II.1. Arrayed TiO<sub>2</sub> nanostructures

- Figure 2.1** FE-SEM images of PS nanotemplates and RTNs. (a) Molecular structures of PS and PMMA; (b,c) Top- and tilt-view images of PS nanoporous template fabricated from PS(46)-PMMA(21); (d,e) RTNs after RIE. Scale bars are 200 nm. .... 17
- Figure 2.2** FE-SEM images of PS nanotemplates. (a,b) Top- and tilt-view images of PS nanoporous template fabricated from PS(140)-PMMA(60); (c,d) Top- and tilt-view images of PS nanoporous template fabricated from mixture of PS(140)-PMMA(60) and PS(5)-PMMA(5). Scale bars are 200 nm. .... 18
- Figure 2.3** PS nanotemplates and DTNs. (a) AFM image of PS nanoporous template fabricated from a mixture of PS(140)-PMMA(60) and PS(5)-PMMA(5); (b,c) AFM and FE-SEM images of DTNs fabricated from PS nanoporous template displayed in (a). Scale bars are 200 nm. .... 19
- Figure 2.4** PS nanotemplates and LTNs. (a,b) AFM and tilt-view FE-SEM images of PS nanogroove template fabricated from PS(80)-PMMA(80); (c,d) AFM and tilt-view FE-SEM image of LTNs fabricated from PS nanogroove template displayed in (a,b). Scale bars are 200 nm. .... 20

## II.2. Arrayed nanoparticles

- Figure 2.5** AFM images of single-layered films of PS-P4VP micelles. (a) Molecular structures of PS and P4VP; (b) PS(51)-P4VP(18); (c) PS(109)-P4VP(27). Scale bars are 200 nm. .... 28
- Figure 2.6** TEM images of single-layered films of PS-P4VP micelles. (a) PS(51)-P4VP(18); (b) PS(109)-P4VP(27). P4VP cores were selectively stained by I<sub>2</sub>. Scale bars are 100 nm. .... 29
- Figure 2.7** TEM images and size distribution histograms of arrayed Au NPs synthesized from PS-P4VP micelles. (a) Au(25-7); (b) Au(32-13); (c) Au(51-18). Scale bars are 100 nm. .... 30
- Figure 2.8** TEM images and size distribution histograms of arrayed Pt NPs synthesized from PS-P4VP micelles. (a) Pt(32-13); (b) Pt(51-18); (c) Pt(109-27). Scale bars are 100 nm. .... 31
- Figure 2.9** SAED pattern of NPs fabricated from PS-P4VP micelles. (a) Au(51-18); (b) Pt(51-18). Lattice planes are marked on each image. Insets are the HR-TEM image of an individual NPs. .... 32

## II.3. Arrayed nanowires

- Figure 2.10** Characterization of PS(25)-P4VP(7) thin films. (a) AFM image of a single-layered film of PS(25)-P4VP(7) micelles; (b,c,d) AFM, TEM, and FE-SEM images of PS(25)-P4VP(7) thin films having cylindrical nanostructures after chloroform solvent vapor annealing. Scale bars are 100 nm. .... 41
- Figure 2.11** FE-SEM images of other PS-P4VP thin films having cylindrical nanostructures after chloroform solvent vapor annealing. (a) PS(19)-P4VP(5); (b) PS(33)-P4VP(8); (c) PS(32)-P4VP(13); (d) PS(50)-P4VP(13). Scale bars are 200 nm. .... 42
- Figure 2.12** TEM images of other PS-P4VP thin films having cylindrical nanostructures after chloroform solvent vapor annealing. (a) PS(19)-P4VP(5); (b) PS(33)-P4VP(8); (c) PS(32)-P4VP(13); (d) PS(50)-P4VP(13). Scale bars are 100 nm. .... 43
- Figure 2.13** FE-SEM images of other PS-P4VP thin films after chloroform solvent vapor annealing. (a) PS(48)-P4VP(20); (b) PS(109)-P4VP(27). Scale bars are 100 nm. .... 44
- Figure 2.14** AFM images of swollen PS-P4VP thin films after the immersion into an acidic Pt salt solution (left) and synthesized Pt NWs (right). (a,b) PS(19)-P4VP(5); (c,d) PS(25)-P4VP(7); (e,f) PS(32)-P4VP(13). Scale bars are 100 nm. .... 45

**Figure 2.15** FE-SEM images for DSA of PS(32)-P4VP(13) and synthesized Pt NWs. (a) Well-aligned PS-P4VP thin films having cylindrical nanostructures after chloroform solvent vapor annealing; (b) Well-aligned arrays of Pt NWs in topographically patterned wafer. Scale bars are 200 nm. .... 46

## II.4. Arrayed nanorings

**Figure 2.16** Chemical structures of EMIm cation and TFSI anion. .... 56

**Figure 2.17** TEM and AFM images of single-layered films of IL-containing PS(109)-P4VP(27). (a,b)  $\mu = 0$ ; (c,d)  $\mu = 0.4$ ; (e,f)  $\mu = 0.8$ . Scale bars are 200 nm. .... 57

**Figure 2.18** TEM images of single-layers of IL-containing PS(109)-P4VP(27). (a)  $\mu = 0$ ; (b)  $\mu = 0.2$ ; (c)  $\mu = 0.4$ ; (d)  $\mu = 0.6$ ; (e)  $\mu = 0.8$ . Scale bars are 200 nm. .... 58

**Figure 2.19** AFM images of single-layers of IL-containing PS(51)-P4VP(18). (a)  $\mu = 0$ ; (b)  $\mu = 0.2$ ; (c)  $\mu = 0.4$ ; (d)  $\mu = 0.6$ ; (e)  $\mu = 0.8$ . Insets are AFM phase mode images of corresponding regions ( $1 \mu\text{m} \times 1 \mu\text{m}$ ). Scale bars are 200 nm. .... 59

**Figure 2.20** DLS results of intensity distributions of pristine and IL-containing PS(51)-P4VP(18) micelles in toluene. .... 60

- Figure 2.21** TEM and AFM images of single-layered films of IL-containing PS(109)-P4VP(27) after immersing into an acidic Pt salt solution. (a,b)  $\mu = 0$ ; (c,d)  $\mu = 0.4$ ; (e,f)  $\mu = 0.8$ . Scale bars are 200 nm. .... 61
- Figure 2.22** TEM images of single-layered films of IL-containing PS(51)-P4VP(18) after immersing into an acidic Pt salt solution. (a)  $\mu = 0$ ; (b)  $\mu = 0.2$ ; (c)  $\mu = 0.4$ ; (d)  $\mu = 0.6$ ; (e)  $\mu = 0.8$ . Scale bars are 100 nm. .... 62
- Figure 2.23** AFM images of single-layered films of IL-containing PS(51)-P4VP(18) after immersing into an acidic Pt salt solution. (a)  $\mu = 0$ ; (b)  $\mu = 0.2$ ; (c)  $\mu = 0.4$ ; (d)  $\mu = 0.6$ ; (e)  $\mu = 0.8$ . Scale bars are 200 nm. .... 63
- Figure 2.24** FE-SEM images of Pt NRs synthesized from single-layered films of IL-containing PS(109)-P4VP(27). (a)  $\mu = 0$ ; (b)  $\mu = 0.2$ ; (c)  $\mu = 0.4$ ; (d)  $\mu = 0.6$ ; (e)  $\mu = 0.8$ . Scale bars are 100 nm. .... 64
- Figure 2.25** FE-SEM images of Pt NRs synthesized from single-layered films of IL-containing PS(51)-P4VP(18). (a)  $\mu = 0$ ; (b)  $\mu = 0.2$ ; (c)  $\mu = 0.4$ ; (d)  $\mu = 0.6$ ; (e)  $\mu = 0.8$ . Scale bars are 100 nm. .... 65
- Figure 2.26** FE-SEM images of other NRs synthesized from single-layered films of IL-containing PS(109)-P4VP(27) ( $\mu = 0.8$ ). (a) Au; (b) PdO; (c) Fe<sub>2</sub>O<sub>3</sub>. Scale bars are 100 nm. .... 66

## II.5. Ordered Complex Arrays

- Figure 2.27** AFM height mode images of copolymer micelles spin-coated on LTN. (a) PS(51)-P4VP(18); (b) PS(32)-P4VP(13). Each inset is magnified AFM phase mode image corresponding to the square marked region. Scale bars are 200 nm. .... 77
- Figure 2.28** FE-SEM images of ordered complex arrays consisting of LTN and (a) Au(51-18) and (b) Au(32-13). Each inset is a magnified image of the square marked region. Scale bars are 200 nm. .... 78
- Figure 2.29** FE-SEM images of ordered complex arrays consisting of LTN Au(51-18) with a higher number density by repeating procedure of the synthesis of Au NPs (a) twice and (b) three times. Each inset is a magnified image of the square marked region. Scale bars are 200 nm. .... 79
- Figure 2.30** AFM height mode images of copolymer micelles spin-coated on DTN. (a) PS(51)-P4VP(18); (b) PS(32)-P4VP(13). Each inset is magnified image with high Z scale contrast. Scale bars are 200 nm. .... 80
- Figure 2.31** FE-SEM images of ordered complex arrays consisting of DTN and (a) Au(51-18) and (b) Au(32-13). Each inset is a magnified image of the square marked region with solid circles for Au NPs and dashed guiding lines. Scale bars are 200 nm. .... 81

- Figure 2.32** Size distribution of DTN and (a) Au(51-18) and (b) Au(32-13) from ordered complex arrays of in the same area. .... 82
- Figure 2.33** AFM images of PS(109)-P4VP(27) micelles spin-coated on (a) LTN and (b) DTN. Scale bars are 200 nm. .... 83
- Figure 2.34** FE-SEM image of ordered complex nanostructures of DTN with Au(51-18) and Au(32-13). Inset is a magnified image of the square marked region. Scale bars are 200 nm. .... 84
- Figure 2.35** AFM images of PS-P4VP micelles spin-coated onto Pt NWs. (a,b) Pt NWs synthesized from PS(32)-P4VP(13) with PS(32)-P4VP(13) micelles spin-coated from 0.5 and 0.3 wt% solution; (c) Pt NWs synthesized from PS(25)-P4VP(7) with PS(25)-P4VP(7) micelles spin-coated from 0.3 wt% solution Scale bars are 100 nm. .... 85
- Figure 2.36** FE-SEM images of ordered complex arrays fabricated from copolymer micelles spin-coated onto Pt NWs displayed in Figure 2.35. (a) Figure 2.35a; (b) 2.35b; (c) 2.35c. Scale bars are 100 nm. .... 86

### III.1. Graphene decorated with arrayed nanoparticles

- Figure 3.1** XRD patterns of (a) graphite powder and (b) GO powder. .... 101
- Figure 3.2** AFM images of (a) GO flakes spin-coated onto a SiO<sub>2</sub>/Si substrate and (b) rGO film fabricated by spin-coating of GO 5 times followed by hydrazine reduction. A height profile along the solid line in each image is also displayed below the corresponding AFM image. .... 102
- Figure 3.3** Characterization of GO (solid) and rGO (dashed) film after hydrazine reduction. (a) XPS; (b) UV-vis absorption spectra; (c) Raman spectra. .... 103
- Figure 3.4** Characterization of rGO decorated with Au(109-27). (a) AFM image of PS(109)-P4VP(27) micelles on rGO; (b) AFM image of Au(109-27) from the micelles; (c) TEM image of Au NPs on rGO; (d) The diameter distribution of the Au NPs measured from the TEM image. The insets in (c) are the HR-TEM image of an individual Au NP and the photo of a transferred rGO film with Au NP (the gray square) on a flexible polymer film. .... 104
- Figure 3.5** (a) XPS spectrum of Au(4f) of Au(109-27); (b) SAED pattern of Au NPs. Lattice planes are marked on (b). .... 105

<b>Figure 3.6</b>	Characterization of rGO decorated with Au(51-18). (a) AFM image of PS(51)-P4VP (18) micelles on rGO; (b) AFM image of Au(51-18); (c) TEM image of the Au NPs on rGO; (d) The diameter distribution of the Au NPs measured from the TEM image. ....	106
<b>Figure 3.7</b>	AFM and TEM images of rGO decorated with Fe <sub>2</sub> O <sub>3</sub> (51-18). ....	107
<b>Figure 3.8</b>	(a,b) AFM and TEM images of rGO decorated with PdO(51-18). (c) XPS spectra of Pd(3d) of rGO decorated with PdO(51-18) before (solid) and after (dashed) hydrazine reduction. The inset in (b) is the HR-TEM image of an individual PdO NP. ....	108
<b>Figure 3.9</b>	Nyquist plots of Fe(CN) <sub>6</sub> <sup>3-/4-</sup> with (a) GCE and (b) ITO/glass electrodes. The scan rate was 100 mV s <sup>-1</sup> . ....	109
<b>Figure 3.10</b>	Cyclic voltammograms of Fe(CN) <sub>6</sub> <sup>3-/4-</sup> with GCE. ....	110
<b>Figure 3.11</b>	Cyclic voltammograms for ORR with rGO films decorated with Au NPs in oxygen-saturated (a) 0.1 M KOH solutions and (b) 0.1 M H <sub>2</sub> SO <sub>4</sub> solutions. The scan rate was 50 mV s <sup>-1</sup> . ....	111
<b>Figure 3.12</b>	Cyclic voltammograms for ORR with rGO films decorated with Au NPs in N <sub>2</sub> - and O <sub>2</sub> -saturated 0.1 M KOH solutions: (a) GCE; (b) rGO; (c) Au(109-27); (d) Au(51-18). Electrochemical measurements were carried out after purging with N <sub>2</sub> or O <sub>2</sub> for 20 min. For comparison, the CV without purging (marked as air) is also displayed. The scan rate was 50 mV s <sup>-1</sup> . ....	112

**Figure 3.13** Linear sweep voltammograms for the ORR with rGO films decorated with (a) Au(109-27) and (b) Au(51-18) in oxygen-saturated 0.1 M KOH solutions. (c) Koutecky-Levich plots. The scan rate was  $5 \text{ mV s}^{-1}$ . The numbers shown in the voltammograms are the rotating rates in rpm. The arrows indicate the scan direction. The background current in an oxygen-free solution was subtracted. 113

**Figure 3.14** Cyclic voltammograms for the ORR with Au(51-18) after 2 h of constant potential at  $-0.6 \text{ V}$  in an oxygen-saturated 0.1 M KOH solution. The scan rate was  $50 \text{ mV s}^{-1}$ . ..... 114

## III.2. Graphene nanodot arrays

**Figure 3.15** OM images of graphene on a  $\text{SiO}_2/\text{Si}$  substrate (a) before and (b) after oxygen plasma treatment. The position of graphene is indicated by the arrow. The scale bars are  $20 \mu\text{m}$ . ..... 123

**Figure 3.16** Fabrication of graphene nanodot arrays. (a) graphene on a  $\text{SiO}_2/\text{Si}$  substrate; (b) Au NPs after oxygen plasma treatment; (c) Arrayed graphene nanodots fabricated from PS(51)-P4VP(18) micelles after the removal of Au NPs. A height profile along the black solid line in each image is displayed below the corresponding AFM image. The insets in (b) and (c) are enlarged images of Au NPs and graphene nanodots, respectively. Scale bars are  $500 \text{ nm}$ . ..... 124

- Figure 3.17** AFM images of (a) graphene on a SiO<sub>2</sub>/Si substrate and (b) a monolayer of PS(51)-P4VP(18) micelles on the same graphene. Scale bars are 200 nm. .... 125
- Figure 3.18** XPS spectra of Au(4f). (a) Au NPs; (b) After the removal of Au NPs. .... 126
- Figure 3.19** Characterization of micelles, Au NPs and graphene nanodots. (a) TEM image of a single layer of PS(51)-P4VP(18) micelles; (b) AFM image of Au(51-18); (c) AFM image of graphene nanodots after the removal of Au NPs. Scale bars are 200 nm. .... 127
- Figure 3.20** Raman spectra of (a) single layer graphene and (b) graphene nanodots fabricated from PS(51)-P4VP(18) micelles. The inset shows an AFM image of graphene nanodots corresponding to Raman spectrum of (b). The band at 960 cm<sup>-1</sup> is the characteristic of the SiO<sub>2</sub> layer of substrates. .... 128
- Figure 3.21** AFM images and size distributions of arrayed graphene nanodots fabricated from PS-P4VP micelles with various molecular weights: (a) PS(51)-P4VP(18); (b) PS(75)-P4VP(25); (c) PS(109)-P4VP(27). Size of AFM images are 1 μm × 1 μm. The inset in each image is a FFT pattern. .... 129

**Figure 3.22** AFM image of rGO nanodots fabricated from PS(109)-P4VP(27).  
 (b) FE-SEM image of ZnO nanorods grown from rGO nanodots.  
 (c) XRD pattern of ZnO nanorod arrays on the rGO nanodots.  
 Scale bars for AFM and TEM images are 500 nm and 100nm,  
 respectively. .... 130

### III.3. Graphene tailored by Pt nanostructures

**Figure 3.23** AFM images for the fabrication of arrayed Pt NPs on rGO. (a) rGO; (b) PS(51)-P4VP(18) micelles with Pt precursors in the cores; (c) Arrayed Pt NPs synthesized on rGO and (d) on a bare SiO<sub>2</sub>/Si substrate; (e) Height histograms of Pt NPs obtained from (c) and (d) are plotted together for comparison. A relative height in each case is shown in the schematic illustration. Scale bars are 200 nm. .... 146

**Figure 3.24** Nanoperforated rGO. (a) AFM image of perforated rGO (inset: a magnified image in 500 nm × 500 nm); (b) TEM image of perforated rGO. Scale bars are 200 nm. .... 147

**Figure 3.25** AFM and TEM images of perforated rGO by (a,b) Pt(32-13) and (c,d) Pt(109-27). Each inset is a magnified image (500 nm × 500 nm). Scale bars are 200 nm. .... 148

**Figure 3.26** (a,b) AFM and FE-SEM images of Pt aggregation on CVD graphene after heating of PS-P4VP micelles with Pt precursors at 400 °C for 30 min in air. Scale bars are 200 nm. .... 149

**Figure 3.27** AFM images for the fabrication of nanoporated CVD graphene. (a) arrayed Pt(51-18) on a bare SiO<sub>2</sub>/Si substrate (schematic i); (b) graphene transferred onto arrayed Pt NPs (schematic ii); (c) perforated graphene with arrayed Pt NPs after heating (schematic iii); (d) perforated graphene transferred onto another SiO<sub>2</sub>/Si substrate. Each inset is a 3D view image with a higher magnification (200 nm × 200 nm). Scale bars are 200 nm. .... 150

**Figure 3.28** AFM images of surface morphology variation of CVD graphene. (a) CVD graphene transferred on the Pt NPs array. (b) AFM image of annealing treated CVD graphene for 5 min; (c) 10 min; (d) 15 min; (e) 25 min; (f) 30 min. Scale bars are 200 nm. .... 151

**Figure 3.29** (a) Raman spectra of graphene on Pt(51-18) after heating with 5 min interval. The variation of the phonon frequencies of (b) the 2D and (c) G modes as a function of annealing time. .... 152

**Figure 3.30** AFM images and Raman spectra of graphene on arrayed NPs. (a) Pt(51-18) after heating in vacuum; (b) SiO<sub>2</sub>(51-18) after heating in air; (c) Au(51-18) after heating in air. Each inset is a 3D view image with a higher magnification (200 nm × 200 nm). Scale bars are 200 nm. .... 153

**Figure 3.31** Controllability studies of pore size and density and catalytic effect of other condition. Nanoperforated CVD graphene by arrayed Pt NPs synthesized from other copolymer micelles: (a) PS(32)-P4VP(13); (b) PS(51)-P4VP(18); (c) PS(109)-P4VP(27). Each inset is a magnified image (500 nm × 500 nm). Raman spectra with respect to each sample are displayed together. Scale bars are 200 nm. .... 154

**Figure 3.32** Simplified reaction coordinate for the oxidation reaction of CVD graphene with and without a Pt NP. (a) The original activation energy without a Pt NP. (b) The activation energy lowered only by mechanical strain. (c) The activation energy decreased by local strain and Pt catalyst. .... 155

**Figure 3.33** AFM images for the fabrication of nanoperforated rGO. (a) rGO transferred onto arrayed Pt(25-7); (b) Perforated rGO with arrayed Pt NPs after heating; (c) Perforated rGO transferred onto another SiO<sub>2</sub>/Si substrate; (d) perforated rGO by Pt(32-13) Scale bars are 200 nm. .... 156

**Figure 3.34** AFM images for the fabrication of arrayed rGO nanoribbons. (a) rGO transferred onto arrayed Pt NWs synthesized from PS(25)-P4VP(7); (b) Tailored rGO with arrayed Pt NWs after heating; (d) Arrayed rGO nanoribbons transferred onto another SiO<sub>2</sub>/Si substrate Scale bars are 100 nm. .... 157

**Figure 3.35** Control of rGO nanoribbons by varying molecular weights of PS-P4VP. (a) PS(19)-P4VP(5); (b) PS(32)-P4VP(13). Scale bars are 100 nm. .... 158

**Figure 3.36** AFM images for the fabrication of perforated rGO nanoribbon arrays. (a) Perforated rGO nanoribbons with ordered complex Pt arrays (Figure 2.36a) after heating; (b) Perforated rGO transferred onto another SiO<sub>2</sub>/Si substrate. Perforated rGO nanoribbons fabricated from other ordered complex arrays shown in (c) Figure 2.36b; (d) Figure 2.36c. Scale bars are 100 nm. .... 159

**Figure 3.37** AFM images for the fabrication of arrayed rGO anti-NRs. (a) rGO transferred onto arrayed Pt nanorings from IL-containing PS(109)-P4VP(27) ( $\mu = 0.8$ ). (b) Arrayed rGO anti-NRs with Pt nanorings after heating; (c) Arrayed rGO anti-NRs transferred onto another SiO<sub>2</sub>/Si substrate. (d) Arrayed rGO anti-NRs from IL-containing PS(51)-P4VP(18) ( $\mu = 0.8$ ). Scale bars are 100 nm. .... 160

# List of Tables

## II.2. Arrayed nanoparticles

**Table 2.1** Synthetic conditions and characteristics of the NPs fabricated from PS-P4VP micelles. † Molar ratio of precursors to pyridine unit was 0.35. .... 33

## II.3. Arrayed nanowires

**Table 2.2** Solubility parameters of chloroform, PS, and P4VP. .... 47

## II.4. Arrayed nanorings

**Table 2.3** Characteristics of pristine and IL-containing PS(51)-P4VP(18) micelles. .... 67

**Table 2.4** Characteristics of Pt NRs fabricated from pristine and IL-containing PS-P4VP micelles. .... 68

## List of Equations

### II.2. Arrayed nanoparticles

Equation 2.1  $Z = Z_o (N_A^\alpha N_B^{-\beta})$  23

Equation 2.2  $\frac{4}{3}\pi R_C^3 = Z N_A v_A$  24

Equation 2.3  $\chi_{eff} \approx \varphi_P (\chi + \Delta\chi)$  37

## Glossary

AAO	anodized aluminum oxide
AFM	atomic force microscope
CV	cyclic voltammetry
CVD	chemical vapor deposition
DLS	dynamic light scattering
DSA	directed self-assembly
DTN	disc-shaped TiO <sub>2</sub> nanostructure
EBL	e-beam lithography
EIS	electrochemical impedance spectroscopy
EMIm	1-ethyl-3-methylimidazolium
FE-SEM	field-emission scanning electron microscope
FET	field effect transistor
FFT	fast Fourier transformation
FWHM	full width at half maximum
GCE	glassy carbon electrode
GO	graphene oxide
HR-TEM	high-resolution transmission electron microscope
IL	ionic liquid
ITO/glass	indium tin oxide-coated glass
LSV	linear-sweep voltammetry
LTN	line-shaped TiO <sub>2</sub> nanostructure
NP	nanoparticle
NR	nanoring

NW	nanowire
OM	optical microscope
ORR	oxygen reduction reaction
PBS	phosphate buffered saline
PDI	polydispersity index
PEO	poly(ethylene oxide)
PS-P2VP	polystyrene- <i>block</i> -poly(2-vinyl pyridine)
PS-P4VP	polystyrene- <i>block</i> -poly(4-vinyl pyridine)
PS-PB	polystyrene- <i>block</i> -polybutadiene
PS-PDMS	polystyrene- <i>block</i> -poly(dimethylsiloxane)
PS-PMMA	polystyrene- <i>block</i> -poly(methyl methacrylate)
RDE	rotating disk electrode
rGO	reduced graphene oxide
RTN	rod-shaped TiO <sub>2</sub> nanostructure
SAED	selected area electron diffraction
SiO <sub>2</sub> /Si	Si wafer having an oxide layer with 300 nm in thickness
TEM	transmission electron microscope
TFSI	bis(trifluoromethylsulfonyl)imide
XPS	X-ray photoelectron spectroscopy
$Z$	aggregation number
$N$	degree of polymerization
$D_c$	diameter of micellar core
$D_h$	diameter of holes after the immersion into acidic solution
$\chi_{eff}$	effective Flory-Huggins interaction parameter
$\Delta H_f$	enthalpy of formation

$\chi$	Flory-Huggins interaction parameter
$\Delta G_f$	Gibbs free energy of formation
$T_g$	glass transition temperature
$D_H$	hydrodynamic diameter of micelles
$D_i$	inner diameter of NRs
$\mu$	molar mass ratio
$M_n$	number-average molecular weight
$D_o$	outer diameter of NRs
$\varphi_P$	polymer volume concentration
$\delta$	solubility parameter
$T$	thickness of NRs

# Chapter I

## Introduction

### 1. Graphene nanopatterning

#### Graphene and its family

Defined as a single carbon layer of graphite structure by the International Union of Pure and Applied Chemistry (IUPAC) Gold Book,<sup>[1]</sup> graphene is a one-atom-thick two-dimensional planar material with the honeycomb lattice of carbon atoms. Since the groundbreaking work in 2004 by Geim and Novoselov *et al.*,<sup>[2]</sup> a considerable amount of attention toward this interesting member of the carbon allotrope family has been drawn from many scientists and engineers in numerous materials science societies given the extraordinary electronic properties of graphene after being isolated using Scotch tape. This mechanical exfoliation method allowed the relatively simple preparation of single-layered graphene on a substrate, enabling various physicochemical characterizations and measurements of graphene to reveal its ultrahigh charge-carrier mobility,<sup>[3]</sup> and its unexpected quantum relativistic effects,<sup>[4,5]</sup> excellent mechanical strength,<sup>[6]</sup> superior thermal conductivity,<sup>[7]</sup> and good optical transparency.<sup>[8]</sup> In particular, the high carrier mobility and elasticity of graphene demonstrated the firm promise of this material to replace silicon in future flexible electronics, thus boosted research on the fabrication of graphene-based electronic devices for practical applications. However, the low lateral dimension of graphene of less than a few micrometers when obtained by mechanical exfoliation is one of major obstacles preventing the realization of graphene electronics. Thus, different methods to produce large-area

graphene of a high quality have been explored and implemented.

One of widely employed method for the generation of large-area graphene is epitaxial growth by chemical vapor deposition (CVD). This growth method utilizes the diffusion of carbon atoms from gaseous precursors adsorbed onto metal substrates to form a graphene layer during the CVD process. Ruoff *et al.* demonstrated the production of single-layered graphene over a large area from Cu foil.<sup>[9]</sup> Additionally, the size of CVD-grown graphene was scaled up to 30-inches with the adoption of a roll-to-roll process in work by Hong *et al.*<sup>[10]</sup> Because the electronic and transport properties of CVD-grown graphene are similar to those of mechanically exfoliated graphene, numerous large-scale flexible electronic devices based on CVD-grown graphene have been demonstrated and continue to be vigorously explored.<sup>[11]</sup>

On the other hand, another chemical approach has been developed for the preparation of large-area graphene films on substrates. As reported more than a century ago,<sup>[12]</sup> graphite can be oxidized to have oxygen-containing functional groups on its basal carbon plane in the presence of strong acids and oxidizing agents. Owing to those functional groups, the van der Waals interaction between graphite layers is severely hindered such that individual layers in graphite can easily be isolated by external mechanical energy (*i.e.*, ultrasonication), resulting in final products of thin carbon layers containing abundant amounts of oxygen, known as graphene oxide (GO). Through this chemical exfoliation process in a solution state, a large amount of graphene oxide as an aqueous dispersion with a mass quantity can be readily obtained, from which two-dimensionally continuous, large-area thin films of graphene oxide can readily be deposited onto substrates by means of spray-coating,<sup>[13]</sup> dip-coating,<sup>[14]</sup> and spin-coating methods.<sup>[15]</sup>

Unlike CVD-grown graphene, GO film has no electronic and transport properties comparable to those of pristine graphene because oxidation severely deteriorates in the  $\pi$ -conjugated structure of the graphitic basal plane. Chemical treatment with reducing agents such as hydrazine,<sup>[16]</sup>  $\text{NaBH}_4$ ,<sup>[17]</sup> or ascorbic acid<sup>[18]</sup> can create  $\text{sp}^2$  bonding between carbon atoms and repair defects on the atomic scale with a substantial decrement of the oxygen content in GO. In spite of the remaining structural defects and vacancies on the basal plane, reduced GO (rGO) leads to a substantial restoration of the electrical conductivity. This property can be used to fabricate electronic devices on flexible polymer substrates.<sup>[19]</sup>

### **Nanopatterned graphene**

Most of the aforementioned extraordinary physicochemical properties of graphene are attributable to its unique electronic band structure. As shown in the first Brillouin zone, two symmetric band structures meet at six points of hexagonal corners (K, K' points) with a linear dispersion relationship. Thus, the gap between the conduction band and the valence band of graphene is nearly zero. For this reason, graphene is classified as an intrinsic semimetal. Although electrons and holes near Dirac points behave as relativistic massless particles with a high charge mobility as defined by the Dirac equation,<sup>[20]</sup> semimetal graphene, lacking a band gap, is incapable of controlling the electric current, which limits the utilization of graphene as an appropriate material for the fabrication of field-effect transistors (FETs) in the modern semiconductor engineering. This implies that opening the band gap in graphene while preserving the high charge mobility is of prime importance for practical applications of graphene to electronic devices. Bilayered graphene has also been investigated for the potential to realize a tunable band gap for symmetry

breaking in its electronic band structures, but the size of the band gap is too small to be utilized for the fabrication of FETs with an appropriate on/off ratio.<sup>[21]</sup>

One promising means of opening the band gap of graphene involves the creation of patterned structures on the nanometer scale. For example, the early theoretical work of Louie *et al.*<sup>[22]</sup> suggested that graphene nanoribbons, where charge carriers can be confined to a quasi-one dimensional system, are theoretically expected to have a band gap which depends on the width and crystallographic orientation. This was followed by experimental observations which proved the semiconducting nature of nanostructured graphenes via the fabrication of a FET based on graphene nanoribbons.<sup>[23]</sup> Moreover, graphene nanomeshes, which have periodic hole arrays with a narrow neck width in the basal plane, were also demonstrated to show a tunable band gap depending on the size and periodicity of the holes in the nanomeshes.<sup>[24,25]</sup>

The phenomenon of band gap opening in graphene is generally elucidated in terms of the quantum confinement and exchange interactions among edge states, which are strongly related to the shapes and dimensions of the graphene nanostructures. Therefore, numerous state-of-the-art nanofabrication techniques have been widely studied to allow the morphologies and sizes of nanopatterned graphene to be highly controllable for accurate control of its electronic properties.

Modern semiconductor manufacturing technologies based on a thin-film process favor graphene nanostructuring because graphene is a two-dimensionally flat, planar carbon material, implying the facile transfer of the pattern onto the etching mask in graphene via an oxygen treatment. A considerable number of graphene-based devices have been fabricated chiefly by electron-beam lithography (EBL). Because the use of an electron beam is well known to be feasible for the generation

of arbitrary structures accurately on the nanometer scale with a high resolution, EBL was utilized for the fabrication of individual graphene-based nanodevices in the initial stages of graphene research. Typically two-dimensional patterning on a photoresist layer by EBL is followed by plasma etching to realize different forms of nanostructured graphene such as graphene quantum dots<sup>[26]</sup> and graphene nanoribbons<sup>[23]</sup> with tunable nanostructural sizes. In addition to EBL, lithographic procedures with pre-fabricated masks by anodized aluminum oxide (AAO) have been applied to create nanometer-sized features in graphene.<sup>[27]</sup>

Photocatalytic degradation by TiO<sub>2</sub> photomasks under UV illumination has also been developed to tailor the shape of graphene.<sup>[28]</sup> In addition, scanning probes have been used as carving knives to cut graphene into nanostructures such as nanoribbons by local oxidation<sup>[29]</sup> or for direct mechanical cleavage near scanning probes.<sup>[30]</sup>

Recently, there have been several interesting reports showing that this form of graphene can also be etched by nanoparticles (NPs), leading to nanostructured graphene.<sup>[31-34]</sup> One of the characteristic features when etching graphene by catalytic NPs is that nanometer-sized trenches in graphene are formed by moving NPs.

## 2. Diblock Copolymers and Their Micelles

### Nanopatterning by diblock copolymers

Diblock copolymers, consisting of two chemically distinct homopolymers linked by a covalent bond, spontaneously assemble into a variety of periodic nanostructures including spheres, cylinders, gyroids, and lamellae, of which the size and morphology can be controlled by the molecular weight, volume ratio, and Flory-Huggins interaction parameters ( $\chi$ ) of the copolymer blocks. In particular, for diblock copolymer films with thicknesses of less than 100 nm, the self-assembly process is strongly influenced by the interface energetics (*i.e.*, film-substrate, and film-free space). When a thin film of diblock copolymers on a strongly preferential surface is thermally annealed over the glass transition temperature ( $T_g$ ) of both blocks, in-plane microdomains in copolymer films evolve. In contrast, provided that the surface of a substrate is modified such that the interfacial energy is identical for both blocks, the microdomains are aligned perpendicular to the substrate.

Thin films of diblock copolymers with periodic nanostructures have been utilized as etching masks to fabricate arrayed nanostructures by an ultrahigh density with taking advantage of different etching rates between two blocks or topological patterns. For example, a pioneering work by Chaikin *et al.* demonstrated that a thin film of asymmetric polystyrene-*block*-polybutadiene (PS-PB) can be utilized for the fabrication of dense arrays of holes and dots on a Si<sub>3</sub>N<sub>4</sub>-coated Si wafer.<sup>[34]</sup> Furthermore, nanostructured copolymer thin films can be utilized as nanotemplates to prepare arrays of diverse metal and oxide nanomaterials via a deposition process or by means of chemical synthesis. In early work by Russell *et al.*, either minor or major blocks in self-assembled thin films of polystyrene-*block*-poly(methyl methacrylate) (PS-PMMA) were removed, followed by the deposition and removal

of metal to fabricate arrayed metal nanodots and a holey metal film.<sup>[35]</sup> Likewise, ordered, periodic nanopatterns of diblock copolymer thin films can easily be transferred onto another materials, and a variety of ordered inorganic nanostructures can be generated without difficulties.

When diblock copolymers are dissolved into a selective solvent for one block, they form spherical micelles with soluble corona blocks and insoluble core blocks. Because precursors of NPs can be selectively loaded into core regions, copolymer micelles can be used as templates to synthesize NPs. In particular, micelles can be spin-coated onto a substrate to prepare a single-layered micellar film, followed by a post-treatment step such as plasma etching or heating to generate arrays of NPs while preserving the original pattern of the copolymer micelles.<sup>[36-39]</sup> Additionally, the sizes and spacings of the NPs can be adjusted on the nanoscale using the molecular weights of the copolymers.<sup>[40,41]</sup>

Because diblock copolymer micelles provide a facile means of preparing arrays of NPs on a substrate, they have been utilized to form complex surface structures with nanoscale features for surface patterning. For example, Au NPs were synthesized from polystyrene-*block*-poly(2-vinyl pyridine) (PS-P2VP) micelles, followed by an anisotropic etching process consisting of various gas plasma treatments to transfer the hexagonal pattern of NPs onto a semiconducting GaAs substrate.<sup>[42]</sup> Because there are few limitations with regard to the choice of substrate when preparing a single-layered film of diblock copolymer micelles, the micellar approach can be extended to the nanopatterning of a large number of materials.

### **Diblock copolymer approach for graphene nanopatterning**

Diblock copolymers can easily be spin-coated onto graphene and its related

materials; hence, the self-assembly of diblock copolymers has been utilized for graphene nanopatterning with a combination of conventional lithographic processes. The most representative work is the fabrication of graphene nanomeshes using a PS-PMMA nanoporous template as an etching mask.<sup>[43]</sup> To achieve appropriate etching contrast during the fabrication of nanomeshes with diblock copolymers, a two-step procedure was employed. First, a nanopattern of diblock copolymers was transferred onto a SiO<sub>2</sub> layer deposited onto graphene. The patterned SiO<sub>2</sub> layer was used as an etching mask to generate graphene nanomeshes by the reactive ion etching (RIE) process. By varying the molecular weights of the diblock copolymers, the periodicity and neck size of the holes in the nanomeshes were controlled, allowing adjustment of electronic properties of the graphene nanomeshes.

In addition, diblock copolymers having high  $\chi$  values such as polystyrene-*block*-poly(dimethylsiloxane) (PS-PDMS) have exhibited great promise with regard to the realization of graphene nanoribbon with sub-10 nm widths.<sup>[44]</sup> PS-PDMS, a silicon-containing diblock copolymer, leaves inorganic oxidized silicon after a treatment with oxygen plasma such that the pattern transfer process onto the substrate is easier and more effective. The directed self-assembly (DSA) of cylinder-forming PS-PDMS within topographical patterns on graphene led to the formation of well-aligned PDMS cylinders in a PS matrix, of which the line patterns were transferred onto graphene to generate arrays of graphene nanoribbons.<sup>[45,46]</sup> A similar approach with sphere-forming PS-PDMS was applied to the fabrication of graphene quantum dots.<sup>[47]</sup>

Kim *et al.* demonstrated the direct formation of self-assembled diblock copolymer structures by tuning the surface energy of rGO with accurate control of

the degree of reduction.<sup>[48]</sup> Copolymer templates on rGO were transformed onto arrays of metal NPs or nanowires (NWs) by conventional pattern transfer methods and were utilized for the nanopatterning of diverse flexible (*i.e.*, PDMS) and nonplanar geometries.<sup>[49]</sup>

The examples of graphene nanopatterning using diblock copolymers mentioned above clearly indicate that the self-assembly of diblock copolymers can be used as a highly effective and versatile tool for the preparation of graphene nanostructures.

### 3. Aims and Objectives

In this dissertation, the fabrication of ordered inorganic nanostructures by diblock copolymers and their micelles is described. Arrays of metal and oxide nanostructures were synthesized on substrates or graphene directly and utilized for graphene nanopatterning. The combination of diblock copolymer micellar lithography with graphene allowed for the tunable nanopatterning of graphene in terms of their shape, size, and periodicity. Specifically, thin films of polystyrene-*block*-poly(4-vinyl pyridine) (PS-P4VP) diblock copolymers are mainly discussed here as a template for the synthesis of metal nanomaterials, which is distinguished from other works regarding graphene patterning by diblock copolymers. The P4VP block can stably coordinate metal ions for the synthesis of metal nanostructures upon a further treatment of heating or oxygen plasma. Thus, the fabrication of arrayed nanostructures such as NPs, NWs and nanorings (NRs) with PS-P4VP is much simpler and easier than fabricating such devices using diblock copolymer templates with the conventional lithographic pattern transfer methodology. Taking advantage of this PS-P4VP approach, an effective means of pattern transfer onto graphene without complex deposition, lift-off processes, and specialized etching equipment is illustrated in this dissertation.

## Chapter II

### Fabrication of Arrayed Inorganic Nanostructures

#### 1. Arrayed TiO<sub>2</sub> nanostructures

TiO<sub>2</sub>, one of typical metal oxide semiconducting materials with a large band gap (~3.0 eV for the rutile and ~3.2 eV for the anatase phase), is commonly used in various water-splitting<sup>[50]</sup> and photovoltaic applications<sup>[51]</sup> due to its powerful photocatalytic effect. In particular, arrays of nanostructured TiO<sub>2</sub> have size-tunable and other interesting properties, which are absent in their bulk counterparts. Thus, there has been much effort to fabricate and characterize arrayed TiO<sub>2</sub> nanostructures.

Several considerations are important during for the synthesis of uniformly arrayed TiO<sub>2</sub> nanomaterials on substrates when using lithography-free methods. For example, the spatial position on a substrate when a synthetic process is used must be accurately controlled. In addition, aggregation should be avoided by adjusting the reaction time and synthesis orientation. The sizes and chemical compositions of nanomaterials must be precisely controlled as well. Because an ordinary free substrate lacks the capability to guide the synthesis of nanoarrays, placing nano-sized templates on a substrate has been proposed to help the controlled synthesis of arrayed nanostructures. This use of a template has been proven to provide a potential solution for the efficient fabrication of well-ordered arrays of nanomaterials with desired morphologies and sizes. For example, AAO membranes having periodic nano-size hole arrays have been widely utilized as a template for the fabrication of nanorods and nanotubes of TiO<sub>2</sub>.<sup>[52]</sup>

Thin films of diblock copolymers with periodic nanostructures can be effectively

utilized as a nanotemplate for the fabrication of ordered TiO<sub>2</sub> nanostructures as reported in earlier works.<sup>[53,54]</sup> A template based on the self-assembly of diblock copolymers can produce diverse TiO<sub>2</sub> morphologies with controlled size and spacing. In this section, the fabrication of rod-shaped TiO<sub>2</sub> nanostructures (RTNs), disc-shaped TiO<sub>2</sub> nanostructures (DTNs), and line-shaped TiO<sub>2</sub> nanostructures (LTNs) is demonstrated using polymeric nanotemplates produced from the self-assembly of PS-PMMA.

## **Experimental section**

*Materials:* Diblock copolymers of PS-PMMA, PS(80)-PMMA(80), PS(46)-PMMA(21), PS(140)-PMMA(60), PS(5)-PMMA(5), and were purchased from Polymer Source, Inc. The molecular structures of PS and PMMA are depicted in Figure 2.1a. The number in the parenthesis is the average molecular weight ( $M_n$ ) in kg/mol. The polydispersity index (PDI) is 1.09, 1.09, 1.08, and 1.09, respectively. Phenethyltrichlorosilane (PETS), titanium tetraisopropoxide (Ti(OCH(CH<sub>3</sub>)<sub>2</sub>)<sub>4</sub>, TTIP), were obtained from Sigma-Aldrich and used as received.

*Preparation of nanotemplates:* A Si wafer was cleaned in piranha solution (70/30 v/v concentrated H<sub>2</sub>SO<sub>4</sub> and 30% H<sub>2</sub>O<sub>2</sub>), thoroughly rinsed with deionized water, and dried with a nitrogen stream. The surface of Si wafer was neutralized to have the same interfacial energy toward both PS and PMMA blocks of the copolymers with PETS self-assembled monolayers (SAMs). For the deposition of the PETS SAMs on a Si wafer, the substrate was immersed into a 0.1 % (v/v) anhydrous toluene solution of PETS for 2 h and then was thoroughly rinsed with ethanol. On the neutralized substrate, the PS-PMMA copolymers were spin-coated from a toluene solution (3.0 wt% for PS(46)-PMMA(21), 1.5 wt% for PS(140)-

PMMA(60), and 2.5 wt% for PS(80)-PMMA(80)) at 4000 rpm for 60 s and were annealed at 230 °C for 4 h in vacuum to self-assemble into perpendicularly ordered periodic nanostructures by the microphase separation. To produce polymer nanotemplates, the PMMA blocks were selectively removed by means of exposing the copolymer film to UV light (254 nm, 15 W) for 2 h in vacuum and rinsing with acetic acid and deionized water.

*Fabrication of TiO<sub>2</sub> nanostructures:* To fabricate TiO<sub>2</sub> nanostructures from the copolymer nanotemplates, the substrates with the nanotemplate were initially treated with oxygen plasma performed at 80 W in 0.038 Torr for 3 s. Plasma-treated substrates were deposited with TTIP sol (TTIP 5.632 g + HCl 1.98 g dissolved in isopropanol 22 mL) by coating using a KSV dip-coater (dipping speed = 85 mm/min, dipping time = 30 s, withdrawing speed = 10 mm/min). The substrates were fully dried by exposure to air. The TiO<sub>2</sub> overlayers on the copolymer nanotemplates were inevitably formed during the dip-coating process, which were removed by means of CF<sub>4</sub> reactive ion etching (RIE). Then the substrates underwent an oxygen plasma treatment which was performed at 100 W in 0.038 Torr for 5 min such that the copolymer nanotemplates were fully removed, resulting in RTNs, DTNs, and LTNs on the substrates.

*Characterization:* The copolymer nanotemplates and TiO<sub>2</sub> nanostructures were analyzed using a field-emission scanning electron microscope (FE-SEM, Hitachi S-4300 at 15 kV) and a multimode 8 atomic force microscope (AFM) with a Nanoscope V controller (Bruker) in tapping mode with Al-coated Si cantilevers.

## **Results and Discussion**

A thin film of the cylinder-forming PS(46)-PMMA(21) was spin-coated onto a

neutralized Si wafer, which self-assembled into perpendicularly-oriented cylindrical structures by thermal annealing at a temperature over  $T_g$ . The FE-SEM image (Figure 2.1b) represents arrayed nanopores (black holes in the image) after the selective removal of the PMMA blocks as described in the experimental section. The diameters and spacings of hexagonally-ordered pores calculated upon this FE-SEM image are  $\sim 14.6 \pm 1.8$  nm and  $\sim 32$  nm, respectively. It should be noted that the calculated pore diameters is different from the real values due to Pt layers deposited onto the polymeric templates prior to the observation by FE-SEM. The deposition rate is approximately 6 nm/min during the sputtering process (20 s). Thus, it is assumed that the difference in the diameters of the nanopores between the result of the measurement and the true value is  $\sim 4$  nm. The FE-SEM image in Figure 2.1c shows that the nanopores are vertically oriented and continuously connected from the bottom to top.

Then the PS nanoporous templates were treated with an oxygen plasma, leading to more hydrophilic surface of the templates. The templates were immersed into TTIP sol and treated with a  $\text{CF}_4$  RIE for the removal of the  $\text{TiO}_2$  overlayer, which was inevitably formed during the dip-coating process. Then the PS nanoporous templates were thoroughly eliminated by an oxygen plasma etching, resulting in the effective template-assisted production of arrayed RTNs on a substrate as displayed in Figure 2.1d and 2.1e. The diameters ( $\sim 18.8 \pm 2.3$  nm) and spacings ( $\sim 33$  nm) of the RTNs are similar to those of original nanopores in the PS nanotemplates. This observation implies that each nanopore produced single  $\text{TiO}_2$  RTN while preserving the size and morphology. However, the height of RTNs ( $\sim 53$  nm) is reduced from the thickness of the templates ( $\sim 90$  nm) due to the over-etching during the RIE process.

To demonstrate the controllability over the sizes and spacings of nanopores by managing the molecular weights of the copolymers, the cylinder-forming PS(140)-PMMA(60) was used. However, the high molecular weight of the copolymers impeded the mobility of the copolymers, the parameter which is essential to form well-ordered arrays of the nanopores with regular sizes, resulting in irregular nanopores as shown in Figure 2.2a and 2.2b. To promote the self-assembly process of the copolymers, as suggested in elsewhere,<sup>[55]</sup> the low molecular weight PS(5)-PMMA(5) was blended with a weight ratio of 0.4. FE-SEM images in Figure 2.2c, 2.2d, and AFM image in Figure 2.3a clearly show the notable improvement in the lateral order of the nanopore arrays. The diameters ( $\sim 28.7 \pm 2.6$  nm) and spacings ( $\sim 69$  nm) of the nanopores were calculated upon FE-SEM images. Since the molecular weight of PS(140)-PMMA(60) is much higher than the previous PS(46)-PMMA(21), the sizes and inter-distances of pores increased. The thickness of the nanoporous template is  $\sim 51$  nm.

The same method of fabricating inverted TiO<sub>2</sub> nanostructures was applied to the PS(140)-PMMA(60) nanoporous templates as well, resulting in the successful production of the arrayed DTNs on a substrate as shown in the AFM image (Figure 2.3b) and the FE-SEM image (Figure 2.3c). The calculated diameters ( $\sim 34.1 \pm 3.9$  nm) and spacings ( $\sim 67$  nm) of the DTNs clearly manifest the effective fabrication of different types of TiO<sub>2</sub> nanostructures from the copolymer nanotemplates. It should be noted that a CF<sub>4</sub> RIE led to the reduction of the height of the DTNs ( $\sim 28$  nm), compared with that of the PS nanoporous templates.

The symmetric PS(80)-PMMA(80) also created the different nanotemplates with lamellar morphology. The AFM image in Figure 2.4a and FE-SEM image in Figure 2.4b show the nanogroove templates of  $\sim 69$  nm thickness. The selective removal

of the PMMA microdomains (the dark lines in Figure 2.4a) resulted in a fingerprint topographic pattern consisting of cross-linked PS nanogrooves (the bright lines in Figure 2.4a). The spacings between the PS nanogrooves ( $\sim 77$  nm) was calculated upon the AFM image by means of spectral density analysis. The PS nanogroove template was used as a mold to produce the arrays of the LTNs with an inverted structure as shown in Figure 2.4c and 2.4d. The spacing of the LTNs ( $\sim 77$  nm) is equal to that of the original PS nanogrooves, while the height of the LTNs ( $\sim 28$  nm) is smaller than the thickness of the PS nanogroove template as explained in previous instance.

These results indicate that the final morphologies and sizes of various types of  $\text{TiO}_2$  nanopatterns can be effectively controlled by polymeric nanotemplates which were produced from the self-assembled thin films of the PS-PMMA.

## **Summary**

The various arrays of the  $\text{TiO}_2$  nanostructures were created from the PS nanotemplates with the cylindrical nanopores and lamellar nanogrooves. The molecular weights of the PS-PMMA determined the morphology, size and spacing of the nanostructures of the templates, which enabled the accurate adjustment of types of inverted  $\text{TiO}_2$  nanostructures, in this case the RTNs, DTNs and LTNs.

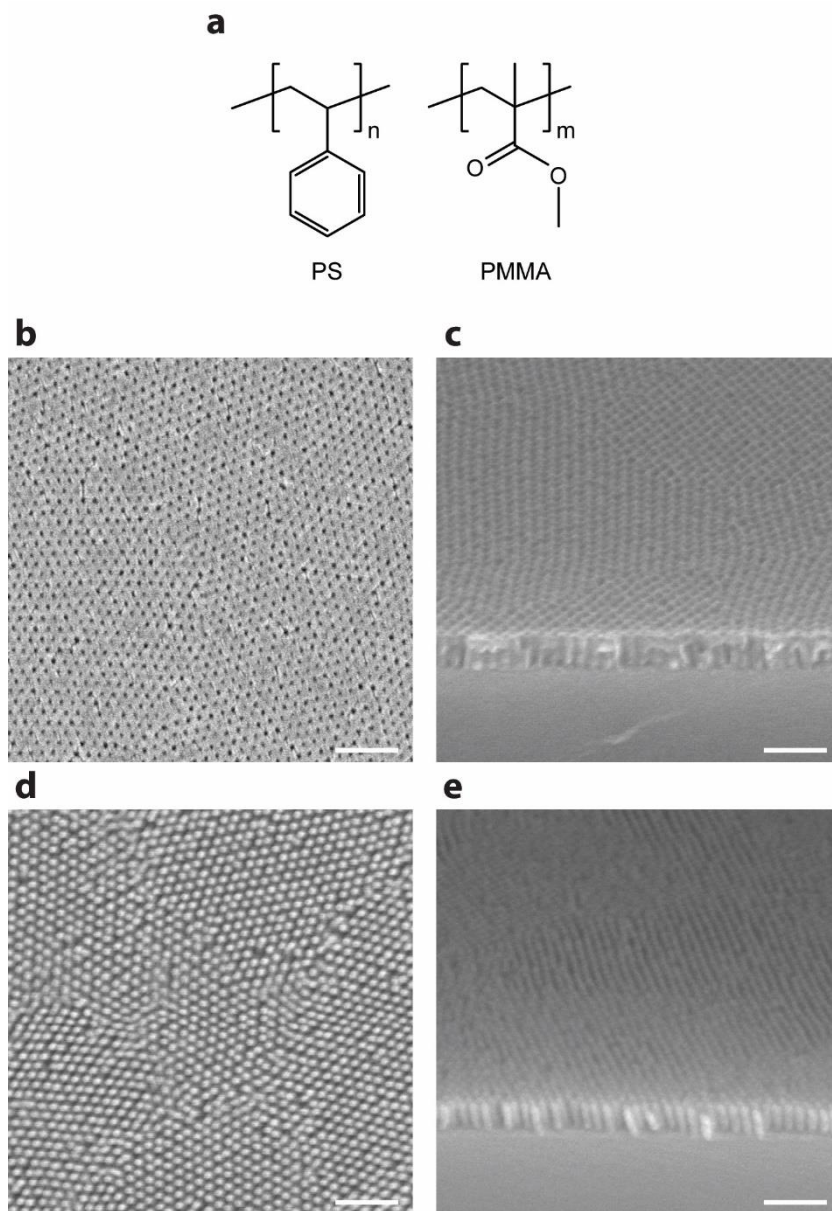


**Figure 2.1.** FE-SEM images of PS nanotemplates and RTNs. (a) Molecular structures of PS and PMMA; (b,c) Top- and tilt-view images of PS nanoporous template fabricated from PS(46)-PMMA(21); (d,e) RTNs after RIE. Scale bars are 200 nm.

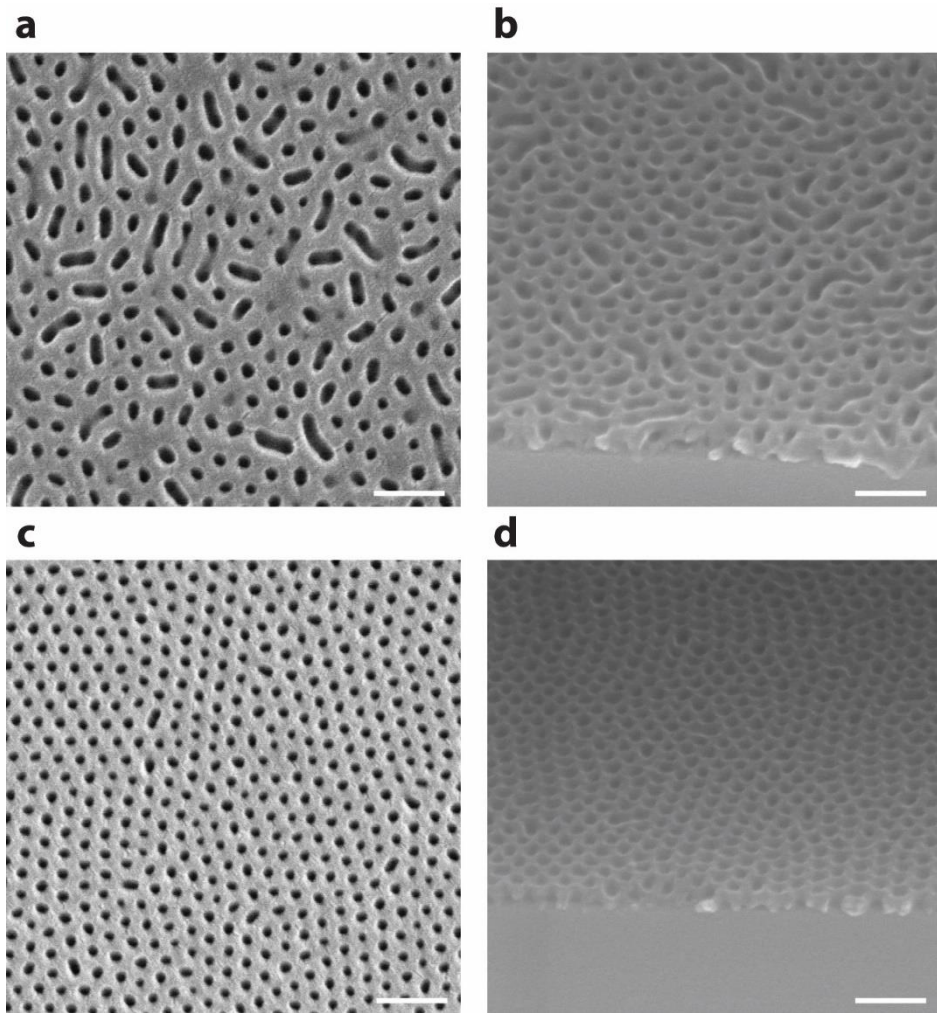


**Figure 2.2.** FE-SEM images of PS nanotemplates. (a,b) Top- and tilt-view images of PS nanoporous template fabricated from PS(140)-PMMA(60); (c,d) Top- and tilt-view images of PS nanoporous template fabricated from mixture of PS(140)-PMMA(60) and PS(5)-PMMA(5). Scale bars are 200 nm.

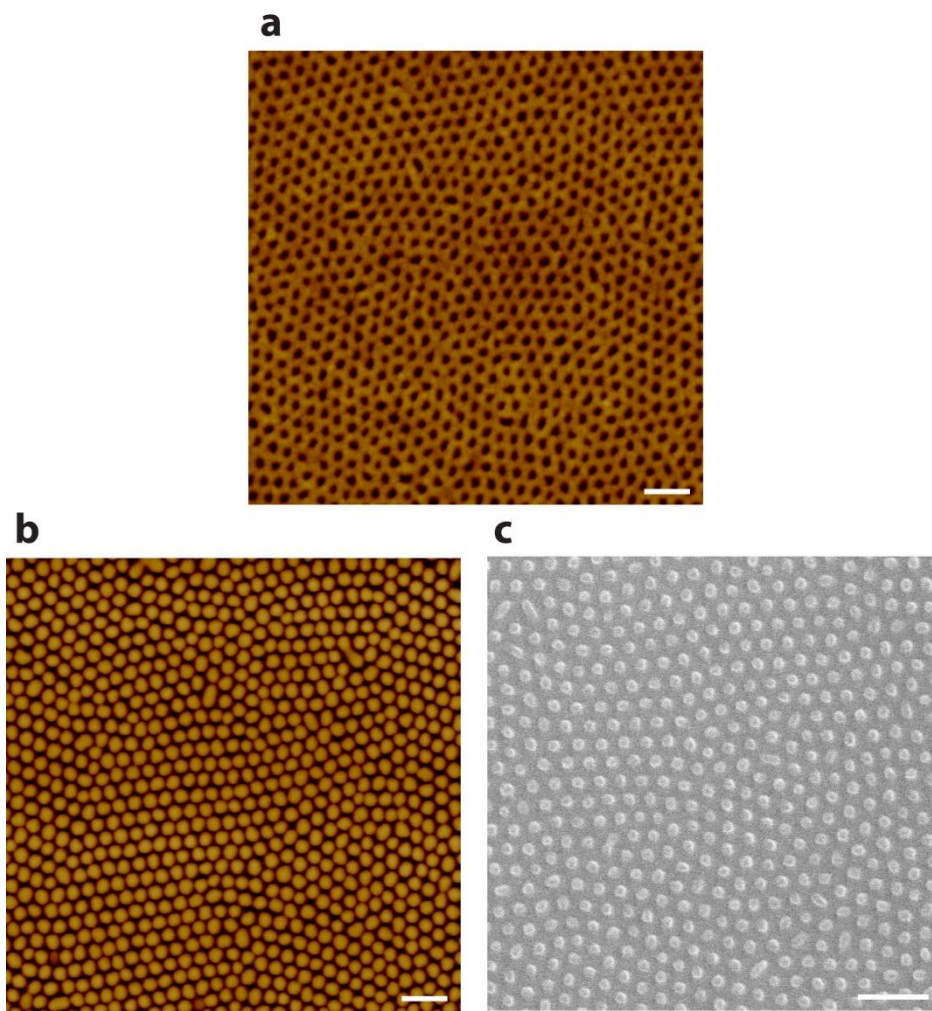


**Figure 2.3.** PS nanotemplates and DTNs. (a) AFM image of PS nanoporous template fabricated from a mixture of PS(140)-PMMA(60) and PS(5)-PMMA(5); (b,c) AFM and FE-SEM images of DTNs fabricated from PS nanoporous template displayed in (a). Scale bars are 200 nm.

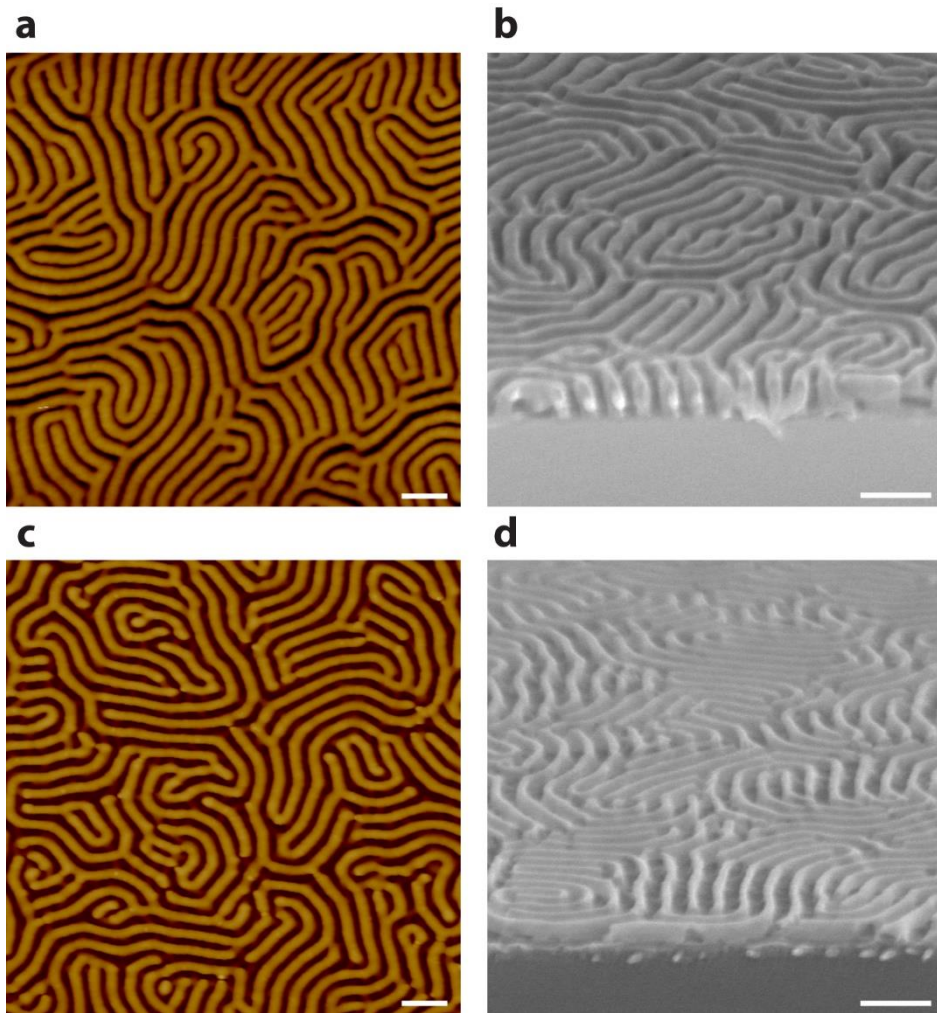


**Figure 2.4.** PS nanotemplates and LTNs. (a,b) AFM and tilt-view FE-SEM images of PS nanogroove template fabricated from PS(80)-PMMA(80); (c,d) AFM and tilt-view FE-SEM image of LTNs fabricated from PS nanogroove template displayed in (a,b). Scale bars are 200 nm.

## 2. Arrayed nanoparticles

NPs, defined as particles with dimensions on the nanometer scale, have remarkably different properties from their bulk counterparts and can be employed for the fabrication of novel electronic, photonic, and chemical nanodevices. Among the range of synthetic strategies currently available, the liquid-phase fabrication method based on reverse micelles consisting of amphiphilic molecules has demonstrated the efficient synthesis of various NPs with a narrow size distribution. This is possible because self-assembled structures in a solution state impose constraints on the growth of NPs in their core regions, acting collectively as a nanoreactor.<sup>[56]</sup> Reverse micelles formed by amphiphilic diblock copolymers such as PS-P4VP have also been thoroughly explored in an effort to synthesize NPs from precursors loaded into the cores of micelles.<sup>[57]</sup>

Diblock copolymer micelles, however, can be transferred onto a substrate to form a monolayered structured assembly of micelles by dip- or spin-coating, which is remarkably distinct from other reverse micelles based on small surfactant molecules. From this micellar film, arrayed monodisperse NPs without aggregation can be synthesized *in situ* by a plasma treatment that transforms precursors in core regions into NPs, resulting in the strongly controlled and precise location of NPs on a solid substrate. In addition, during the plasma treatment, copolymers as a capping agent for NPs are clearly removed to produce a pure surface without extra layers on the NPs. Moreover, because the size and spacing of the NPs can easily be adjusted via the molecular weights of the copolymers, the copolymer micellar approach is useful for studying size- and number-dependent properties of arrayed NPs.

This section describes the fabrication of various metal and oxide NP arrays from

a single-layered films of PS-P4VP reverse micelles. The molecular weights of the copolymers were tuned to alter the diameter and spacing of the NPs on the nanoscale.

## **Experimental Section**

*Materials:* Diblock copolymers of PS-P4VP, PS(25)-P4VP(7), PS(33)-P4VP(8), PS(32)-P4VP(13), PS(51)-P4VP(18), PS(48)-P4VP(21), PS(75)-P4VP(25), and PS(109)-P4VP(27) were purchased from Polymer Source, Inc. The molecular structures of PS and P4VP are illustrated in Figure 2.5a. The number in the parenthesis is the average molecular weight ( $M_n$ ) in kg/mol. The polydispersity index (PDI) is 1.10, 1.10, 1.08, 1.15, 1.14, 1.09, and 1.15, respectively. Tetrachloroauric(III) acid ( $\text{HAuCl}_4$ ) and chloroplatinic(IV) acid ( $\text{H}_2\text{PtCl}_6$ ) as precursors of Au and Pt NPs, respectively, were obtained from Sigma-Aldrich and used as received.

*Diblock copolymer micelles containing precursors of NPs:* The PS-P4VP diblock copolymers were dissolved in toluene, a strongly selective solvent for the PS block, with a concentration of 0.5 wt%. The solution was stirred for 24 h at room temperature and for 3 h at 85 °C and then cooled to a room temperature. The precursors of the NPs were added to the micellar solution. The molar ratio of the precursors to pyridine units in the P4VP block was fixed to 0.5 for both cases. The solution was stirred for at least 7 days at a room temperature.

*Synthesis of NPs:* Prior to the spin-coating of the PS-P4VP micellar solution, a Si wafer was cleaned in a piranha solution at 90 °C for 30 min, and thoroughly rinsed with deionized water several times, and then blown dry with a nitrogen stream, while indium tin oxide (ITO)-coated glass (ITO/glass) substrates (15~20  $\Omega/\text{sq}$ )

were cleaned by the ultrasonication with isopropanol, acetone, and methanol for 10 min each and were dried with a nitrogen stream. The single-layered film of PS-P4VP micelles containing the precursors of the NPs in their core regions was spin-coated at 2000 or 4000 rpm for 60 s onto the Si wafer, ITO/glass, and a freshly cleaved mica. To synthesize the NPs, copolymer micellar film was treated with an oxygen plasma performed at 100 W in 0.038 Torr for 5 min.

*Characterization:* The PS-P4VP micelles, NPs were analyzed using a Multimode 8 atomic force microscope (AFM) with a Nanoscope V controller (Bruker) in tapping mode with Al-coated Si cantilevers and a transmission electron microscopy (TEM, Hitachi 7600 at 100 kV). For the observation by TEM, the micellar film and arrayed NPs were floated off from the substrate onto deionized water by delamination, and collected on carbon-coated copper TEM grids. The detailed description regarding the delamination process will be mentioned in the subsequent part. To acquire micrographs with a high contrast, the TEM grids with the PS-P4VP micellar film were exposed to I<sub>2</sub> prior to the observation. A high-resolution TEM (HR-TEM) was performed on a JEM-2100 at 200 kV to obtain magnified TEM images of the individual NPs and the selected area electron diffraction (SAED) pattern.

## **Results and Discussion**

Under the condition of an appropriate condition for spin-coating speed and concentration of copolymer micellar solution, a hexagonal assembly of micelles can be prepared on a substrate. The AFM images in Figure 2.5 represents that the single-layered films of copolymer micelles with different molecular weights have a quasi-hexagonal order, which is evenly coated over the entire substrate. The spacings of arrayed micelles of PS(51)-P4VP(18), and PS(109)-P4VP(27) were

obtained to be ~53 nm, and ~118 nm, respectively. Generally the size of the copolymer micelle is related to the aggregation number ( $Z$ ), the number of copolymer chains per single micelle, which can be expressed by

$$Z = Z_o \left( N_A^\alpha N_B^{-\beta} \right) \quad (2.1)$$

where  $N_A$  and  $N_B$  are the degree of polymerization of the core and corona block, respectively, and the parameter  $Z_o$  is related to  $\chi$  and the monomer volume. Equation 2.1 implies that the diameter of the micelles becomes larger as the molecular weights of copolymers increase. Thus, the spacing of the micelle increase as well.

The micellar films on a freshly cleaved mica were delaminated and floated onto the water, which were transferred onto a Cu mesh grid for the observation by TEM. Each TEM image in Figure 2.6 corresponds to the same copolymer micellar film previously investigated by AFM (Figure 2.5). The P4VP cores were selectively stained by  $I_2$  and appeared as dark spheres in the TEM images. The measured diameter of the PS(51)-P4VP(18) and PS(109)-P4VP(27) micellar cores displayed in Figure 2.6 are ~25 nm, and ~34 nm, respectively. Since core regions are composed of insoluble P4VP core blocks, the core size of micelles depends on the length of P4VP chain. The relationship between the size and the degree of polymerization of the core blocks is represented by equation 2.2.

$$\frac{4}{3} \pi R_C^3 = Z N_A v_A \quad (2.2)$$

where  $R_C$  and  $v_A$  is the radius of core blocks and the molar volume of core monomers, respectively. This denotes the size of the whole micelles and core regions can easily be tuned by managing the molecular weights of the diblock copolymers.

To utilize the PS-P4VP micelles as nanoreactors for the synthesis of the NPs, metal salts were added to the micellar toluene solution. The metal salt powders

remain intact initially at the bottom of the solution owing to their poor solubility in toluene. With stirring for several days, the metal precursors are eventually dissolved in toluene to form a colored homogeneous solution. This phenomenon entails a couple of the chemical interactions: the coordination and electrostatic interactions. Polymers such as P4VP and poly(ethylene oxide) (PEO) can interact with the transition metal salts to form the coordination complexes through heteroatoms with lone pair electrons (nitrogen for P4VP and oxygen for PEO). Additionally, the nitrogen atom in pyridine unit of P4VP can be quaternized in an acidic condition, which allows for the interaction with metal-containing complex anions.  $\text{HAuCl}_4$  and  $\text{H}_2\text{PtCl}_6$ , the metal salts used in this experiment, can protonate the nitrogen atoms in the pyridine units to build the coordination complex with  $[\text{AuCl}_4]^-$  and  $[\text{PtCl}_6]^{2-}$ , while the incorporated metal salts are well distributed in P4VP core regions.

The  $\text{HAuCl}_4$ -containing copolymer micelles were spin-coated onto an ITO/glass to form a single-layered film, followed by an oxygen plasma. Unlike copolymers,  $\text{HAuCl}_4$  cannot be removed but agglomerates into the Au NPs at the confined local region of the P4VP micellar core blocks. During this process, the reduction process by the intermediate oxidation products of the polymer such as CO and electrons from the plasma assists the formation of the Au NPs from the precursors. To characterize the synthesized Au NPs by TEM, the PMMA layer was spin-coated onto an ITO/glass with arrayed Au NPs, which was delaminated from the substrate by an exposure to a HCl droplet. Since ITO is quickly dissolved by the strong acid such as HCl, the PMMA layer with arrayed Au NPs can easily be floated off onto the deionized water and transferred onto a Cu TEM grid. TEM images in Figure 2.7 show various arrays of the Au NPs synthesized from the PS-P4VP having

different molecular weights; PS(25)-P4VP(7), PS(32)-P4VP(13), and PS(51)-P4VP(18). Hereafter, for the convenience, the NPs synthesized from PS(x)-P4VP(y) are denoted as (x-y); for example, the Au NPs synthesized from PS(51)-P4VP(18) to Au(51-18). Table 2.1 summarizes the spacing, number density, and diameter of the Au NPs measured upon those TEM images. Since the Au NPs are synthesized at the core regions of the micelles while preserving the hexagonal order of the original micelles, the spacing of the Au NPs is similar to that of the copolymer micelles, which increases with total molecular weights of the copolymers (compare **1, 2, 3, 5, 6** in Table 2.1). In addition, the spin-coating speed can also control the spacing of the Au NPs (**3, 4** in Table 2.1). Moreover, the copolymer micelles with a higher molecular weight P4VP block produce larger Au NPs, because the NPs are synthesized from the greater amount of H<sub>2</sub>AuCl<sub>4</sub> in the larger P4VP core (**4, 5** in Table 2.1). These results strongly indicate that the size and spacing of arrayed Au NPs can be precisely adjusted in nanoscale by managing molecular weights of PS-P4VP and spin-coating conditions.

To synthesize the Pt NPs, H<sub>2</sub>PtCl<sub>6</sub> was loaded into the core blocks of the PS-P4VP micelles. The single-layered films of the H<sub>2</sub>PtCl<sub>6</sub>-containing micelles were transferred onto a Si<sub>3</sub>N<sub>4</sub> TEM grid, which was heated in air at 400 °C for 30 min. The copolymers were thermally decomposed at a high temperature, and H<sub>2</sub>PtCl<sub>6</sub> formed the Pt NPs at the core region as shown in Figure 2.8. As mentioned in the discussion regarding the synthesis of the Au NPs, the diameters and spacings of arrayed Pt NPs strongly rely on the molecular weights of the PS-P4VP. The diameter and spacing values of Pt(32-13), Pt(51-18), and Pt(109-27) are summarized in Table 2.1.

Note that the synthesized Au and Pt NPs are crystalline NPs with lack of oxides

according to the SAED patterns and the lattice fringes observed in the magnified HR-TEM images of single NPs (Figure 2.9). This can be explained by the thermodynamic consideration of oxide formation. The enthalpy of formation ( $\Delta H_f$ ) of Au and Pt oxides are positive, and  $\Delta S$  is negative in the oxidation reaction of metals, making the free energy of formation of oxides ( $\Delta G_f$ ) positive. Due to their instability, Au and Pt oxides are easily convert to Au and Pt at high temperature (even at room temperature for Au).<sup>[57]</sup> Thus, Au and Pt NPs without oxides were obtained in this experiment.

## **Summary**

The hexagonal nanopatterns of arrayed Au and Pt NPs were prepared from the monolayered film of the PS-P4VP micelles. The NPs were synthesized from the precursors incorporated into the P4VP core regions while preserving the hexagonal order of the original copolymer micelles. In addition, an accurate control of diameter and spacing of NPs on the nanometer scale by changing molecular weights of copolymers was demonstrated.

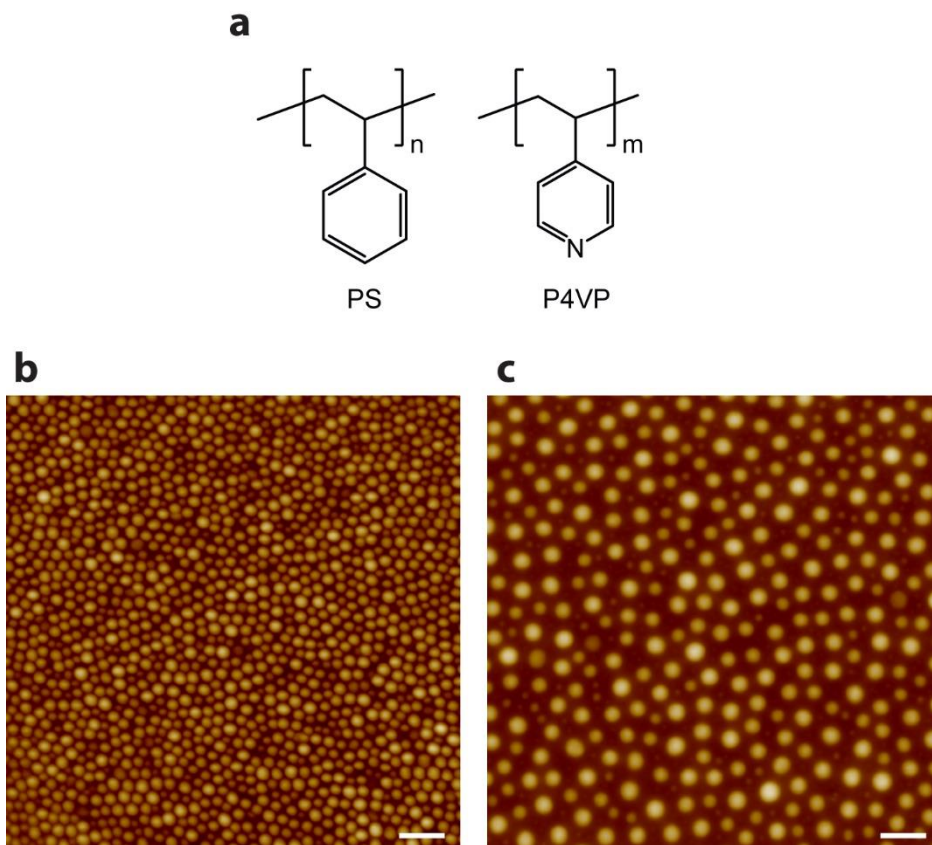


**Figure 2.5.** AFM images of single-layered films of PS-P4VP micelles. (a) Molecular structures of PS and P4VP; (b) PS(51)-P4VP(18); (c) PS(109)-P4VP(27). Scale bars are 200 nm.

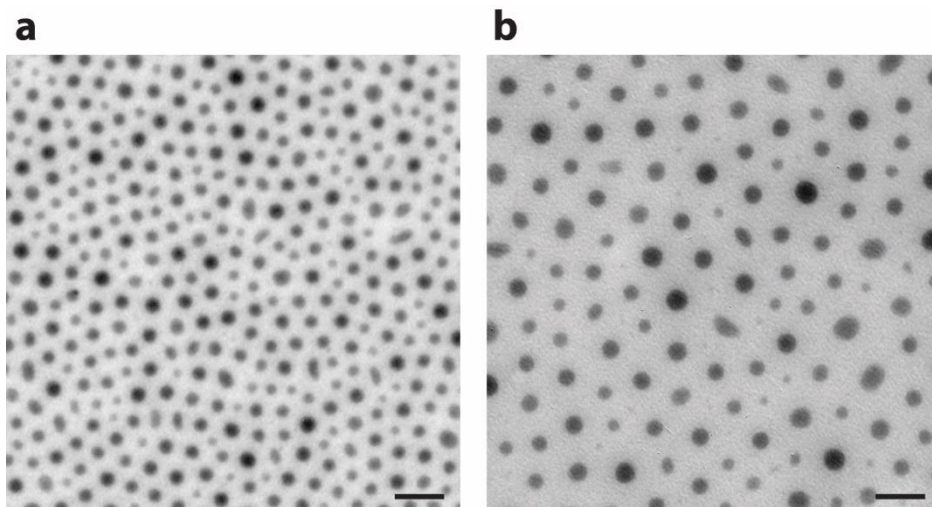


**Figure 2.6.** TEM images of single-layered films of PS-P4VP micelles. (a) PS(51)-P4VP(18); (b) PS(109)-P4VP(27). P4VP cores were selectively stained by I<sub>2</sub>. Scale bars are 100 nm.

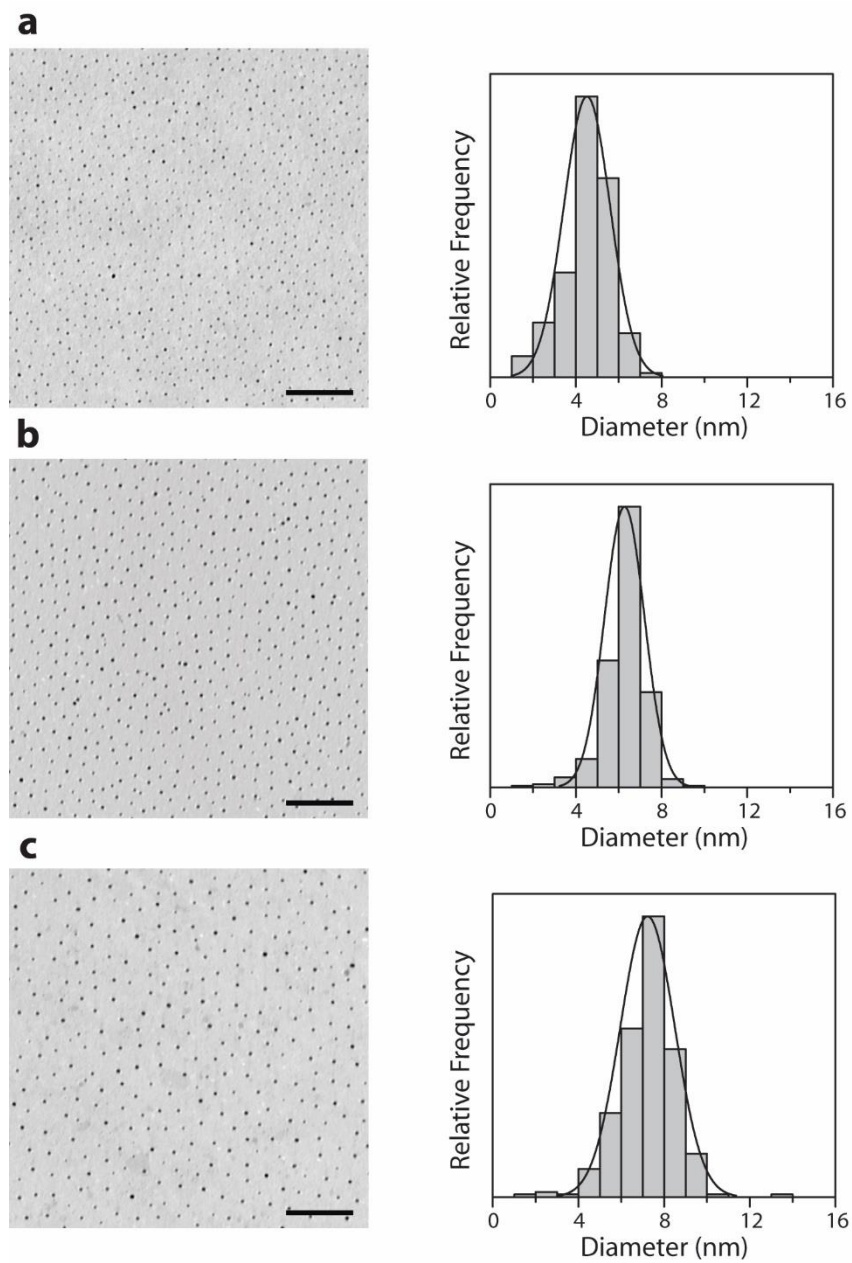


**Figure 2.7.** TEM images and size distribution histograms of arrayed Au NPs synthesized from PS-P4VP micelles. (a) Au(25-7); (b) Au(32-13); (c) Au(51-18). Scale bars are 100 nm.

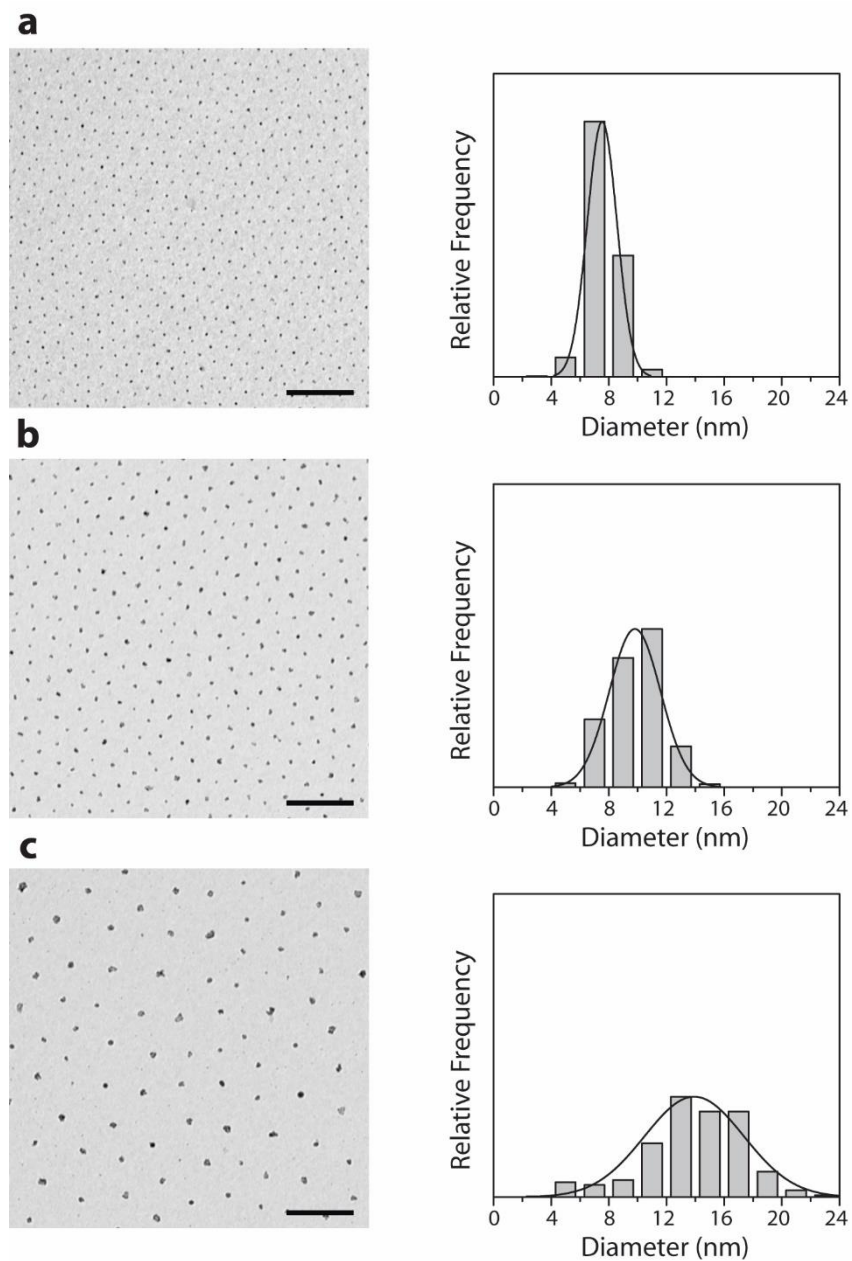


**Figure 2.8.** TEM images and size distribution histograms of arrayed Pt NPs synthesized from PS-P4VP micelles. (a) Pt(32-13); (b) Pt(51-18); (c) Pt(109-27). Scale bars are 100 nm.

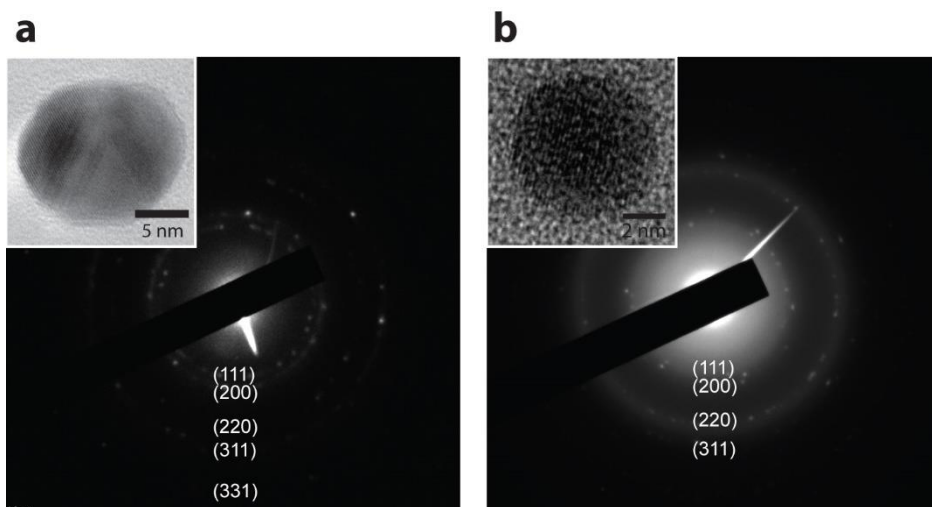


**Figure 2.9.** SAED pattern of NPs fabricated from PS-P4VP micelles. (a) Au(51-18); (b) Pt(51-18). Lattice planes are marked on each image. Insets are the HR-TEM image of an individual NPs.

Entry	Nanoparticles	rpm	Diameter (nm)	Spacing (nm)
1	Au(25-7)	4000	$4.5 \pm 1.1$	27
2	Au(32-13)	4000	$6.3 \pm 0.9$	35
3	Au(51-18)	4000	$6.8 \pm 1.3$	51
4	Au(51-18)	2000	$7.2 \pm 1.3$	46
5	Au(48-21)	2000	$8.6 \pm 1.1$	45
6	Au(75-25)	2000	$9.0 \pm 2.4$	60
7	Pt(32-13)	4000	$7.5 \pm 2.4$	35
8	Pt(51-18)	2000	$9.8 \pm 1.8$	51
9	Pt(109-27) <sup>†</sup>	2000	$13.9 \pm 3.4$	105

<sup>†</sup> molar ratio of precursors to pyridine unit was 0.35.

**Table 2.1.** Synthetic conditions and characteristics of the NPs fabricated from PS-P4VP micelles.

### 3. Arrayed nanowires

Diblock copolymer micelles preserve their original spherical shape during spin-coating because the micellar film exists in a kinetically frozen state due to the fast evaporation of the solvent. Thus, spherical core blocks as a nanoreactor allow for the effective fabrication of spherical metal NPs on a substrate, as demonstrated in the previous section, implying that the shape of the final metal nanostructures synthesized *in situ* resembles that of self-assembled microdomains. A self-assembled nanostructure of copolymer micelles can easily be transformed into other nanostructures, such as cylinders and lamellae by thermal annealing<sup>[58]</sup> or a solvent vapor treatment,<sup>[59]</sup> by which the synthetic approach by self-assembly of diblock copolymers can be extended to prepare one-dimensional metal or oxide nanostructures.

Compared with thermal annealing, solvent vapor annealing especially provides an effective means with which to control the morphology and orientation of the polymeric self-assembly process on a shorter time scale. When exposed to solvent vapors, diblock copolymer thin films become swollen with greatly enhanced mobility of polymer chains at a temperature below  $T_g$ , enabling the film to reach thermodynamically preferred nanostructures.<sup>[60]</sup> By adjusting several factors such as the temperature, degree of solvent uptake, and the drying time, a variety of ordered nanostructures can be generated from the same diblock copolymer thin film.

In this section, cylindrical nanostructures of diblock copolymers are realized by a treatment of the saturated vapor of a nonselective solvent, after which they are utilized as nanotemplates to synthesize arrayed NWs on a substrate. The spacing between the NWs is tuned by the molecular weights of the copolymers. In addition, combined with graphoepitaxy for the directed self-assembly (DSA) of copolymers,

the fabrication of well-aligned NWs is demonstrated.

## **Experimental Section**

*Materials:* Diblock copolymers of PS-P4VP, PS(19)-P4VP(5), PS(25)-P4VP(7), PS(33)-P4VP(8), PS(32)-P4VP(13), PS(50)-P4VP(13), PS(48)-P4VP(20), and PS(109)-P4VP(27) were purchased from Polymer Source, Inc. The number in the parenthesis is the average molecular weight ( $M_n$ ) in kg/mol. The polydispersity index (PDI) is 1.10, 1.10, 1.10, 1.08, 1.05, 1.13, and 1.15, respectively. Sodium hexachloroplatinate(IV) hexahydrate ( $\text{Na}_2\text{PtCl}_6 \cdot 6\text{H}_2\text{O}$ ) as the precursors of the Pt NWs was obtained from Sigma-Aldrich and used as received.

*Solvent vapor annealing for cylindrical nanostructures:* Prior to the spin-coating of the PS-P4VP micellar solution, a Si wafer having an oxide layer with 300 nm thickness ( $\text{SiO}_2/\text{Si}$ ) was cleaned in a piranha solution at 90 °C for 30 min, and thoroughly rinsed with deionized water several times, and then blown dry with a nitrogen stream. The PS-P4VP copolymers were spin-coated from a toluene solution (0.6 ~ 0.8 wt%) at 4000 rpm for 60 s, which were exposed to the saturated chloroform vapor in a closed 125 mL-jar at a room temperature for 30 min. After the solvent vapor annealing, the sample was removed to an ambient atmosphere immediately and dried rapidly.

*Fabrication of arrayed Pt NWs:*  $\text{SiO}_2/\text{Si}$  with the cylindrical PS-P4VP thin films were immersed in an acidic Pt salt aqueous solution for 3 h. This Pt precursor solution was prepared by mixing 18 mL of  $\text{Na}_2\text{PtCl}_6 \cdot 6\text{H}_2\text{O}$  aqueous solution (0.010 M) and 2 mL of 1.0 % HCl. Then the sample was dried under a nitrogen stream without rinsing with water or other organic solvents, followed by an oxygen plasma treatment for 5 min (0.038 Torr, 100 W).

*Trench fabrication on SiO<sub>2</sub>/Si:* 500-nm-wide line patterns on 6-inch SiO<sub>2</sub>/Si wafer were developed by a stepper (Nikon, NSR-2005i10C) with a 365 nm wavelength UV light source, followed by the CF<sub>4</sub> RIE to transfer the pattern onto SiO<sub>2</sub>/Si wafer to form 50-nm-deep trenches. The reticle used in this stepper process has the Cr mask deposited onto a quartz substrate by the photolithography.

*Characterization:* The cylindrical PS-P4VP thin films and arrayed Pt NWs were analyzed using an FE-SEM (Hitachi S-4300 at 15 kV), a multimode 8 AFM with a Nanoscope V controller (Bruker) in tapping mode with Al-coated Si cantilevers, and a TEM (Hitachi 7600 at 100 kV). To increase the topographic contrast by swelling, the copolymer films were immersed into ethanol at 50 °C for 2 h before the observation by FE-SEM. To prepare the observation by TEM, the copolymer films were floated off from the substrate onto deionized water by delamination, and collected on carbon-coated copper TEM grids. The delamination was done by the exposure of the sample to a NaOH droplet as described in the previous section. To acquire micrographs with a high contrast, TEM grids with the PS-P4VP film were exposed to I<sub>2</sub> prior to the observation.

## **Results and Discussion**

A single-layered film of the PS(25)-P4VP(7) micelles is displayed in Figure 2.10a. This micellar film was swollen by the saturated chloroform vapor in a closed glass jar to change the morphology from the micelles to the cylinders as shown in Figure 2.10b. Because the monolayer of the P4VP cylinders are perfectly embedded in PS matrix, the surface topographic contrast of the cylindrical PS-P4VP thin film is negligible. For a better observation, the copolymer films were transferred onto a TEM grid, followed by the selective staining with I<sub>2</sub>. The TEM image in Figure

2.10c clearly shows the line patterns of P4VP cylinders displayed as black lines. The spacing between cylinders was calculated to be  $\sim 33$  nm by means of fast Fourier transformation (FFT). Cylindrical nanostructures of the PS-P4VP can easily be characterized by FE-SEM after the surface reconstruction in ethanol, a good solvent for P4VP but a non-solvent for PS. Thus, the immersion of the sample into ethanol successfully swells the P4VP blocks only, while the PS structures remain intact without losing the structural integrity.<sup>[61]</sup> The spacing between the cylinders measured upon FE-SEM image of the cylindrical PS(25)-P4VP(7) films is same to the value obtained from the TEM image.

Considering solubility parameters ( $\delta$ ) (Table 2.2) and the calculated interaction parameters for chloroform-PS (0.35) and chloroform-P4VP (0.67),<sup>[62]</sup> chloroform is a non-selective solvent having a slight preference toward PS blocks. During the chloroform vapor annealing, the solvent vapors are uniformly dispersed in the entire PS-P4VP film to enhance the chain mobility. Embedded solvent molecules reduce  $T_g$  of polymers, enabling the reorientation of copolymer nanostructures. In addition, the solvent uptake at the diblock copolymer films decreases the effective repulsion between both blocks, leading to the reduction of  $\chi$  as defined by the equation 2.3.<sup>[62-64]</sup>

$$\chi_{eff} \approx \varphi_P(\chi + \Delta\chi) \quad (2.3)$$

where  $\chi$  is the interaction parameter in bulk,  $\varphi_P$  is the polymer volume concentration, and  $\Delta\chi$  is the difference between interaction parameters of a solvent with each block. Consequently, the effective segregation strength, defined as  $\chi_{eff}N$  where  $N$  is the degree of polymerization, decreases drastically while the volume fraction of the blocks remains constant, resulting in the transformation of the swollen PS-P4VP micelles to the disordered state. The rapid drying process leads to the reconstruction

of arrayed cylinders in copolymer films, of which the orientation is affected by the affinity of blocks toward the substrate or free space (air-polymer interface).<sup>[65,66]</sup>

The FE-SEM images in Figure 2.11 show the cylindrical nanostructures of the PS-P4VP having different molecular weights. The inter-distances of each single-layered cylinder are ~26 nm, ~31 nm, ~39 nm, and ~51 nm, respectively, which are governed by the total molecular weight of the copolymers. This can be also confirmed by TEM images displayed in Figure 2.12. Note that the thin films of the PS(50)-P4VP(13) contains the minor domains consisting of the spherical structures due to the relatively shorter annealing time for the generation of fully connected cylinders compared with other small molecular weight copolymers.

However, when the P4VP block chain is longer than the certain value, the morphological transformation does not occur during the chloroform solvent vapor annealing. Figure 2.13 shows the hexagonal arrays of nanopores cavitated by ethanol swelling of the thin films of PS(48)-P4VP(20) and PS(109)-P4VP(27) after the solvent vapor annealing. The same result can be obtained when the thin films are annealed in a selective solvent for the PS block such as toluene, implying that the solubility of P4VP in chloroform decreases as the molecular weight increases.  $\chi_{eff}N$  values of those copolymers are relatively higher such that micellar structures are maintained during the chloroform vapor annealing.

To synthesize the Pt NWs, the substrates with the cylindrical PS-P4VP thin films were immersed into an acidic  $\text{Na}_2\text{PtCl}_6$  aqueous solution. During this dipping process, the P4VP blocks were swollen to the surface by protonation and given the positive charge, facilitating the electrostatic interaction with the anionic metal salt ( $[\text{PtCl}_6]^{2-}$  in this experiment). AFM images in the left column of Figure 2.14 clearly represent the swollen P4VP cylinders with a substantially improved topographic

contrast (compare to Figure 2.10b before swelling). This swelling process has been described in detail elsewhere.<sup>[58,67]</sup> Dried fully under a nitrogen stream, the substrates were treated with an oxygen plasma to remove the copolymers and produce arrayed Pt NWs. AFM images in the right column of Figure 2.14 show synthesized arrays of the Pt NWs. The inter-distances of the Pt NWs synthesized from PS(19)-P4VP(5) (~26 nm), PS(25)-P4VP(7) (~34 nm), and PS(32)-P4VP(13) (~37 nm) are similar to those of the P4VP nanocylinders observed from each copolymer. In addition, the width of the Pt NWs are ~6 nm, ~7 nm, and ~8 nm, respectively. The cylindrical nanostructures of the diblock copolymers can be utilized as nanotemplates to generate arrays of the one-dimensional NWs efficiently.

The self-assembly process of the diblock copolymers generally forms ordered nanostructures having randomly oriented nanodomains with a poor long-range order. To realize a well-aligned nanodomains over a large area, the self-assembly process of the diblock copolymers can be induced in the confined space on the sub-micrometer scale by the DSA. The PS(32)-P4VP(13) micellar solution (0.6 wt%) was spin-coated onto topographically patterned substrates. Figure 2.15a shows the FE-SEM image of the PS-P4VP copolymer film after the chloroform solvent annealing for 2 h. Unlike the fingerprint-like pattern shown in Figure 2.11c and 2.12c, the trenches guided the alignment of the in-plane P4VP cylinders along the wall. The Pt precursors were loaded into the P4VP blocks in the trenches, which produced a line pattern of the well-aligned Pt NWs in the trenches as shown in Figure 2.15b. The spacing of the aligned Pt NWs were calculated to be ~39 nm. Likewise, the combination of the solvent vapor annealing and graphoepitaxy can provide a powerful means of synthesizing arrayed metallic NWs with a high aspect ratio.

## **Summary**

Arrayed Pt NWs with a fingerprint pattern were synthesized from the self-assembled PS-P4VP thin films having the monolayered P4VP cylinders. Except copolymer with higher molecular weight P4VP, the cylindrical nanostructures were formed from the initial micellar structures by the chloroform vapor annealing, which were characterized by AFM, FE-SEM, and TEM. The Pt NWs were produced from the precursors loaded into the P4VP cylinders by the treatment of an oxygen plasma, and the spacing of the Pt NWs was adjusted by changing the molecular weights of the copolymers. In addition, the topographically defined trench structures of the substrate contributed to the long-range alignment of the P4VP cylinders by the DSA, resulting in parallel arrays of Pt NWs with a high aspect ratio.

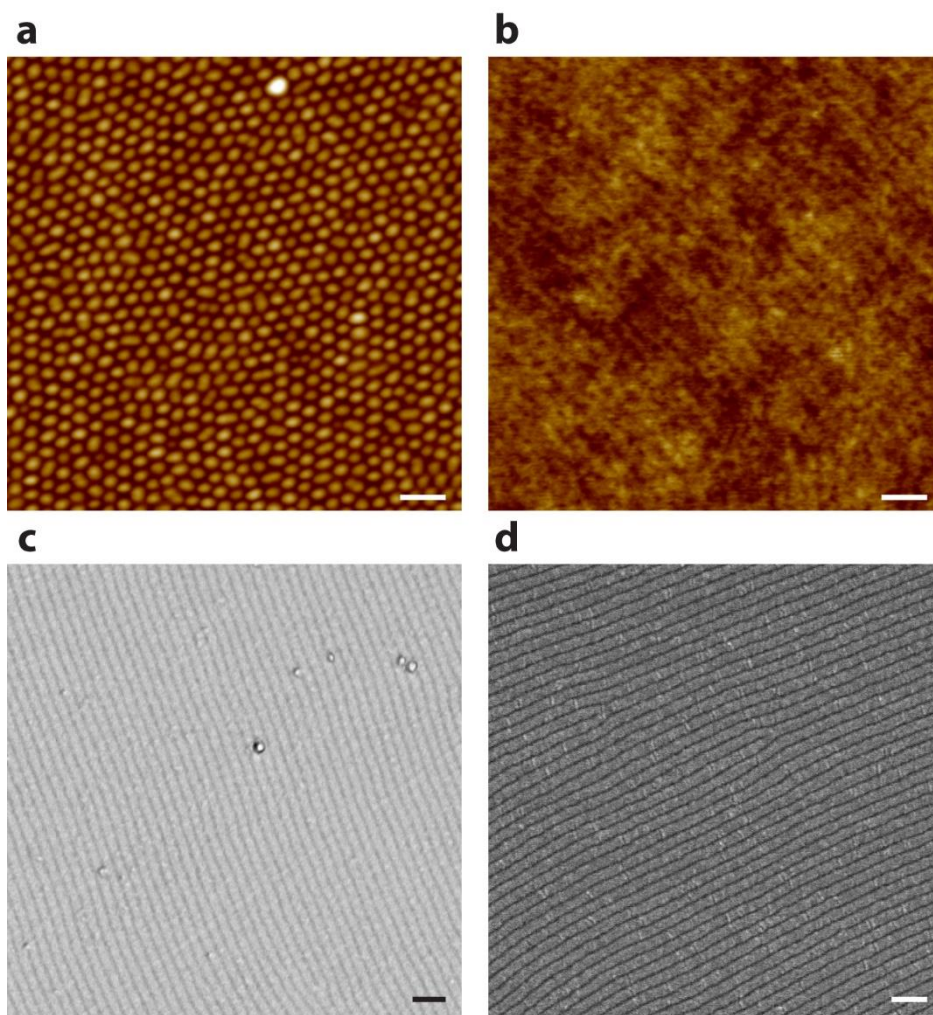


**Figure 2.10.** Characterization of PS(25)-P4VP(7) thin films. (a) AFM image of a single-layered film of PS(25)-P4VP(7) micelles; (b,c,d) AFM, TEM, and FE-SEM images of PS(25)-P4VP(7) thin films having cylindrical nanostructures after chloroform solvent vapor annealing. Scale bars are 100 nm.

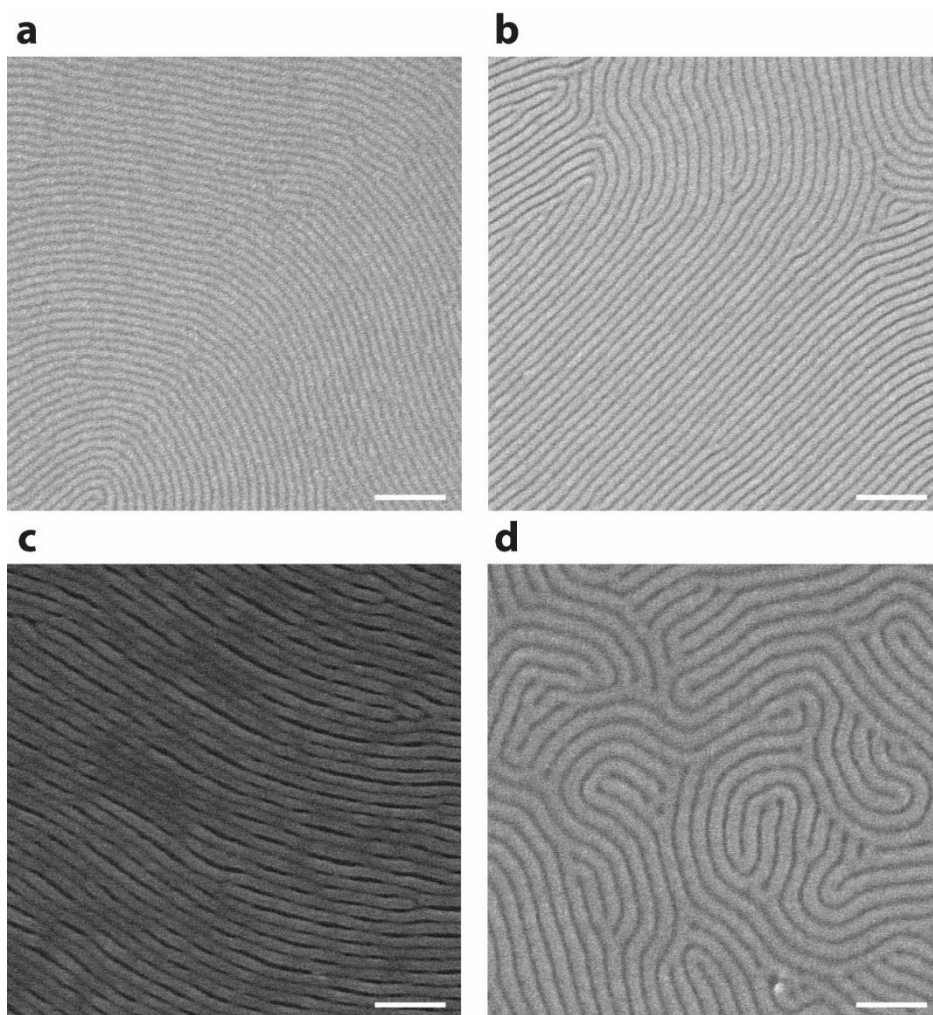


**Figure 2.11.** FE-SEM images of other PS-P4VP thin films having cylindrical nanostructures after chloroform solvent vapor annealing. (a) PS(19)-P4VP(5); (b) PS(33)-P4VP(8); (c) PS(32)-P4VP(13); (d) PS(50)-P4VP(13). Scale bars are 200 nm.

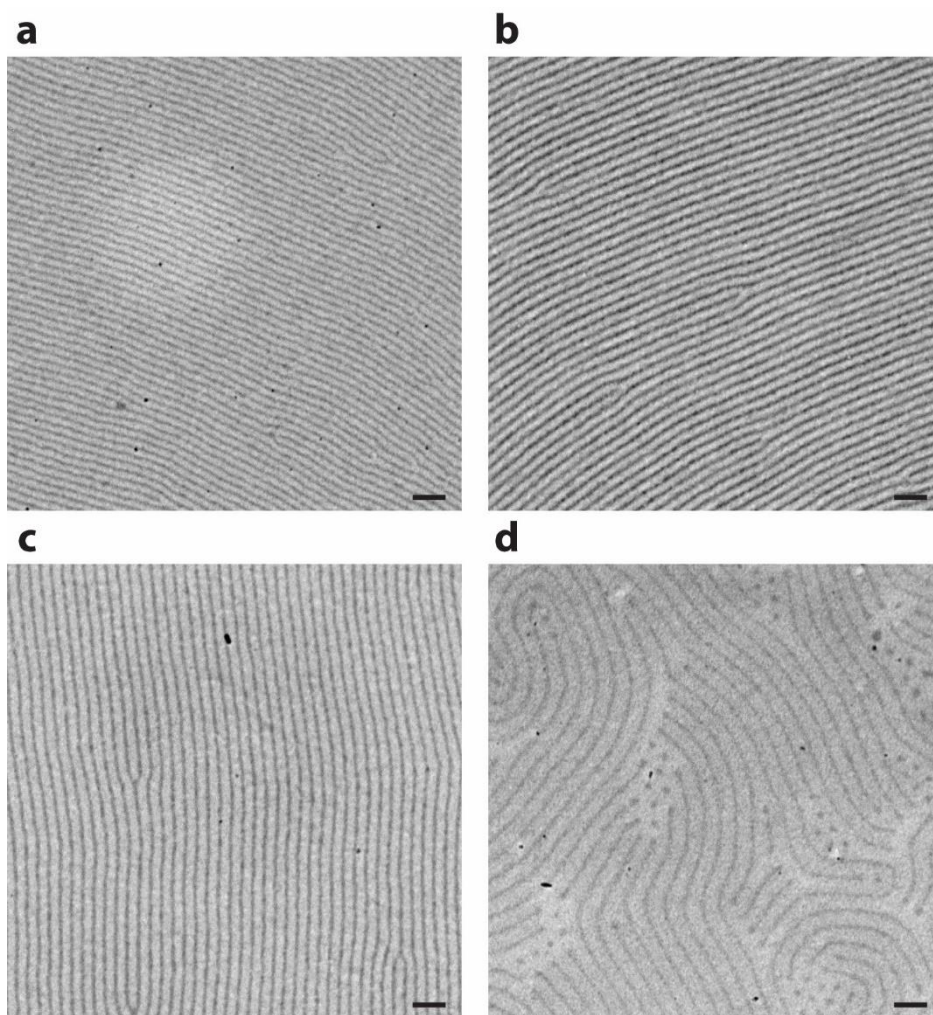


**Figure 2.12.** TEM images of other PS-P4VP thin films having cylindrical nanostructures after chloroform solvent vapor annealing. (a) PS(19)-P4VP(5); (b) PS(33)-P4VP(8); (c) PS(32)-P4VP(13); (d) PS(50)-P4VP(13). Scale bars are 100 nm.

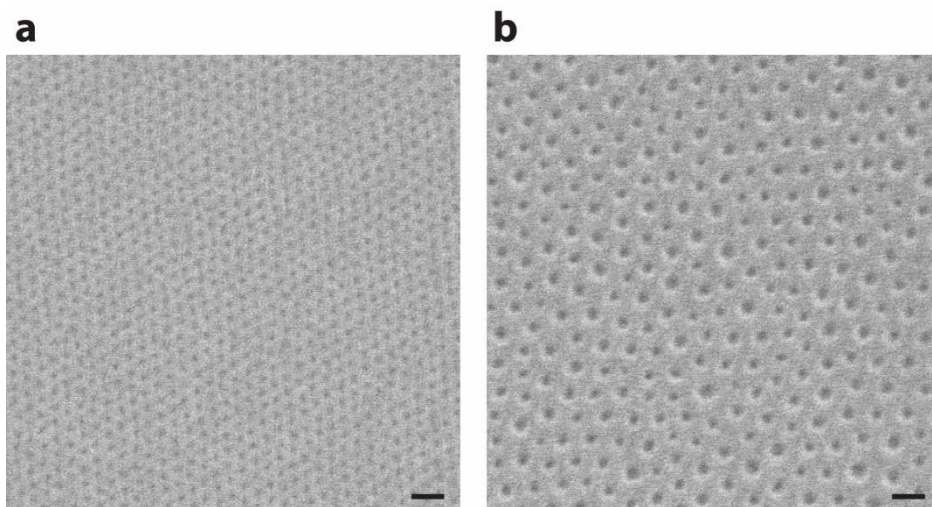


**Figure 2.13.** FE-SEM images of other PS-P4VP thin films after chloroform solvent vapor annealing. (a) PS(48)-P4VP(20); (b) PS(109)-P4VP(27). Scale bars are 100 nm.

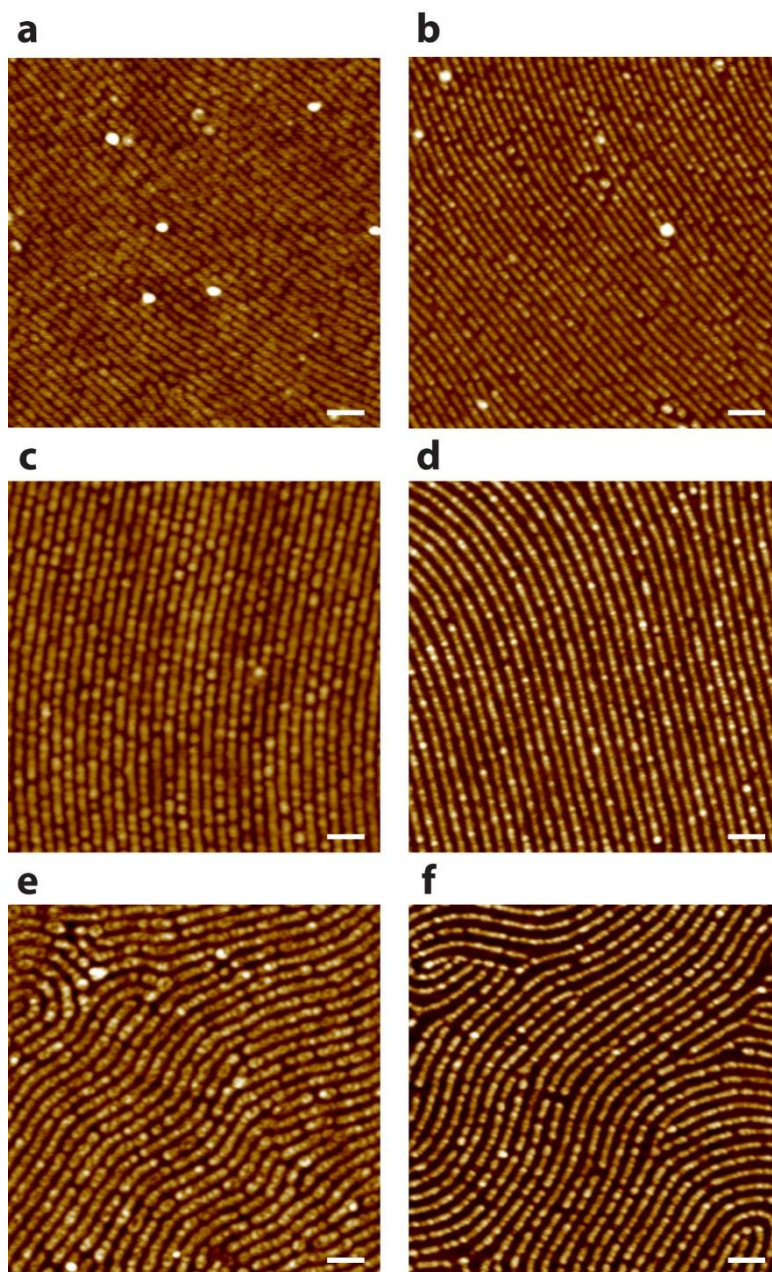


**Figure 2.14.** AFM images of swollen PS-P4VP thin films after the immersion into an acidic Pt salt solution (left) and synthesized Pt NWs (right). (a,b) PS(19)-P4VP(5); (c,d) PS(25)-P4VP(7); (e,f) PS(32)-P4VP(13). Scale bars are 100 nm.

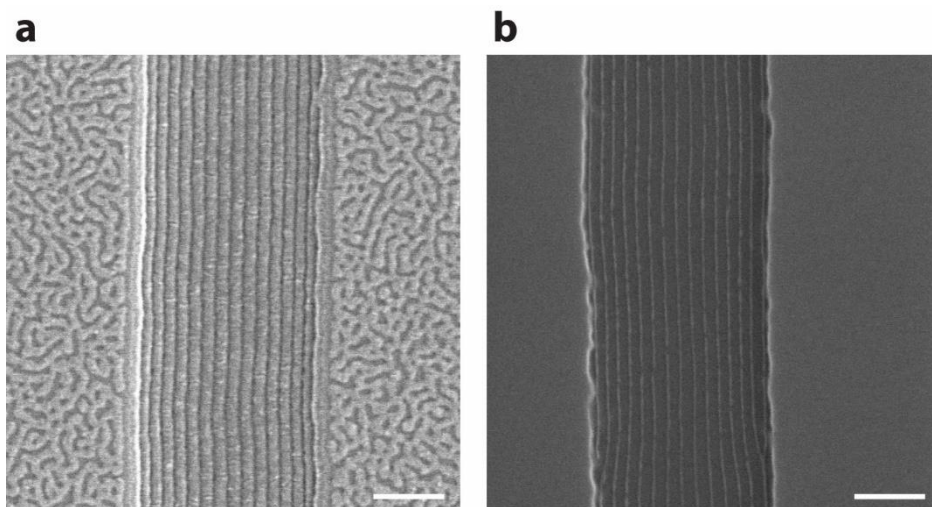


**Figure 2.15.** FE-SEM images for DSA of PS(32)-P4VP(13) and synthesized Pt NWs. (a) Well-aligned PS-P4VP thin films having cylindrical nanostructures after chloroform solvent vapor annealing; (b) Well-aligned arrays of Pt NWs in topographically patterned wafer. Scale bars are 200 nm.

Materials	Solubility parameter (MPa <sup>1/2</sup> )
chloroform	19.0
PS	18.6
P4VP	22.2

**Table 2.2.** Solubility parameters of chloroform, PS, and P4VP

## 4. Arrayed nanorings

Toroidal ring-shaped nanomaterials have received much scientific interest given their unique plasmonic,<sup>[68]</sup> magnetic,<sup>[69]</sup> and spintronic<sup>[70]</sup> properties, which are even fairly distinctive from those of spherical NPs or nanodisks. For example, Au NRs exhibit much larger shifts in their localized surface plasmon resonance peaks, with which biosensors based on NRs show higher sensitivity levels.<sup>[71]</sup> Because these characteristics of NRs depend on their inner and outer diameters, accurate control over these factors is of great importance. Thus, template-assisted methods are widely used for the fabrication of arrayed NRs. PS colloidal particles<sup>[72]</sup> and AAO<sup>[73]</sup> as templates have frequently been combined with metal deposition and etching techniques to produce arrays of size-controlled NRs over a large area.

Spherical micelles consisting of self-assembled diblock copolymers generally produce spherical NPs with an oxygen plasma treatment because the precursors of metal NPs agglomerate into single NPs as discussed in the previous section. Recently Shin and Kim *et al.* demonstrated that PS-P4VP thin films can be used to generate a diversity of Au nanomaterials when varying the orientation of the nanodomains, the level of cross-linking, and the copolymer etching method.<sup>[74]</sup> Among these approaches, the authors showed that Au NRs can be generated from PS-P4VP templates when the sample is dipped into an acidic Au salt solution and then undergoes an oxygen plasma etching treatment. P4VP domains become swollen to form ring-like structures, from which Au NRs can be generated with the rapid removal of copolymers by oxygen plasma preventing Au precursors from diffusing into the oxygenated PS matrix. However, size-controllability was not demonstrated in their study. To adjust the diameter and thickness of NRs fabricated by this synthetic route, these parameters of the swollen P4VP microdomains should

be accurately controlled, though this can scarcely be accomplished by mere dipping into an acidic solution.

This section introduces a novel method which can be used to fabricate metal and oxide NRs with controlled diameters through the tuning of the size of the copolymer micellar cores. Ionic liquids (ILs), salts in a liquid state with a melting point generally lower than 100 °C, were used as a filling material in core blocks to be sequestered at the centers of the micelles. Compared to pristine diblock copolymer micelles, IL-containing micelles have larger swollen nanodomains to produce larger NRs, of which the diameters can be precisely controlled by managing the amount of ILs added to the copolymer micelles.

## **Experimental Section**

*Materials:* Diblock copolymers of PS-P4VP, PS(51)-P4VP(18), and PS(109)-P4VP(27) were purchased from Polymer Source, Inc. The number in the parenthesis is the average molecular weight ( $M_n$ ) in kg/mol. The polydispersity index (PDI) is 1.15. 1-Ethyl-3-methylimidazolium bis(trifluoromethylsulfonyl) imide ([EMIm][TFSI]) was purchased from Sigma-Aldrich, and the molecular structures of [EMIm] cation and [TFSI] anion are depicted in Figure 2.16. Sodium tetrachloroaurate(III) dehydrate ( $\text{NaAuCl}_4$ ), sodium hexachloroplatinate(IV) hexahydrate ( $\text{Na}_2\text{PtCl}_6 \cdot 6\text{H}_2\text{O}$ ), potassium ferricyanide ( $\text{K}_3[\text{Fe}(\text{CN})_6]$ ), and sodium tetrachloropalladate(II) ( $\text{Na}_2\text{PdCl}_4$ ) as precursors of Pt, Au,  $\text{Fe}_2\text{O}_3$ , and PdO NRs were obtained from Sigma-Aldrich and used as received.

*Diblock copolymer micelles containing ILs:* The PS-P4VP diblock copolymers were dissolved in toluene, a strongly selective solvent for the PS block, with a concentration of 2.5 wt%. The solution was stirred for 24 h at a room temperature

and for 3 h at 85 °C and then cooled to a room temperature. [EMIm][TFSI] were added to the micellar solution. The mass ratio of [EMIm][TFSI] to pyridine units in the P4VP block was defined as  $\mu$  in the range of 0 ~ 1.0. The solution was stirred for at least 3 days at a room temperature until the homogeneous micellar solution is obtained, followed by the dilution to 0.5 wt% by adding the appropriate amount of toluene.

*Fabrication of arrayed NRs:* Prior to the spin-coating of the PS-P4VP micellar solution, a SiO<sub>2</sub>/Si wafer was cleaned in a piranha solution at 90 °C for 30 min, and thoroughly rinsed with deionized water several times, and then blown dry with a nitrogen stream. The pristine and IL-containing PS-P4VP copolymers were spin-coated from a toluene solution at 2000 rpm for 60 s onto a freshly cleaved mica or SiO<sub>2</sub>/Si substrates. To synthesize the NRs on a SiO<sub>2</sub>/Si substrate, the samples were immersed in an acidic salt aqueous solution for 3 h. This precursor solution was prepared by mixing 18 mL of the metal salts (as mentioned in materials part above) aqueous solution (0.010 M) and 2 mL of 1.0 % HCl. The samples were subsequently dried under a nitrogen stream without rinsing with deionized water or other organic solvents, followed by the treatment with an oxygen plasma for 5 min (0.038 Torr, 100 W).

*Characterization:* The pristine and IL-containing PS-P4VP thin films and arrayed NRs were analyzed using an FE-SEM (Hitachi S-4300 at 15 kV and FEI Helios 650 at 5 kV), a multimode 8 AFM with a Nanoscope V controller (Bruker) in tapping mode with Al-coated Si cantilevers, and a TEM (Hitachi 7600 at 100 kV). To prepare the observation by TEM, the copolymer films were floated off from the substrate onto deionized water by the delamination and collected on a carbon-coated copper TEM grid. The delamination process from a mica and SiO<sub>2</sub>/Si wafer

was same as described in the previous sections. To acquire the micrographs with a high contrast, TEM grids with PS-P4VP film were exposed to I<sub>2</sub> prior to the observation. The intensity distributions of the copolymer micelles were obtained by a dynamic light scattering (DLS) (Otsuka Electronics, DLS-7000). For the DLS measurement, the micellar solutions were diluted to 0.025 wt%.

## Results and Discussion

Imidazolium-based ionic liquids have been incorporated in microdomains of diblock copolymers for the control of morphology<sup>[75,76]</sup> and the enhancement of ionic conductivity.<sup>[77,78]</sup> [EMIm][TFSI], an aprotic ionic liquid capable of dissolving P2VP to some degree as a selective solvent, was added to the PS-P4VP micellar solution. The TEM images of the single-layered pristine and IL-containing PS(109)-P4VP(27) micelles are displayed in Figure 2.17. The selective staining of the P4VP chains enables to observe that the diameter of micellar core ( $D_c$ ) is increased with  $\mu$  (Table 2.3). In addition, after adding the certain amount of the IL, the darkness contrast is remarkably reduced, and the voids as white circles in the TEM images at the center of micellar cores are observed. It can be assumed that [EMIm][TFSI] prefers to be located in the core region of micelles because [EMIm][TFSI] is not dissolved in toluene nor in PS but has the affinity to P4VP core blocks, leading to the swelling of the micellar core to enlarge its volume. This phenomenon was also illustrated in the work of Thomas *et al.*<sup>[79]</sup> where the P2VP lamellar phase was selectively swollen by adding the ILs.

The surface topography of the single-layered films of the copolymer micelles was investigated by AFM. Surprisingly, The AFM images of the IL-containing PS(109)-P4VP(27) micelles in the right column of Figure 2.17 show the collapsed

core regions of the micelles as  $\mu$  increases, obviously contrasted with the hemisphere-shaped pristine copolymer micelles (Figure 2.17a). The core region of pristine PS-P4VP micelles consists of the densely packed P4VP chains due to their solvophobicity. Thus, the sphere-form micellar core remained intact after the spin-coating process. In contrast, as the TEM images show, the core region of the IL-containing PS-P4VP micelles has the sequestered [EMIm][TFSI] pocket, allowing the core blocks to rebuild their structures during the deposition onto the substrate by spin-coating process with the removal of the solvent.

This trend can clearly be perceived in TEM and AFM images of the pristine and IL-containing PS(51)-P4VP(18) micelles as well (Figure 2.18 and 2.19). Since the core size of PS(51)-P4VP(18) is smaller than that of PS(51)-P4VP(18), the variation by the addition of the ILs (*i.e.*, formation of voids in core regions) was monitored in detail. The swelling of the micellar core and collapsed core regions are equally observed in both TEM and AFM images. In particular, the reconstructing role of the IL in the micellar cores is clearly supported by the AFM phase mode images in insets of Figure 2.19. The core and corona blocks are indistinguishable in the phase mode images (inset of Figure 2.19a) because the whole surface is covered with the corona PS blocks and there is little difference in mechanical properties between PS and P4VP. However, in the phase mode images of the IL-containing micelles, dark circles at core regions are observed and growing (2.19b to 2.19e), implying that the material property of the core blocks is changed due to the incorporation of the ILs. Since the size of concave region in the height mode images and that of dark circles in phase mode images are identical, it is reasonable to assume that [EMIm][TFSI] in the micellar cores contributed to the reconstruction of the micellar core shapes.

Interestingly, although the size of the micellar cores depends on  $\mu$ , there is no clear relationship between the diameters of the whole micelles and  $\mu$ . The spacing of hexagonally arrayed IL-containing micelles is same to that of pristine micelles (Table 2.3), which indicates that the whole size of the micelles is identical regardless to the addition of the ILs to the micellar cores. The scattering intensity distributions of the copolymer micelles obtained by DLS (Figure 2.20) show the negligible change in average hydrodynamic diameters ( $D_H$ ) by ILs (Table 2.3). Thus, the addition of ILs provides the effective way to control the core regions with no change in whole micellar structures.

The single-layered films of the pristine PS(109)-P4VP(27) micelles were immersed into an acidic Pt salt aqueous solution to load the Pt precursors into the P4VP blocks. In the TEM images in Figure 2.21a, the hexagonal arrays of the white holes are observed. The same arrays of holes at the centers of the ring-like P4VP cores can be observed in the AFM images in Figure 2.21b. The inter-distances of holes are identical to those of the original copolymer micelles. Thus, these holes were generated from the micellar cores. This morphological change in the pristine micelles can be explained in terms of the core-corona inversion by the swelling and protonation.<sup>[74,80,81]</sup> During the drying process with a nitrogen stream, the swollen P4VP chains rapidly shrink and are pulled towards the interfacial region of PS and P4VP to form a ring-like morphology.<sup>[82]</sup> However, during the swelling process in an acidic solution, the sequestered ILs eventually escape from the micellar cores, enlarging the size of holes ( $D_h$ ) with  $\mu$  (Table 2.3).

The same Pt loading process was applied to the IL-containing PS(51)-P4VP(18) micelles to generate similar hexagonal arrays of the holes as shown in TEM images (Figure 2.22) and AFM images (Figure 2.23). Those observations also support that

the diameters and depths of holes become larger as  $\mu$  increases. This is attributable to the presence of [EMIm][TFSI] at the center of the micellar cores as a core spacer.

Subsequently, all samples were treated with an oxygen plasma to remove the copolymers and synthesize arrayed Pt NRs as shown in Figure 2.24 and Figure 2.25. The outer and inner diameters of the Pt NRs elevate with increasing  $\mu$  (Table 2.4), while the thickness ( $T$ ) of NRs, defined as half of the difference between outer ( $D_o$ ) and inner ( $D_i$ ) diameters (Table 2.4), decreases. Note that the entire size of the NRs synthesized from PS(109)-P4VP(27) (Figure 2.24) is much larger than that from PS(51)-P4VP(18) (Figure 2.25) and the spacing is identical to the original pristine and IL-containing copolymer micelles. Interestingly, some Pt NRs from the copolymer micelles with a high  $\mu$  suffer from the lack of the structural connectivity to have a crescent-like structure (see Figure 2.24e and 2.25e) due to the low P4VP chain segment density.

As demonstrated in the previous sections, one of merits of the diblock copolymer micellar approach is ability to synthesize diverse nanomaterials by choosing different precursors. A range of different metal complex anions ( $[\text{AuCl}_4]^-$ ,  $[\text{PdCl}_4]^{2-}$ , and  $[\text{Fe}(\text{CN})_6]^{3-}$ ) were used to generate different metal and oxide NRs. The FE-SEM images in Figure 2.26 show the Au, PdO, and  $\text{Fe}_2\text{O}_3$  NRs synthesized from the precursors loaded into the IL-containing PS(109)-P4VP(27) ( $\mu = 0.8$ ). Unlike other NRs, discrete Au NPs are arranged along the imaginary circumference of the NRs (Figure 2.26a). This staccato deposition of Au is due to the absence of HF.<sup>[58]</sup>

## Summary

The ring-form diblock copolymer nanotemplates for the synthesis of the metal and oxide NRs were fabricated by the combination of [EMIm][TFSI] and the PS-

P4VP micelles. [EMIm][TFSI] was added to the micellar toluene solution, which was incorporated in and swelled P4VP cores effectively while preserving the spherical micellar structures. The IL-containing PS-P4VP micelles were swollen and protonated by dipping into an acidic salt aqueous solution, resulting in the formation of the ring-like P4VP swollen structures where the metal ions are anchored. With oxygen plasma etching, arrayed metal and oxide NRs were synthesized, and the diameters and thicknesses of the NRs were controlled by managing molecular weights and the amount of [EMIm][TFSI] in the micellar cores. This synthetic approach may provide an effective means of fabricating various NR arrays for optical, magnetic, and electronic devices.

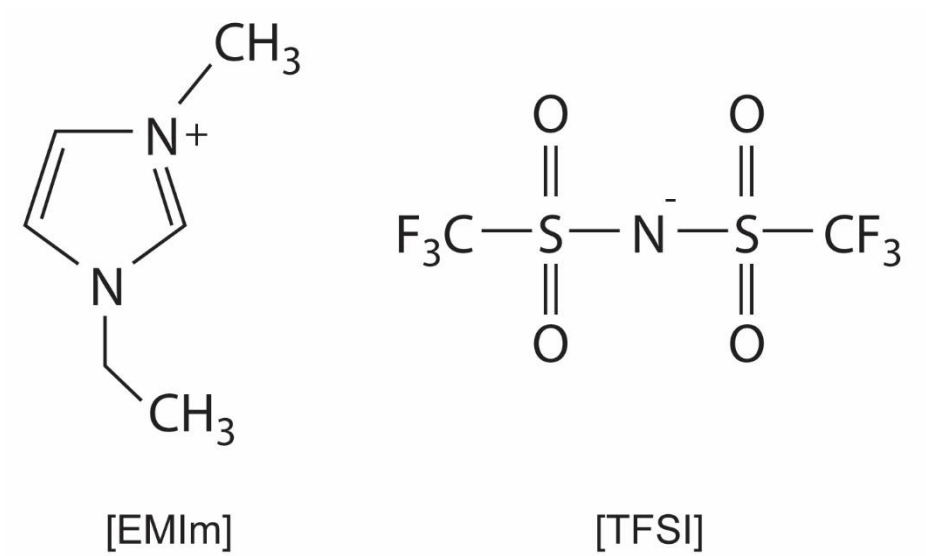


**Figure 2.16.** Chemical structures of EMIm cation and TFSI anion.

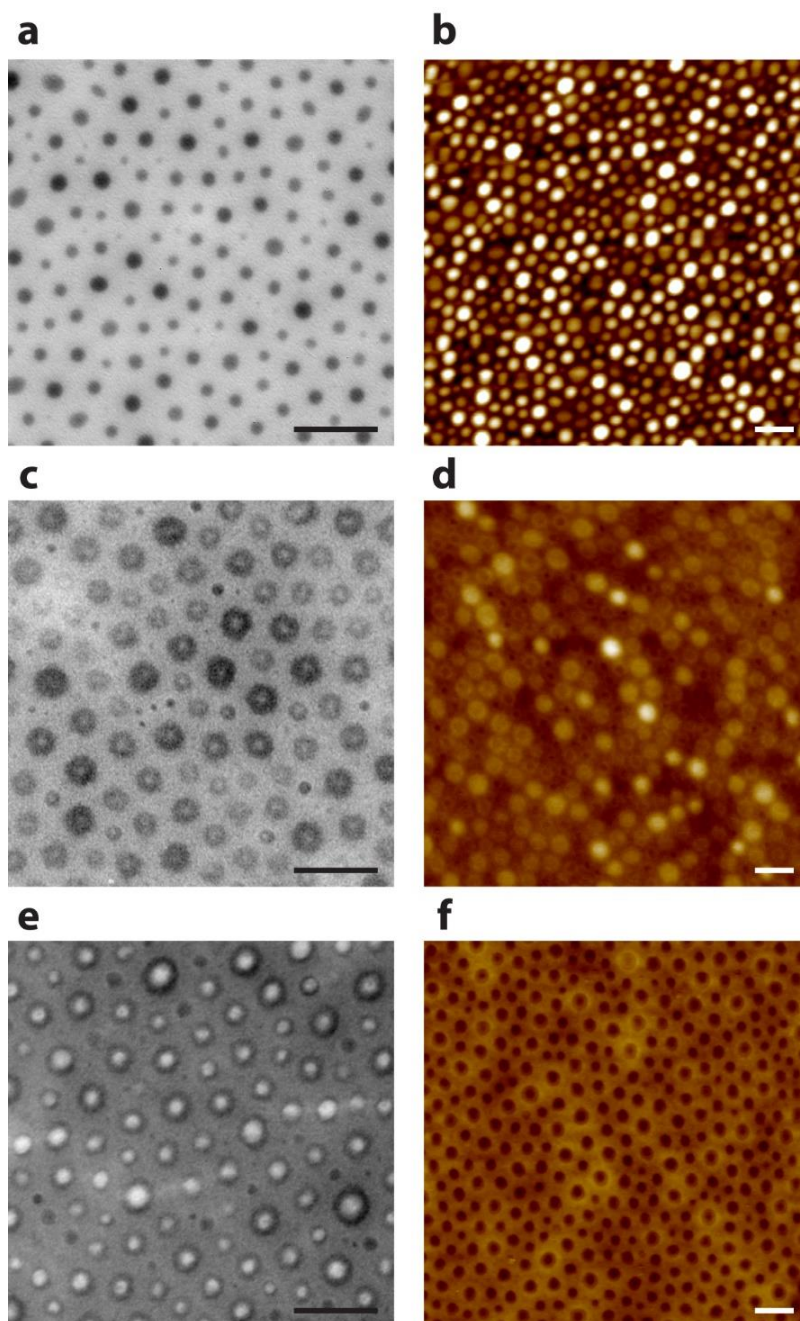


**Figure 2.17.** TEM and AFM images of single-layered films of IL-containing PS(109)-P4VP(27). (a,b)  $\mu = 0$ ; (c,d)  $\mu = 0.4$ ; (e,f)  $\mu = 0.8$ . Scale bars are 200 nm.

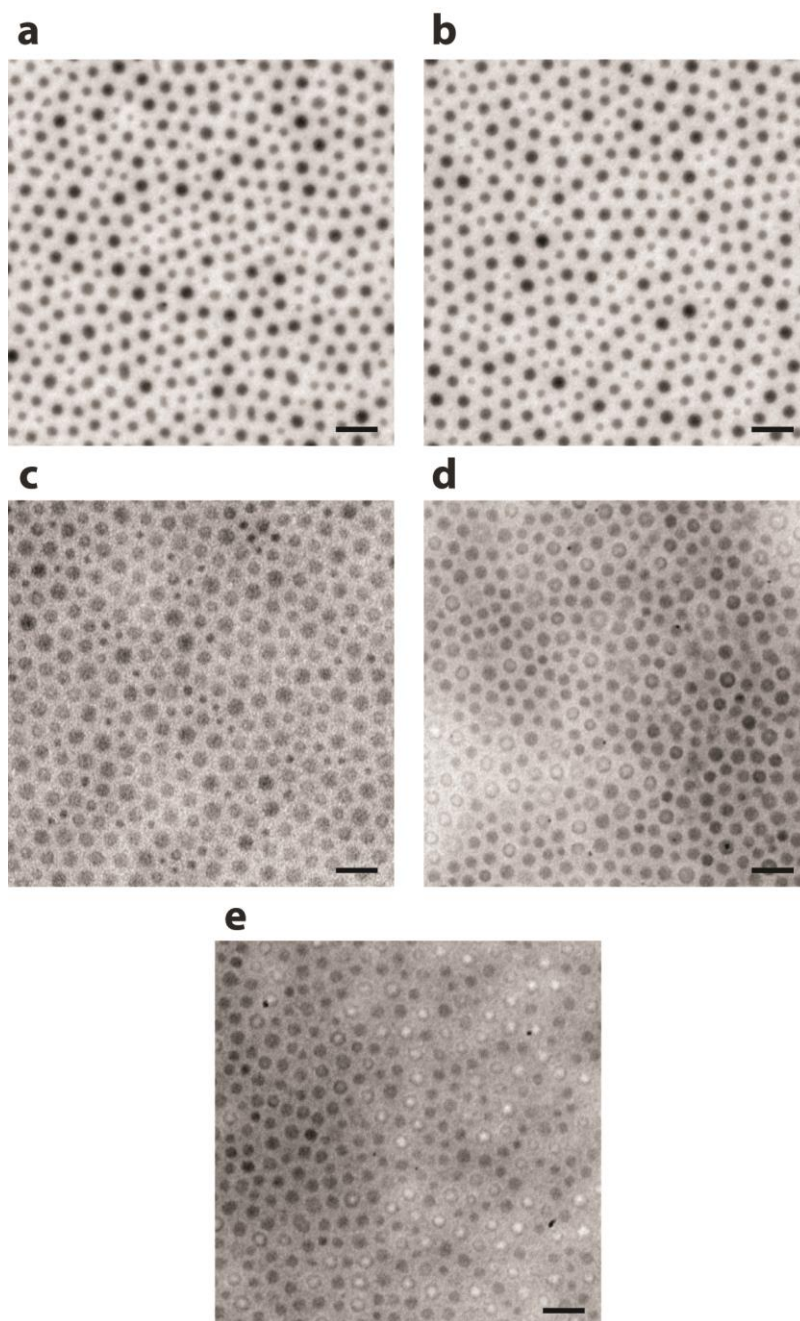


**Figure 2.18.** TEM images of single-layers of IL-containing PS(109)-P4VP(27). (a)  $\mu = 0$ ; (b)  $\mu = 0.2$ ; (c)  $\mu = 0.4$ ; (d)  $\mu = 0.6$ ; (e)  $\mu = 0.8$ . Scale bars are 200 nm.

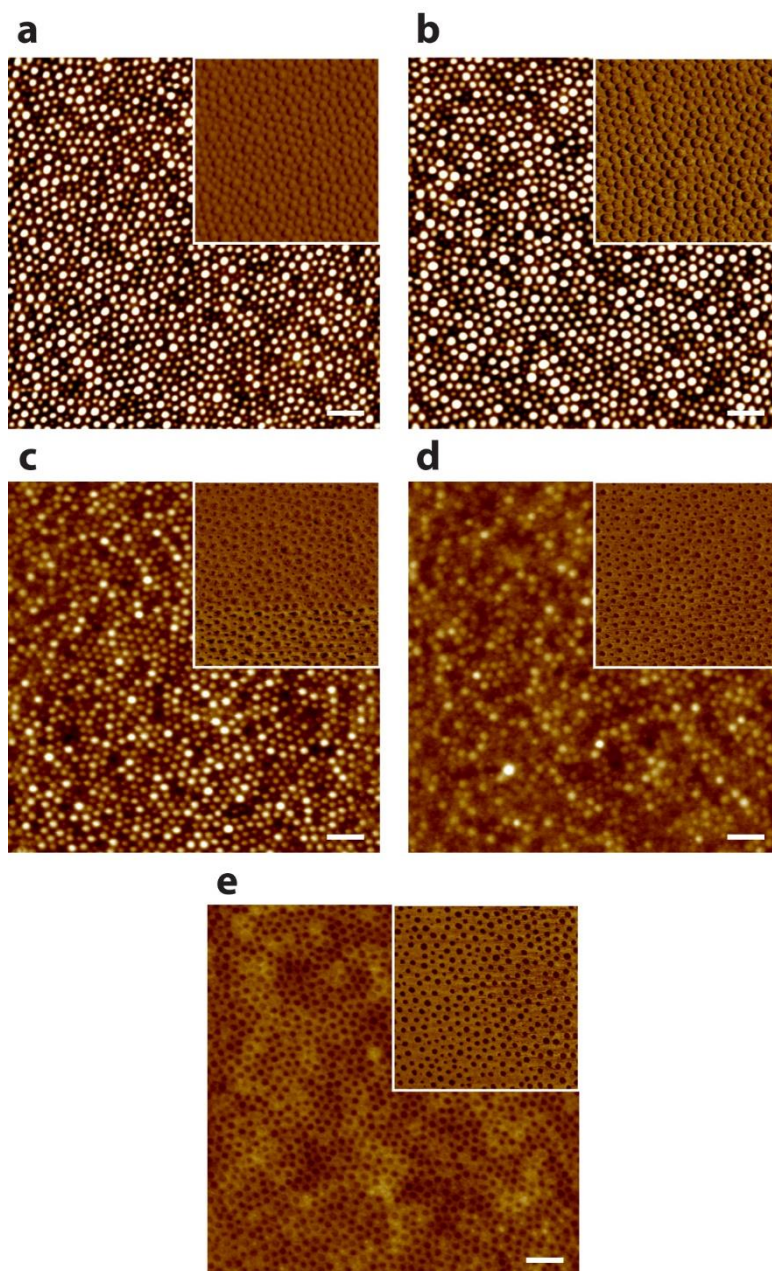


**Figure 2.19.** AFM images of single-layers of IL-containing PS(51)-P4VP(18). (a)  $\mu = 0$ ; (b)  $\mu = 0.2$ ; (c)  $\mu = 0.4$ ; (d)  $\mu = 0.6$ ; (e)  $\mu = 0.8$ . Insets are AFM phase mode images of corresponding regions ( $1 \mu\text{m} \times 1 \mu\text{m}$ ). Scale bars are 200 nm.

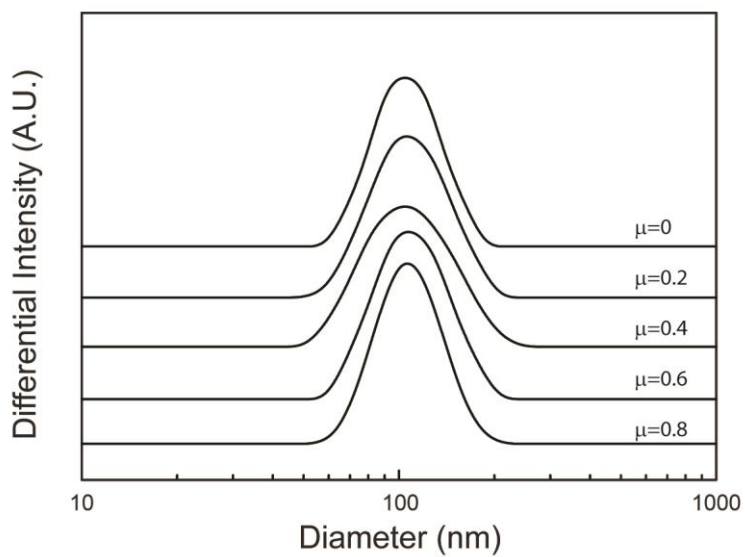


**Figure 2.20.** DLS results of intensity distributions of pristine and IL-containing PS(51)-P4VP(18) micelles in toluene.

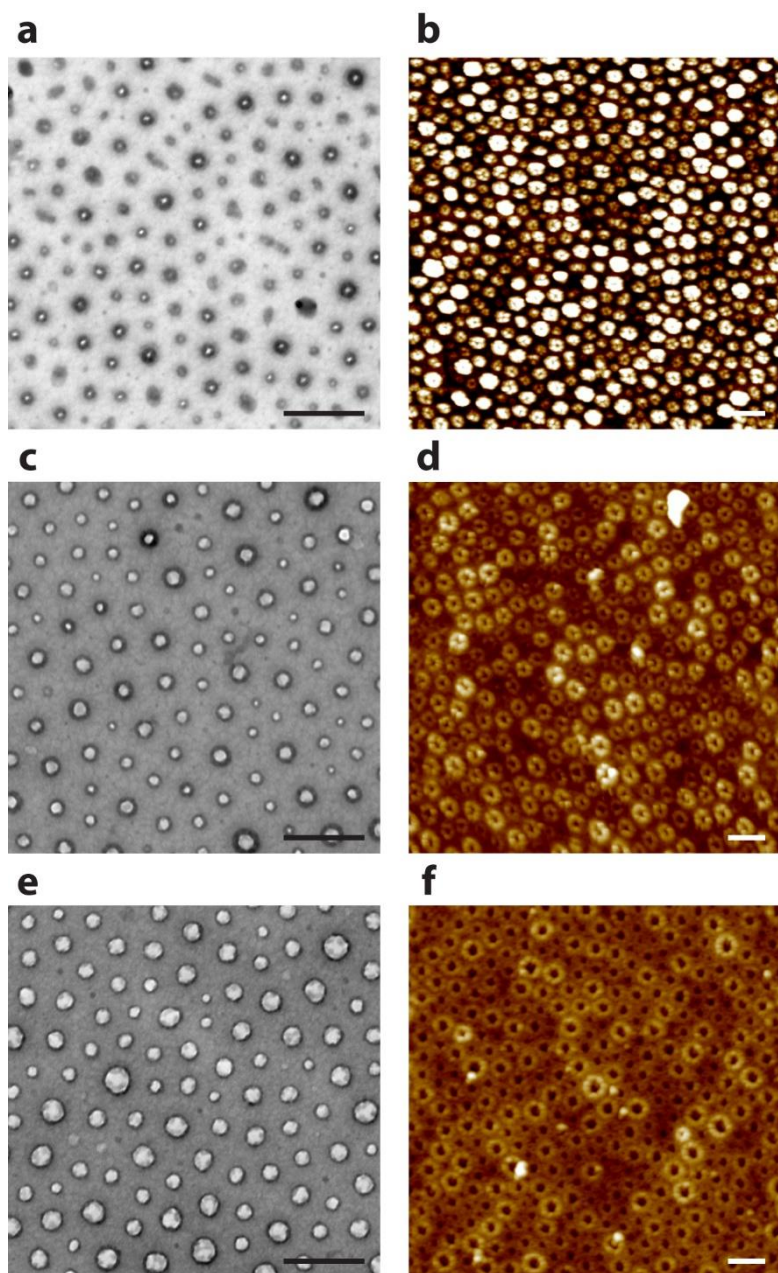


**Figure 2.21.** TEM and AFM images of single-layered films of IL-containing PS(109)-P4VP(27) after immersing into an acidic Pt salt solution. (a,b)  $\mu = 0$ ; (c,d)  $\mu = 0.4$ ; (e,f)  $\mu = 0.8$ . Scale bars are 200 nm.

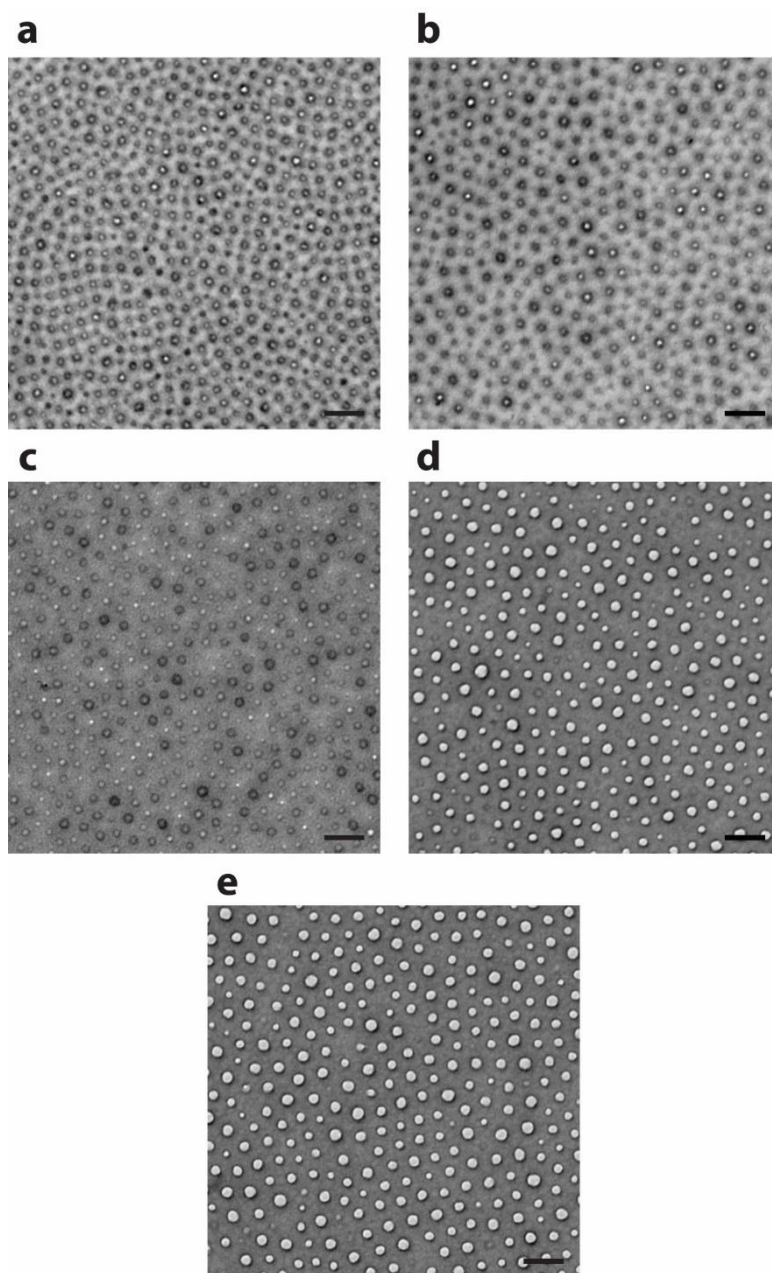


**Figure 2.22.** TEM images of single-layered films of IL-containing PS(51)-P4VP(18) after immersing into an acidic Pt salt solution. (a)  $\mu = 0$ ; (b)  $\mu = 0.2$ ; (c)  $\mu = 0.4$ ; (d)  $\mu = 0.6$ ; (e)  $\mu = 0.8$ . Scale bars are 100 nm.

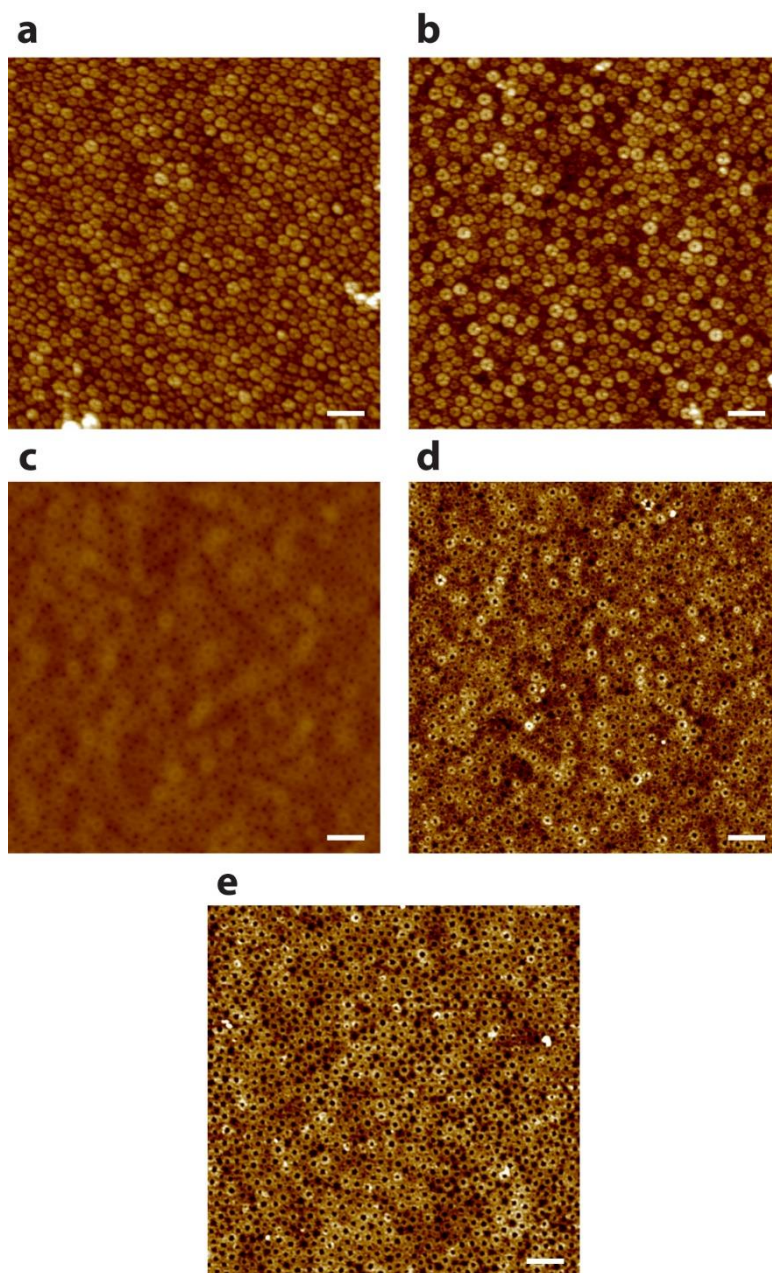


**Figure 2.23.** AFM images of single-layered films of IL-containing PS(51)-P4VP(18) after immersing into an acidic Pt salt solution. (a)  $\mu = 0$ ; (b)  $\mu = 0.2$ ; (c)  $\mu = 0.4$ ; (d)  $\mu = 0.6$ ; (e)  $\mu = 0.8$ . Scale bars are 200 nm.

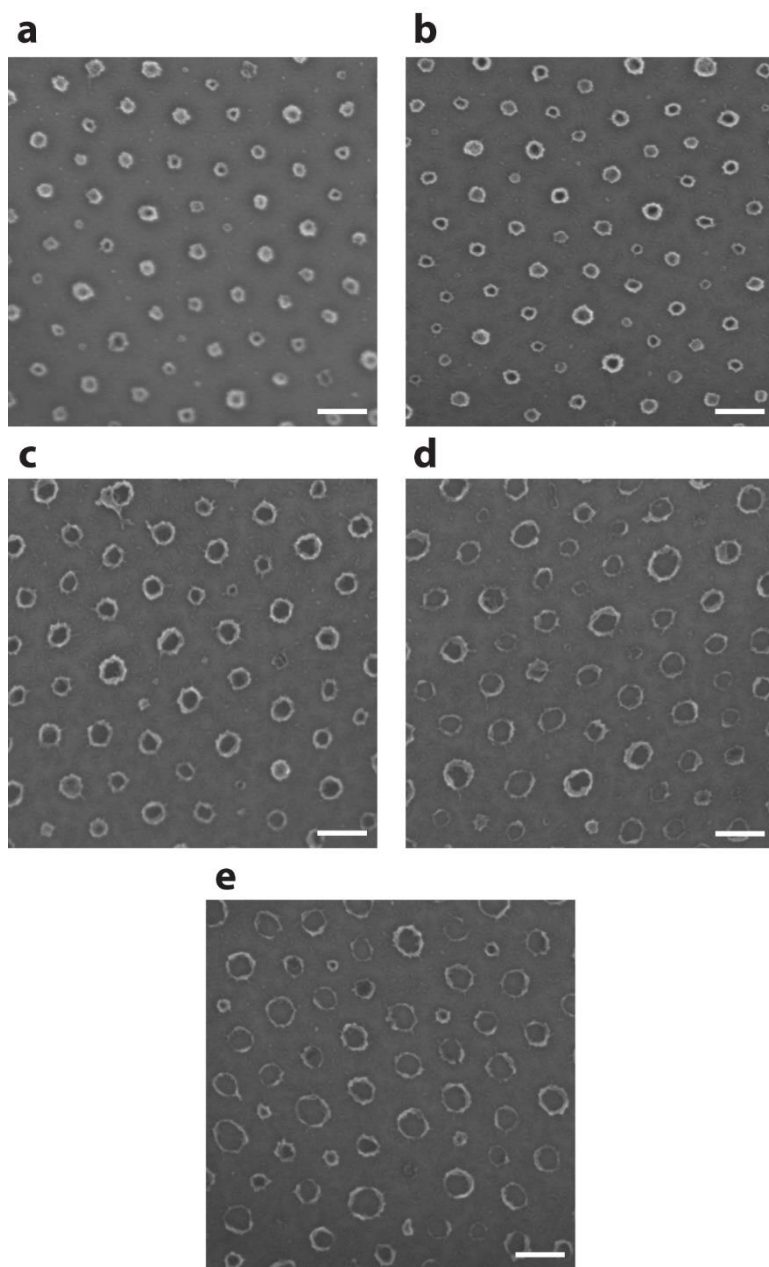


**Figure 2.24.** FE-SEM images of Pt NRs synthesized from single-layered films of IL-containing PS(109)-P4VP(27). (a)  $\mu = 0$ ; (b)  $\mu = 0.2$ ; (c)  $\mu = 0.4$ ; (d)  $\mu = 0.6$ ; (e)  $\mu = 0.8$ . Scale bars are 100 nm.

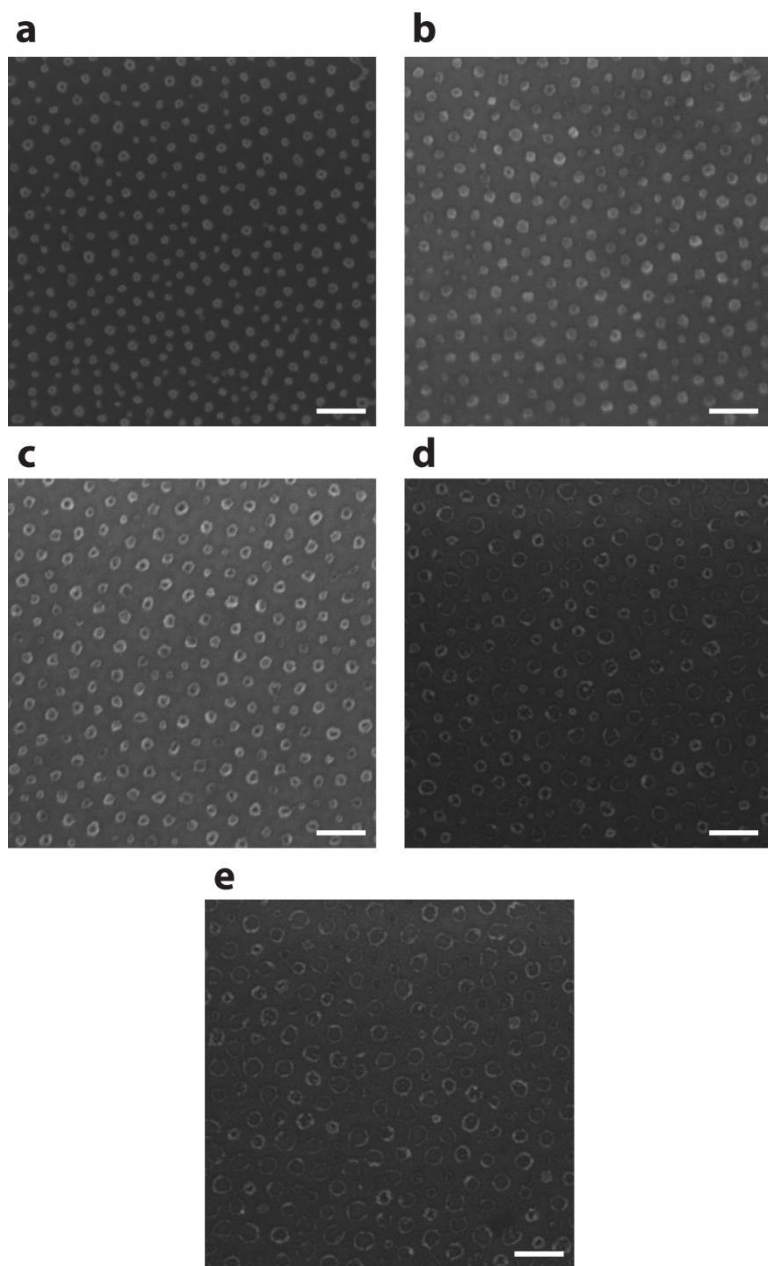


**Figure 2.25.** FE-SEM images of Pt NRs synthesized from single-layered films of IL-containing PS(51)-P4VP(18). (a)  $\mu = 0$ ; (b)  $\mu = 0.2$ ; (c)  $\mu = 0.4$ ; (d)  $\mu = 0.6$ ; (e)  $\mu = 0.8$ . Scale bars are 100 nm.

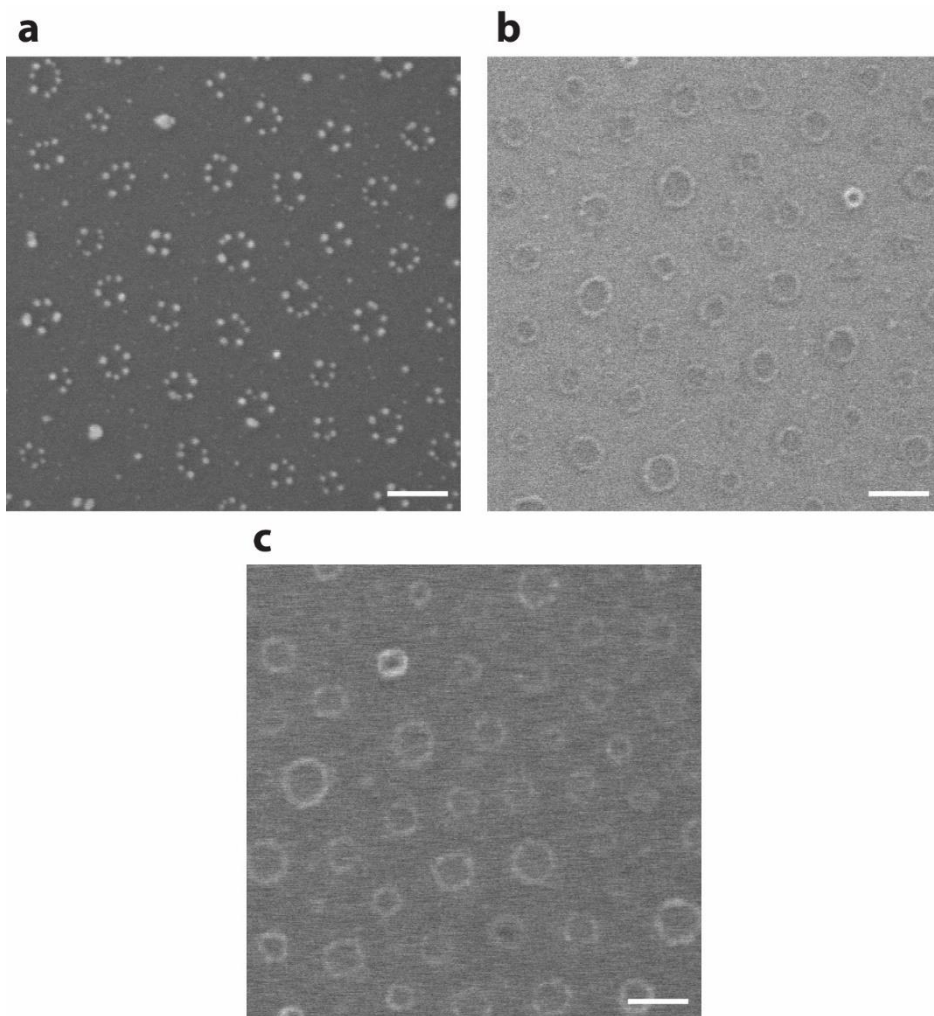


**Figure 2.26.** FE-SEM images of other NRs synthesized from single-layered films of IL-containing PS(109)-P4VP(27) ( $\mu = 0.8$ ). (a) Au; (b) PdO; (c) Fe<sub>2</sub>O<sub>3</sub>. Scale bars are 100 nm.

Polymer	$\mu$	Spacing (nm)	$D_c$ (nm)	$D_h$ (nm)	$D_H$ (nm)
PS(109)- P4VP(27)	0	95	$34.3 \pm 9.4$	$11.4 \pm 2.4$	-
	0.2	92	-	$16.7 \pm 3.8$	-
	0.4	91	$67.9 \pm 12.1$	$23.1 \pm 5.4$	-
	0.6	90	-	$29.7 \pm 9.8$	-
	0.8	88	$70.1 \pm 9.9$	$33.8 \pm 7.7$	-
PS(51)- P4VP(18)	0	48	$24.9 \pm 7.2$	$7.5 \pm 2.4$	104.8
	0.2	50	$25.0 \pm 7.0$	$8.2 \pm 3.5$	104.6
	0.4	49	$30.2 \pm 8.1$	$14.8 \pm 2.9$	104.2
	0.6	50	$29.7 \pm 5.3$	$17.3 \pm 4.0$	104.8
	0.8	50	$29.5 \pm 5.5$	$19.9 \pm 4.3$	105.7

**Table 2.3.** Characteristics of pristine and IL-containing PS(51)-P4VP(18) micelles.

Polymer	$\mu$	$D_o$ (nm)	$D_i$ (nm)	$T$ (nm)
PS(109)-P4VP(27)	0	$33.8 \pm 6.0$	$13.1 \pm 4.1$	$10.4 \pm 3.6$
	0.2	$34.5 \pm 4.6$	$20.6 \pm 3.7$	$7.0 \pm 3.0$
	0.4	$44.6 \pm 10.6$	$32.7 \pm 4.8$	$5.9 \pm 5.8$
	0.6	$52.0 \pm 10.4$	$40.7 \pm 7.8$	$5.6 \pm 6.5$
	0.8	$52.2 \pm 14.1$	$46.6 \pm 8.0$	$2.8 \pm 8.1$
PS(51)-P4VP(18)	0	$20.2 \pm 2.3$	$5.6 \pm 1.7$	$7.2 \pm 1.9$
	0.2	$22.8 \pm 5.6$	$6.4 \pm 2.3$	$8.2 \pm 3.0$
	0.4	$24.8 \pm 4.8$	$9.9 \pm 2.1$	$7.4 \pm 2.6$
	0.6	$27.8 \pm 6.2$	$12.6 \pm 3.4$	$7.6 \pm 3.5$
	0.8	$29.4 \pm 6.1$	$15.5 \pm 5.7$	$7.0 \pm 4.2$

**Table 2.4.** Characteristics of Pt nanorings fabricated from pristine and IL-containing PS-P4VP micelles.

## 5. Ordered complex arrays

Although nanomaterials in a periodic array have been successfully fabricated using thin films or micelles of diblock copolymers as shown previously, they mostly consisted of single types of nanomaterials with identical chemical compositions and shapes. If more than one type of nanomaterials is organized on a substrate, the unique functionalities of diverse nanomaterials, depending on their chemical constituents, shapes and sizes, can be combined. For this purpose, each type of nanomaterials should be arranged at a desired position with a specific order instead of being mixed arbitrarily, as this can yield a nanostructure with a complex composition in an ordered arrangement. Typical examples of such ordered complex nanostructures are a super-lattice of two or more types of NPs and self-assemblies of NWs and NPs. Recently two attempts to realize ordered complex nanostructures by diblock copolymers were reported. The repetitive use of templates of diblock copolymer thin films led to the production of multicomponent nanopatterns.<sup>[82]</sup> In addition, by repeating the coating of diblock copolymer micelles, hierarchical heterostructures were produced.<sup>[83]</sup> In these cases, diblock copolymer thin films or micelles were independently implemented.

This section describes the combination of various metal and oxide nanostructures demonstrated in previous sections, in this case TiO<sub>2</sub> nanostructures, metal NPs and NWs. The nanostructure synthesized initially from thin films of diblock copolymers on the substrate can act as a template to facilitate the placement of successively spin-coated micelles by capillary force. NPs can be generated from micelles by an oxygen plasma treatment, leading to the construction of ordered complex nanostructures. In addition, this arrangement of nanostructures is easily controlled by managing the molecular weights and spin-coating conditions.

## **Experimental Section**

*Ordered complex arrays consisting of TiO<sub>2</sub> nanostructures and Au NPs:* The H<sub>2</sub>AuCl<sub>4</sub>-containing PS-P4VP copolymers were spin-coated from a toluene solution at 4000 rpm for 60 s on the substrate with the TiO<sub>2</sub> nanostructures (*i.e.*, LTN and DTN). To synthesize the NPs from the copolymer micelles, the substrates were treated with an oxygen plasma performed at 100 W in 0.038 Torr for 5 min, followed by the calcination at 400 °C for 30 min in air. The spin-coating and oxygen plasma processes can be repeated to create ordered nanostructures with a higher complexity.

*Ordered complex arrays consisting of Pt NWs and NPs:* The H<sub>2</sub>PtCl<sub>6</sub>-containing PS-P4VP copolymers were spin-coated from a toluene solution at 4000 rpm for 60 s on the substrate with arrayed Pt NWs. To synthesize the NPs from copolymer micelles, substrates were treated with an oxygen plasma performed at 100 W in 0.038 Torr for 5 min.

*Characterization:* The PS-P4VP micelles and ordered complex arrays were analyzed using a multimode 8 AFM with a Nanoscope V controller (Bruker) in tapping mode with Al-coated Si cantilevers, and an FE-SEM (Hitachi S-4300 at 15 kV).

## **Results and Discussion**

The PS(51)-P4VP(18) micelles were spin-coated onto the LTN. The AFM height mode image in Figure 2.27a displays that the linearly-aligned arrays of copolymer micelles are placed between the LTNs. This linear chain of the spherical micelles between the LTNs are better illustrated in the AFM phase mode image of the magnified region in Figure 2.27a (see inset). Subsequently, the PS(32)-P4VP(13)

micelles were spin-coated onto the LTN. Since the size of the copolymer micelles is smaller than the previous case, arrays of the copolymer micelles are hardly observed in the AFM height mode image in Figure 2.27b. In contrast, the AFM phase mode image of the magnified region in Figure 2.27b (see inset) clearly shows the zigzag chain of the micelles between the LTNs. Thus, the size of the copolymer micelles led to the change in the internal structure among the copolymer micelles arranged between the LTNs. These linear and zigzag arrangement of the copolymer micelles are different from the hexagonally-ordered placement of micelles when spin-coated onto a flat substrate as mentioned in the previous sections (see Figure 2.5).

These unique arrangements can be attributed to the capillary force toward the LTNs. During the rapid evaporation of the solvent by the spin-coating process, the capillary force induces the copolymer micelles to be eventually placed between the LTNs. Xia *et al.* had reported the template-assisted self-assembly of the colloidal particles of which the alignment is determined by the size ratio between the NPs and template.<sup>[84,85]</sup> The colloidal particles having the comparable diameter to the width of the linear trenches organize into the linear chain by templating against the template, whereas smaller particles assemble into a closely packed structure within the trench.

In this experiment, the precursors of the Au NPs have been already loaded into copolymer micellar cores prior to spin-coating. The PS(51)-P4VP(18) micelles spin-coated onto the LTNs produced a linear array of the Au NPs as shown in the FE-SEM image (Figure 2.28a). The linear alignment of the Au NPs is similar to that of the copolymer micelles because the NPs are generated at the region of the micellar cores with the preservation of its original position. In result, the ordered

complex nanostructures consisting of the LTNs and the linear arrays of the Au NPs were obtained. On the other hand, the zigzag alignment of the Au NPs was obtained from the smaller PS(32)-P4VP(13) micelles spin-coated onto the LTNs (Figure 2.28b). Thus, the molecular weights of the copolymer micelles eventually determined the final shape of the ordered complex arrays.

The ordered complex arrays with more dense arrays of the Au NPs can be produced by repeating the process of the NP synthesis twice and three times as shown in Figure 2.29a and 2.29b, respectively. Increased number of the Au NPs between the LTNs is clearly observed in each FE-SEM image, while the inter-particle distance among the Au NPs is reduced.

The PS-P4VP micelles can be also spin-coated onto the DTNs for the preparation of the different ordered complex arrays. Although the PS(51)-P4VP(18) micelles and the DTN are indistinguishable in the AFM images (Figure 2.30a), arrays of the dark holes equivalent to the bare substrate are observed, indicating that the copolymer micelles are placed at the hexagonal interstitial sites of the DTNs. In other word, the individual micelles are eventually surrounded by three TiO<sub>2</sub> nanodiscs, which will be discussed later. On the other hand, PS(32)-P4VP(13) micelles, discerned by size from the DTNs in the AFM image (Figure 2.30b), are placed at the gap between adjacent two TiO<sub>2</sub> nanodiscs.

As discussed in the LTN case, the difference in the spatial placement of the copolymer micelles are determined by the capillarity toward the DTNs and the size of the micelles. In result, the PS(51)-P4VP(18) micelles favor the interstitial sites of the DTNs with the balanced capillary forces and the size exclusion effect, while smaller PS(32)-P4VP(13) micelles are pulled toward the gap between nanodiscs where the strongest capillary force is oriented. Again, the size of micelles play a

pivotal role in their arrangement.

These arrangement are preserved when the Au NPs were synthesized from the PS-P4VP micelles spin-coated onto the DTNs as shown in Figure 2.31. The solid circles and dashed guiding lines were added in the magnified images (insets of Figure 2.31) for a better visualization of the ordered complex arrays. Figure 2.31a shows the combined structure of the DTNs and the hexagonal arrays of the Au NPs placed at the void spaces of the DTNs where the original copolymer micelles used to be arranged. And this arrangement resembles the lattice of stacking layers to build a hexagonally close-packed crystal structures. On the other hand, Figure 2.31b shows more complex structure of the DTNs with arrays of the Au NPs arranged at the midpoint of the neighboring DTNs. Joining the position of the Au NPs as shown the inset of Figure 2.31b forms a trihexagonal tiling composed of interlaced triangles of which the lattice points have four neighboring points each (Kagome lattice).

Each NP placement can be examined in detail by counting numbers of the TiO<sub>2</sub> nanodiscs and Au NPs. Unlike the copolymer micelles observed by AFM, the hexagonally arrayed Au NPs in Figure 2.31a are certainly distinguishable from the DTNs, enabling to obtain their size distributions as displayed in Figure 2.32a. The diameters of the DTNs and Au(51-18) were calculated to be  $34 \pm 4$  nm and  $12 \pm 3$  nm, respectively, with the number ratio of 1:1.1. It should be noted that the statistical interference can be excluded in this analysis due to little overlapping between two size distributions. Provided a perfect arrangement of Au NPs only at the interstitial sites of the DTNs, each DTN is surrounded by three Au NPs, while surrounding Au NPs are shared by adjacent three DTNs. Then the theoretical number ratio of this ideal complex arrays should be 1:1 ( $= 3/3$ ), which is similar to

the calculated value (1:1.1). This consideration can be also employed for the ordered complex arrays of the DTNs with Kagome arrays of the Au NPs (Figure 2.31b). Their size distributions (Figure 2.32b) are clearly separated from each other. And the diameters of the DTNs and Au NPs in a Kagome array were  $35 \pm 3$  nm and  $8 \pm 2$  nm, respectively, with the number ratio of 1:2.7. For the DTNs with a perfect Kagome arrays of the Au NPs, the number of the Au NPs organized around each DTN is 6. And each Au NP is placed at the gap between two adjacent DTN. Thus, the number ratio of DTN to Au NPs in a Kagome array should be 1:3 ( $=6/2$ ), and this hypothesis is agreed by the result obtained by counting from FE-SEM image (1:2.7).

Note that the size of micelles used above were comparable to or less than the dimension of the TiO<sub>2</sub> nanostructures. If the size of the copolymer micelles is too large, the special arrangement of the micelles cannot be realized. AFM images in Figure 2.33 show that only a few PS(109)-P4VP(27) micelles were placed in TiO<sub>2</sub> nanostructures. Based on a broad size distribution of PS(109)-P4VP(27), presumably most of the micelles with larger diameter are scarcely placed but thrown away out of the substrates during the spin-coating process.

Consisting of two different nanoarrays, ordered complex arrays demonstrated above can be classified into the binary superstructures. Since the spin-coating process can be repeated to synthesize the Au NPs as described above (Figure 2.29), more complex arrays with the ternary superstructures can be prepared on substrates. The FE-SEM image in Figure 2.34 shows the ordered complex arrays consisting of three different nanoarrays. To fabricate this nanostructures, the PS(51)-P4VP(18) micelles were spin-coated on the DTNs with the Kagome arrays of the Au NPs (Figure 2.31b), followed by an oxygen plasma treatment to generate the hexagonal

arrays of the Au NPs as the third component. However, when PS(32)-P4VP(13) micelles were spin-coated on the DTNs with hexagonal arrays of Au NPs (Figure 2.31a), identical ternary superstructures were hardly attainable. This implies that PS(51)-P4VP(18) micelles were spin-coated onto the DTNs as if they had not recognized the presence of the small Au NPs in a Kagome array, but the arrangement of PS(32)-P4VP(13) micelles was severely interrupted by pre-placed large Au NPs in a hexagonal array. In other word, the NPs can also contribute to the templating effect for the placement of the copolymer micelles in spite of their low height, which can be extended to another metal or oxide nanostructures such as NWs and NRs.

The AFM images in Figure 2.35 show the PS-P4VP micelles spin-coated onto arrayed Pt NWs. In this experiment, the molecular weights of the PS-P4VP for the synthesis of both Pt NWs and Pt NPs are identical such that the width scale between the Pt NWs is approximately comparable to the diameter of the spin-coated micelles. Since the height of the Pt NWs are much smaller than that of the copolymer micelles, the directed arrangement of the micelles is hardly noticeable. But an oxygen plasma etching reveals that, as shown in FE-SEM images in Figure 2.36, most of NPs are placed with forming a linear arrangement between Pt NWs. When the concentration of the copolymer micellar solution increased, the inter-distance of linearly arranged Pt NPs was reduced due to its more close-packed placement between the Pt NWs. (compare Figure 2.36a to 2.36b). The low molecular weight PS-P4VP generated the complex ordered arrays of the Pt NWs and NPs with a higher density (Figure 2.36c). From these results, it is confirmed that the Pt NWs can also act as a template to guide the placement of the copolymer micelles efficiently.

## Summary

The selective placement of PS-P4VP micelles on the pre-existing templates, in this case TiO<sub>2</sub> nanostructures and Pt NWs was controlled to fabricate the ordered complex arrays. By the template-assisted self-assembly of the copolymer micelles during the spin-coating process, a range of unusual arrangements (*i.e.*, linear, zigzag, Kagome arrays) of the copolymer micelles were induced by the capillary force toward the templates. A following oxygen plasma etching generated NPs at the micellar cores with holding the original position of the micelles to realize the ordered complex nanostructures consisting of multiple nanoarrays. The morphologies and spacings of arrangements were precisely adjusted by controlling spin-coating conditions and the molecular weights of the copolymers. The tunability of the diblock copolymers and their micelles to create each component of the ordered complex arrays, the simplicity of whole process, and the controllability over the dimension and shape of arrays show great promise for a wide range of novel applications such as multifunctional devices with complex structures.

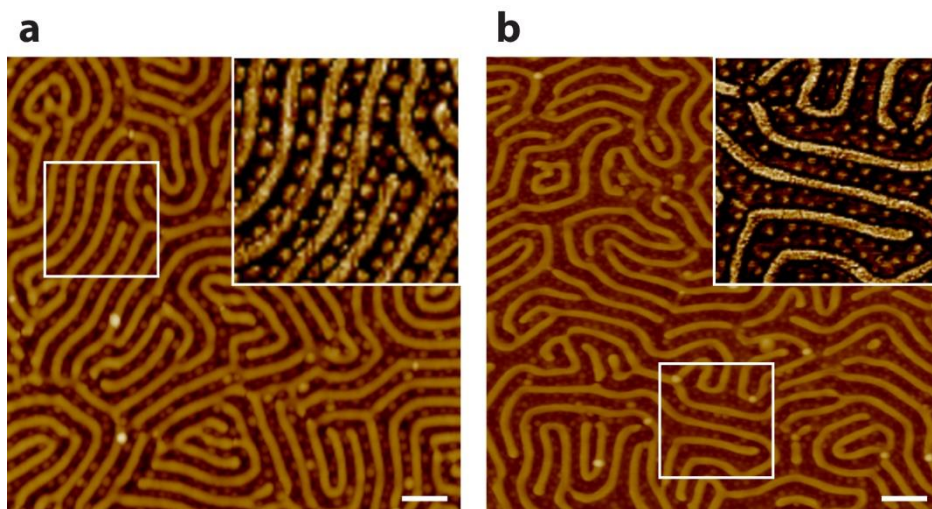


**Figure 2.27.** AFM height mode images of copolymer micelles spin-coated on LTN. (a) PS(51)-P4VP(18); (b) PS(32)-P4VP(13). Each inset is magnified AFM phase mode image corresponding to the square marked region. Scale bars are 200 nm.

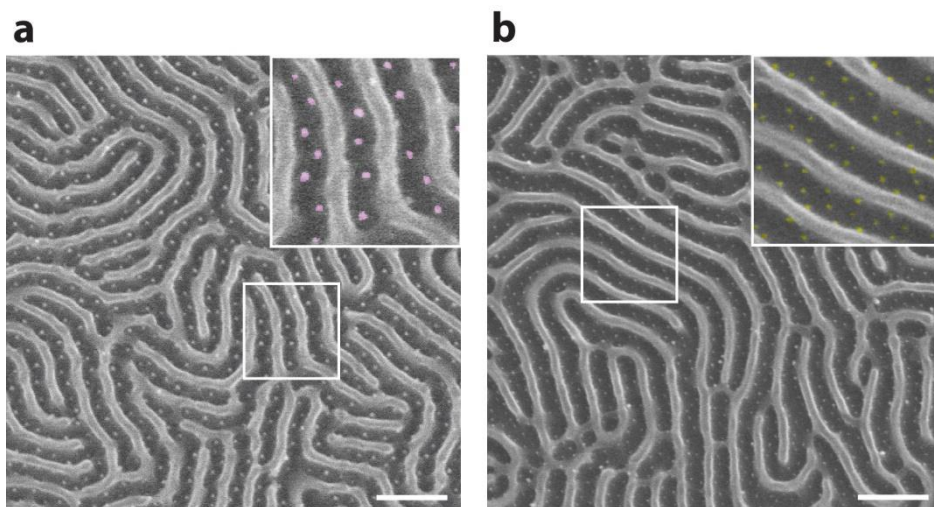


**Figure 2.28.** FE-SEM images of ordered complex arrays consisting of LTN and (a) Au(51-18) and (b) Au(32-13). Each inset is a magnified image of the square marked region. Scale bars are 200 nm.

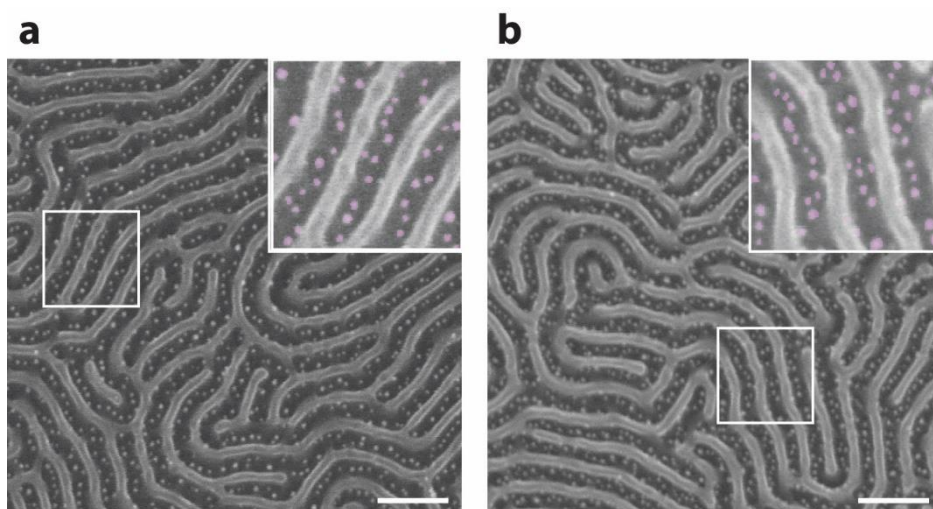


**Figure 2.29.** FE-SEM images of ordered complex arrays consisting of LTN Au(51-18) with a higher number density by repeating procedure of the synthesis of Au NPs (a) twice and (b) three times. Each inset is a magnified image of the square marked region. Scale bars are 200 nm.

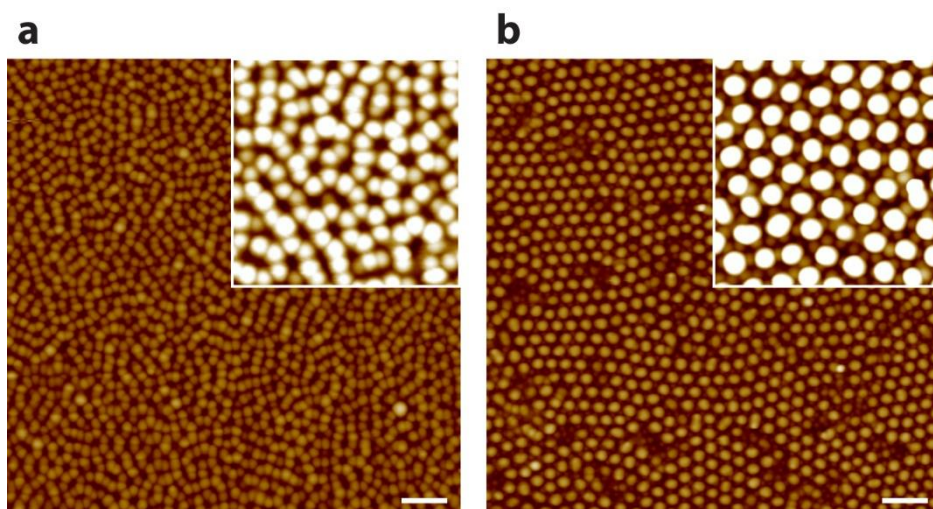


**Figure 2.30.** AFM height mode images of copolymer micelles spin-coated on DTN. (a) PS(51)-P4VP(18); (b) PS(32)-P4VP(13). Each inset is magnified image with high Z scale contrast. Scale bars are 200 nm.

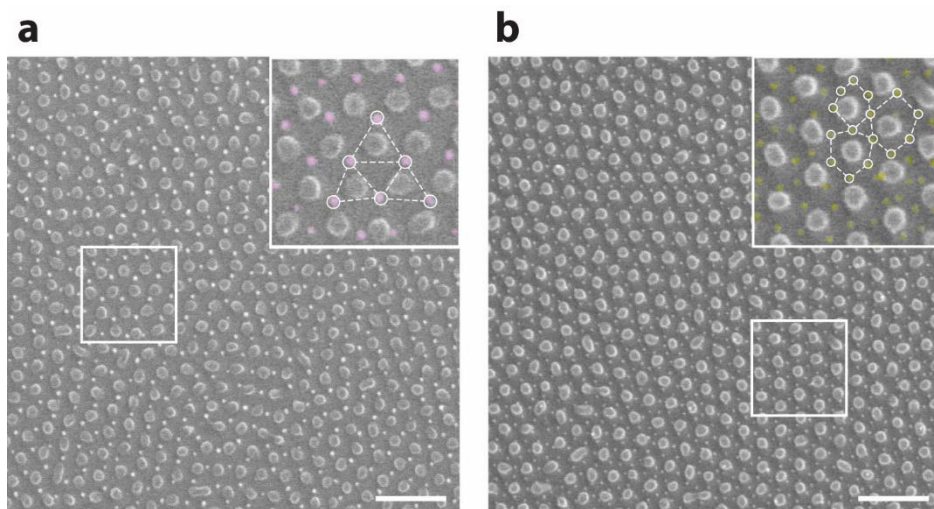


**Figure 2.31.** FE-SEM images of ordered complex arrays consisting of DTN and (a) Au(51-18) and (b) Au(32-13). Each inset is a magnified image of the square marked region with solid circles for Au NPs and dashed guiding lines. Scale bars are 200 nm.

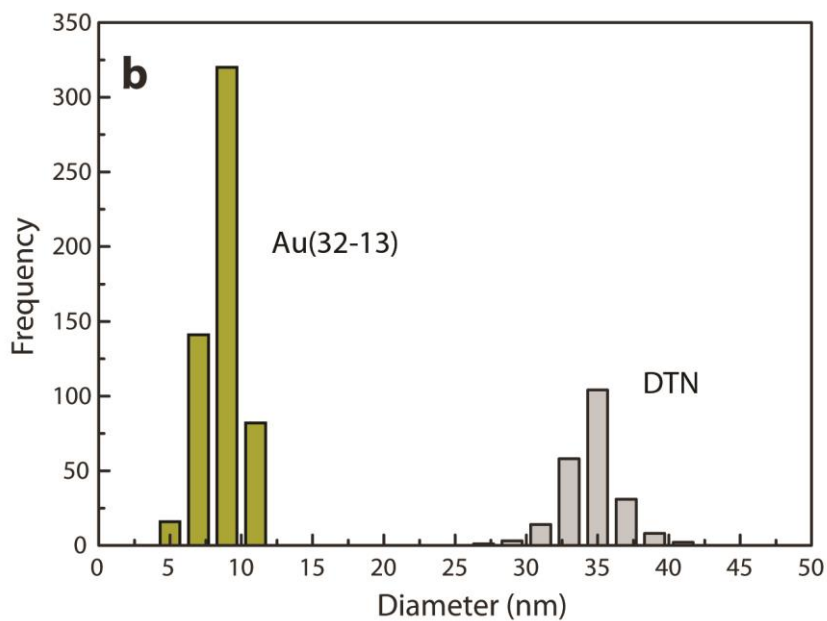
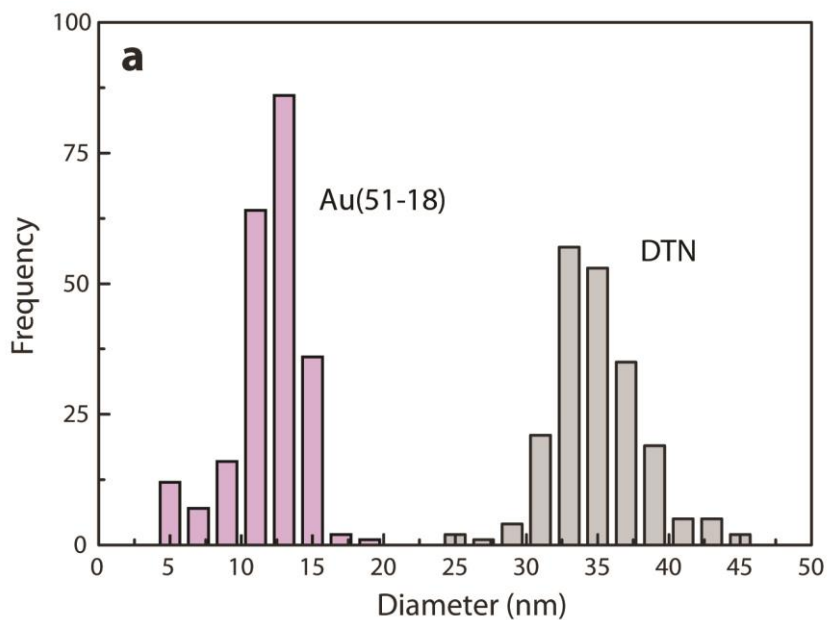


**Figure 2.32.** Size distribution of DTN and (a) Au(51-18) and (b) Au(32-13) from ordered complex arrays of in the same area.

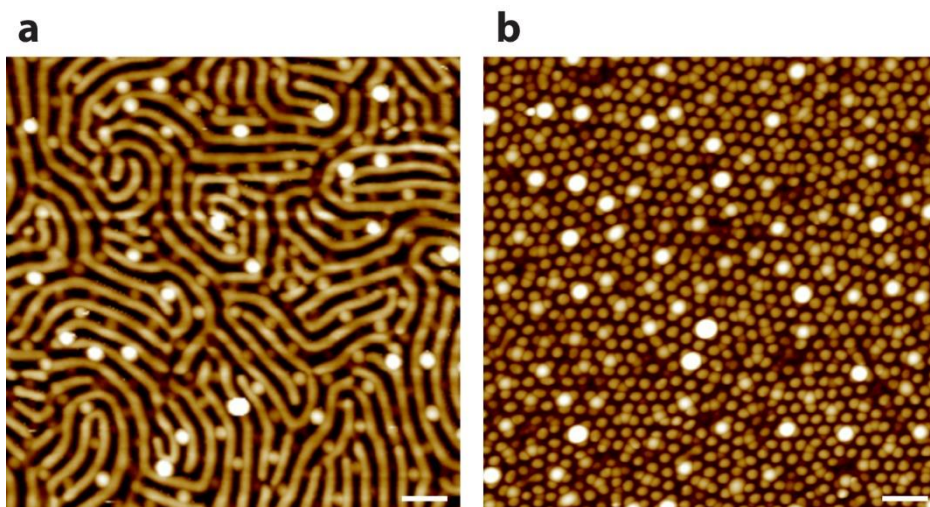


**Figure 2.33.** AFM images of PS(109)-P4VP(27) micelles spin-coated on (a) LTN and (b) DTN. Scale bars are 200 nm.

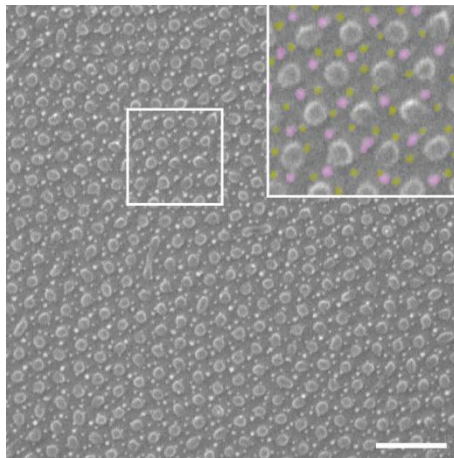


**Figure 2.34.** FE-SEM image of ordered complex nanostructures of DTN with Au(51-18) and Au(32-13). Inset is a magnified image of the square marked region. Scale bars are 200 nm.

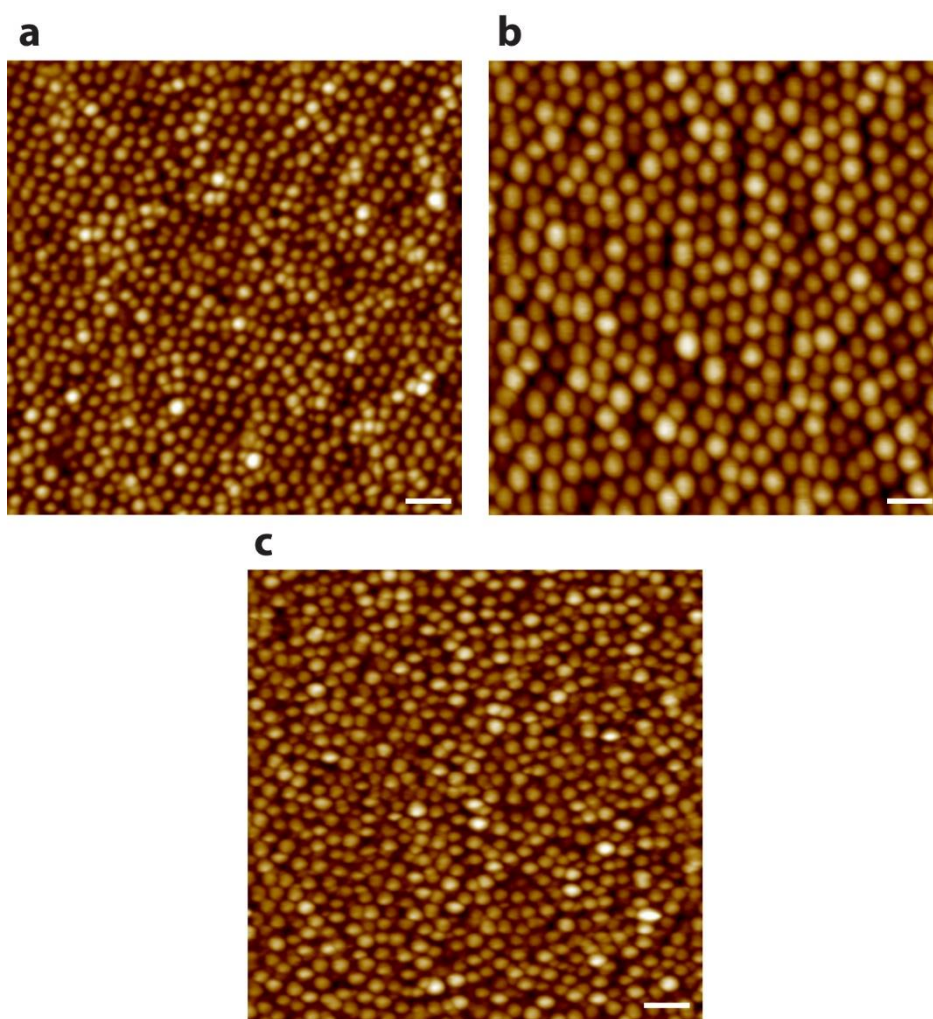


**Figure 2.35.** AFM images of PS-P4VP micelles spin-coated onto Pt NWs. (a,b) Pt NWs synthesized from PS(32)-P4VP(13) with PS(32)-P4VP(13) micelles spin-coated from 0.5 and 0.3 wt% solution; (c) Pt NWs synthesized from PS(25)-P4VP(7) with PS(25)-P4VP(7) micelles spin-coated from 0.3 wt% solution Scale bars are 100 nm.

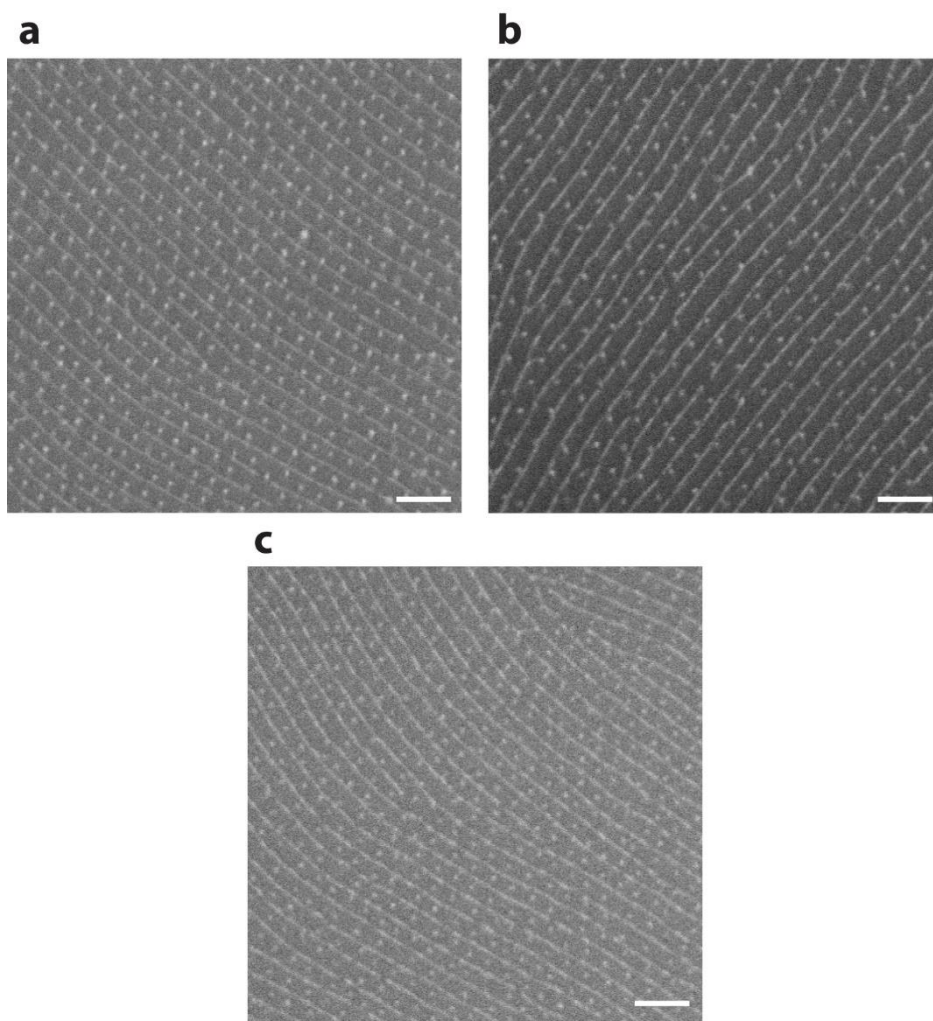


**Figure 2.36.** FE-SEM images of ordered complex arrays fabricated from copolymer micelles spin-coated onto Pt NWs displayed in Figure 2.35. (a) Figure 2.35a; (b) 2.35b; (c) 2.35c. Scale bars are 100 nm.

## Chapter III

### Fabrication of Nanopatterned Graphene

#### 1. Graphene decorated with arrayed nanoparticles

Graphene has a two-dimensional and conductive structure that can effectively support NPs. Thus many experiments have been carried out to grow or attach highly catalytic NPs of metals or metal oxides such as Pt,<sup>[84]</sup> Au,<sup>[85]</sup> Ag,<sup>[86]</sup> and TiO<sub>2</sub>,<sup>[87]</sup> on graphene sheets for various purposes, including for the enhanced electrocatalytic activity, sensing, and actuating performance of graphene. For example, Dai *et al.*<sup>[88]</sup> recently reported the improved catalytic activity of a hybrid material consisting of rGO and Co<sub>3</sub>O<sub>4</sub> NPs, compared to that of rGO alone or Co<sub>3</sub>O<sub>4</sub> NPs themselves. They ascribed the improved electrocatalytic activity to the synergetic chemical coupling between the rGO and the NPs.

Controlling the size and amount of NPs attached to graphene is of great importance for practical applications, as the electrochemical properties are significantly dependent on these factors.<sup>[89]</sup> However, current techniques for the attachment of NPs onto graphene do not show sufficient controllability. The majority of the methods to attach, anchor, or grow NPs onto graphene have employed an *in situ* synthesis of NPs from the precursors at the surface of the GO or rGO.<sup>[84-87]</sup> Despite the simplistic synthesis of graphene-NP hybrid materials, the NPs on GO or rGO sheets from the *in situ* synthesis are generally of an irregular size, shape, and may be agglomerated.

As an alternative method, NPs were synthesized *ex situ* and then mixed with a GO dispersion to be adsorbed onto the surface of graphene.<sup>[90,91]</sup> However, the

physisorption of NPs onto graphene was not adequate to control the amount of NPs on the graphene, although the size and shape of the *ex situ* synthesized NPs were regular. Furthermore, stabilizers such as surfactants or polymers on the surface of *ex situ* synthesized NPs could hinder the catalytic interaction.<sup>[92]</sup>

Particularly for electrochemical applications, graphene attached with NPs, whether they were synthesized *in situ* or *ex situ*, should be coated on carbon electrodes, which presents the challenge of avoiding agglomeration of the graphenes attached with NPs. To take full advantage of the unique characteristics of graphene, such as flexibility, transparency, and transferability,<sup>[93]</sup> it is necessary to produce aggregation-free NPs on a continuous thin film of graphene. Numerous methods including layer-by-layer assembly, printing-based transfer of NPs, transfer of NPs assembled at an interface, electrodeposition, and sputtering are available to produce NPs on a continuous substrate.<sup>[94]</sup> However, few of these methods can satisfy the requirement of synthesizing aggregation-free NPs with tunable size and number density on a continuous, large-area graphene sheet.

The diblock copolymer approach has been used to synthesize arrayed NPs on large-area substrates and is a potential candidate to decorate NPs on graphene to meet the criteria of synthesizing aggregation-free NPs with controllability. To apply the nanostructures of copolymers to graphene, however, the surface of graphene should be chemically modified<sup>[48,49]</sup> or covered with an additional layer<sup>[24,25,45,95]</sup> to induce perpendicularly oriented nanostructures, which are necessary for the application of diblock copolymers to templates and masks. To avoid additional treatment of the graphene surface, an approach involving nanoscale micelles of diblock copolymers may be a plausible answer for the tunable synthesis of NPs on graphene.

In this section, we decorated rGO films with arrays of Au NPs using diblock copolymer micelles. The rGO film with Au NPs was transferable without deterioration of the Au NPs array. Then we modified glassy carbon electrodes (GCE) by transferring the rGO decorated with Au NPs, which showed high electrocatalytic performance in a redox reaction. In addition, we applied rGO films with Au NPs to the oxygen reduction reaction (ORR), which is an important electrochemical reaction for a variety of energy conversion devices, including fuel cells. Furthermore, we were able to differentiate the ORR mechanisms between Au NPs having different diameters, which were effectively controlled by the micellar dimensions.

## **Experimental Section**

*Materials:* Diblock copolymers of PS-P4VP, PS(51)-P4VP(18), and PS(109)-P4VP(27) were purchased from Polymer Source, Inc. The number in the parenthesis is the average molecular weight ( $M_n$ ) in kg/mol. The polydispersity index (PDI) is 1.15. Tetrachloroauric(III) acid ( $\text{HAuCl}_4$ ), iron(III) chloride ( $\text{FeCl}_3$ ), and palladium(II) acetate ( $\text{Pd}(\text{O}_2\text{CCH}_3)_2$ ) as precursors of Au and  $\text{Fe}_2\text{O}_3$ , PdO NPs were obtained from Sigma-Aldrich and used as received. Hydrazine monohydrate (98%) was purchased from Sigma-Aldrich.

*Diblock copolymer micelles containing precursors of NPs:* PS(51)-P4VP(18) and PS(109)-P4VP(27) were dissolved in toluene with a concentration of 0.5 wt%. The solution was stirred for 24 h at a room temperature and for 3 h at 85 °C and then cooled to a room temperature. The precursors of the NPs ( $\text{HAuCl}_4$ ,  $\text{FeCl}_3$ , and  $\text{Pd}(\text{O}_2\text{CCH}_3)_2$ ) were added to the micellar solution. The molar ratio of precursors to pyridine units in the P4VP block was fixed to 0.5 for both cases. The solution was

stirred for at least 7 days at room temperature.

*rGO films decorated with arrayed NPs:* GO was synthesized by the modified Hummers method as described elsewhere.<sup>[96,97]</sup> GO powder was added to deionized water (0.1 wt%), which was ultrasonicated for 2 h, followed by centrifugation at 3000 rpm for 1 h and removal of the precipitates, resulting in a yellow-brown homogeneous dispersion. SiO<sub>2</sub>/Si substrate was cleaned in piranha solution (70/30 v/v concentrated H<sub>2</sub>SO<sub>4</sub> and 30% H<sub>2</sub>O<sub>2</sub>) at 90 °C for 30 min, and thoroughly rinsed with deionized water several times, and then blown dry with nitrogen. On the cleaned substrate, a GO solution was spin-coated five times at 2000 rpm for 30 s to construct continuous GO layer and dried in a vacuum oven at 40 °C overnight. The chemical reduction of GO films was carried out by hydrazine vapor. A fully dried GO film on the substrate was placed in a closed glass vessel containing hydrazine monohydrate and heated at 160 °C for 1 day. On this rGO film, a layer of PS-P4VP micelles containing the precursors of NPs in their cores was spin-coated, at 2000 rpm for 60 s. To synthesize the NPs along with the removal of the copolymer, the rGO film decorated with the copolymer micelles was heated in air at 400 °C for 30 min.

*Transfer of rGO films with NPs onto various substrates:* PMMA (M<sub>n</sub> = 51k, PDI = 1.06) was dissolved in toluene with a concentration of 1.0 wt% and spin-coated onto an rGO film decorated with arrays of NPs prepared on the SiO<sub>2</sub>/Si substrate. An additional thick PMMA film was drop-cast on top of the spin-coated PMMA. A droplet of NaOH solution (0.1 M) was added to an edge of the substrate, which led to delamination of the rGO film from the substrate. The delaminated film floated off onto deionized water and was transferred to a designated substrate such as a GCE or an ITO/glass for electrochemical measurements. The transferred film was

dried under ambient conditions overnight. For the removal of the PMMA supporting layer, the composite film was heated in air at 400 °C for 30 min or immersed in acetone for 1 h.

*Electrochemical Measurements:* Cyclic voltammograms, Nyquist plots, amperometry curves, and linear sweep voltammograms were obtained with a CHI 660A electrochemical workstation (CH instruments). For electrochemical measurements, plate-type GCE (ALS Co.) and ITO/glass substrates were used. The geometric surface area was 0.28 cm<sup>2</sup>. A glassy carbon disk electrode with a diameter of 5 mm (Pine Research Instrumentation) was employed as a rotating disk electrode (RDE). GCE and RDE were carefully polished with alumina powder and rinsed with double distilled water to remove alumina residues. A platinum wire was used as a counter electrode and Ag/AgCl as a reference electrode. 0.01 M phosphate buffered saline (PBS) containing 5 mM of Fe(CN)<sub>6</sub><sup>3-/4-</sup> (1:1) was used for electrochemical characterizations. Nyquist plots were recorded at the equilibrium potential of Fe(CN)<sub>6</sub><sup>3-/4-</sup> over the frequency range of 0.5 to 1000 Hz. The impedance data were analyzed using Zsimpwin 3.0 software (Echem Software).

*Characterization:* rGO films, PS-P4VP micelles, and rGO films with NPs were analyzed using a Multimode 8 AFM with a Nanoscope V controller (Bruker) in tapping mode with Al-coated Si cantilevers. For TEM, rGO films with NPs were floated off from the substrate onto deionized water by delamination with NaOH solution, as described above, and collected on carbon-coated copper TEM grids. TEM was performed on a Hitachi 7600 operating at 100 kV, a JEM-2100 (JEOL) at 200 kV, and a JEM-3010 (JEOL) at 300 kV. X-ray diffraction (XRD) patterns were obtained on a D8-Advance with Cu K<sub>α1</sub> radiation. X-ray photoelectron spectroscopy (XPS) was performed using a Sigma Probe (ThermoVG) with a

monochromatic Al  $K_{\alpha}$  X-ray source operating at 100 W.

## Results and Discussion

GO powder synthesized from graphite by the modified Hummers method<sup>[96,97]</sup> was characterized by XRD. The XRD patterns displayed in Figure 3.1 show a large shift in the peak signal from  $\theta = 26.5^{\circ}$  to  $12.3^{\circ}$  after the oxidation process, which is equivalent to the increment of the interplanar distance from  $\sim 0.34$  nm to  $\sim 0.72$  nm. An expansion in the GO thickness is due to abundant oxygen-containing functional groups on its basal plane.<sup>[98]</sup> Those hydrophilic functional groups enable GO to be dispersed in deionized water, thus this aqueous dispersion of GO can be spin-coated onto a  $\text{SiO}_2/\text{Si}$  substrate. The AFM image of the spin-coated GO (Figure 3.2a) shows a number of overlapped flakes having a thickness of  $\sim 1.0$  nm, which is larger than that of one-atom-thick single-layered pristine graphene ( $\sim 0.6$  nm). The successive spin-coating process eventually provided continuous, two-dimensional GO films over a large area. The thickness was controllable by adjusting the concentration of the GO dispersion, the spinning speed, and the number of repeats of spin-coating.<sup>[99]</sup> The spin-coated GO was then reduced to rGO using hydrazine as a reducing agent. The rGO film showed a uniform surface with a thickness of  $\sim 2.3$  nm (Figure 3.2b) with an average roughness of  $\sim 0.4$  nm.

Prepared rGO film was further characterized by XPS, UV-vis spectrophotometry, and Raman spectroscopy. The XPS spectra of C(2s) in Figure 3.3a clearly show a considerable decrease in peaks assigned to oxygenated carbon atoms after the reduction process by hydrazine vapor. Non-oxygenated ring C, assigned to the most prominent peak ( $\sim 284.8$  eV) in the XPS spectrum, is dominant in rGO, and N atoms are inserted onto the platelet edges as well as the basal planes to recover the

graphene network.<sup>[100]</sup> This observation is also supported by comparing the UV-vis absorption spectra of GO and rGO films (Figure 3.3b). The appearance of an absorption peak ( $\sim 270$  nm) of rGO is related to the spectral band of  $\pi$ - $\pi^*$  transitions in aromatic C-C bonds, which indicates the restoration of conjugated structures in the basal plane. Raman spectrum of rGO film (Figure 3.3c) represents G band at  $1601\text{ cm}^{-1}$  and D band at  $1353\text{ cm}^{-1}$  as widely discussed in other works as well.

The surface of the rGO films was coated with a single layer of PS(109)-P4VP (27) micelles with  $\text{HAuCl}_4$ , the precursor of Au NPs, in the P4VP cores. The AFM image in Figure 3.4a shows an array of spherical micelles without overlapping, implying a single layer of copolymer micelles. Then, copolymers were removed by heating at  $400\text{ }^\circ\text{C}$ , which resulted in the generation of Au NPs in the core regions of the micelles as shown in Figure 3.4b. The spacing ( $\sim 111$  nm) and number density ( $\sim 7.60 \times 10^9\text{ cm}^{-2}$ ) of the Au NPs measured by FFT analysis are similar to those of the original copolymer micelles ( $\sim 118$  nm and  $\sim 7.62 \times 10^9\text{ cm}^{-2}$ ), implying successful fabrication of an array of non-overlapped Au NPs directly decorated on rGO with preservation of the order of the copolymer micelles. It is worthwhile to note that Au NPs with well-defined spacing and without agglomeration could not be easily synthesized on rGO by either *in situ* or *ex situ* methods.

In the XPS analysis of the Au NPs (Figure 3.5a), no peaks associated to oxides were observed, indicating pure Au NPs. Because rGO films can be delaminated from  $\text{SiO}_2/\text{Si}$  substrates by exposing them to a solution of NaOH to be transferred onto a copper grid for TEM analysis. Figure 3.4c presents non-overlapped Au NPs with more or less regular spacing on the rGO film whose edge is visible at the left side of the image. The Au NPs have an average diameter of 11.0 nm (histogram in Figure 3.4d) and a face-centered cubic crystalline structure (HR-TEM in Figure

3.4c and SAED pattern in Figure 3.5b). It is of more importance that this TEM image confirms that the array of Au NPs on the rGO was well maintained during the transfer process, suggesting that it is possible to transfer Au NPs on rGO to any substrate, including a hydrophobic GCE or a flexible polymer film (see inset of Figure 3.4c). Moreover, no additional layer was observed on the surface of the Au nanoparticles in the HR-TEM image (Figure 3.4c), indicating a pure Au surface, which is particularly suitable for catalytic applications.<sup>[101]</sup>

To demonstrate the controllability, a lower molecular weight copolymer PS-P4VP (51k-18k) than previously utilized PS-P4VP (109k-27k) was employed with the same procedure. Because both core and corona are smaller than before, and they effectively govern the diameter and the spacing of the synthesized NPs, respectively, the average diameter of the Au NPs was reduced to 8.6 nm (Figure 3.6d), and the spacing also decreased to ~53 nm, which results in a 4.8-fold increase in the number density ( $3.62 \times 10^{10} \text{ cm}^{-2}$ ). The more crowded NPs are visible in the AFM (Figure 3.6b) and TEM images (Figure 3.6c). However, we still have a single layer of Au NPs without agglomeration or overlapping. Thus, rGO films decorated with smaller Au NPs in a higher number density was efficiently produced.

With diblock copolymer micellar approach, diverse NPs were able to decorate rGO films by changing the precursors loaded into the cores of the copolymer. Figure 3.7 and 3.8 shows rGO decorated with a single layer of  $\text{Fe}_2\text{O}_3$  and PdO NPs without agglomeration by altering the precursor from  $\text{HAuCl}_4$  to  $\text{FeCl}_3$  and  $\text{Pd}(\text{O}_2\text{CCH}_3)_2$ , respectively, which were loaded in the P4VP cores of PS-P4VP (51k-18k) micelles. PdO NPs were further reduced by additional treatment of hydrazine vapor as before to reduce GO films. Shifts in XPS spectra of Pd(3d) (Figure 3.7c) and crystalline structure in HR-TEM image (inset of Figure 3.7b) indicates the

successful reduction of PdO to Pd.

As demonstrated, the diblock copolymer micellar approach allows the decoration of Au NPs on rGO films with controllable diameter and number density. Furthermore, when TEM samples were prepared, the array of Au NPs on rGO films was not affected during the transfer, indicating that electrochemical electrode can be modified by transferring rGO films decorated with Au NPs as they were made.

Before characterizing the ORR performance, the general electrocatalytic features of rGO decorated with arrayed Au NPs were studied by the redox reaction of  $\text{Fe}(\text{CN})_6^{3-/4-}$  with electrochemical impedance spectroscopy (EIS) and cyclic voltammetry (CV). rGO films with arrayed Au NPs were directly transferred onto a GCE, as demonstrated with a flexible polymer film as well as a TEM sample (Figures 3.3c and 3.5c). It should be noted again that Au(51-18) has a smaller diameter with a higher number density than Au(109-27).

In the Nyquist plot of Figure 3.9a, the diameter of a semicircle corresponds to the charge transfer resistance ( $R_{ct}$  in the equivalent circuit) at the interface between electrodes and electrolytes during the electrochemical reaction.<sup>[101]</sup> The rGO alone exhibits a semicircle with an electrical resistance of  $\sim 191 \Omega$ , whereas both rGO films decorated with arrayed Au NPs do not show semicircles as the GCE itself, implying very low resistances. Similar results when ITO electrodes were employed instead of a GCE (Figure 3.9b). The charge transfer resistance calculated from an equivalent circuit was  $1106 \Omega$ ,  $575 \Omega$ , and  $573 \Omega$  for the ITO electrode with rGO, Au(109-27), and Au(51-18), respectively. Because rGO films consist of flakes, there could be a discontinuity in the films due to defects of oxygen-containing functional groups such as hydroxyls and epoxides even after the reduction process of GO.<sup>[103]</sup> Such discontinuity could cause a high resistance to charge transfer.

However, the decoration of Au NPs on rGO films effectively revealed the decreased resistance, presumably by providing electrical connectivity between rGO flakes. The low resistances of rGO with Au NPs are advantageous for electrocatalytic applications.

Both rGO films decorated with arrayed Au NPs exhibited higher peak currents and smaller peak potential differences than rGO itself, as shown by the CV data of the redox reaction of  $\text{Fe}(\text{CN})_6^{3-/4-}$  (Figure 3.10), implying the enhancement of the electrocatalytic activities of rGO films by Au NPs.<sup>[104]</sup> The peak current was linearly proportional to the square root of the scan rate, indicating that the electrochemical reaction on the rGO film decorated with arrays of Au NPs is diffusion-controlled, *i.e.*, a kinetically fast process (see Appendix A.1 for detailed discussion on this topic).<sup>[105]</sup> Au(51-18) shows superior activity to Au(109-27), which can be attributed to the larger electrochemical surface of Au(51-18). Thus, it is expected that decorating rGO films with Au NPs will be beneficial for electrocatalytic applications, including the ORR.

The ORR performance of rGO films decorated with Au NPs was further characterized under basic conditions (an oxygen-saturated KOH solution), which is relevant to practical applications such as fuel cells.<sup>[106]</sup> Because the ORR is an irreversible reaction, a single peak current was detected at -0.34 V for rGO films with Au NPs, but not for rGO alone (Figure 3.11a). A high peak current implies that a large number of electrons can be effectively transferred to the oxygen molecules and more oxygen molecules are reduced in the time unit, with the same number of electrons per oxygen molecule. Thus, decorating rGO with Au NPs increased the ORR activity of rGO. Peaks were primarily associated with the ORR by observing that the magnitude of the peak current depended on the oxygen content in the

solution (Figure 3.12). In Figure 3.10, Au(51-18) shows a higher peak current (265  $\mu\text{A}$ ) than Au(109-27) (194  $\mu\text{A}$ ), indicating that more oxygen molecules can interact with smaller and denser Au NPs available, and thus more get reduced. In addition, similar results were also observed under acidic conditions (an oxygen-saturated  $\text{H}_2\text{SO}_4$  solution) (Figure 3.11b). A relatively broad current peak is observed at -0.42 V for rGO films with Au NPs, but not for rGO alone. This observation implies that decorating rGO with Au NPs also increased the ORR activity of rGO under acidic conditions.

Electrochemical analysis based on an RDE was also carried out to study the difference in ORR activities between two different Au NP cases, *i.e.*, Au(109-27) and Au(51-18). In this system, arrayed Au NPs, which were uniformly distributed on a single graphene sheet, had pure Au surfaces without any extra layers and no additional material such as Nafion was required to stabilize them on the rapidly rotating electrode. Therefore, it can be assumed that all Au NPs were equally exposed to reactants, *e.g.*, oxygen in this case. Furthermore, the unusual transferability of this system to the RDE allows to conduct a rigorous electrochemical evaluation of arrayed Au NPs on rGO films. The rGO with Au NPs transferred onto the RDE was confirmed to be very stable, and no decrease of the electrochemical activity after several repeats of the measurement was observed.

In most cases, ORR electrocatalysts are evaluated on an RDE after being mixed with commercialized carbon and Nafion as a stabilizer. This methodology can deteriorate the electrocatalysts and deter the mass transfer by the aggregation and/or agglomeration of carbon and NPs. Furthermore, Nafion is temperature dependent, which is a critical problem in the development of practical fuel cell systems. In this sense, the proposed system possesses a nearly ideal structure of the triple-phase

boundary for electrocatalysis since all of NPs on rGO films were exposed to the solution without any stabilizer. Calcination by heat treatment, as shown in Figure 3.4c, and the absence of stabilizer ensured that all Au NPs on the rGO were clean enough to maximize their electrocatalytic activity.

In the linear-sweep voltammetry (LSV) curves of Figure 3.13, the currents for both Au NPs increased with an increase in the rotating rate because more reactants can reach the electrode at faster rotations. From the LSV data from -0.4 V to -0.5 V Koutecky-Levich plots, *i.e.*, (current density)<sup>-1</sup> versus (rotating rate)<sup>-1</sup>, was obtained (Figure 3.13c and Appendix A.2 for detailed discussion on Koutecky-Levich plots). For clarity, only the plots at -0.45 V and -0.5 V are displayed. The number of electrons involved in the ORR was extracted from the slope of each plot. In the case of Au(109-27), the slopes were in the range of 1.7 – 2.3, indicating a dominant 2-electron process, *i.e.*, serial reduction of O<sub>2</sub> to H<sub>2</sub>O<sub>2</sub>.<sup>[107]</sup> In contrast, slopes of 3.7 – 4.0 was obtained for Au(51-18), which implies a 4-electron process, *i.e.*, direct reduction of O<sub>2</sub> to H<sub>2</sub>O, which is desirable for practical applications.<sup>[107]</sup> According to previous studies on the ORR with Au NPs, the occurrence of a 2- or 4-electron process is primarily dependent on the size of the Au NPs.<sup>[108]</sup> And the effect of NP density on the change from a macroscopic 2- to a 4-electron reduction can be explained by desorption, re-adsorption, and reduction scheme for the formed H<sub>2</sub>O<sub>2</sub> during ORR, so that the denser NPs have the higher probability to reduce the desorbed H<sub>2</sub>O<sub>2</sub> to H<sub>2</sub>O.<sup>[109,110]</sup> Consequently, Au NPs with a diameter smaller than 10 nm undergo a 4-electron process, which explains our observations: a 4-electron process for Au(51-18), having an average diameter of 8.6 nm and high density of Au NPs, and a 2-electron process for Au(109-27), with an average diameter of 11 nm and low density of Au NPs.<sup>[110]</sup> Note that 2- and 4-electron reactions could not

occur completely independently because of the size distribution of the Au NPs, as shown in Figures 3.3d and 3.5d. It is also confirmed that there were no noticeable changes in the current of the ORR with Au NPs at a constant potential of -0.6 V after 2 h (Figure 3.14), manifesting the electrochemical stability of the Au NPs. Thus, the controllability of the size of Au NPs with copolymer micelles and the transferability of NPs with rGO films enabled the fabrication of rGO films decorated with arrayed Au NPs, which are suitable for practical ORR applications and exhibited a 4-electron reduction process.

## Summary

The approach with PS-P4VP copolymer micelles allowed the decoration of non-overlapping arrays of Au NPs on rGO films with controllable diameter and number density. These factors were effectively controlled by the molecular weights of the PS-P4VP copolymer. The Au NPs have a pure Au surface without extra layers. These rGO films with Au NPs were transferred onto a glassy carbon electrode without deterioration of the array of Au NPs. They showed high electrocatalytic activities in the redox reaction of  $\text{Fe}(\text{CN})_6^{3-/4-}$  and the ORR. Furthermore, we were able to differentiate the ORR mechanisms of Au(109-27) and Au(51-18) by RDE analysis. Au(51-18) has a smaller diameter and mainly exhibited a 4-electron direct reduction pathway of  $\text{O}_2$  to  $\text{H}_2\text{O}$ . Thus, the controllability of the size of the Au NPs with copolymer micelles and their transferability made the proposed system suitable for ORR applications. The electrocatalytic activities were enhanced by the clean surfaces of the Au NPs on the rGO, which were prepared by calcination and stabilizer-free processes. It is possible to obtain arrays of various metal or metal oxide NPs on graphene with tunable number density and size simply by changing

the precursors and molecular weights of the diblock copolymer micelles. In addition, the facile, large-area synthesis of rGO films decorated with NPs would be an interesting target. The methodology of combining copolymer micelles and rGO films can be extended to prepare various NPs on graphene in a controlled way, which has potential in numerous applications, including biosensors, supercapacitors, and electro- and photo-catalysts.

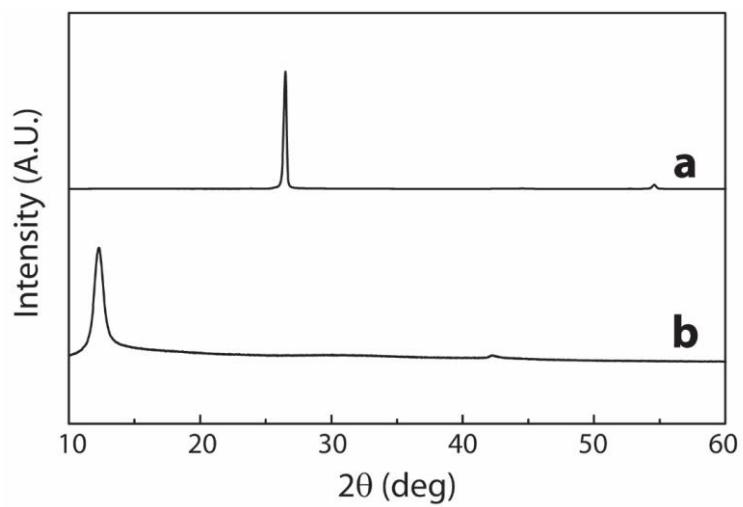


**Figure 3.1.** XRD patterns of (a) graphite powder and (b) GO powder.

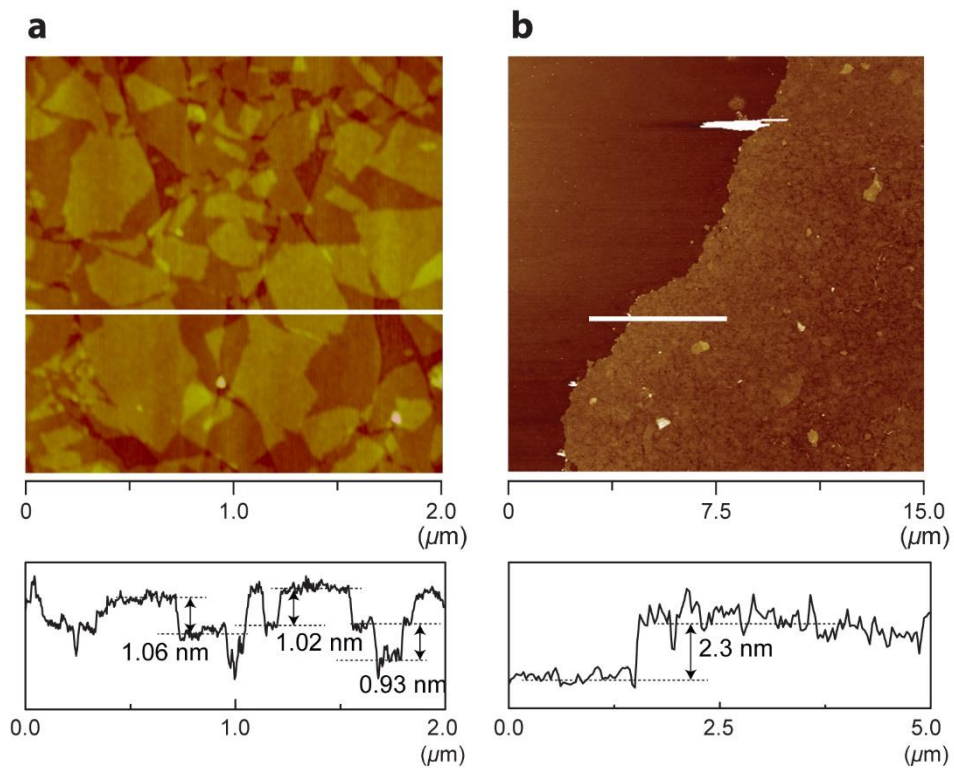


**Figure 3.2.** AFM images of (a) GO flakes spin-coated onto a SiO<sub>2</sub>/Si substrate and (b) rGO film fabricated by spin-coating of GO 5 times followed by hydrazine reduction. A height profile along the solid line in each image is also displayed below the corresponding AFM image.

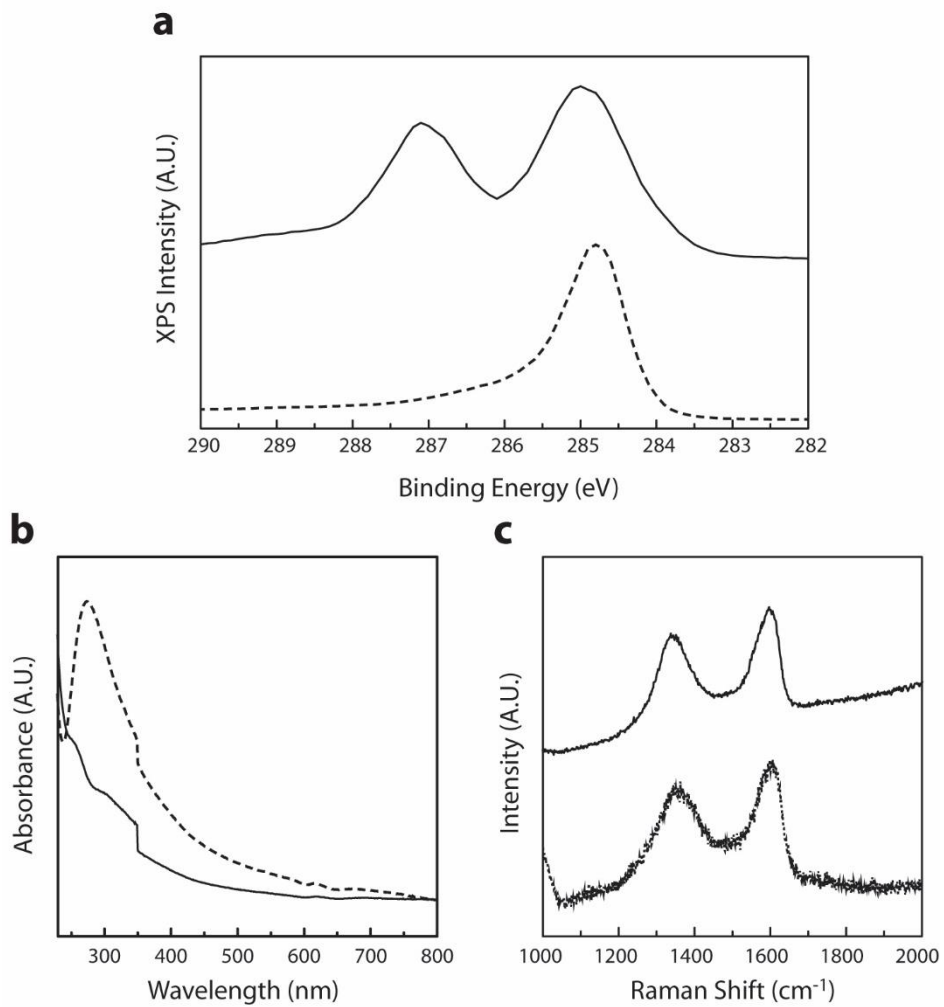


**Figure 3.3.** Characterization of GO (solid) and rGO (dashed) film after hydrazine reduction. (a) XPS; (b) UV-vis absorption spectra; (c) Raman spectra.

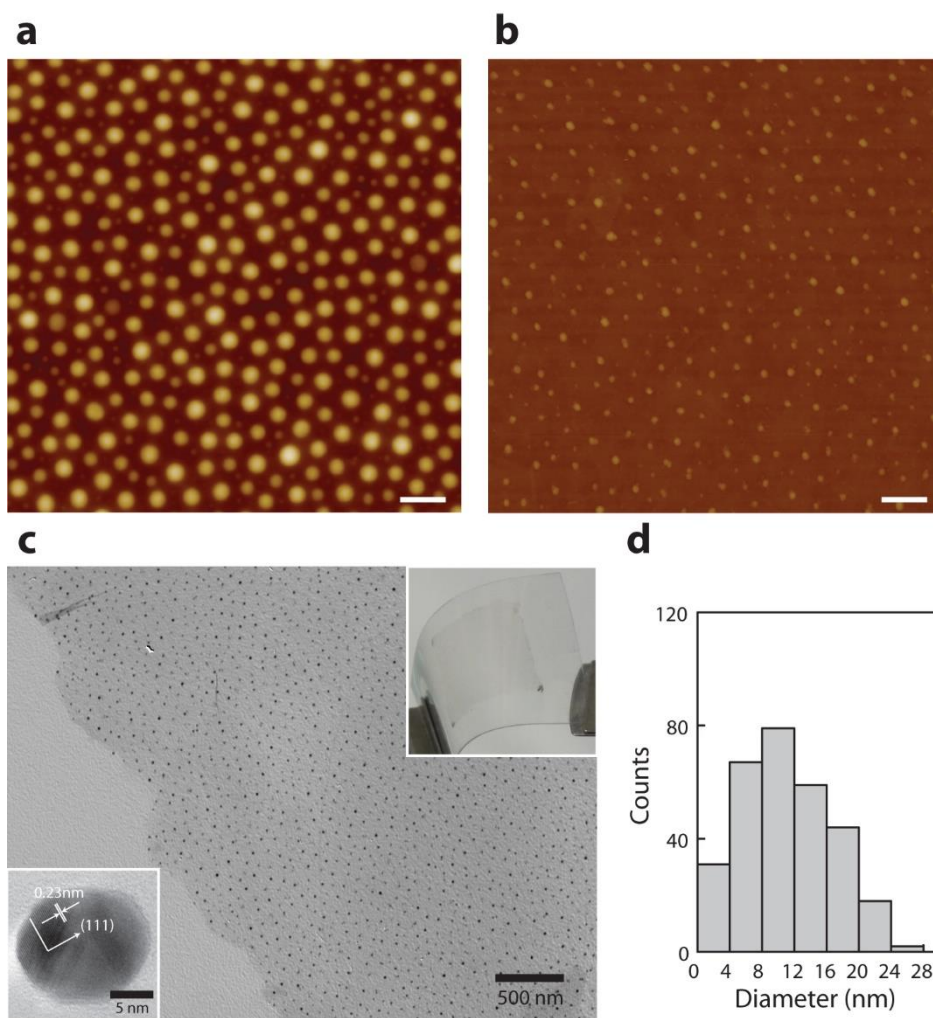


**Figure 3.4.** Characterization of rGO decorated with Au(109-27). (a) AFM image of PS(109)-P4VP(27) micelles on rGO; (b) AFM image of Au(109-27) from the micelles; (c) TEM image of Au NPs on rGO; (d) The diameter distribution of the Au NPs measured from the TEM image. The insets in (c) are the HR-TEM image of an individual Au NP and the photo of a transferred rGO film with Au NP (the gray square) on a flexible polymer film.

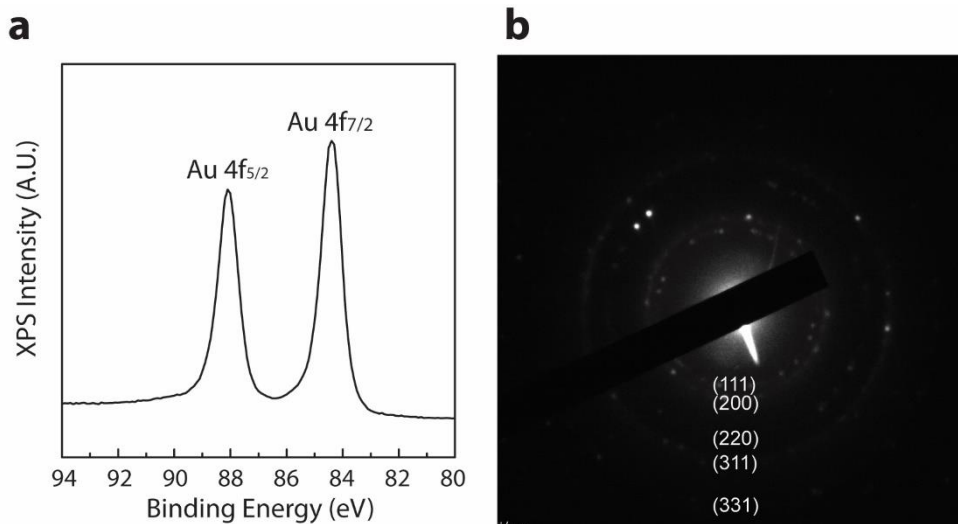


**Figure 3.5.** (a) XPS spectrum of Au(4f) of Au(109-27); (b) SAED pattern of Au NPs. Lattice planes are marked on (b).

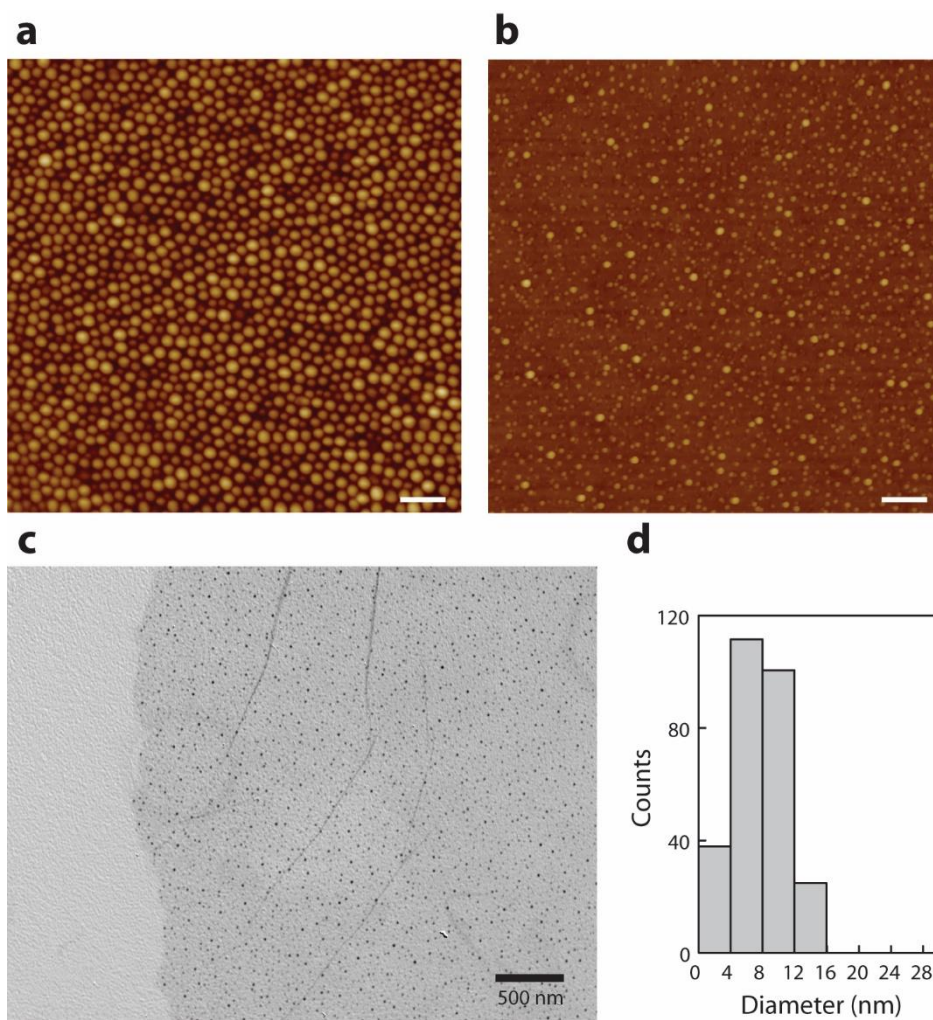


**Figure 3.6.** Characterization of rGO decorated with Au(51-18). (a) AFM image of PS(51)-P4VP (18) micelles on rGO; (b) AFM image of Au(51-18); (c) TEM image of the Au NPs on rGO; (d) The diameter distribution of the Au NPs measured from the TEM image.

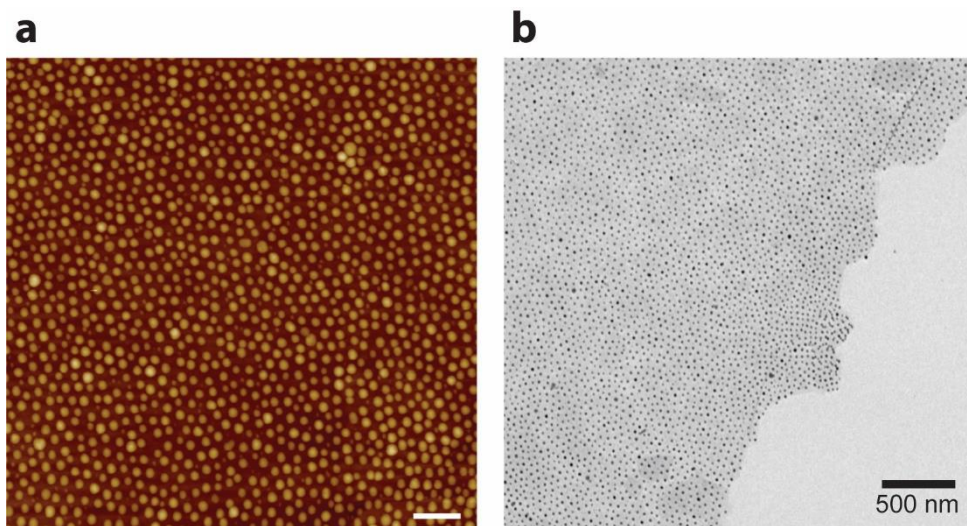


**Figure 3.7.** AFM and TEM images of rGO decorated with  $\text{Fe}_2\text{O}_3$ (51-18).

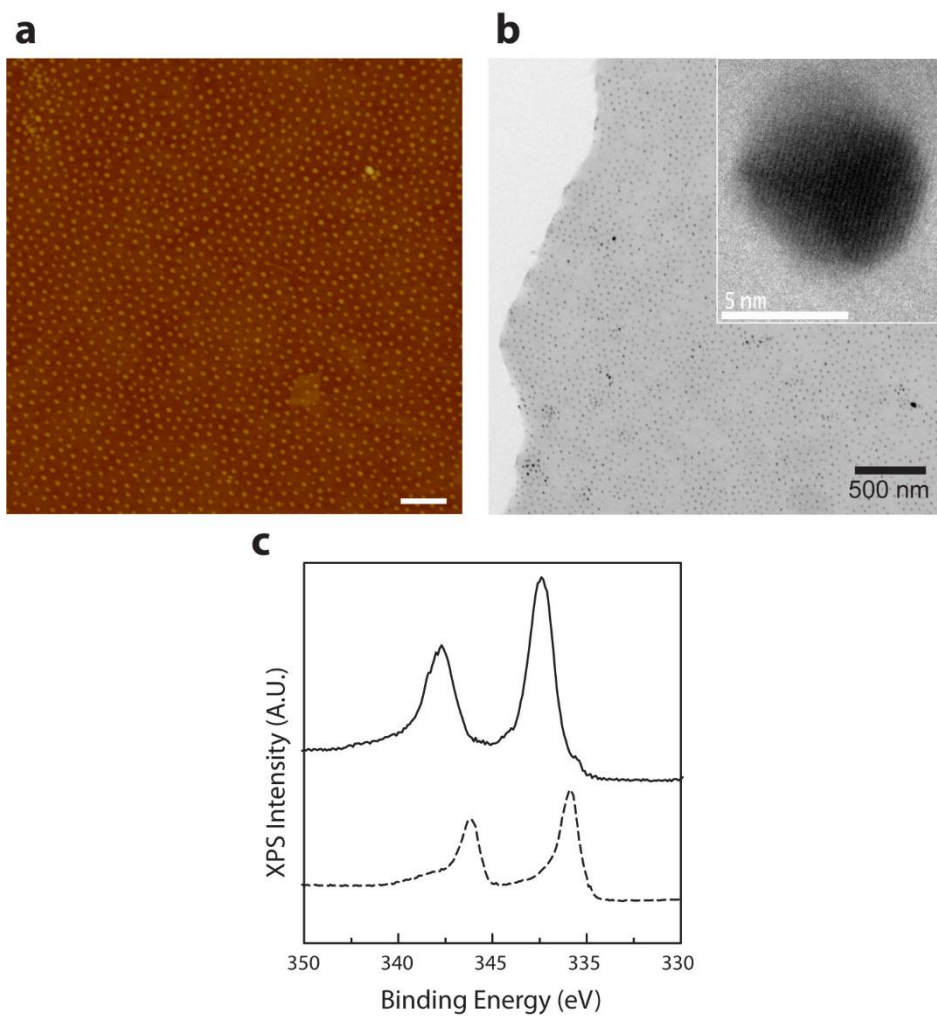


**Figure 3.8.** (a,b) AFM and TEM images of rGO decorated with PdO(51-18). (c) XPS spectra of Pd(3d) of rGO decorated with PdO(51-18) before (solid) and after (dashed) hydrazine reduction. The inset in (b) is the HR-TEM image of an individual PdO NP.

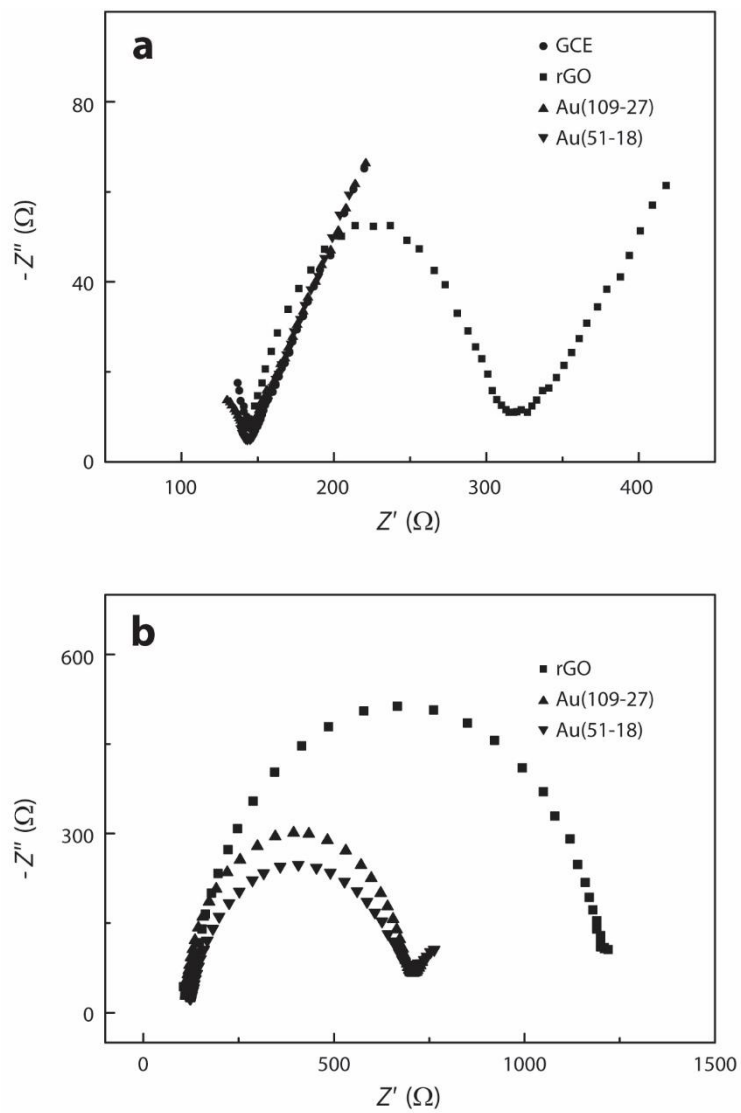


**Figure 3.9.** Nyquist plots of  $\text{Fe}(\text{CN})_6^{3-/4-}$  with (a) GCE and (b) ITO/glass electrodes. The scan rate was  $100 \text{ mV s}^{-1}$ .

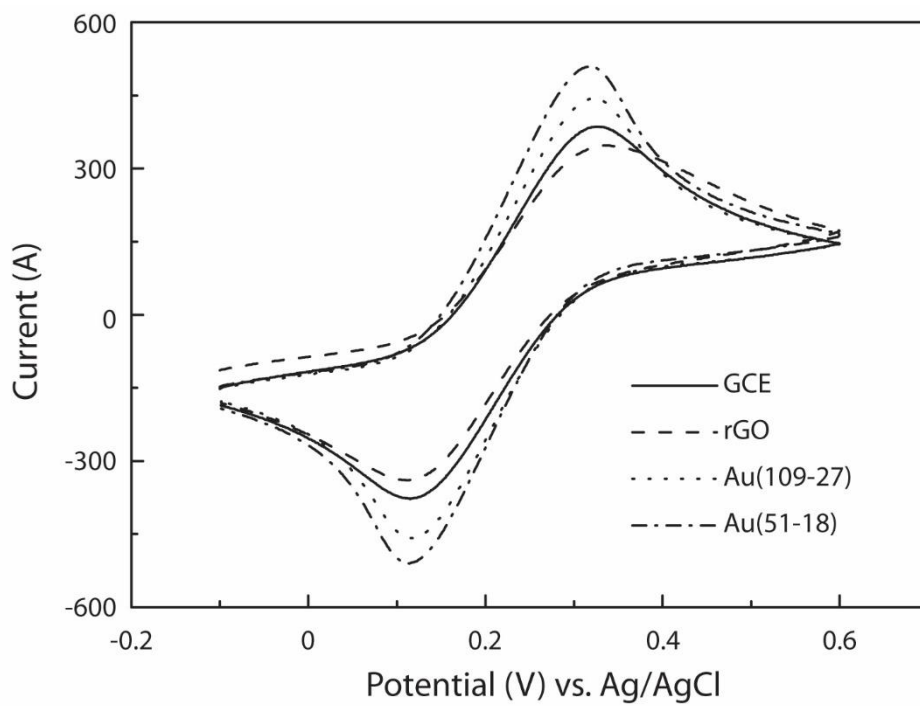


**Figure 3.10.** Cyclic voltammograms of  $\text{Fe}(\text{CN})_6^{3-/4-}$  with GCE.

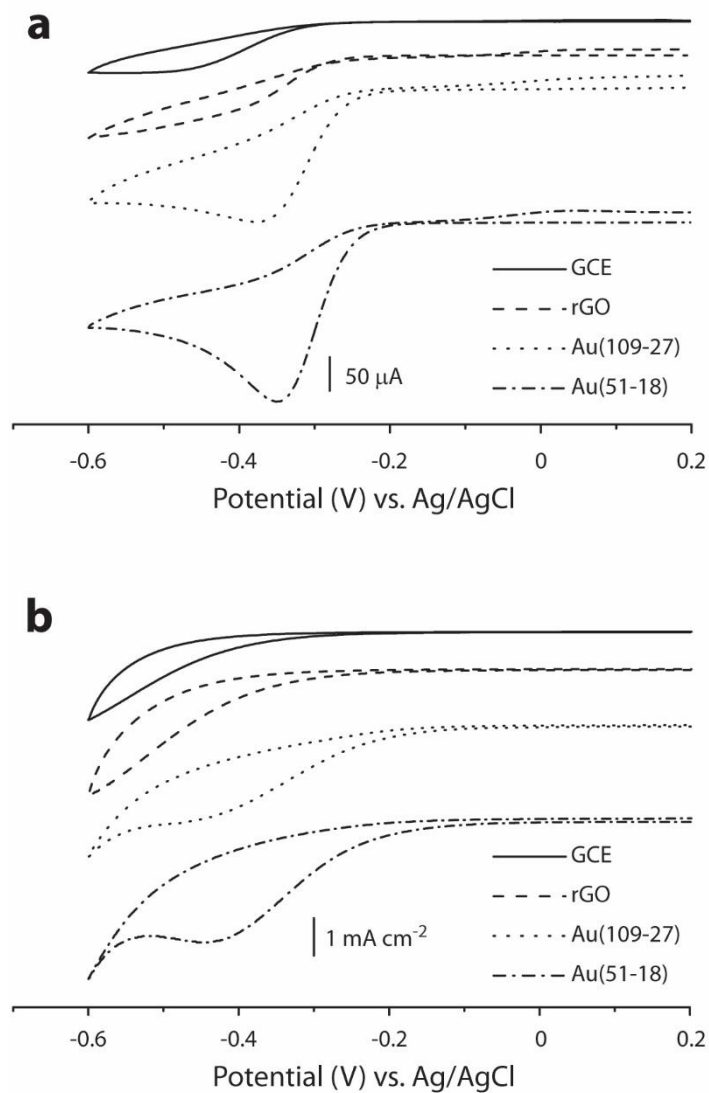


**Figure 3.11.** Cyclic voltammograms for ORR with rGO films decorated with Au NPs in oxygen-saturated (a) 0.1 M KOH solutions and (b) 0.1 M H<sub>2</sub>SO<sub>4</sub> solutions. The scan rate was 50 mV s<sup>-1</sup>.

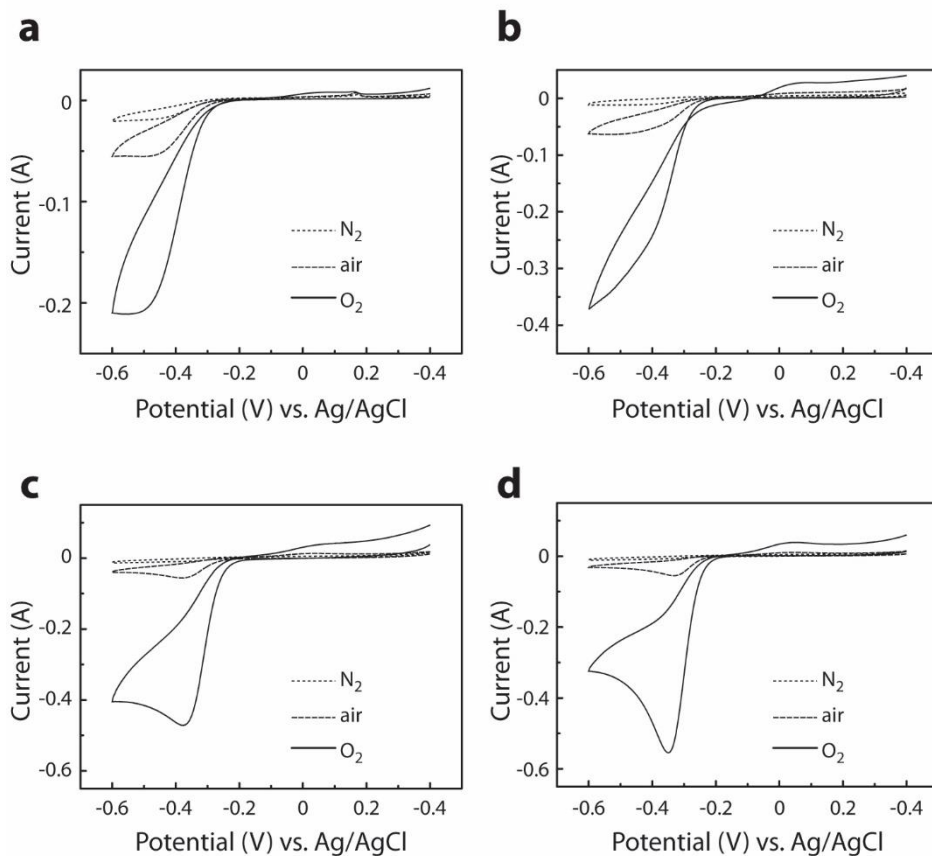


**Figure 3.12.** Cyclic voltammograms for ORR with rGO films decorated with Au NPs in  $N_2$ - and  $O_2$ -saturated 0.1 M KOH solutions: (a) GCE; (b) rGO; (c) Au(109-27); (d) Au(51-18). Electrochemical measurements were carried out after purging with  $N_2$  or  $O_2$  for 20 min. For comparison, the CV without purging (marked as air) is also displayed. The scan rate was  $50 \text{ mV s}^{-1}$ .

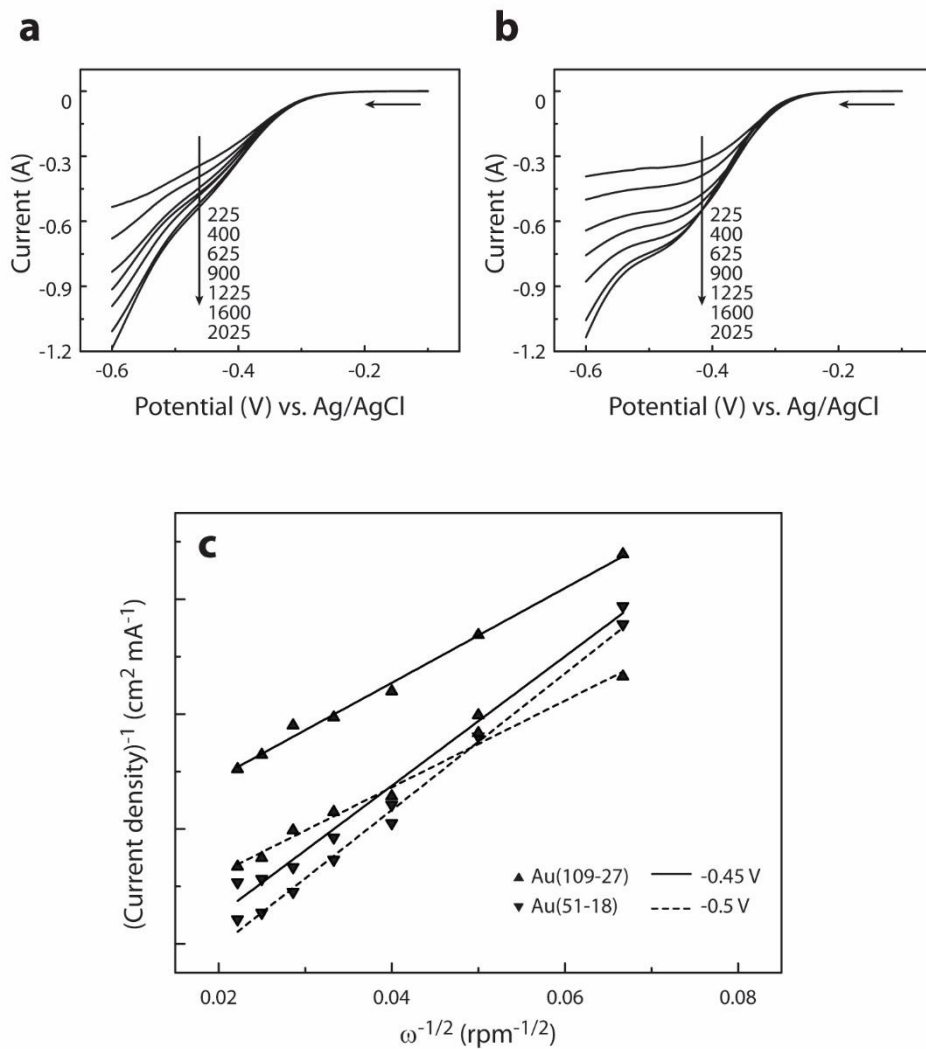


**Figure 3.13.** Linear sweep voltammograms for the ORR with rGO films decorated with (a) Au(109-27) and (b) Au(51-18) in oxygen-saturated 0.1 M KOH solutions. (c) Koutecky-Levich plots. The scan rate was  $5 \text{ mV s}^{-1}$ . The numbers shown in the voltammograms are the rotating rates in rpm. The arrows indicate the scan direction. The background current in an oxygen-free solution was subtracted.

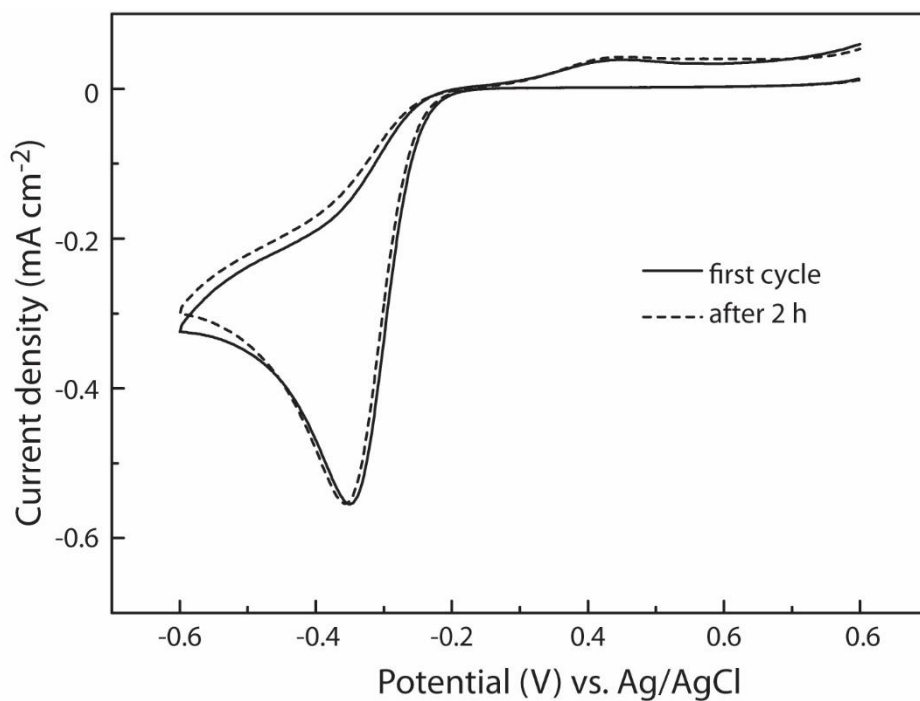


**Figure 3.14.** Cyclic voltammograms for the ORR with Au(51-18) after 2 h of constant potential at -0.6 V in an oxygen-saturated 0.1 M KOH solution. The scan rate was 50 mV s<sup>-1</sup>.

## 2. Graphene nanodot arrays

Recently, a number of attempts to fabricate nanodevices by combining nanopatterned graphenes and state-of-the-art lithographic techniques were made. Although EBL has been widely implemented to fabricate a considerable number of graphene-based devices, the nature of the serial process in EBL has severe limitations with regard to the mass production of nanopatterned materials over a large area. Moreover, it is a sophisticated and costly processes with low productivity. In contrast, bottom-up approaches which use molecular self-assemblies have garnered strong attractions among researchers because they effectively enable the fabrication of nanostructured materials or devices over a large area. These approaches were also recently utilized for nanostructured graphenes. Among the various techniques currently available, the diblock copolymer approach can be applied for the effective creation of nanostructured graphenes. Because the nanostructures formed by diblock copolymers rely on the molecular weight of the copolymers, nanostructured thin films of diblock copolymers show great promise for the controlled nanopatterning of diverse materials over a large area.

The previous section demonstrated the utilization of diblock copolymer micelles as templates to produce NPs on rGO. Copolymers on rGO films were heated in air to be removed by degradation at a ehigh temperature. Although an oxygen plasma treatment can be used to synthesize NPs with the removal of copolymers, the graphene underneath, consisting of  $sp^2$ -bonded carbon atoms, can then also be subjected to etching by highly reactive oxygen species, leading to a loss of structural integrity in graphene films. However, this alludes to the applicability of copolymer thin films as an etching mask for graphene nanopatterning. In practice, arrayed NPs synthesized by diblock copolymer micelles have been used as an

etching mask to transfer its hexagonal pattern to a substrate for the generation of nanodots or vertically oriented nanorods.<sup>[37]</sup>

In this section, we demonstrate the fabrication of arrays of graphene nanodots with tunable sizes and spacings over a large area by the diblock copolymer micellar approach. A plasma treatment of hexagonally ordered micelles containing Au precursors coated onto graphene enabled the synthesis of Au NPs in the micellar cores and the removal of all graphenes and copolymers apart from the graphene under synthesized Au NPs, resulting in an array of graphene nanodots. The size and inter-distance of the graphene nanodots were effectively controlled by adjusting the molecular weight of the copolymers. In addition, fabricated arrays of graphene nanodots were utilized as a seed layer of the ZnO nanorod arrays grown subsequently.

## **Experimental Section**

*Materials:* Diblock copolymers of PS-P4VP, PS(51)-P4VP(18), PS(75)-P4VP(25), and PS(109)-P4VP(27) were purchased from Polymer Source, Inc. The number in the parenthesis is the average molecular weight ( $M_n$ ) in kg/mol. The polydispersity index (PDI) is 1.15, 1.09, and 1.15, respectively. Tetrachloroauric(III) acid ( $\text{HAuCl}_4$ ) as precursors of Au NPs were obtained from Sigma-Aldrich and used as received. Graphite powders (synthetic conducting grade, ~235 mesh, 99.9995 %) were purchased from Alfa Aesar.

*Preparation of graphene:*  $\text{SiO}_2/\text{Si}$  substrate was cleaned by the ultrasonication in acetone, followed by rinsing with acetone. Graphene was transferred onto the cleaned substrate from graphite powders by the mechanical exfoliation.

*Diblock copolymer micelles with Au precursors:* The PS-P4VP diblock copolymers

were dissolved in toluene, a strongly selective solvent for the PS block, with a concentration of 0.5 wt%. The solution was stirred for 24 h at a room temperature and for 3 h at 85 °C, and then cooled down to a room temperature. H<sub>Au</sub>Cl<sub>4</sub>, the precursor of the Au NPs, was added to the micellar solution. The molar ratio of H<sub>Au</sub>Cl<sub>4</sub> to the pyridine unit in the P4VP block was fixed at 0.5. The solution was stirred at least for 7 days at room temperature.

*Fabrication of arrayed graphene nanodots:* Single layer of the PS-P4VP micelles with H<sub>Au</sub>Cl<sub>4</sub> was spin-coated (typically at 2000 rpm, 60 s) on the substrate covered with graphene. The copolymer micellar array was treated with an oxygen plasma (100 W, 38 mTorr) for 15 s. The synthesized Au NPs were removed by dipping into aqua regia (a concentrated mixture of HCl and HNO<sub>3</sub>) for 15 min.

*Characterization:* The PS-P4VP micelles, Au NPs, graphene, and graphene nanodots were analyzed using an AFM with Nanoscope IIIa (Digital Instruments) in tapping mode with Al-coated Si cantilevers. XPS was performed using Sigma Probe (ThermoVG) with monochromatic Al-K<sub>α</sub> X-ray source operating at 100 W. Raman spectra were obtained using a Renishaw 2000 with a 514.5 nm line from an Ar ion laser as an excitation source.

## **Results and Discussion**

Graphene on SiO<sub>2</sub>/Si substrates was prepared from graphite powders by mechanical exfoliation, which was identified by optical microscopy (OM) (Figure 3.15a). Generally graphene in single layer on SiO<sub>2</sub>/Si substrates appears pale purple due to the light, whereas few layers of graphene look bluish purple.<sup>[111,112]</sup> Prepared graphene was further characterized by AFM. Graphene is on the left part of the white dotted line in Figure 3.16a. The height profile along the white solid line in

the image shows that the graphene is 4.5 nm thick, indicating approximately 12 graphene layers.<sup>[113]</sup> In this experiment, a few layers of graphene like this graphene was chiefly observed because of its clear visualisation by OM and AFM. We also used single layer of graphene for the Raman analysis of graphene nanodots (Figure 3.20) to confirm that our approach works fine with single layer of graphene.

A monolayer of PS-P4VP micelles containing H<sub>2</sub>AuCl<sub>4</sub>, a precursor of Au nanoparticles, in the P4VP cores was fabricated on a mechanically exfoliated graphene by spin-coating. This micellar film has periodic variation of the thickness because of the spherical form of micelles, which can be directly applied to an etching mask.<sup>[114]</sup> However, this pristine micellar film would not be an effective etching mask to pattern carbon-based graphene because of no appreciable difference in etching rates between PS coronas and P4VP cores as well as the small thickness variation in the micellar film. Since we selectively loaded H<sub>2</sub>AuCl<sub>4</sub> into the P4VP cores, the etching contrast was dramatically enhanced because Au nanoparticles were synthesised in the core area during the oxygen plasma treatment. When Au NPs were synthesised, all other materials including copolymers and graphene were etched out except graphenes under Au NPs which are graphene nanodots.

A monolayer of PS(51)-P4VP(18) containing H<sub>2</sub>AuCl<sub>4</sub> in the P4VP cores was coated on the entire substrate including the part covered with mechanically exfoliated graphene (Figure 3.17). The plasma treatment on the micellar monolayer resulted in the formation of an array of Au NPs on the entire substrate with the preservation of the micellar order as shown in Figure 3.16b. Finally, to obtain a pure array of graphene nanodots, Au NPs were selectively removed by aqua regia. The complete removal of Au NPs by aqua regia was confirmed by disappearance

of the Au(4f) peaks in XPS spectrum (Figure 3.18). Note that a weak peak around 90 eV in Figure 3.19a is associated with gold oxides formed on the surface of Au NPs by oxygen plasma, which are thermodynamically unstable at room temperature so that they turn to gold after several days.<sup>[115]</sup>

After the removal of Au NPs, the area covered with graphene nanodots no longer shows bluish purple in the OM image (Figure 3.15b). The disappearance of the light interference implies that this region cannot be a continuous two-dimensional graphene anymore. Figure 3.16c shows an AFM image of graphene nanodots which are only observed in the left part of the white dotted line where graphene was initially located. In contrast, the bare substrate is observed in the right part because Au NPs synthesised directly on the substrate (Figure 3.16b) were completely removed by aqua regia. The height of graphene nanodots is about 4.5 nm, identical to the thickness of the original graphene, implying the successful fabrication of arrayed graphene nanodots in the entire area of mechanically exfoliated graphene.

The radius and inter-distance of fabricated graphene nanodots have close relationship with those of PS(51)-P4VP(18) micelles and Au NPs. They are 12 nm ( $\pm 3.0$  nm) (core only) and  $\sim 47$  nm for the micelles, 11 nm ( $\pm 3.4$  nm) and  $\sim 47$  nm for the Au NPs, and 11 nm ( $\pm 4.3$  nm) and  $\sim 44$  nm for the graphene nanodots, respectively (Figure 3.19). Thus, it is confirmed that the size and order of the micelles were successfully transferred into those of graphene nanodots.

Next single-layered graphene nanodots from PS(51)-P4VP(18) micelles were analyzed by Raman spectroscopy. In the Raman spectrum of the graphene employed in this case (Figure 3.20a), G band ( $1584\text{ cm}^{-1}$ ) and 2D band ( $2681\text{ cm}^{-1}$ ) are observed. Their intensity ratio ( $I_{2D}/I_G$ ) is 0.32. In addition, the 2D band consists of one symmetric sharp peak. These observations are directly related to the

characteristics of single-layered graphene.<sup>[116,117]</sup>

Same single-layered graphene was used to fabricate arrayed graphene nanodots. Figure 3.20b shows the Raman spectrum of graphene dots whose AFM image is also included together. The intensity of the G band decreased significantly and the 2D band nearly disappeared, implying the decrease of the number of sp<sup>2</sup>-bonded carbons in graphene nanodots compared to pristine continuous graphene. In contrast, a disorder-activated D band (1350 cm<sup>-1</sup>) was discovered, indicating the generation of abundant edge states in graphene nanodots.<sup>[117,118]</sup> Thus, the micellar approach can be applied to fabricate graphene nanodots of single layer as well as a few layers.

Since the size and order of PS-P4VP micelles can be transferred into those of graphene nanodots, the size and spacing of graphene nanodots were controlled by varying the molecular weight of PS-P4VP copolymers. Figure 3.21a is a magnified AFM image of Figure 3.16c for graphene nanodots from PS(51)-P4VP(18) micelles with the radius distribution of about 800 nanodots. The average radius is 11 nm ( $\pm 4.3$  nm). By the FFT result of the image (inset in Figure 3.21a), the spacing of graphene nanodots is  $\sim 44$  nm. When the larger molecular weights for both core and corona blocks, *i.e.*, PS(75)-P4VP(25), were used, the size and inter-distance of nanodots were increased to 14 nm ( $\pm 4.1$  nm) and  $\sim 50$  nm, respectively (Figure 3.21b). Furthermore, by employing PS(109)-P4VP (27) which has a similar size core block but a larger corona block compared to PS(75)-P4VP(25), the inter-distance ( $\sim 85$  nm) was only increased with keeping the radius (15 nm  $\pm$  4.9 nm) almost unchanged as shown in Figure 3.21c. Thus, the radius of graphene nanodots can be controlled by the size of the micellar core and their spacing by the size of the micellar corona.

Same procedure was applied to rGO films as well as graphene obtained by mechanical exfoliation. H<sub>2</sub>AuCl<sub>4</sub>-containing PS(109)-P4VP(27) micelles were spin-coated onto rGO films, followed by the oxygen plasma treatment. Figure 3.22a shows hexagonally ordered rGO nanodot arrays on SiO<sub>2</sub>/Si substrate, maintaining the hexagonal order of original copolymer micelles. Spacing (~95 nm) and diameter (~31 nm) of rGO nanodot were almost same as those of graphene nanodots fabricated from mechanically exfoliated graphene by same molecular weight copolymers as described above. All copolymers and rGO film were removed except the rGO under Au NPs synthesized from core regions of copolymer micelles. Hence, abundant wrinkles or boundaries in the rGO films were no longer observed.

The crystal nucleation and growth behavior of ZnO altered drastically when rGO nanodot arrays were used as seed layers. With no presence of rGO nanodots, ZnO nanorod arrays were grown uniformly and homogeneously over the entire surface of the substrates due to the formation of ZnO buffer layers on the substrates.<sup>[119]</sup> By contrast, as illustrated in Figure 3.22b, the FE-SEM image clearly displays that the vertically well-aligned ZnO nanorod arrays were selectively grown on the rGO nanodot arrays, but not on the SiO<sub>2</sub> surface. This observation strongly indicates that crystal nucleation and growth of ZnO on the rGO nanodot are much enhanced than that on the SiO<sub>2</sub> surface due to low energy barrier for ZnO nucleation on the rGO surface.<sup>[120]</sup> A flat top surface with a hexagon-shaped plane and well-faceted sidewalls of the ZnO are clearly observed, indicating that the single-crystalline nanorod grew on the rGO nanodots. Crystalline structures of ZnO nanorods were investigated by XRD (Figure 3.22c). Two dominant peaks ( $\theta = 34.5^\circ$  and  $72.6^\circ$ ) corresponds to Bragg reflections from (0002) and (0004) planes of ZnO, which indicates that ZnO nanorods on rGO nanodots have an out-of-plane

crystallographic orientation. Optical characteristics of grown ZnO nanorods on rGO nanodots are discussed in Appendix B.

## **Summary**

By utilizing a monolayer of PS-P4VP micelles, arrays of graphene nanodots with tunable size and inter-distance were successfully fabricated. Au NPs were synthesized in the P4VP cores effectively worked as shielding nanostructures during the etching process of graphene by oxygen plasma. Removing Au NPs resulted in the observation of arrayed graphene nanodots of which size and inter-distance have close relationship with those of the copolymer micelles employed. Thus, the size and inter-distance of graphene nanodots were effectively controlled by the molecular weight of PS-P4VP copolymers. Moreover, single-crystalline ZnO nanorod arrays were fabricated on arbitrary substrates using rGO nanodot arrays as seed layers. Electron microscopy and XRD revealed that the vertically well-aligned ZnO nanorod arrays were heteroepitaxially grown on the rGO nanodots with uniform distributions in their diameters and lengths. Since the diblock copolymer micellar approach demonstrated here to generate graphene nanodots can be applied to single layer as well as a few layers of graphene, this method can be utilized for an effective fabrication of a tunable, large-area array of graphene nanodots for various electronic, optical, and plasmonic applications.

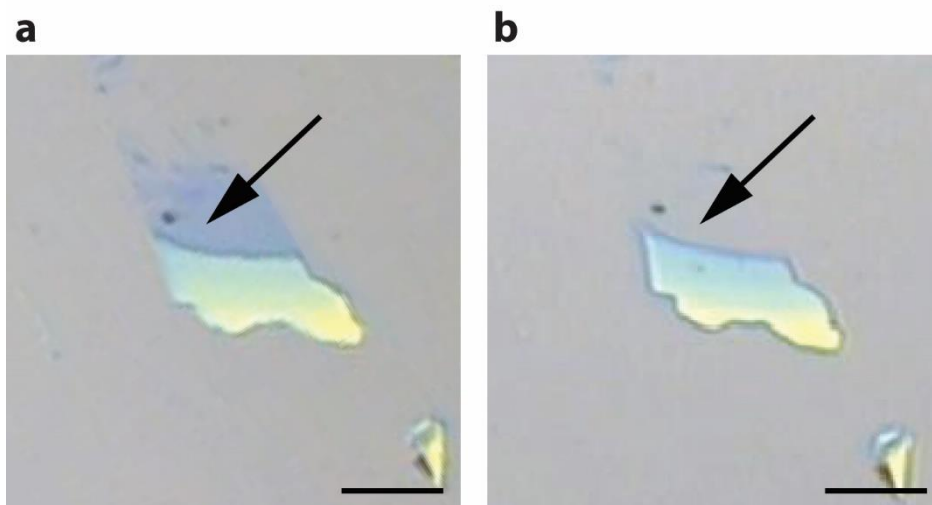


**Figure 3.15.** OM images of graphene on a SiO<sub>2</sub>/Si substrate (a) before and (b) after oxygen plasma treatment. The position of graphene is indicated by the arrow. The scale bars are 20  $\mu\text{m}$ .

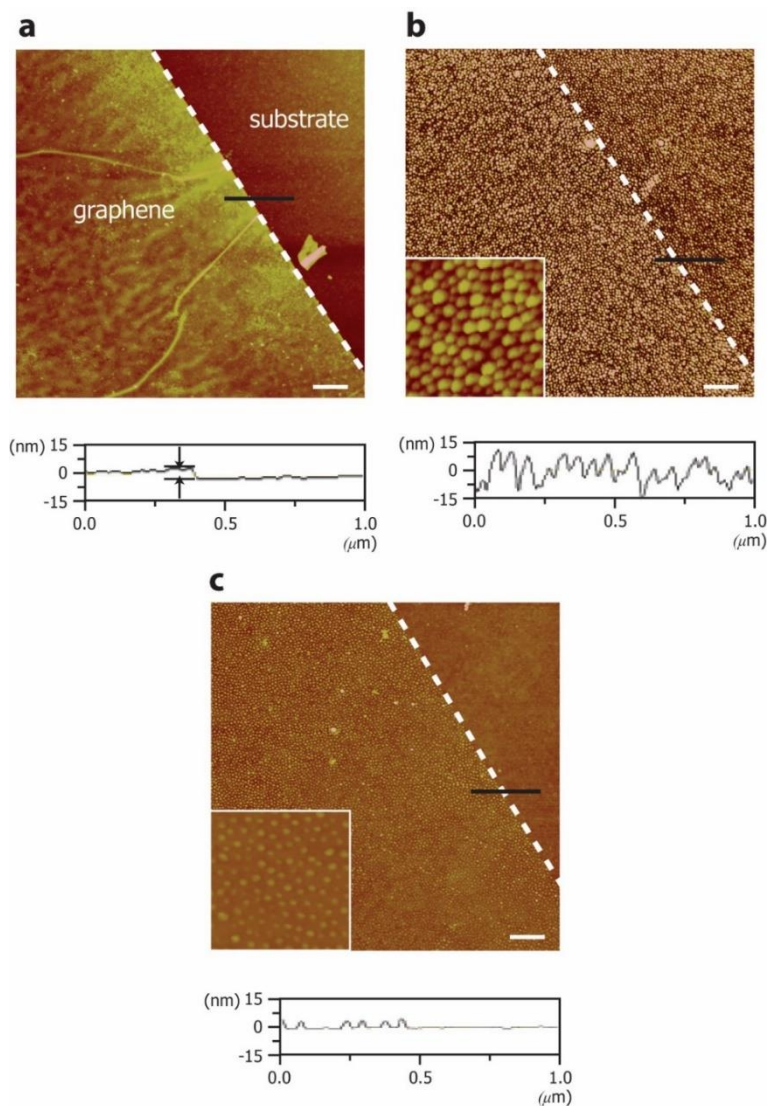


**Figure 3.16.** Fabrication of graphene nanodot arrays. (a) graphene on a  $\text{SiO}_2/\text{Si}$  substrate; (b) Au NPs after oxygen plasma treatment; (c) Arrayed graphene nanodots fabricated from PS(51)-P4VP(18) micelles after the removal of Au NPs. A height profile along the black solid line in each image is displayed below the corresponding AFM image. The insets in (b) and (c) are enlarged images of Au NPs and graphene nanodots, respectively. Scale bars are 500 nm.

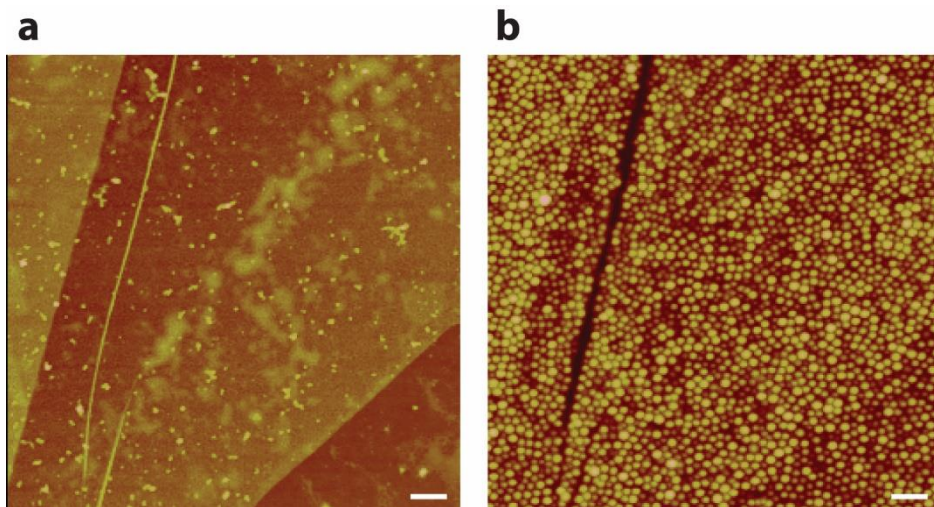


**Figure 3.17.** AFM images of (a) graphene on a SiO<sub>2</sub>/Si substrate and (b) a monolayer of PS(51)-P4VP(18) micelles on the same graphene. Scale bars are 200 nm.

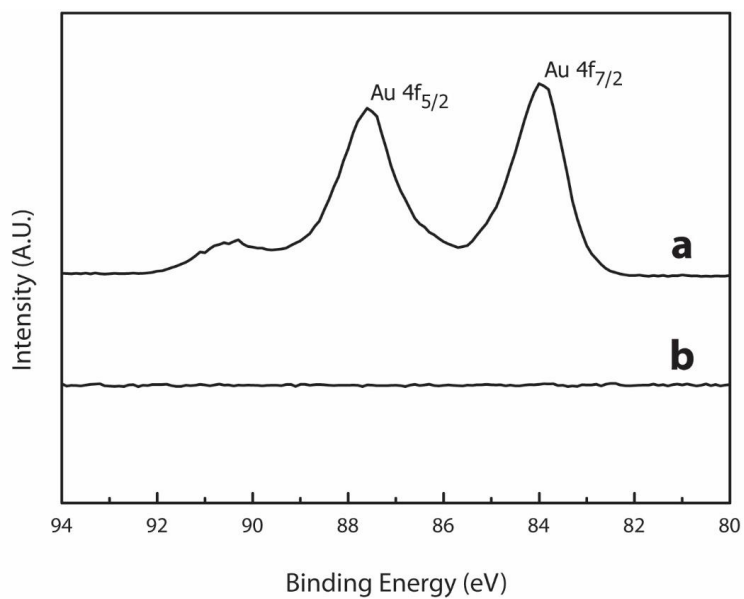


**Figure 3.18.** XPS spectra of Au(4f). (a) Au NPs; (b) after the removal of Au NPs.

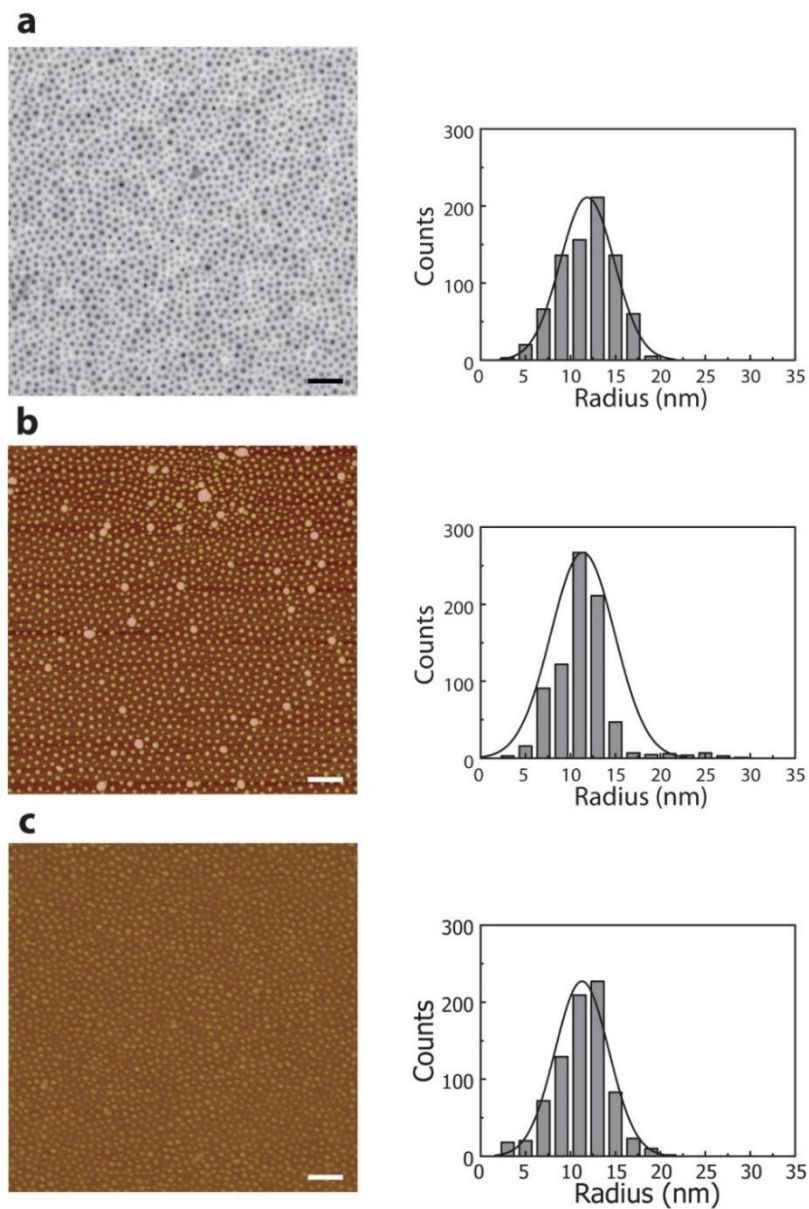


**Figure 3.19.** Characterization of micelles, Au NPs and graphene nanodots. (a) TEM image of a single layer of PS(51)-P4VP(18) micelles; (b) AFM image of Au(51-18); (c) AFM image of graphene nanodots after the removal of Au NPs. Scale bars are 200 nm.

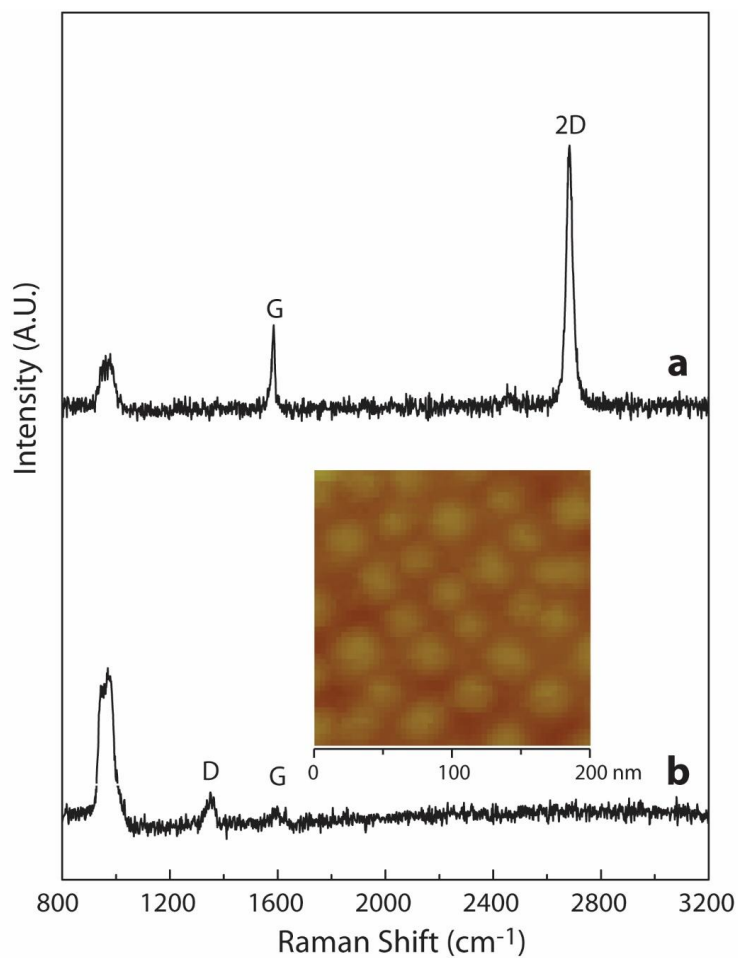


**Figure 3.20.** Raman spectra of (a) single layer graphene and (b) graphene nanodots fabricated from PS(51)-P4VP(18) micelles. The inset shows an AFM image of graphene nanodots corresponding to Raman spectrum of (b). The band at 960 cm<sup>-1</sup> is the characteristic of the SiO<sub>2</sub> layer of substrates.

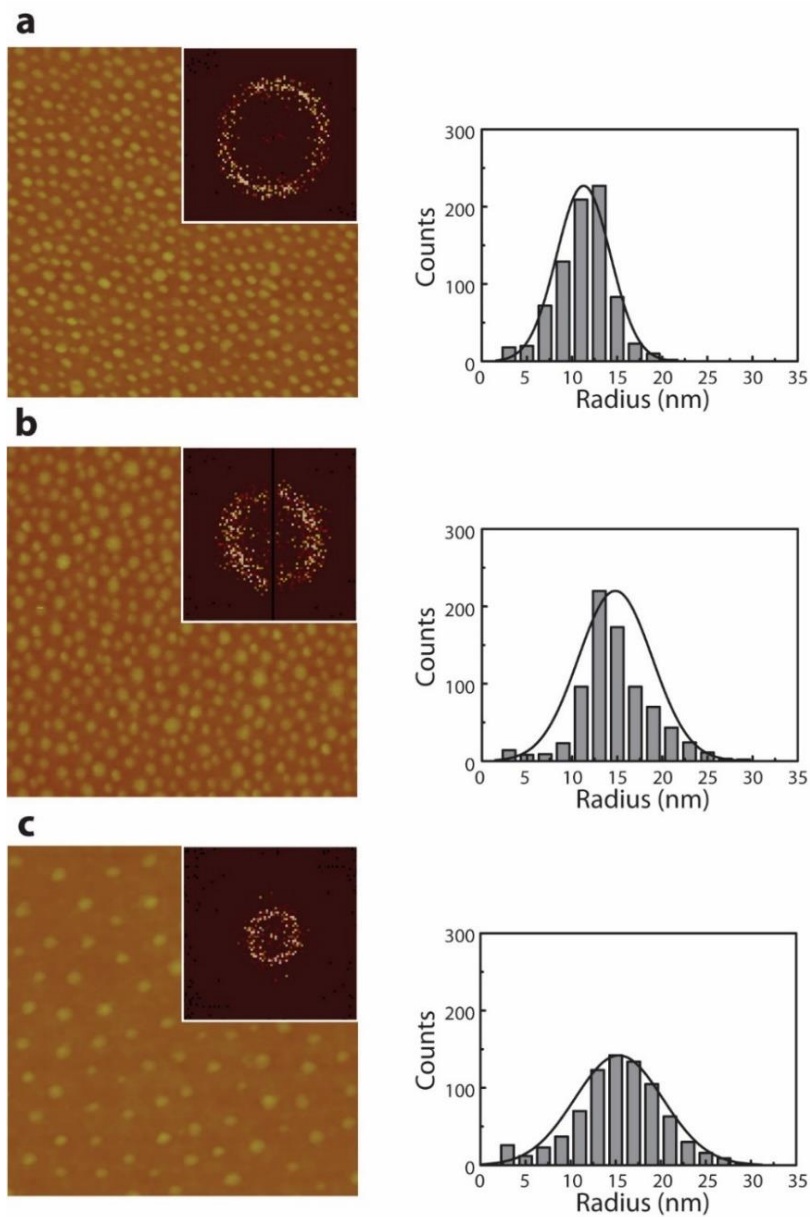


**Figure 3.21.** AFM images and size distributions of arrayed graphene nanodots fabricated from PS-P4VP micelles with various molecular weights: (a) PS(51)-P4VP(18); (b) PS(75)-P4VP(25); (c) PS(109)-P4VP(27). Size of AFM images are  $1\ \mu\text{m} \times 1\ \mu\text{m}$ . The inset in each image is a FFT pattern.

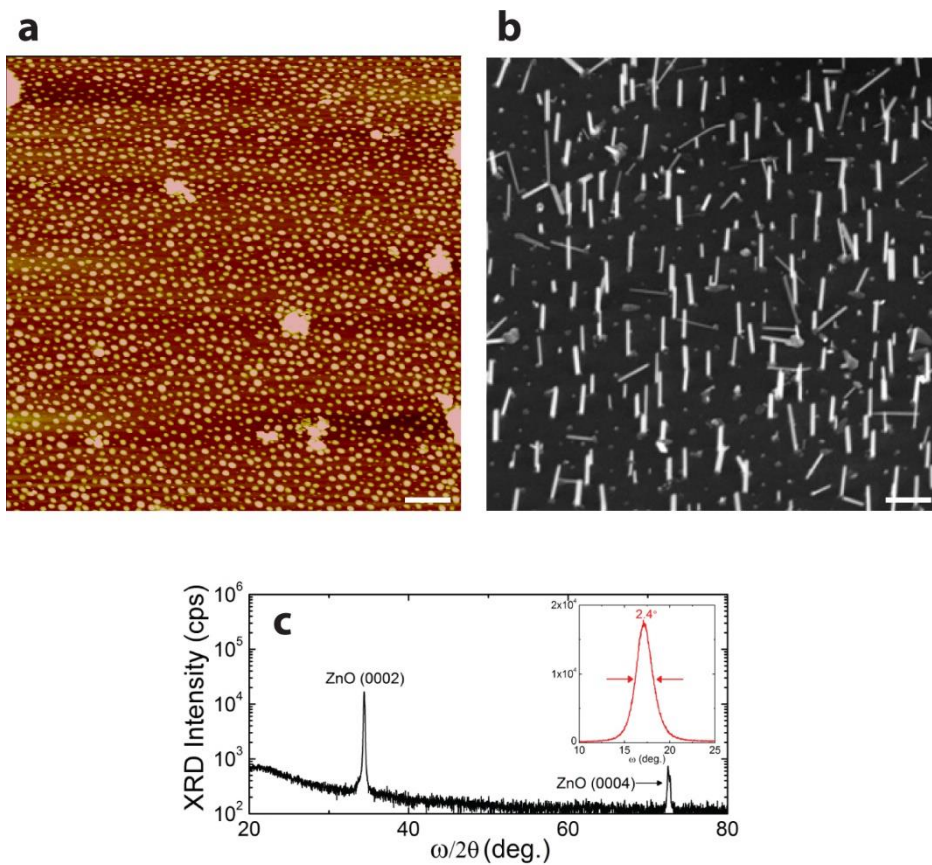


**Figure 3.22.** (a) AFM image of rGO nanodots fabricated from PS(109)-P4VP(27). (b) FE-SEM image of ZnO nanorods grown from rGO nanodots. (c) XRD pattern of ZnO nanorod arrays on the rGO nanodots. Scale bars for AFM and TEM images are 500 nm and 100nm, respectively.

### 3. Graphene tailored by Pt nanostructures

As shown in the previous section, owing to its high reactivity toward carbon atoms, oxygen plasma etching is a typical method which can be used to cleave carbon bonds in graphitic basal plane for graphene nanopatterning. With pre-designed etching masks fabricated by state-of-the-art top-down lithographic methods as well as bottom-up self-assembling materials, various arbitrary nanostructures can be transferred onto graphene. This lift-off method has been widely utilized in modern semiconductor industry such that most graphene patterning processes now include a single or serial process involving a treatment with oxygen or another type of plasma gas. However, graphene nanostructures shaped by oxygen plasma etching generally have rough edges, which may lead to anomalous behavior in the nanographene materials, of which the electronic and transport properties significantly depend on the edge chirality, *i.e.*, zigzag or armchair. In addition, oxygen plasma introduce oxygen-containing functional groups as well as dangling bonds at the edge structures.

NP-assisted lithography, taking advantage of the catalytic reactions induced by mobile NPs to degrade carbon atoms in graphene, can carve graphene with good crystallographic selectivity, leading to the creation of nanostructured graphene with well-defined edge states through the creation of trenches.<sup>[121]</sup> For example, Fe NPs cut graphene to form long and straight trenches at a high temperature in a hydrogen atmosphere,<sup>[31]</sup> of which the directions are commensurate with the honeycomb lattice of the graphene. Also in an oxygen atmosphere, Ag NPs can produce similar trenches in graphene.<sup>[32]</sup> These types of graphene etching techniques can be understood as the catalytic hydrogenation or oxidation of graphene by NPs, resulting in the removal of carbon atoms. Etching by NPs typically starts at a defect

site of a graphene edge, after which NPs migrate along the newly formed rim by etching to reduce the high surface energy of the rim.<sup>[32]</sup> Continuously repeated steps of the etching and migration of NPs generate a trench with a size proportional to the diameter of the NPs.<sup>[33]</sup> However, movement during the etching of the NPs cannot be accurately controlled, implying that the morphology of final nanographene cannot easily be designed. Moreover, as mobile NPs always cut trenches along specific crystallographic directions, tailored graphene only has long linear edges. Therefore, conventional NP-assisted lithography is not effective for fabricating nanostructured graphene with pre-designed arbitrary shapes.

However, if NPs are not allowed to migrate during the catalytic etching of graphene, holes instead of trenches can be induced in graphene, resulting in nanoporated graphene. This scheme can be extended to other static nanostructures capable of inducing catalytic reactions to tailor graphene. This approach will resolve the aforementioned problem which arises in conventional NP-assisted lithography and provide higher degree of freedom for graphene nanopatterning.

This section describes the nanoscale tailoring of graphene with arrayed Pt nanostructures at a relatively low temperature, at which the nanostructures become immobile and most characteristics of the graphene remain intact. Both rGO and graphene grown by CVD were tailored with arrayed Pt nanostructures which were synthesized using diblock copolymers and their micelles. Unlike rGO tailoring, CVD graphene requires an additional enhancement of the chemical reactivity of graphitic carbon atoms, which is attained by strain engineering. The size and spacing of the tailored graphene nanostructures can be effectively controlled by managing these parameters of Pt nanostructures through the tuning of the molecular

weights of the copolymers.

## **Experimental Section**

*Materials:* Diblock copolymers of PS-P4VP, PS(19)-P4VP(5), PS(25)-P4VP(7), PS(32)-P4VP(13), PS(51)-P4VP(18), and PS(109)-P4VP(27) were purchased from Polymer Source, Inc. The number in the parenthesis is the average molecular weight ( $M_n$ ) in kg/mol. The polydispersity index (PDI) is 1.10, 1.10, 1.08, 1.15, and 1.15, respectively. 1-Ethyl-3-methylimidazolium bis(trifluoromethylsulfonyl) imide ([EMIm][TFSI]) was purchased from Sigma-Aldrich. Chloroplatinic(IV) acid ( $H_2PtCl_6$ ) and sodium hexachloroplatinate(IV) hexahydrate ( $Na_2PtCl_6 \cdot 6H_2O$ ) as precursors of Pt nanostructures, and tetrachloroauric(III) acid ( $HAuCl_4$ ) and silicon tetrachloride ( $SiCl_4$ ) as precursors of Au and  $SiO_2$  NPs were obtained from Sigma-Aldrich and used as received. Graphite powders (synthetic conducting grade, ~235 mesh, 99.9995 %) were purchased from Alfa Aesar.

*Perforation of rGO films by arrayed Pt NPs:* The preparation of two-dimensionally continuous large-area rGO films and PS-P4VP micelles containing the precursors of the NPs were described in the previous sections. Onto an rGO film, the single layer of PS-P4VP micelles containing the precursors of the Pt NPs was spin-coated for 60 s at 4000 rpm for PS(32)-P4VP(13), and at 2000 rpm for PS(51)-P4VP(18) and PS(109)-P4VP(27). To perforate the rGO film by synthesizing the Pt NPs with the removal of the copolymers, the micellar film on the rGO film was heated at 400 °C for 30 min in air. For the transfer of the rGO film perforated by the Pt NPs, the rGO film coated with a PMMA supporting layer was delaminated from the  $SiO_2/Si$  substrate by exposing it to an aqueous NaOH solution (1.0M). After transferring to another  $SiO_2/Si$  substrate, the supporting layer was removed by the ultrasonication

in acetone.

*Perforation of CVD graphene by arrayed Pt NPs:* To perforate graphene grown by the CVD, the Pt NPs were first synthesized on a SiO<sub>2</sub>/Si substrate with the same procedure for the synthesis of the Pt NPs on an rGO film using the PS-P4VP copolymer micelles. The single-layered graphene was then transferred onto the top of the Pt NPs using the transfer technique as described previously. The thermal annealing (400 °C) was exerted to each sample, which was 20 mins for PS(32)-P4VP(13), 30min for PS(51)-P4V(18) and 40min for PS(109)-P4VP(27) respectively. The perforated graphene was transferred to another SiO<sub>2</sub>/Si with the same method used for perforated rGO films.

*Tailoring of rGO films by arrayed Pt nanostructures:* Arrays of the Pt NWs and NRs, and the ordered complex array consisting of the Pt NWs and NPs were prepared on a SiO<sub>2</sub>/Si substrate as illustrated previously. The rGO films were transferred onto the top of the Pt nanostructures using the transfer technique as described previously. The thermal annealing (400 °C) was exerted to each sample. Tailored rGO samples were subsequently transferred onto another SiO<sub>2</sub>/Si with the same method as described above.

*Characterization:* The Pt nanostructures, pristine and nanostructured rGO films or CVD graphene were analyzed using a Multimode 8 AFM with a Nanoscope V controller (Bruker) in tapping mode with Al-coated Si cantilevers and FE-SEM (Hitachi S-4300) at 15 kV. TEM was performed on a Hitachi 7600 operating at 100 kV and a JEM-3010 (JEOL) at 300 kV. Raman spectra were obtained using a Renishaw 2000 with a 514.5 nm line from an Ar ion laser as an excitation source.

## Results and Discussion

A single-layered film of the PS(51)-P4VP(18) micelles with  $\text{H}_2\text{PtCl}_6$  in the P4VP cores was spin-coated onto an rGO film (Figure 3.23b). The AFM image in Figure 3.23b shows an array of spherical micelles without overlapping, implying a single layer of copolymer micelles. The spacing of the micelles obtained by a FFT analysis of the image is  $\sim 51$  nm. Then, the copolymers were removed by heating at  $400^\circ\text{C}$  in air, which resulted in the generation of the Pt NPs in the core regions of the micelles as shown in Figure 3.23c. The heating temperature of  $400^\circ\text{C}$  is known to be safe not to degrade rGO.<sup>[122]</sup> The spacing of non-aggregated Pt NPs ( $\sim 51$  nm) is identical to that of the original micelles, implying that an array of non-overlapped Pt NPs were successfully fabricated with the preservation of the order of the copolymer micelles.

In the AFM image of Figure 3.23c, apparently Pt NPs are sitting on the rGO film without penetration. However, when the height histogram of Pt NPs on rGO is compared to that of the Pt NPs synthesized on a bare  $\text{SiO}_2/\text{Si}$  substrate which is not covered with rGO (Figure 3.23d), the height of Pt NPs on rGO is 2.4 nm smaller. This value is equal to the thickness of rGO ( $\sim 2.3$  nm), implying that Pt NPs penetrated the rGO film and reside on the  $\text{SiO}_2/\text{Si}$  substrate (the schematic illustration of Figure 3.23).

To confirm the perforation in rGO, the sample shown in Figure 3.23c was delaminated and transferred onto another  $\text{SiO}_2/\text{Si}$  substrate for AFM analysis and also on a TEM grid. In the AFM image of the transferred rGO (Figure 3.24a), arrayed holes with the depth of  $\sim 2.2$  nm are clearly observed, which is again equivalent to the thickness of rGO ( $\sim 2.3$  nm). Note that most Pt NPs were separated from the rGO film during the transferring process in which washing and sonication

to remove a supporting layer were executed, although some Pt NPs were still transferred together and observed in the image. These arrayed holes are evidently noticeable in the TEM image (Figure 3.24b). The spacing of holes (~49 nm in AFM, ~50 nm in TEM) is almost identical to that of Pt NPs (~51 nm), indicating that holes were produced by arrayed Pt NPs with maintaining the order. The shape of holes is not clearly round but the sizes are comparable. The apparent diameter of holes determined from the TEM image is ~15 nm, which is larger than that of Pt NPs (~10 nm) directly synthesized on a silicon nitride membrane of a TEM grid (Figure 2.8b), of which the crystalline structure of Pt NPs was confirmed by the SAED pattern (Figure 2.9b).

When the Pt NPs were synthesized on rGO, they directly contacted the rGO surface at the beginning. Since rGO has many oxygen-containing defective sites on its surface,<sup>[99]</sup> catalytic oxidation of rGO by the Pt NPs could be initiated from these surface defects and facilitated by oxygen molecules in air, resulting in the formation of holes in rGO by eliminating carbon atoms near the Pt NPs. Once the Pt NPs touched the substrate by etching the rGO around the Pt NPs, no further oxidation by the catalytic Pt NPs could proceed in lateral directions. The Pt NPs were immobile when they were synthesized on a bare SiO<sub>2</sub>/Si substrate at 400 °C. Thus, the Pt NPs perforated rGO from the top of rGO. Since the size of holes (~15 nm) is larger than the diameter of the NPs (~10 nm), there would be a small positional drift of the NPs.

One of the merits of the diblock copolymer micellar approach is the controllability of the size and spacing of NPs, which can determine those of nanoholes in rGO, by adjusting the molecular weights of the copolymer. To demonstrate the controllability on the sizes and spacings of nanoholes in rGO, the

PS-P4VP copolymers having different molecular weights were selected: a lower molecular weight copolymer PS(32)-P4VP(13) and a higher one PS(109)-P4VP(27) than previously utilized PS(51)-P4VP(18). The same procedure was repeated as before to generate nanoholes in rGO. Since the length of the PS corona block eventually governs the spacing of nanoholes, a smaller spacing of holes (~34 nm) with PS(32)-P4VP(13), *i.e.*, dense holes, and a larger one (~101 nm) with PS(109)-P4VP(27), *i.e.*, sparse holes, were obtained as shown in AFM and TEM images (Figure 3.25). These spacing values are consistent with those of Pt NPs (Figure 2.8a and 2.8c). For the size of holes, which depends on the length of the P4VP core block, smaller holes (~8 nm) and larger holes (~19 nm) were produced by PS(32)-P4VP(13) and PS(109)-P4VP(27), respectively (Figure 3.25). These sizes are again larger than the diameters of Pt NPs, which are ~7 nm with PS(32)-P4VP(13) and ~14 nm with PS(109)-P4VP(27) (Figure 2.8a and 2.8c). Overall, arrays of discrete nanoholes in rGO with controllable sizes and spacing were effectively regulated by the molecular weights of copolymers.

This diblock copolymer micellar approach to perforating graphene grown by CVD where the same procedure in the previous rGO case was employed. However, instead of the perforation, only large aggregations of the Pt NPs was observed on CVD graphene (Figure 3.26). Similar aggregations of the particles on graphene have been reported, which were understood due to the low surface energy of graphene.<sup>[123,124]</sup> In addition, no formation of trenches is attributable to a relatively low temperature (400 °C) to produce trenches by catalytic NPs.

Alternatively, arrayed Pt NPs were first synthesized on a bare SiO<sub>2</sub>/Si substrate and subsequently transferred CVD graphene on the top of them. Figure 3.27a shows Pt(51-18) on a SiO<sub>2</sub>/Si substrate. Then, single-layered graphene grown by CVD

was transferred on the Pt NPs (Figure 3.27b). After covered by graphene, individual NPs were hardly visible but linear or areal wrinkles of graphene, which cover several neighbouring Pt NPs together. The part indicated by the arrow is visualized in a 3D view (the inset of Figure 3.27b), in which the Pt NPs covered by graphene and graphene suspended between particles are discernible. This arrangement is illustrated in the schematic (ii) in Figure 3.27.

After heating this sample at 400 °C for 30 min in air, all large wrinkles disappear but arrayed Pt NPs appear again as shown in Figure 3.27c. No appreciable change in the AFM image was found by longer heating. Due to the negative thermal expansion coefficient,<sup>[125]</sup> graphene contracted so that the areas of wrinkles became reduced and graphene started to wrap individual NPs (Figure 3.28), which are evident after 10 min heating (the areas marked by the circle and by the arrows in Figure 3.28c). After 30 min heating, the Pt NPs were protruded over the graphene. Comparing the 3D view images before (Figure 3.27b) and after heating (Figure 3.27c), protrusion of the Pt NPs is noticeable, which is depicted in the schematic (iii) of Figure 3.27. Thus, the CVD graphene was perforated by arrayed Pt NPs from the bottom of graphene. In addition, the sharp linear creases between some NPs are formed in Figure 3.27c. During the heating process, the graphene suspended between the NPs could contract, adhere together, and form these creases which are well visible in the 3D view image of Figure 3c.

To confirm the perforation in CVD graphene, the sample shown in Figure 3.27c was delaminated and transferred onto another SiO<sub>2</sub>/Si substrate by the same procedure for transferring rGO. The AFM image of the transferred graphene (Figure 3.27d) clearly displays arrayed holes. The spacing of holes (~56 nm) is close to that of the Pt NPs (~51 nm) as like the previous perforated rGO. The shape

of the holes is not clearly round again. The diameter of the holes (~21 nm) is also larger than that of the Pt NPs (~10 nm). Thus, the CVD graphene was successfully perforated by arrayed Pt NPs from the bottom in contrast to the perforation of rGO from the top. It should be noted that no Pt NPs were observed after transferring the graphene.

The phenomenon of perforation in the CVD graphene by arrayed Pt NPs was deeply characterized by using Raman spectroscopy (Figure 3.29). Before heating at 400 °C, the characteristic G and 2D bands of pristine graphene are only observed at 1582 cm<sup>-1</sup> and 2676 cm<sup>-1</sup>, respectively. After 5 min heating, the D band at 1345 cm<sup>-1</sup> appears, which is associated with first-order zone boundary phonons activated by defective sites of graphene including edges. In addition, the observation of the D' band at 1640 cm<sup>-1</sup> after heating, which is also associated with defective sites, supports the formation of edges around holes in graphene.

The etching of graphene using conventional lithographic methods to obtain nanopatterned graphene normally induces an increase of the full width at half maximum (FWHM) of G band, indicating the deterioration of graphene.<sup>[126]</sup> However, the FWHM of the G band here shows little change, implying no further alteration in the degree of disorder in graphene other than holes (Figure 3.29a and see Appendix C). In fact, the FWHD of the G band slightly decreased due to the hole doping of graphene by oxygen species.<sup>[127]</sup> Such doping of graphene is also evident by observing that the position of the G band at 1582 cm<sup>-1</sup> and the 2D band at 2676 cm<sup>-1</sup> moved to the right after heating (Figure 3.29b and 3.29c).<sup>[128]</sup> However, the mechanical strain exerted on graphene also considerably contributes to the variation in the position of Raman peaks. This effect can be separated from the contribution by charge doping by the correlation analysis of the F and 2D modes as

described in elsewhere,<sup>[129]</sup> which will be introduced and discussed in Appendix C for deeper understanding on the mechanism of the perforation process.

To study prerequisites for the perforation of graphene, further several control experiments were carried out. First, graphene on a bare substrate heated at 400 °C in air did not show any physical changes, except oxygen doping by Raman spectroscopy, because the temperature of 400 °C is not high enough for oxygen alone to etch graphene.<sup>[130]</sup> Second, when graphene on the top of arrayed Pt NPs was heated at 400 °C in vacuum, perforation of graphene was not observed (Figure 3.30a), implying that oxygen is necessary for perforation. Note that creases between some NPs were noticeable in this case. Third, instead of the Pt NPs, graphene was transferred on the top of arrayed SiO<sub>2</sub> or Au NPs, which were synthesized using the same copolymer micelles, and then heated at 400 °C in air. Similarly, perforation of graphene but creases on both types of the NPs (Figure 3.30b and 3.30c), suggesting that the Pt NPs are needed to perforate graphene. It is noted that the SiO<sub>2</sub> or Au NPs are non-catalytic in terms of trench formation in graphene by oxidation, although there is a report that the SiO<sub>2</sub> NPs can etch graphene at 850~1,100 °C in a hydrogen flow.<sup>[131]</sup> Although other types of the catalytic NPs such as Fe, Ni, and Ag were employed in this experiment, which have shown an ability to form trenches on graphene at high temperatures, they can be potential candidates for alternative NPs of Pt to perforate graphene.

From these control experiments, catalytic Pt NPs and oxygen molecules play a major role in the oxidation reaction of graphene to induce perforation. The Raman analysis (Figure 3.29) tells that graphene was doped with oxygen at 400 °C. At the beginning, this oxygen-doped graphene can be oxidized by the catalytic Pt NPs which directly contact with graphene from the bottom. Once the oxidation reaction

starts, atmospheric oxygen molecules can expedite further oxidation of graphene near Pt NPs, resulting in protrusion of Pt NPs over graphene. However, this reasoning cannot explain the large aggregation of Pt on graphene without perforation when we tried to perforate graphene from the top by synthesizing Pt NPs directly on graphene (Figure 3.26). In this case, the requirements learned from the control experiments for perforating graphene, *i.e.*, catalytic Pt NPs and atmospheric oxygen molecules, are at least satisfied.

The evident difference between two cases is the shape of graphene. The graphene located under the Pt aggregation is evenly flat (Figure 3.26). In sharp contrast, graphene placed on the top of arrayed Pt NPs is severely curved. When graphene on arrayed Pt NPs was heated, graphene contracted and started to wrap individual NPs, which can cause substantial mechanical strains on graphene. The ultimately strained graphene due to the Pt NPs can be found in the case that graphene on Pt NPs was heated in vacuum so that graphene only wrapped the spherical NPs without perforation (inset of Figure 3.30a). It has been reported that a high local curvature in the lattice consisting of  $sp^2$ -bonded carbon atoms can considerably increase the chemical reactivity of those carbon atoms.<sup>[132-135]</sup> Thus, the strained graphene on the spherical Pt NP can be effectively oxidized at 400 °C in air, compared to the flat graphene. Therefore, CVD graphene was perforated from the bottom with the Pt NPs. No trench was formed during the perforation because Pt NPs synthesized on a  $SiO_2/Si$  substrate were immobile at 400 °C.

By changing the molecular weight of PS-P4VP copolymers, the controllability on the size and spacing of nanoholes in graphene was demonstrated. As shown in Figure 3.31, the sizes and spacings of nanoholes in graphene become larger as the increase of those of the Pt NPs. The spacing values are quite consistent with those

of the NPs. For the size of the holes, we observed slightly larger values than those of Pt NPs as like the case of perforation of rGO. Additionally, in the Raman spectra (Figure 3.31d), the D band at  $1345\text{ cm}^{-1}$  as well as the D' band at  $1640\text{ cm}^{-1}$  are prominent in smaller and denser holes (Figure 3.31a), which have more edges than others. Furthermore, the FWHM in all three cases are almost unchanged compared to that of pristine graphene, indicating again that graphene excluding holes was scarcely damaged.

In conclusion, the nanoperforation of the CVD graphene by the Pt NPs indicates that the perforation reaction is catalyzed by the Pt NPs lowering the activation energy barriers for the oxidation reaction of carbon atoms, where the mechanical strain should be additionally considered for the perforation of the CVD graphene (Figure 3.32).

As done in the case of the CVD graphene perforation, now rGO films were transferred onto arrayed Pt(25-7) (Figure 3.33a), followed by heating to induce the perforation from the bottom (Figure 3.33b). Protruded Pt NPs in the AFM image (Figure 3.32c) shows the successful perforation of rGO films from the bottom, as observed in the case of the CVD graphene perforation. The perforated rGO film was transferred onto another  $\text{SiO}_2/\text{Si}$  substrate, and the removal of the Pt NPs eventually disclosed arrays of the holes in a hexagonal order (Figure 3.33d). The spacing of arrayed holes is  $\sim 27\text{ nm}$ . Note that the nanoperforated rGO has similar wrinkles and creases as shown in the nanoperforated CVD graphene as indicated with white arrows in Figure 3.33c. Figure 3.33d shows rGO films perforated by Pt(32-13). Since molecular weight is higher than previous copolymer, the spacing ( $\sim 39\text{ nm}$ ) of the holes became larger, which can be comparable to those of Pt(32-13).

This process was extended as a general method to tailor rGO films by the Pt nanostructures fabricated on SiO<sub>2</sub>/Si substrate: (i) synthesizing the Pt nanostructures, (ii) transferring rGO films, (iii) heating at 400 °C, (iv) transferring nanopatterned rGO with removing the Pt nanostructures. As the first example of extended work, the Pt NWs from cylindrically nanostructured PS-P4VP thin films were employed. An rGO film was transferred onto the Pt NWs synthesized from PS(25)-P4VP(7) (Figure 3.34a). The wrinkles induced by the underneath Pt NWs are clearly observed in the AFM image. Note that some part of rGO film contacts to SiO<sub>2</sub>/Si substrate, while other part is suspended by the adjacent Pt NWs. Heating process made the Pt NWs fully exposed, allowing for the observation by AFM (Figure 3.34b) as well as the transfer their nanopatterns to the rGO film. The tailored rGO film was delaminated from a SiO<sub>2</sub>/Si substrate and transferred onto another substrate as shown in Figure 3.33c. The nanopatterning by the Pt nanostructures transfer inverted nanopatterns to rGO, and the dark lines in the AFM image indicate that the Pt NWs cut continuous rGO films into arrayed graphene nanoribbons. The periodicity of the densely arrayed rGO nanoribbons (the width between two lines illustrated in Figure 3.34c) is ~32 nm, which is similar to that of the Pt NWs (Figure 2.14d). Since the width of the Pt NWs synthesized from PS(25)-P4VP(7) was measured to be ~6 nm, the width of rGO nanoribbon is ~25 nm. Thus, using arrayed Pt NWs, arrayed rGO nanoribbons can be efficiently fabricated on the substrate.

Figure 3.35 represents the controllability of rGO nanoribbons by managing the molecular weights of the copolymers. Arrayed rGO nanoribbons tailored by the Pt NWs synthesized from PS(19)-P4VP(5) (~25nm) and PS(32)-P4VP(13) (~40 nm) exhibit different periodicities. Then the width of rGO nanoribbons are ~19 nm and

~32 nm, respectively. It should be noted that the width of rGO nanoribbons can be further reduced to a half value by self-assembled bilayers of cylindrical domains to effectively double the pattern density.<sup>[136]</sup> Here again it is confirmed that rGO nanopattern greatly relies on the molecular weight of the copolymers.

As demonstrated in the previous chapter, the Pt NWs and NPs can be combined to form an ordered complex arrays (Figure 2.36). Those ordered complex arrays can be also utilized to tailor rGO films as well. Figure 3.36a shows the protruded Pt NWs and Pt(32-13) and an rGO film after heating at 400 °C for 30 min, leading to the formation of nanoperforated rGO nanoribbon arrays. The periodicity of the holes and ribbons can be controlled by varying the molecular weights of the PS-P4VP and spin-coating condition as demonstrated in Figure 3.36c and Figure 3.36d.

Besides NPs and NWs, the Pt NRs were also employed to tailor rGO films into their inverse nanopatterns. Since only rGO on the Pt NRs is etched, the final morphology of tailored rGO is composed of large hole arrays and smaller nanodots at the center of each hole as an island, which can be called rGO anti-NRs (Figure 3.37c). As shown in the previous chapter, the diameters and spacings of the anti-NRs can be accurately adjusted by controlling the molecular weights of the copolymers as well as  $\mu$ . Figure 3.37d represents rGO anti-NRs with the different sizes and spacings, achieved by the lower molecular weight PS-P4VP copolymers.

## Summary

rGO films and CVD graphene were tailored by the Pt nanostructures synthesized using PS-P4VP diblock copolymers and their micelles. A highly reactive surface of the Pt NPs were able to catalyze the oxidation process between carbon atoms and an oxygen species to degrade rGO and graphene, resulting in the nanoperforated

rGO. When the direct synthesis of the Pt NPs was applied to the CVD graphene, however, only large aggregations of Pt on graphene were obtained. The CVD graphene was only perforated from the bottom by transferring it onto the top of arrayed Pt NPs synthesized on a SiO<sub>2</sub>/Si substrate. By using Raman spectroscopy, it was confirmed that the stained graphene on the NPs can play an important role in localized catalytic oxidation of graphene. The Raman analysis also disclosed that graphene other than holes after perforation was not much changed, which would be beneficial to use the perforated graphene in the practical applications. The controllability of the sizes and spacings of the nanoholes in rGO and graphene was demonstrated by tuning those of the Pt NP with the variation of the molecular weight of the PS-P4VP copolymers.

Moreover, different Pt nanostructures were employed to tailor rGO films by applying same procedure as done for nanoperforation. Arrayed Pt NWs, complex ordered arrays, and NRs resulted in arrays of rGO nanoribbons with and without the nanoperforation, and anti-NRs, respectively, of which dimension and number density were accurately controlled by managing the molecular weights of the PS-P4VP.

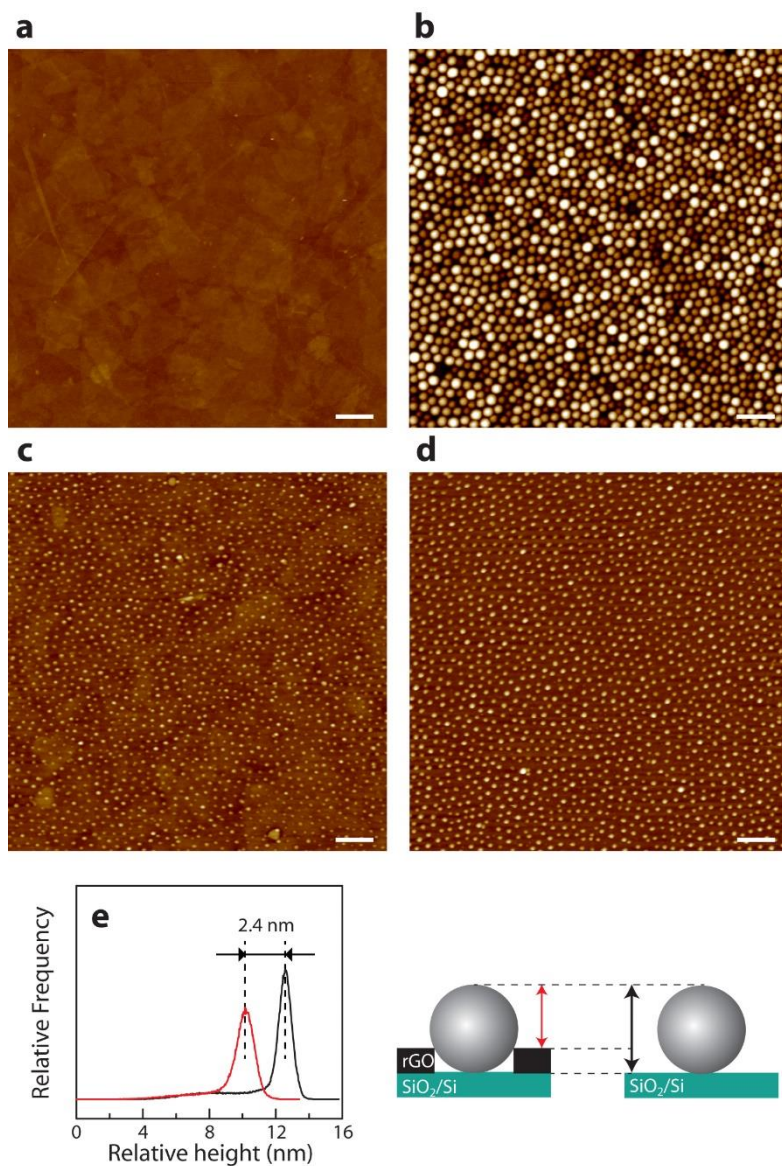


**Figure 3.23.** AFM images for the fabrication of arrayed Pt NPs on rGO. (a) rGO; (b) PS(51)-P4VP(18) micelles with Pt precursors in the cores; (c) Arrayed Pt NPs synthesized on rGO and (d) on a bare SiO<sub>2</sub>/Si substrate; (e) Height histograms of Pt NPs obtained from (c) and (d) are plotted together for comparison. A relative height in each case is shown in the schematic illustration. Scale bars are 200 nm.

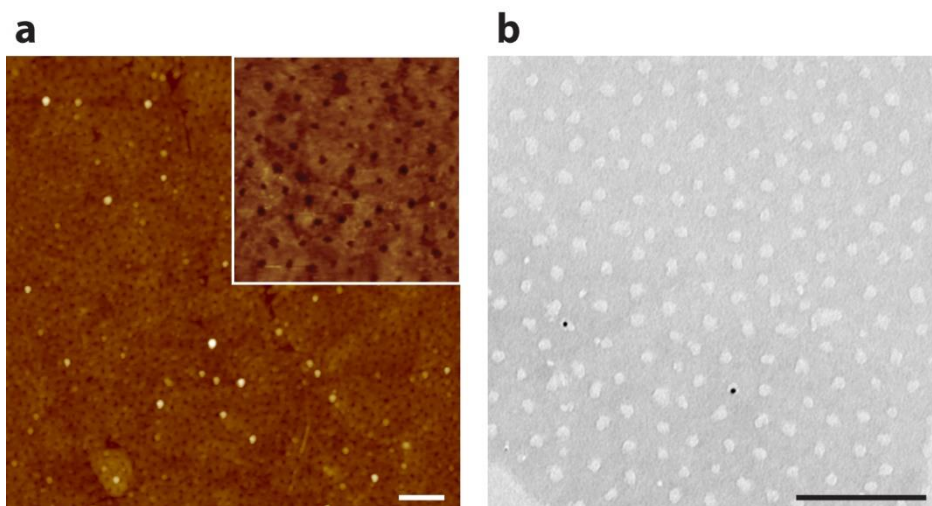


**Figure 3.24.** Nanoperforated rGO. (a) AFM image of perforated rGO (inset: a magnified image in  $500\text{ nm} \times 500\text{ nm}$ ); (b) TEM image of perforated rGO. Scale bars are 200 nm.

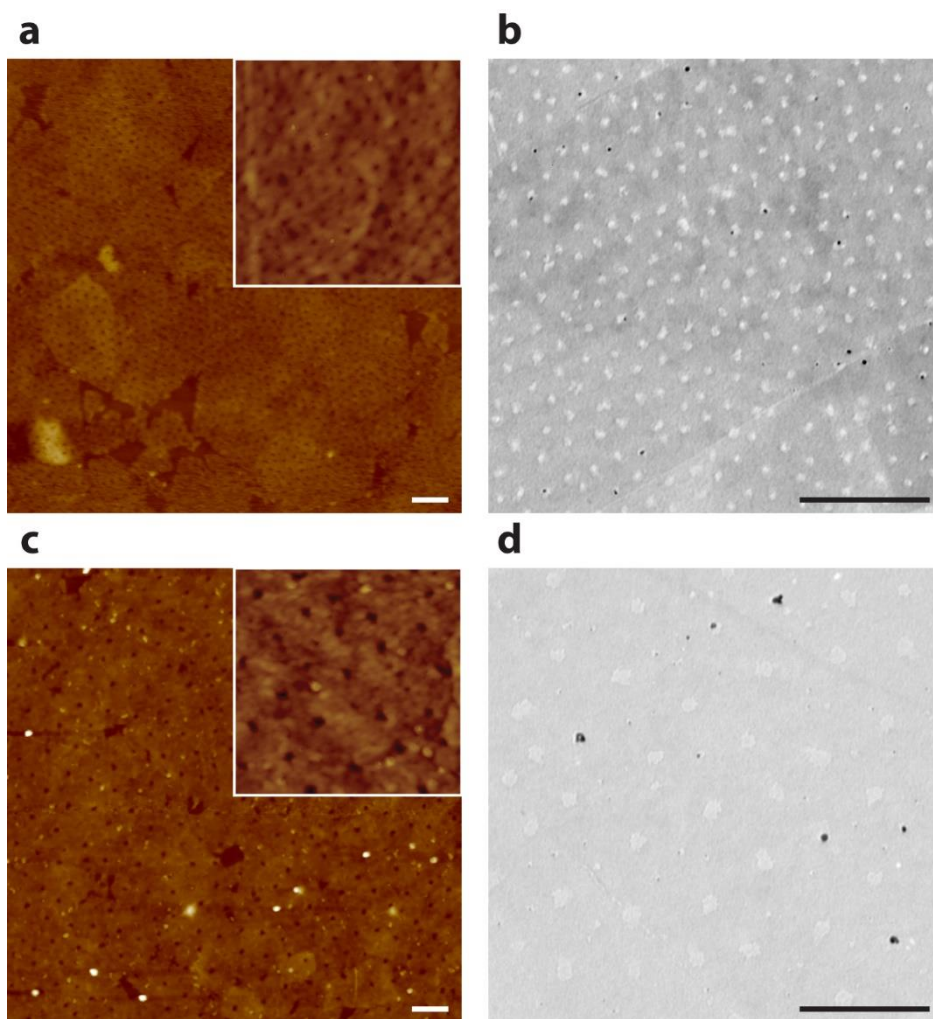


**Figure 3.25.** AFM and TEM images of perforated rGO by (a,b) Pt(32-13) and (c,d) Pt(109-27). Each inset is a magnified image (500 nm  $\times$  500 nm). Scale bars are 200 nm.

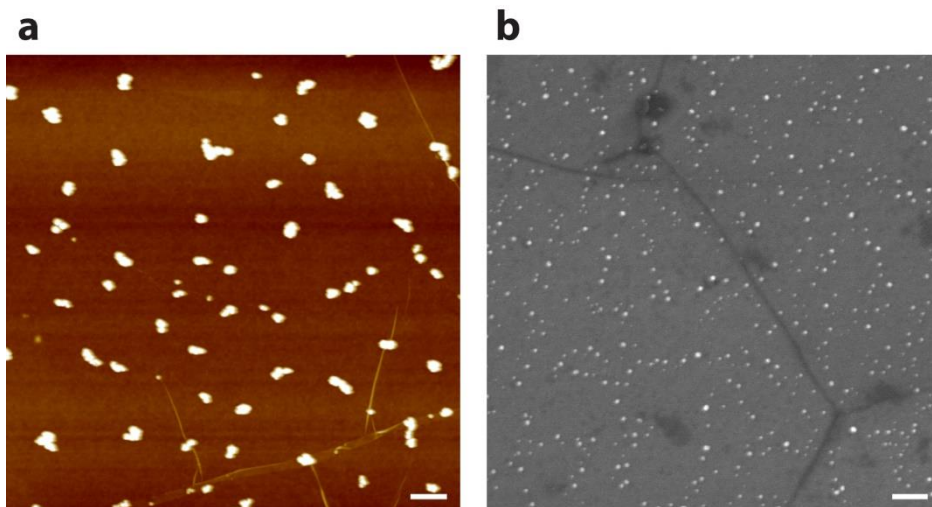


**Figure 3.26.** (a,b) AFM and FE-SEM images of Pt aggregation on CVD graphene after heating of PS-P4VP micelles with Pt precursors at 400 °C for 30 min in air. Scale bars are 200 nm.

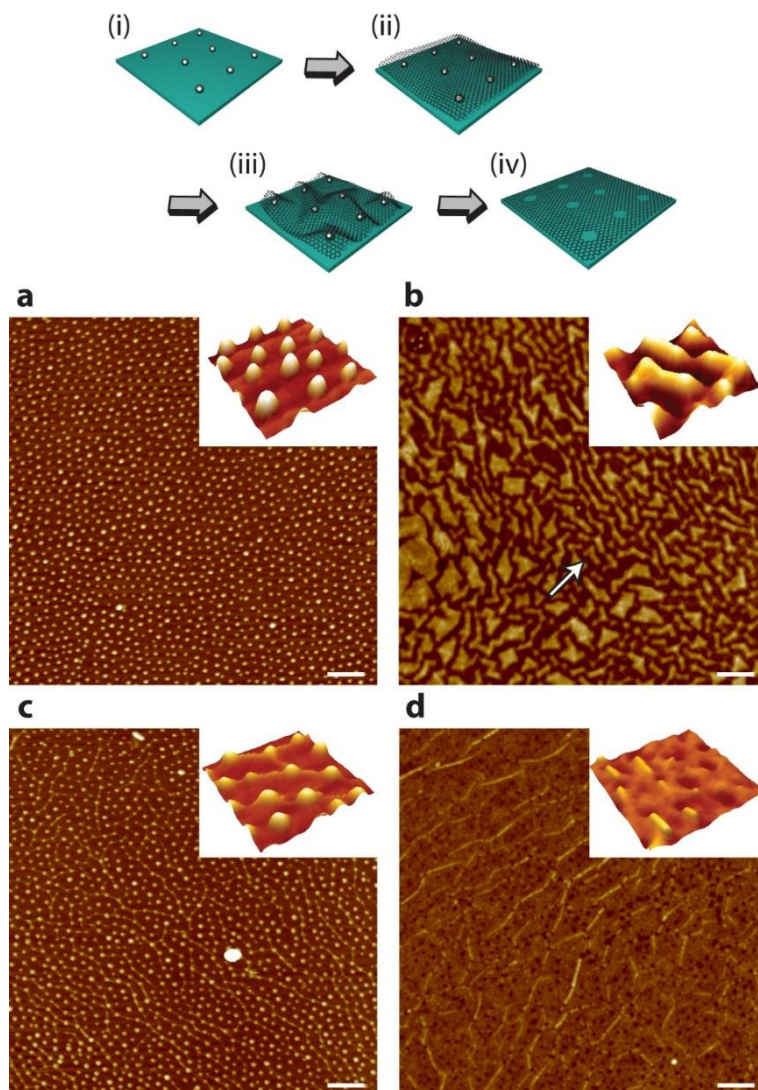


**Figure 3.27.** AFM images for the fabrication of nanoperoforated CVD graphene. (a) arrayed Pt(51-18) on a bare  $\text{SiO}_2/\text{Si}$  substrate (schematic i); (b) graphene transferred onto arrayed Pt NPs (schematic ii); (c) perforated graphene with arrayed Pt NPs after heating (schematic iii); (d) perforated graphene transferred onto another  $\text{SiO}_2/\text{Si}$  substrate. Each inset is a 3D view image with a higher magnification ( $200 \text{ nm} \times 200 \text{ nm}$ ). Scale bars are 200 nm.

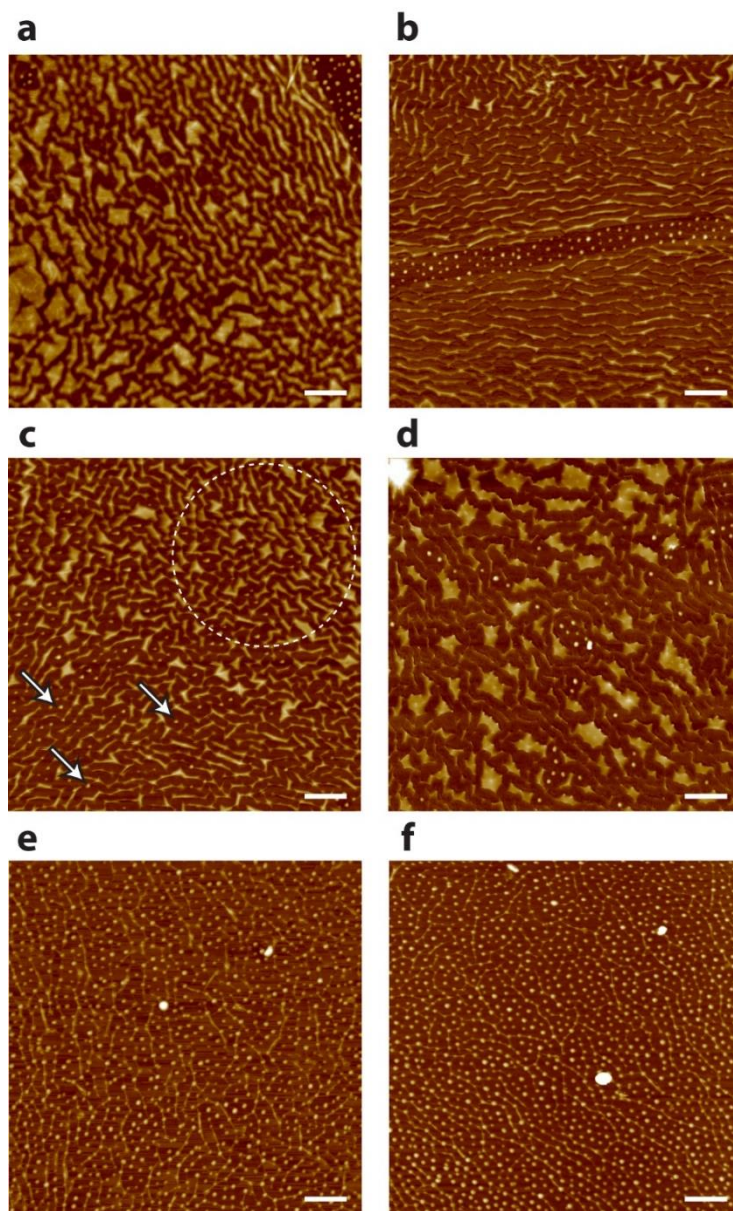


**Figure 3.28.** AFM images of surface morphology variation of CVD graphene. (a) CVD graphene transferred on the Pt NPs array. (b) AFM image of annealing treated CVD graphene for 5 min; (c) 10 min; (d) 15 min; (e) 25 min; (f) 30 min. Scale bars are 200 nm.

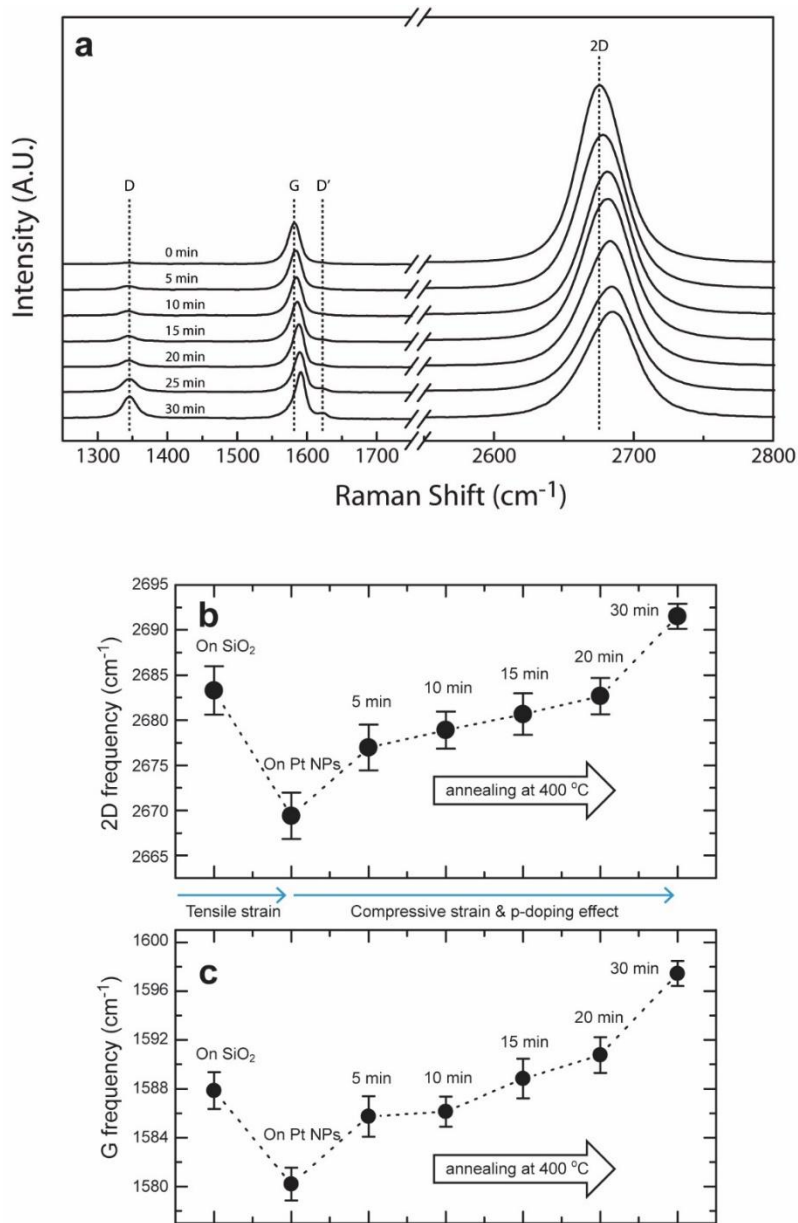


**Figure 3.29.** (a) Raman spectra of graphene on Pt(51-18) after heating with 5 min interval. The variation of the phonon frequencies of (b) the 2D and (c) G modes as a function of annealing time.

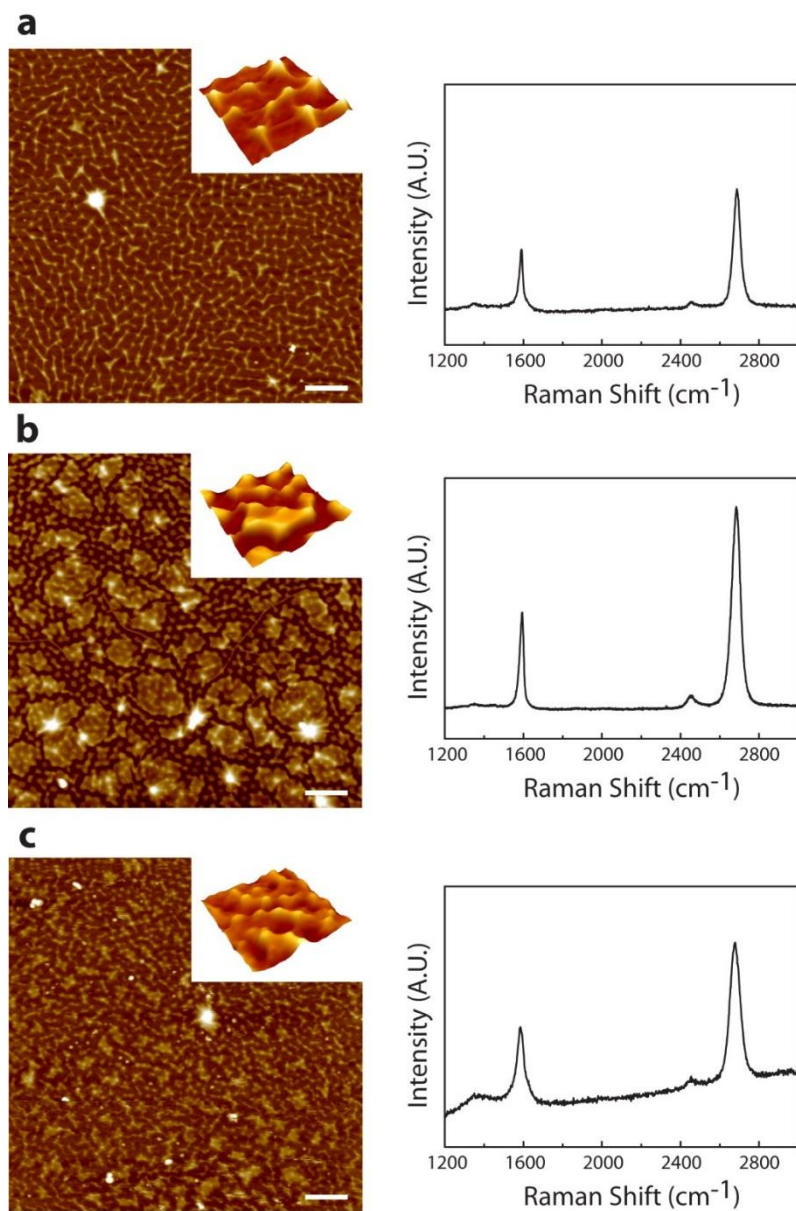


**Figure 3.30.** AFM images and Raman spectra of graphene on arrayed NPs. (a) Pt(51-18) after heating in vacuum; (b) SiO<sub>2</sub>(51-18) after heating in air; (c) Au(51-18) after heating in air. Each inset is a 3D view image with a higher magnification (200 nm × 200 nm). Scale bars are 200 nm.

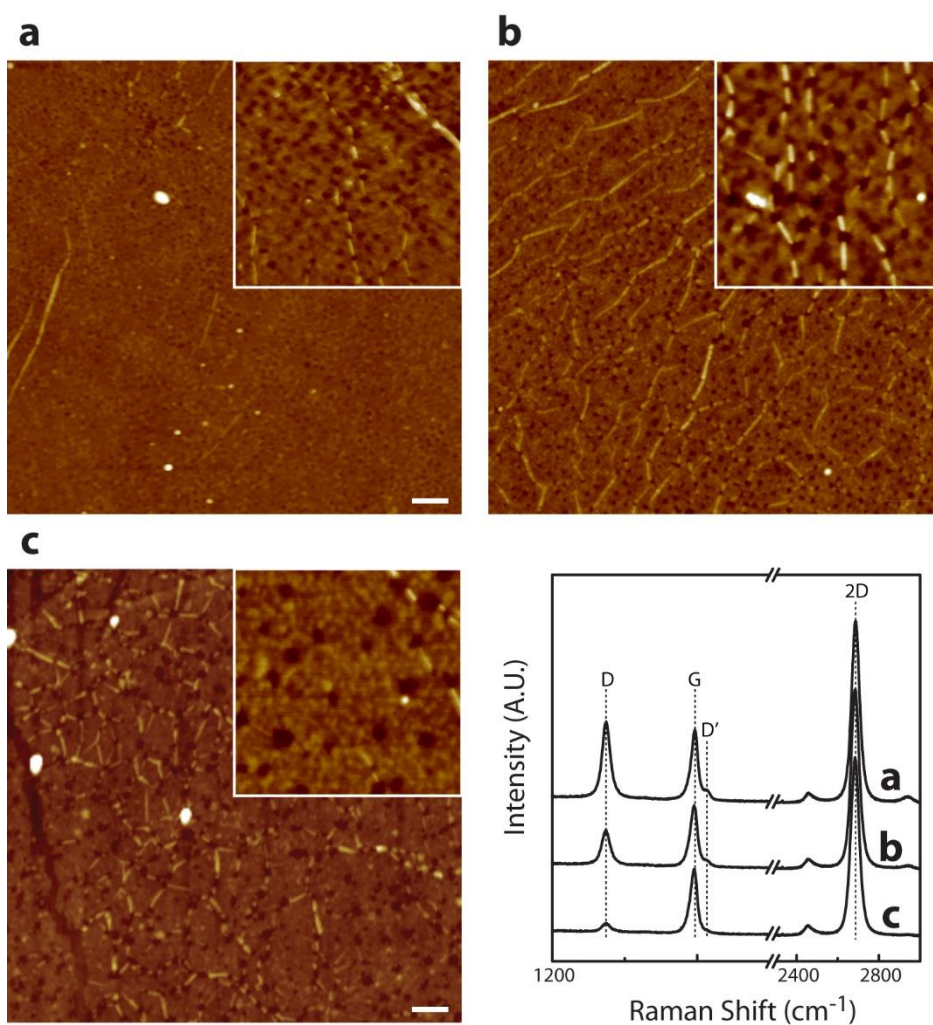


**Figure 3.31.** Controllability studies of pore size and density and catalytic effect of other condition. Nanoperforated CVD graphene by arrayed Pt NPs synthesized from other copolymer micelles: (a) PS(32)-P4VP(13); (b) PS(51)-P4VP(18); (c) PS(109)-P4VP(27). Each inset is a magnified image (500 nm × 500 nm). Raman spectra with respect to each sample are displayed together. Scale bars are 200 nm.

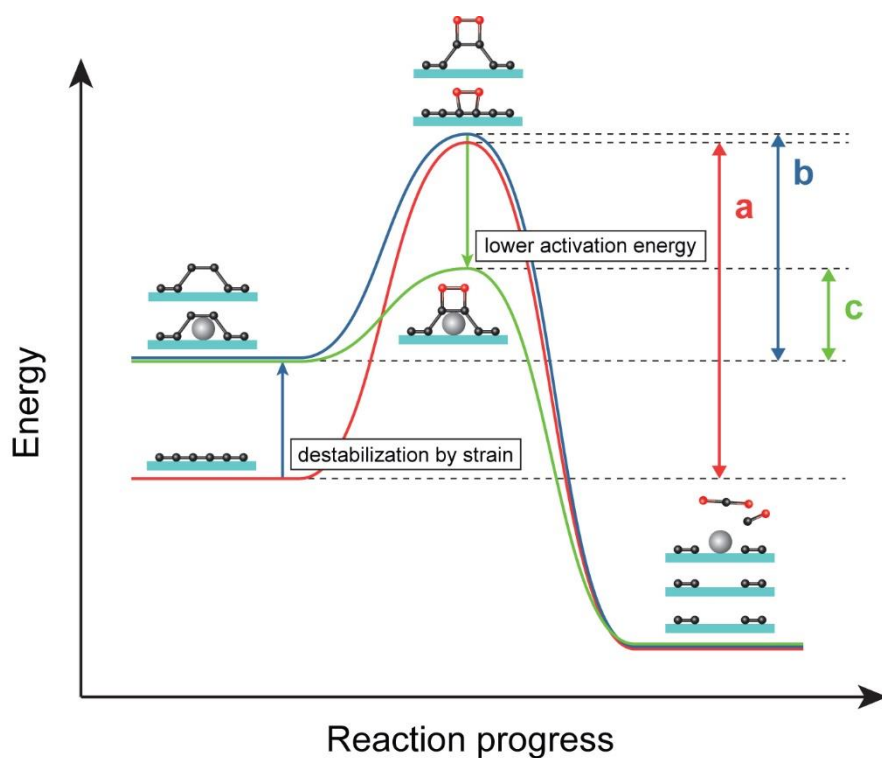


**Figure 3.32.** Simplified reaction coordinate for the oxidation reaction of CVD graphene with and without a Pt NP. (a) The original activation energy without a Pt NP. (b) The activation energy lowered only by mechanical strain. (c) The activation energy decreased by local strain and Pt catalyst.

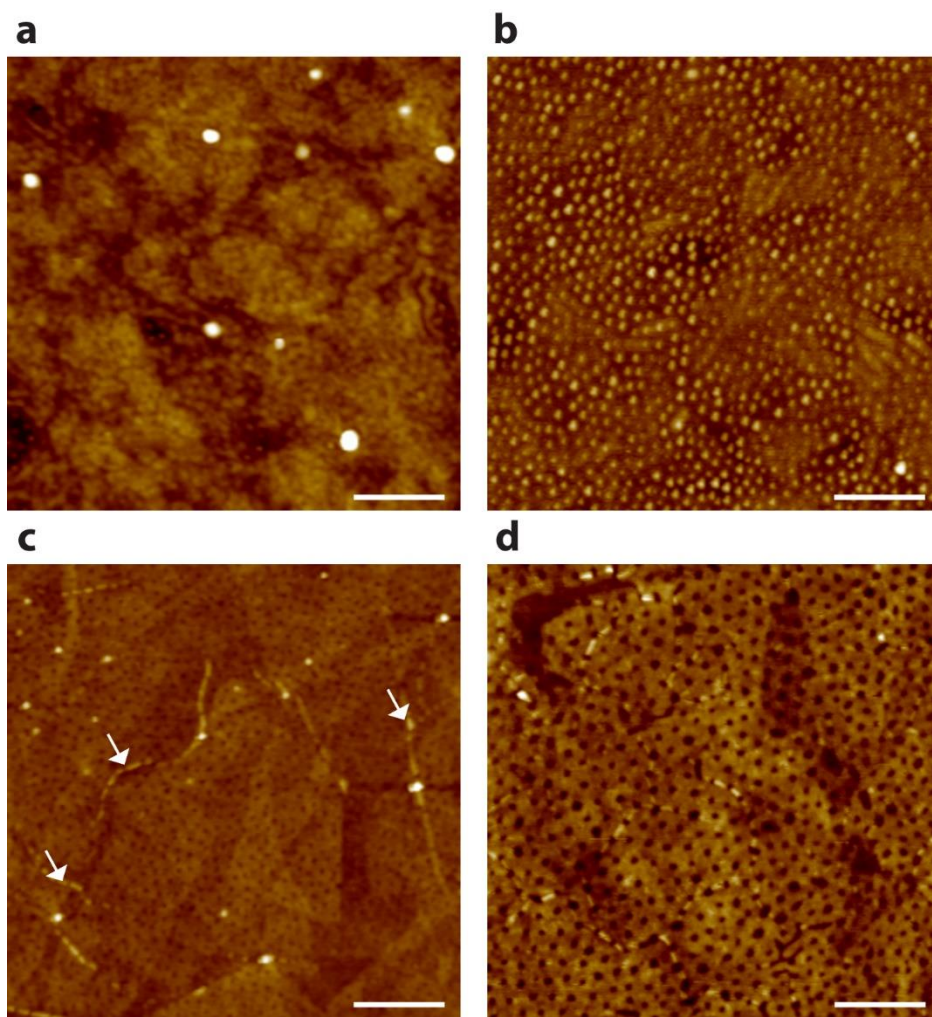


**Figure 3.33.** AFM images for the fabrication of nanoporated rGO. (a) rGO transferred onto arrayed Pt(25-7); (b) Perforated rGO with arrayed Pt NPs after heating; (c) Perforated rGO transferred onto another SiO<sub>2</sub>/Si substrate; (d) perforated rGO by Pt(32-13) Scale bars are 200 nm.

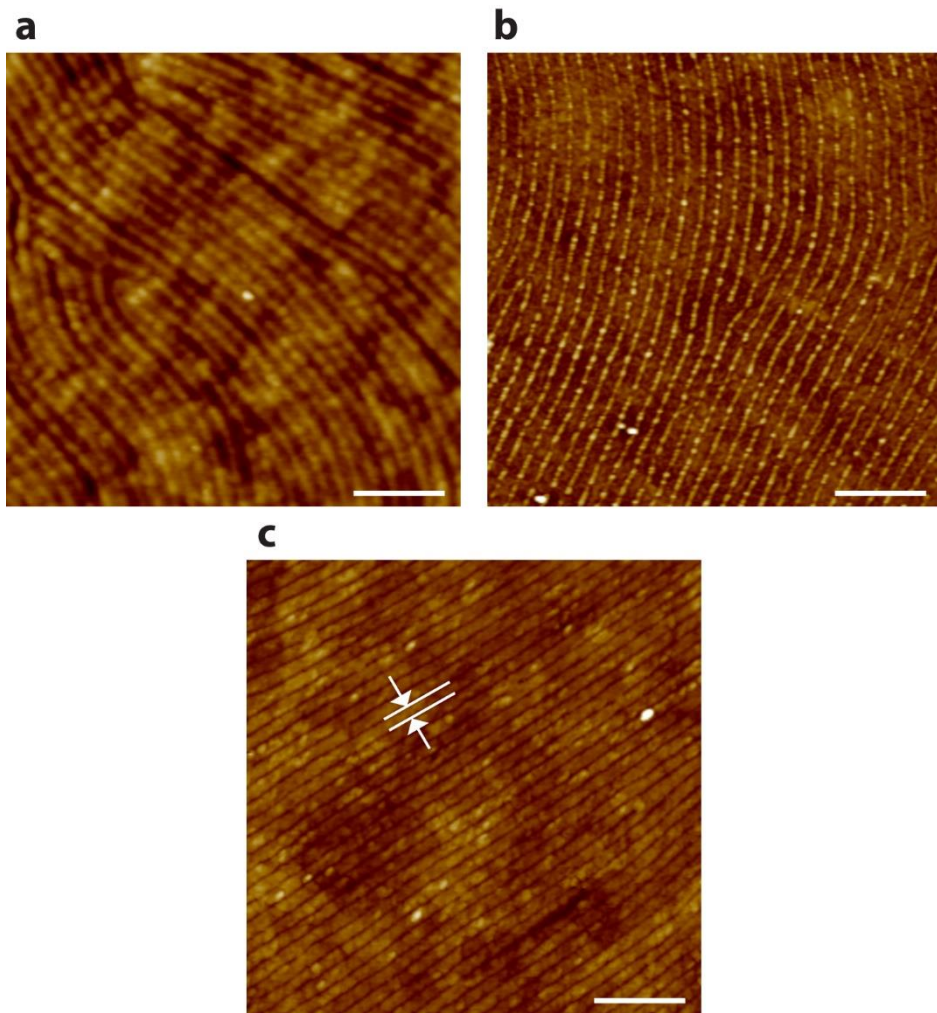


**Figure 3.34.** AFM images for the fabrication of arrayed rGO nanoribbons. (a) rGO transferred onto arrayed Pt NWs synthesized from PS(25)-P4VP(7); (b) Tailored rGO with arrayed Pt NWs after heating; (d) Arrayed rGO nanoribbons transferred onto another SiO<sub>2</sub>/Si substrate Scale bars are 100 nm.

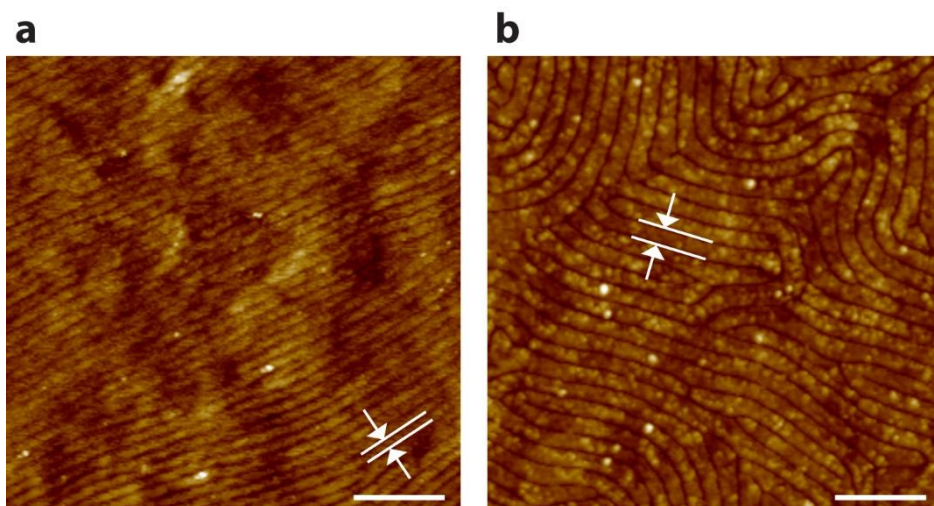


**Figure 3.35.** Control of rGO nanoribbons by varying molecular weights of PS-P4VP. (a) PS(19)-P4VP(5); (b) PS(32)-P4VP(13). Scale bars are 100 nm.

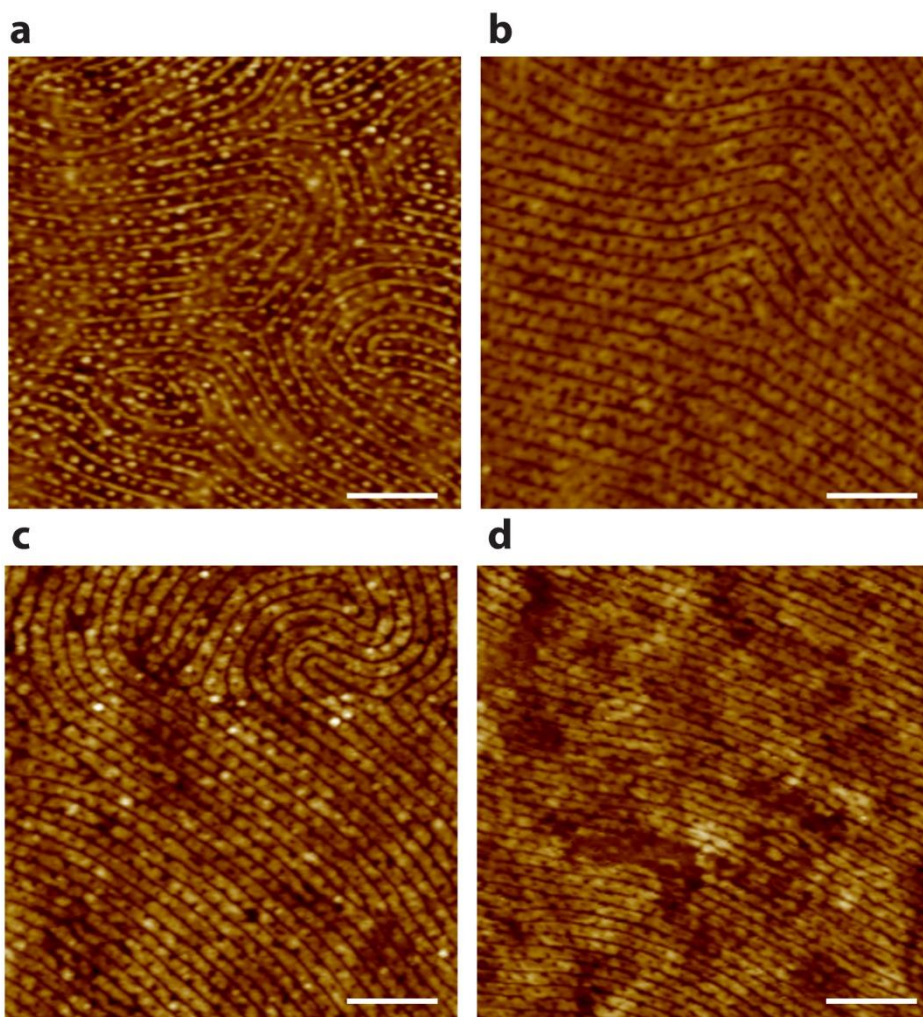


**Figure 3.36.** AFM images for the fabrication of perforated rGO nanoribbon arrays. (a) Perforated rGO nanoribbons with ordered complex Pt arrays (Figure 2.36a) after heating; (b) Perforated rGO transferred onto another SiO<sub>2</sub>/Si substrate. Perforated rGO nanoribbons fabricated from other ordered complex arrays shown in (c) Figure 2.36b; (d) Figure 2.36c. Scale bars are 100 nm.

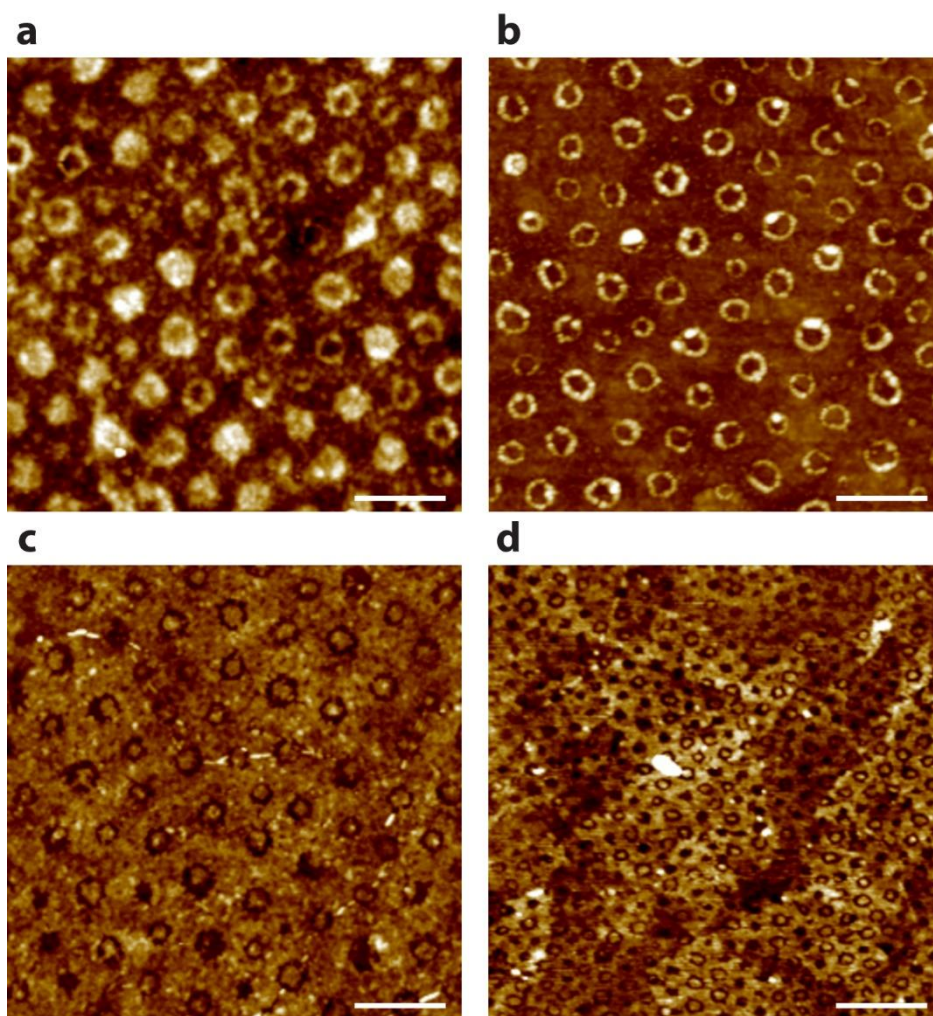


**Figure 3.37.** AFM images for the fabrication of arrayed rGO anti-NRs. (a) rGO transferred onto arrayed Pt nanorings from IL-containing PS(109)-P4VP(27) ( $\mu = 0.8$ ). (b) Arrayed rGO anti-NRs with Pt nanorings after heating; (c) Arrayed rGO anti-NRs transferred onto another SiO<sub>2</sub>/Si substrate. (d) Arrayed rGO anti-NRs from IL-containing PS(51)-P4VP(18) ( $\mu = 0.8$ ). Scale bars are 100 nm.

## Chapter IV

### Summary and Outlook

The diblock copolymer approach for graphene nanopatterning proposed here is a promising bottom-up technique which can be used to generate nanostructures of various materials over a large area without sophisticated lithographic requirements. From self-assembled thin films of PS-PMMA and PS-P4VP, ordered arrays of diverse metal and oxide nanostructures, including NPs, NWs, NRs, as well as complex nanostructures were fabricated, and then effectively used as a nanotemplate or an etching mask to transfer their regular nanopatterns onto graphene. In this dissertation, three different graphene nanopatterning types which use diblock copolymers and their micelles were discussed. A summary is given below:

1. Single layers of PS-P4VP micelles were spin-coated onto rGO to produce graphene-decorating NPs arrays with a hexagonal order.
2. Arrayed Au NPs synthesized from a single layer of film of PS-P4VP micelles were utilized as an etching mask to transfer their hexagonal nanopatterns onto graphene to generate arrayed graphene nanodots after an oxygen plasma treatment.
3. Arrayed Pt nanostructures were fabricated from thin films of PS-P4VP tailored graphene into ordered arrays of graphene nanostructures by a catalytic oxidation reaction.

With regard to the aforementioned graphene nanopatterning process, in every instance the dimension and shape of the graphene nanopatterns formed by the

diblock copolymers were precisely controlled by the molecular weight of the copolymers.

Because these types of nanopatterns are difficult to realize by conventional lithographic methods, the methodology established here can be effectively utilized to explore the unique properties of various nanopatterned graphenes and may lead to the practical applications as well, such as electronic devices, biosensors, and membranes. For example, continuous rGO film with a thickness of several hundred nanometers can be perforated by Pt NPs to fabricate a free-standing, rigid rGO membrane with a regular array of nanopores. Nano-sized holes can be effective when used to filter various nanomaterials as well as microorganisms such as bacteria. Moreover, given its conductivity, membranes based on nanoperforated rGO film may have electrically tunable filtration properties through an external bias condition.

Beyond the physical nanopatterning of graphene as discussed in this dissertation, chemical nanopatterning can also be achieved by diblock copolymers and their micelles. Local strain, which is known to alter the chemical reactivity of graphene, can be exerted onto graphene which is transferred onto arrayed NPs. The strain can be controlled by managing the sizes and spacings of the NPs, parameters which are governed by the molecular weights of the copolymers. Thus, the diblock copolymer approach may provide a very effective means of graphene strain engineering for the chemical modification of graphene on the nanometer scale.

## References

- [1] E. Fitzer, K.-H. Kochling, H. P. Boehm, H. Marsh, *Pure Appl. Chem.* **1995**, *67*, 473.
- [2] K. S. Novoselov, A. K. Geim, S. V. Morozov, D. Jiang, Y. Zhang, S. V. Dubonos, I. V. Grigorieva, A. A. Firsov, *Science* **2004**, *306*, 666.
- [3] M. I. Katsnelson, K. S. Novoselov, A. K. Geim, *Nat. Phys.* **2005**, *2*, 620.
- [4] Y. B. Zhang, Y. W. Tan, H. L. Stormer, P. Kim, *Nature* **2005**, *438*, 201.
- [5] S. V. Morozov, K. S. Novoselov, M. I. Katsnelson, F. Schedin, D. C. Elias, J. A. Jaszczak, A. K. Geim *Phys. Rev. Lett.* **2008**, *100*, 016602.
- [6] C. Lee, X. D. Wei, J. W. Kysar, J. Hone, *Science* **2008**, *321*, 385.
- [7] A. A. Baladin, S. Ghosh, W. Bao, I. Calizo, D. Teweldebrhan, F. Miao, C. N. Lau, *Nano Lett.* **2008**, *8*, 902.
- [8] R. R. Nair, P. Blake, A. N. Grigorenko, K. S. Novoselov, T. J. Booth, T. Stauber, N. M. R. Peres, A. K. Geim, *Science* **2008**, *320*, 1308.
- [9] X. Li, W. Cai, J. An, S. Kim, J. Nah, D. Yang, R. Piner, A. Velamakanni, I. Jung, E. Tutuc, S. K. Banerjee, L. Colombo, R. S. Ruoff, *Science* **2009**, *324*, 1312.
- [10] S. Bae, H. Kim, Y. Lee, X. Xu, J.-S. Park, Y. Zheng, J. Balakrishnan, T. Lei, H. R. Kim, Y. I. Song, Y.-J. Kim, K. S. Kim, B. Özyilmaz, J.-H. Ahn, B. H. Hong, S. Iijima, *Nat. Nanotechnol.* **2010**, *5*, 574.
- [11] S.-M. Lee, J.-H. Kim, J.-H. Ahn, *Materials Today* **2015**, *in press*.
- [12] B. C. Brodie, *Phil. Trans. R. Soc. Lond.* **1859**, *149*, 249.
- [13] S. Gijie, S. Han, M. Wang, K. L. Wang, R. B. Kaner, *Nano Lett.* **2007**, *7*, 3394.
- [14] X. Wang, L. Zhi, K. Müllen, *Nano Lett.* **2008**, *8*, 323.
- [15] J. T. Roinson, M. Zalalutdinov, J. W. Baldwin, E. S. Snow, Z. Wei, P. Sheehan, B. G. Houston, *Nano Lett.* **2008**, *8*, 3441.

- [16] S. Stankovich, D. A. Dikin, R. D. Piner, K. A. Kohlhaas, A. Kleinhammes, Y. Jia, Y. Wu, S. T. Nguyen, R. S. Ruoff, *Carbon* **2007**, *45*, 1558.
- [17] Y. Si, E. T. Samulski, *Nano Lett.* **2008**, *8*, 1679.
- [18] M. J. Fernández-Merino, L. Guardia, J. I. Paredes, S. Villar-Rodil, P. Solís-Fernández, A. Martínez-Alonso, J. M. D. Tascón, *J. Phys. Chem. C* **2010**, *114*, 6426.
- [19] X. Wan, Y. Huang, Y. Chen, *Acc. Chem. Res.* **2012**, *45*, 598.
- [20] A. K. Geim, K. S. Novoselov, *Nat. Mater.* **2007**, *6*, 183.
- [21] T. Ohta, A. Bostwick, T. Seyller, K. Horn, E. Rotenberg, *Science* **2006**, *313*, 951.
- [22] Y. W. Son, M. L. Cohen, S. G. Louie, *Nature* **2006**, *444*, 347.
- [23] M. Y. Han, B. Ozyilmaz, Y. B. Zhang, P. Kim, *Phys. Rev. Lett.* **2007**, *98*, 206805.
- [24] J. W. Bai, X. Zhong, S. Jiang, Y. Huang, X. F. Duan, *Nat. Nanotechnol.* **2010**, *5*, 190.
- [25] M. Kim, N. S. Safron, E. Han, M. S. Arnold, P. Gopalan, *Nano Lett.* **2010**, *10*, 1125.
- [26] L. A. Ponomarenko, F. Schedin, M. I. Katsnelson, R. Yang, E. W. Hill, K. S. Novoselov, A. K. Geim, *Science*, **2008**, *320*, 3568.
- [27] L. Zhang, S. Diao, Y. Nie, K. Yan, N. Liu, B. Dai, Q. Xie, A. Reina, J. Kong, Z. Liu, *J. Am. Chem. Soc.* **2011**, *133*, 2706.
- [28] L. Tapasztó, G. Dobrik, P. Lambin, L. P. Biró, *Nat. Nanotechnol.* **2008**, *3*, 397.
- [29] Y. He, H. Dong, T. Li, C. Wang, W. Shao, Y. Zhang, L. Jiang, W. Hu, *Appl. Phys. Lett.* **2010**, *97*, 133301.
- [30] S. S. Datta, D. R. Strachan, S. M. Khamis, A. T. Charlie Johnson, *Nano Lett.* **2008**, *8*, 1912.
- [31] N. Severin, S. Kirstein, I. M. Sokolov, J. P. Rabe, *Nano Lett.* **2009**, *9*, 457.

- [32] L. C. Campos, V. R. Manfrinato, J. D. Sanchez-Yamagishi, J. Kong, P. Jarillo-Herrero, *Nano Lett.* **2009**, *9*, 2600.
- [33] L. Ci, L. Song, D. Jariwala, A. L. Elías, W. Gao, M. Terrones, P. M. Ajayan. *Adv. Mater.* **2009**, *21*, 4487.
- [34] M. Park, C. Harrison, P. M. Chaikin, R. A. Register, D. H. Adamson, *Science* **1997**, *276*, 1401.
- [35] K. Shin, K. A. Leach, J. T. Goldbach, D. H. Kim, J. Y. Jho, M. Tuominen, C. J. Hawker, T. P. Russell, *Nano Lett.* **2002**, *2*, 933.
- [36] B.-H. Sohn, J.-M. Choi, S. I. Yoo, S.-H. Yun, W.-C. Zin, J. C. Jung, M. Kanehara, T. Hirata, T. Teranishi, *J. Am. Chem. Soc.* **2003**, *125*, 6368.
- [37] J. P. Spatz, T. Herzog, S. Mößmer, P. Ziemann, M. Möller, *Adv. Mater.* **1999**, *11*, 149.
- [38] A. Ethirajan, U. Wiedwald, H.-G. Boyen, B. Kern, L. Han, A Klimmer, F. Weigl, G. Kästle, P. Ziemann, K. Fauth, J. Cai, R. J. Behm, A. Romanyuk, P. Oelhafen, P. Walther, J. Biskupek, U. Kaiser, *Adv. Mater.* **2007**, *19*, 406.
- [39] M. Aizawa, J. M. Buriak, *J. Am. Chem. Soc.* **2005**, *127*, 8932.
- [40] J. P. Spatz, S. Mößmer, C. Hartmann, M. Möller, T. Herzog, M. Krieger, H.-G. Boyen, P. Ziemann, B. Kabius, *Langmuir* **2000**, *16*, 407.
- [41] S. Förster, M. Antonietti, *Adv. Mater.* **1998**, *10*, 195.
- [42] M. Haupt, S. Miller, R. Glass, M. Arnold, R. Sauer, K. Thonke, M. Möller, J. P. Spatz, *Adv. Mater.* **2003**, *15*, 829.
- [43] J. Bai, X. Zhong, S. Jiang, Y. Huang, X. Duan, *Nat. Nanotechnol.* **2010**, *5*, 190.
- [44] Y. S. Jung, C. A. Ross, *Nano Lett.* **2007**, *7*, 2046.
- [45] X. Liang, S. Wi, *ACS Nano* **2012**, *6*, 9700.
- [46] J. G. Son, M. Son, K.-J. Moon, B. H. Lee, J.-M. Myoung, M. S. Strano, M.-H. Ham, C. A. Ross, *Adv. Mater.* **2013**, *25*, 4723.
- [47] J. Lee, K. Kim, W. I. Park, B.-H. Kim, J. H. Park, T.-H. Kim, S. Bong, C.-H. Kim, G. S. Chae, M. Jun, Y. Hwang, Y. S. Jung, S. Jeon, *Nano Lett.* **2012**, *12*,

6078.

- [48] B. H. Kim, J. Y. Kim, S.-J. Jeong, J. O. Hwang, D. H. Lee, D. O. Shin, S.-Y. Choi, S. O. Kim, *ACS Nano* **2010**, *4*, 5464.
- [49] J. Y. Kim, B. H. Kim, J. O. Hwang, S.-J. Jeong, D. O. Shin, J. H. Mun, Y. J. Choi, H. M. Jin, S. O. Kim, *Adv. Mater.* **2013**, *25*, 1331.
- [50] A. Fujishima, K. Honda, *Nature* **1972**, *238*, 37.
- [51] M. A. Grätzel, *Nature* **2001**, *409*, 575.
- [52] Z. Miao, D. Xu, J. Ouyang, G. Guo, X. Zhao, Y. Tang, *Nano Lett.* **2002**, *2*, 717.
- [53] E. J. W. Crossland, M. Kamperman, M. Nedelcu, C. Ducati, U. Wiesner, D.M. Smilgies, G. E. S. Toombes, M. A. Hillmyer, S. Ludwigs, U. Steiner, H. J. Snaith, *Nano Lett.* **2009**, *9*, 2807.
- [54] E. J. W. Crossland, M. Nedelcu, C. Ducati, S. Ludwigs, M. A. Hillmyer, U. Steiner, H. J. Snaith, *Nano Lett.* **2009**, *9*, 2813.
- [55] D. O. Shin, J.-R. Jeong, T. H. Han, C. M. Koo, H.-J. Park, Y. T. Kim, S. O. Kim, *J. Mater. Chem.* **2010**, *20*, 7241.
- [56] J. Eastoe, M. J. Hollamby, L. Hudson, *Adv. Colloid Interface Sci.* **2006**, *128*, 5.
- [57] S.-H. Yun, S. I. Yoo, J. C. Jung, W.-C. Zin, and B.-H. Sohn, *Chem. Mater.* **2006**, *18*, 5646.
- [58] J. Chai, D. Wang, X. Fan, J. M. Buriak, *Nat. Nanotechnol.* **2007**, *2*, 500.
- [59] S.-M. Jeon, S. H. Lee, S. I. Yoo, B.-H. Sohn, *Langmuir* **2011**, *27*, 12191.
- [60] C. Sinturel, M. Vayer, M. Morris, M. A. Hillmyer, *Macromolecules* **2013**, *46*, 5399.
- [61] J. Yin, X. Yao, J.-Y. Liou, W. Sun, Y.-S. Sun, Y. Wang, *ACS Nano* **2013**, *7*, 9961.
- [62] E. Helfand, Y. Tagami, *J. Chem. Phys.* **1972**, *56*, 3592.
- [63] T. Hashimoto, M. Shibayama, H. Kawai, *Macromolecules* **1983**, *16*, 1093.

- [64] E. Bhoje Gowd, T. Koga, M. K. Endoh, K. Kumar, M. Stamm, *Soft Matter* **2014**, *10*, 7753.
- [65] S. Park, B. Kim, J. Y. Wang and T. P. Russell, *Adv. Mater.* **2008**, *20*, 681.
- [66] S. Park, J. Y. Wang, B. Kim, J. Xu and T. P. Russell, *ACS Nano* **2008**, *2*, 766–772.
- [67] J. Chai, J. M. Buriak, *ACS Nano* **2008**, *2*, 489.
- [68] J. Aizpurua, P. Hanarp, D. S. Sutherland, M. Käll, Garnett W. Bryant, and F. J. García de Abajo, *Phys. Rev. Lett.* **2003**, *90*, 057401.
- [69] J.-G. Zhu, Y. Zheng, G. A. Prinz, *J. Appl. Phys.* **2000**, *87*, 6668.
- [70] Z. K. Wang, H. S. Lim, H. Y. Liu, S. C. Ng, M. H. Kuok, L. L. Tay, D. J. Lockwood, M. G. Cottam, K. L. Hobbs, P. R. Larson, J. C. Keay, G. D. Lian, M. B. Johnson, *Phys. Rev. Lett.* **2005**, *94*, 137208
- [71] E. M. Larsson, J. Alegret, M. Käll, D. S. Sutherland, *Nano Lett.* **2007**, *7*, 1256.
- [72] M. Winzer, M. Kleiber, N. Dix, R. Wiesendanger, *Appl. Phys. A.* **1996**, *63*, 617.
- [73] K. L. Hobbs, P. R. Larson, G. D. Lian, J. C. Keay, M. B. Johnson, *Nano Lett.* **2004**, *4*, 167.
- [74] J. H. Mun, S. K. Cha, H. Kim, H.-S. Moon, J. Y. Kim, H. M. Jin, Y. J. Choi, J. E. Baek, J. Shin, S. O. Kim, *Small* **2014**, *10*, 3742.
- [75] L. Meli, T. P. Lodge, *Macromolecules* **2009**, *42*, 580.
- [76] J. M. Virgili, A. Hexemer, J. A. Pople, N. P. Balsara, R. A. Segalman, *Macromolecules* **2009**, *42*, 4604.
- [77] M. J. Park, *Nat. Commun.* **2010**, *1*, 88.
- [78] M. W. Schulze, L. D. McIntosh, M. A. Hillmyer, T. P. Lodge, *Nano Lett.* **2014**, *14*, 122.
- [79] A. Noro, Y. Tomita, Y. Shinohara, Y. Sageshima, J. J. Walish, Y. Matsushita, E. L. Thomas, *Macromolecules* **2014**, *47*, 4103.
- [80] B.-H. Sohn, S.-I. Yoo, B.-W. Seo, S.-H. Yun, S.-M. Park, *J. Am. Chem. Soc.*

**2001**, 123, 12734.

- [81] L. Wang, F. Montagne, P. Hoffmann, R. Pugin, *Chem. Commun.* **2009**, 45, 3798.
- [82] D. O. Shin, J. H. Mun, G.-T. Hwang, J. M. Yoon, J. Y. Kim, J. M. Yun, Y.-B. Yang, Y. Oh, J. Y. Lee, J. Shin, K. J. Lee, S. Park, J. U. Kim, S. O. Kim, *ACS Nano* **2013**, 7, 8899.
- [83] V. Suresh, S. Madapusi, S. Krishnamoorthy, *ACS Nano* **2013**, 7, 7513.
- [84] B. Seger, P. V. Kamat, *J. Phys. Chem. C* **2009**, 113, 7990.
- [85] R. Muszynski, B. Seger, P. V. Kamat, *J. Phys. Chem. C* **2008**, 112, 5263.
- [86] L. Lu, J. Liu, Y. Hu, Y. Zhang, W. Chen, *Adv. Mater.* **2013**, 25, 1270.
- [87] I. V Lightcap, T. H. Kosel, P. V Kamat, *Nano let.* **2010**, 10, 577.
- [88] Y. Liang, Y. Li, H. Wang, J. Zhou, J. Wang, T. Regier, H. Dai, *Nat. Mater.* **2011**, 10, 780.
- [89] W. Chen, S. Chen, *Angew. Chem. Int. Ed.* **2009**, 48, 4386.
- [90] W. Hong, H. Bai, Y. Xu, Z. Yao, Z. Gu, G. Shi, *J. Phys. Chem. C* **2010**, 114, 1822.
- [91] F. Xiao, J. Song, H. Gao, X. Zan, R. Xu, H. Duan, *ACS Nano* **2012**, 6, 100.
- [92] D. Li, C. Wang, D. Tripkovic, S. Sun, N. M. Markovic, V. R. Stamenkovic, *ACS Catal.* **2012**, 2, 1358.
- [93] Y. Zhu, S. Murali, W. Cai, X. Li, J. W. Suk, J. R. Potts, R. S. Ruoff, *Adv. Mater.* **2010**, 22, 3906.
- [94] A. N. Shipway, E. Katz, I. Willner, *ChemPhysChem* **2000**, 1, 18.
- [95] G. Liu, Y. Wu, Y.-M. Lin, D. B. Farmer, J. a Ott, J. Bruley, A. Grill, P. Avouris, D. Pfeiffer, A. a Balandin, C. Dimitrakopoulos, *ACS Nano* **2012**, 6, 6786.
- [96] W. S. Hummers, R. E. Offeman, *J. Am. Chem. Soc.* **1958**, 80, 1339.
- [97] N. I. Kovtyukhova, P. J. Ollivier, B. R. Martin, T. E. Mallouk, S. A. Chizhik,

- E. V. Buzaneva, A. D. Gorchinskiy, *Chem. Mater.* **1998**, *11*, 771.
- [98] oxygen functional
- [99] G. Eda, M. Chhowalla, *Adv. Mater.* **2010**, *22*, 2392.
- [100] S. Park, Y. Hu, J. O. Hwang, E.-S. Lee, L. B. Casabianca, W. Cai, J. R. Potts, H.-W. Ha, S. Chen, J. Oh, S. O. Kim, Y.-H. Kim, Y. Ishii, R. S. Ruoff, *Nat. Commun.* **2011**, *3*, 638.
- [101] H. Yin, H. Tang, D. Wang, Y. Gao, Z. Tang, *ACS Nano* **2012**, *6*, 8288.
- [102] Y.-R. Kim, S. Bong, Y.-J. Kang, Y. Yang, R. K. Mahajan, J. S. Kim, H. Kim, *Biosens. Bioelectron.* **2010**, *25*, 2366.
- [103] S. Park, R. S. Ruoff, *Nat. Nanotechnol.* **2009**, *4*, 217.
- [104] K. Saha, S. S. Agasti, C. Kim, X. Li, *Chem. Rev.* **2012**, *112*, 2739.
- [105] A. J. Bard, L. R. Faulkner, in *Electrochemical Methods, Fundamentals and Applications*, 2nd ed.; John Wiley and Sons: New York, 2001.
- [106] N. M. Markovic, T. J. Schmidt, V. Stamenkovic, P. N. Ross, *Fuel Cells* **2001**, *1*, 105.
- [107] C. Song, Zhang, J. in *PEM Fuel Cell Electrocatalysts and Catalyst Layers*, (Eds: Zhang, J.), Springer: Vancouver, **2008**.
- [108] W. Tang, H. Lin, A. Kleiman-Shwarsstein, G. D. Stucky, E. W. McFarland, *J. Phys. Chem. C* **2008**, *112*, 10515.
- [109] S. Chen, A. Kucernak, *J. Phys. Chem. B* **2004**, *108*, 3262.
- [110] A. Schneider, L. Colmenares, Y. E. Seidel, Z. Jusys, B. Wickman, B. Kasemo, R. J. Behm, *Phys. Chem. Chem. Phys.* **2008**, *10*, 1931.
- [111] P. Blake, E. W. Hill, A. H. C. Neto, K. S. Novoselov, D. Jiang, R. Yang, T. J. Booth, A. K. Geim, *Appl. Phys. Lett.* **2007**, *91*, 063124.
- [112] S. Roddaro, P. Pingue, V. Piazza, V. Pellegrini, F. Beltram, *Nano Lett.* **2007**, *7*, 2707.
- [113] A. Gupta, G. Chen, P. Joshi, S. Tadigadapa, P. C. Eklund, *Nano Lett.* **2006**, *6*,

2667.

- [114] S. Krishnamoorthy, R. Pugin, J. Brugger, H. Heinzelmann, A. C. Hoogerwerf, C. Hinderling *Langmuir* **2006**, *22*, 3450.
- [115] H. C. Tsai, E. Hu, K. Perng, M. K. Chen, J. C. Wu, Y. S. Chang, *Surf. Sci.* **2003**, *537*, L447.
- [116] D. Graf, F. Molitor, K. Ensslin, C. Stampfer, A. Jungen, C. Hierold, L. Wirtz, *Nano Lett.* **2007**, *7*, 238.
- [117] A. C. Ferrari, J. C. Meyer, V. Scardaci, C. Casiraghi, M. Lazzeri, F. Mauri, S. Piscanec, D. Jiang, K. S. Novoselov, S. Roth, A. K. Geim, *Phys. Rev. Lett.* **2006**, *97*, 187401.
- [118] C. Casiraghi, A. Hartschuh, H. Qian, S. Piscanec, C. Georgi, A. Fasoli, K. S. Novoselov, D. M. Basko, A. C. Ferrari, *Nano Lett.* **2009**, *9*, 1433.
- [119] W. I. Park, D. H. Kim, S.-W. Jung, G.-C. Yi, *Appl. Phys. Lett.* **2002**, *80*, 4232.
- [120] Y.-J. Kim, J.-H. Lee, G.-C. Yi, *Appl. Phys. Lett.* **2009**, *95*, 213101.
- [121] L. P. Biró, P. Lambin, *Carbon* **2010**, *48*, 2677.
- [122] S. Stankovich, D. A. Dikin, R. D. Piner, K. A. Kohlhaas, A. Kleinhammes, Y. Jia, Y. Wu, S. T. Nguyen, R. S. Ruoff, *Carbon* **2007**, *45*, 1558.
- [123] L. Bardotti, P. Jensen, A. Hoareau, M. Treilleux, B. Cabaud, A. Perez, F. Cadete Santos Aires, *Surf. Sci.* **1996**, *367*, 276.
- [124] A. V. Khomenko, N. V. Prodanov, *J. Phys. Chem. C.* **2010**, *114*, 19958.
- [125] K. V. Zakharchenko, M. I. Katsnelson, A. Fasolino, *Phys. Rev. Lett.* **2009**, *102*, 046808.
- [126] S. Ryu, J. Maultzsch, M. Y. Han, P. Kim, L. E. Brus, *ACS Nano* **2011**, *5*, 4123.
- [127] A. Das, S. Pisana, B. Chakraborty, S. Piscanec, S. K. Saha, U. V. Waghmare, K. S. Novoselov, H. R. Krishnamurthy, A. K. Geim, A. C. Ferrari, A. K. Sood. *Nat. Nanotechnol.* **2008**, *3*, 210.
- [128] D. Graf, F. Molitor, K. Ensslin, C. Stampfer, A. Jungen, C. Hierold, L. Wirtz, *Nano Lett.* **2007**, *7*, 238.

- [129] J. E. Lee, G. Ahn, J. Shim, Y. S. Lee, S. Ryu, *Nat. Commun.* **2012**, *3*, 1024.
- [130] L. Liu, S. Ryu, M. R. Tomasik, E. Stolyarova, N. Jung, M. S. Hybertsen, M. L. Steigerwald, L. E. Brus, G. W. Flynn, *Nano Lett.* **2008**, *8*, 1965.
- [131] L. Gao, W. Ren, B. Liu, Z.-S. Wu, C. Jiang, H.-M. Cheng, *J. Am. Chem. Soc.* **2009**, *131*, 13934.
- [132] R. C. Haddon, *Science* **1993**, *261*, 1545.
- [133] K. D. Ausman, H. W. Rohrs, M. Yu, R. S. Ruoff, *Nanotechnology* **1999**, *10*, 258.
- [134] Q. Wu, Y. Wu, Y. Hao, J. Geng, M. Charlton, S. Chen, Y. Ren, H. Ji, H. Li, D. W. Boukhvalov, R. D. Piner, C. W. Bielawski, R. S. Ruoff, *Chem. Commun.* **2013**, *49*, 677.
- [135] D. W. Boukhvalov, M. I. Katsnelson, *J. Phys. Chem. C* **2009**, *113*, 14176.
- [136] N. L. Y. Wu, X. Zhang, J. N. Murphy, J. Chai, K. D. Harris, J. M. Buriak, *Nano Lett.* **2012**, *12*, 264.

# Appendices

## A. Electrochemical analysis

### 1. Randles-Sevcik equation

Randles-Sevcik equation is defined as below:

$$i_p = (2.69 \times 10^5) n^{\frac{3}{2}} A D^{\frac{1}{2}} C^* \nu^{\frac{1}{2}} \quad (\text{A.1})$$

where  $n$ ,  $A$ ,  $D$ , and  $C^*$  are the number of electrons transferred, the electrochemical surface area, the diffusion coefficient of the redox species, and the bulk concentration of the redox species, respectively. As shown in Figure A.1, the peak current ( $i_p$ ) on Au(51k-18k) was linearly proportional ( $R^2 = 0.99$ ) to the square root of the scan rate ( $\nu^{1/2}$ ), which indicates that the electrochemical processes of  $\text{Fe}(\text{CN})_6^{3-/4-}$  with Au(51-18) were diffusion-controlled.

The electrochemical surface area was also estimated by the Randles-Sevcik equation. The value of  $6.30 \times 10^{-6} \text{ cm}^2 \text{ s}^{-1}$  was used as the diffusion coefficient of  $\text{Fe}(\text{CN})_6^{3-/4-}$ . The electrochemical surface areas of Au(109-27) ( $0.42 \text{ cm}^2$ ) and Au(51-18) ( $0.48 \text{ cm}^2$ ) are larger than that of the GCE itself ( $0.36 \text{ cm}^2$ ). The incorporation of Au nanoparticles increased the electrochemical surface area. The estimated geometric areas of Au nanoparticles are  $0.004 \text{ cm}^2$  for Au(109-27) and  $0.01 \text{ cm}^2$  for Au(51-18), assuming a hemispherical surface of each NPs. Although these additional surface areas provided by NPs were relatively small, large enhancements of electrochemical surface areas were observed for both NP cases, implying that each NP can be considered an effective nanoelectrode.

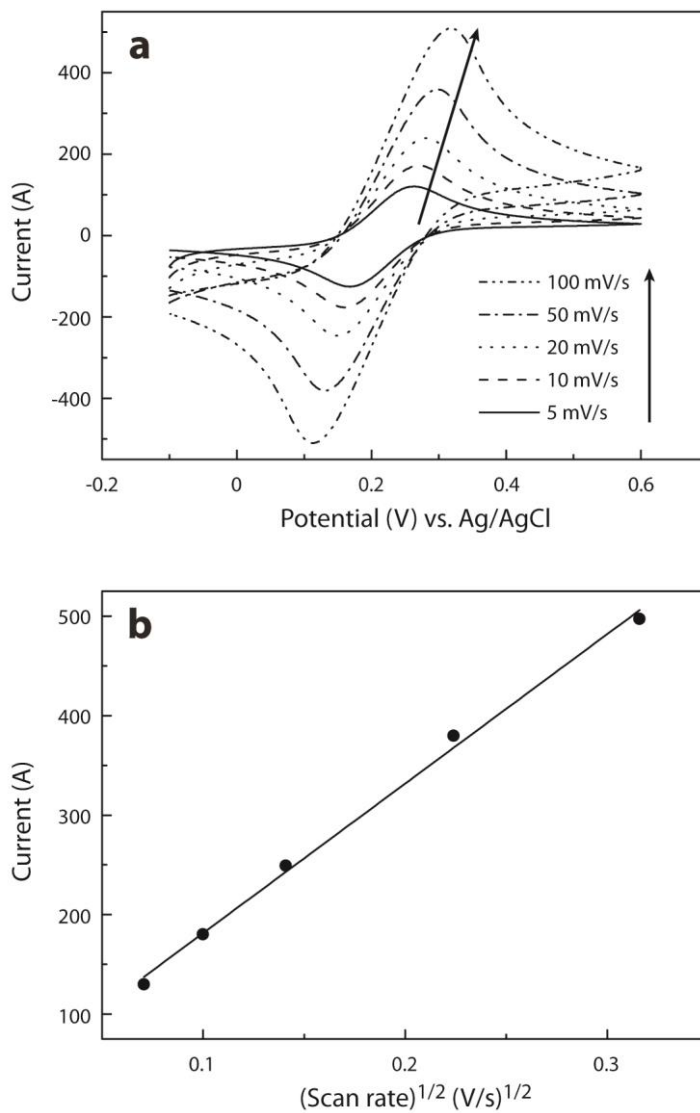


**Figure A.1.** (a) Cyclic voltammograms of  $\text{Fe}(\text{CN})_6^{3-/4-}$  with Au(51-18) at various scan rates; (b) plot of the peak current vs. the square root of the scan rate.

## 2. Koutecky-Levich plots

Koutecky-Levich (K-L) plots ( $J^{-1}$  vs.  $\omega^{-1/2}$ ) using the following equations (A.2) – (A.4) were obtained. The linearity of the K-L plots indicates first-order reaction kinetics with respect to the concentration of dissolved oxygen.

$$\frac{1}{J} = \frac{1}{J_K} + \frac{1}{J_L} = \frac{1}{J_K} + \frac{1}{B\omega^{1/2}} \quad (\text{A. 2})$$

$$B = 0.62nFC_o(D_o)^{2/3}\nu^{-1/6} \quad (\text{A. 3})$$

$$J_K = nFkC_o \quad (\text{A. 4})$$

$J$  is the measured current density,  $J_K$  is the kinetic-limiting current density,  $J_L$  is the diffusion-limiting current density,  $\omega$  is the electrode rotating rate ( $\omega = 2\pi N$ ,  $N$  is the linear rotating speed),  $n$  is the number of electrons transferred,  $F$  is the Faraday constant ( $F = 96,485 \text{ C mol}^{-1}$ ),  $C_o$  is the bulk concentration of  $\text{O}_2$  ( $C_o = 1.2 \times 10^{-3} \text{ mol L}^{-1}$ ),  $D_o$  is the diffusion coefficient of  $\text{O}_2$  ( $D_o = 1.9 \times 10^{-5} \text{ cm}^2 \text{ s}^{-1}$ ),  $\nu$  is the kinematic viscosity of the electrolyte ( $0.1 \text{ m}^2 \text{ s}^{-1}$ ) in 0.1 M KOH, and  $k$  is the electron transfer rate constant.

## B. Photoluminescence from ZnO nanorods

The optical characteristics of the ZnO nanorod arrays on the rGO nanodot arrays were investigated using temperature-dependent PL spectroscopy with He-Cd laser (325 nm) as the source of optical excitation. As displayed in Figure B.1, a series of PL spectra of ZnO nanostructures were measured at different temperatures ranging from 10 to 300 K. From the PL spectrum of ZnO nanorods measured at 10 K, two distinct near-band edge emission peaks were observed at 3.36 and 3.32 eV. A sharp and strong peak at 3.36 eV with a FWHM value of 10 meV is tentatively attributed from neutral-donor bound exciton peak ( $I_{bx}$ ). An additional near-band edge emission peak at 3.32 eV displays an energy difference of 40 meV from  $I_{bx}$ , which is similar to the separation energy of the two electron satellite from neutral-donor bound excitons in ZnO. From the temperature-dependent PL spectra, this emission peak was observed up to 120 K and disappeared at temperatures above 150 K. The rapid thermal quenching and the energy difference from  $I_{bx}$  strongly suggest that the emission at 3.32 eV is assigned to the two electron satellite transition of neutral-donor bound excitonic emission of ZnO. More importantly, from the PL spectra, no additional exciton peak associated with carbon impurities was observed at 3.356 eV, implying that no degradation or impurity incorporation by carbon atoms occurred during the growth process. The observation of a strong, sharp near-band edge emission peaks with no carbon-related defect peak indicates the high optical quality of the ZnO nanostructures without carbon contamination.

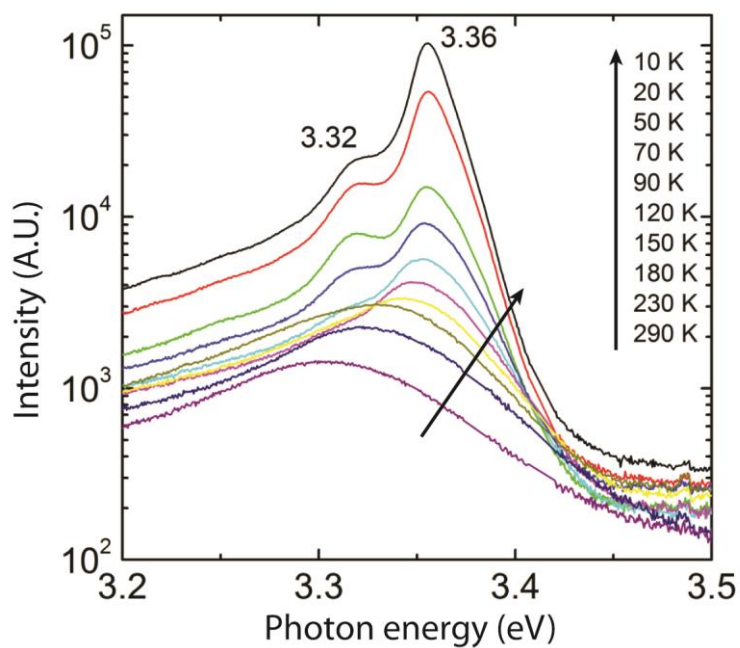


**Figure B.1.** Optical characteristics of ZnO nanorod arrays on rGO nanodots at various temperatures. Temperature-dependent PL spectra of the ZnO nanostructures grown on the rGO nanodot arrays. The values of dominant emission peaks are indicated.

### C. Correlation analysis of nanoperforated graphene

A two-dimensional Raman spectra in Figure C.1. was obtained by the correlation of G and 2D modes to elucidate the detailed mechanism of perforation by Pt NPs, which indicates that the strained graphene by Pt NPs follows the uniaxial slope ( $\Delta\omega_{2D}/\Delta\omega_G = 2.2 \pm 0.2$ ) as well as the hole doping slope ( $0.75 \pm 0.04$ ) with annealing time.

The graphene on SiO<sub>2</sub> substrates typically shows the p-doping of  $\sim 3.55 \times 10^{12} \text{ cm}^{-2}$  and the compressive strain ( $\epsilon_C$ ) of  $\sim 0.15\%$  that is caused by slippage and shrinkage during the drying process at  $\sim 80 \text{ }^\circ\text{C}$  (circles in Figure C.1). On the other hand, the graphene on NPs arrays remarkably experiences the tensile strain ( $\epsilon_T$ ) of  $\sim 0.16\%$  (point A in Figure C.1), resulting in the downshift of G peaks at  $\sim 1577.1 \text{ cm}^{-1}$  (diamonds in Figure C.1). The hole doping level is  $\sim 3.8 \times 10^{12} \text{ cm}^{-2}$  (point B in Figure C.1), which is similar to the graphene on SiO<sub>2</sub>. The shift of data points after transfer onto Pt NP arrays looks parallel to the uniaxial slope in general, but rather wide distributions and relatively steeper slopes imply the coexistence of suspended regions that leads to the biaxial buckling graphene as shown in Figure 3.27a. After 10 min annealing, the distribution mostly changes back to confined quasi linearity and follows the uniaxial type (squares in Figure C.1). This spectral change indicates that the negative thermal expansion of graphene tends to form uniaxial strain along the linear wrinkles bridged by adjacent Pt NPs rather than biaxial strain as shown in Figure 3.27c. In addition, the region of distribution is upshifted with a slightly declined slope, suggesting that the graphene was p-doped. The appearance of the hole doping ( $6.0 \times 10^{12} \text{ cm}^{-2}$ ) is possibly caused by the attachment of oxygen molecules on the graphene surface. After 20 min annealing, the degree of distribution is more perturbed and the slope is declined towards the hole doping

slope. The spectral inhomogeneity after 20 min annealing is presumably originated from the increased hole doping by oxidation reaction at structurally deformed sites (triangles in Figure C.1). The continuing annealing up to 30 min further p-dopes the deformed graphene on Pt NP arrays, and finally, the compressive strain is released as the graphene is perforated by the Pt NP-assisted oxidation reaction (See inverse triangles with no linearity assigned to strain in Figure C.1). After complete perforation, the final compressive strain is appeared to be  $\sim 0.22\%$  at a p-doping level of  $\sim 1.2 \times 10^{13} \text{ cm}^{-2}$  (Table C.1). The gradual appearance of defect-related D and D' peaks as well as the shift of G and 2D peaks also support that the perforation proceeds with increasing annealing time (Figure 3.29). Thus, the localized strain and the oxidation reaction by Pt NPs cooperatively contribute the strain-assisted perforation of graphene.

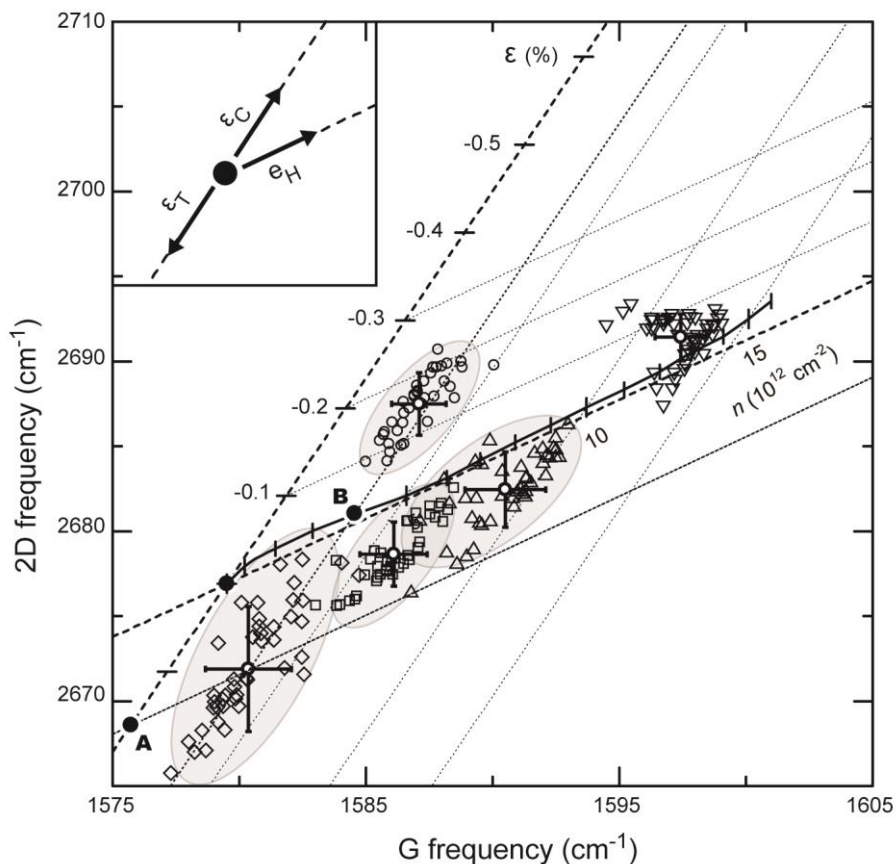


**Figure C.1.** Correlation between the G and 2D modes varied by annealing time: on SiO<sub>2</sub> substrate ( $\circ$ ), on Pt NPs ( $\diamond$ ), annealing for 10 min ( $\square$ ), 20 min ( $\Delta$ ), and 30 min ( $\nabla$ ). The black dashed line indicates the charge neutral graphene under randomly oriented uniaxial strain. The black solid line indicates doped graphene with varying density of holes. Black dot indicates the charge neutral and strain-free graphene. (Inset: decomposition of hole doping and strain types using unit vectors;  $\epsilon_C$ : compressive strain,  $\epsilon_T$ : tensile strain,  $e_H$ : hole doping effect, magenta dashed line: average value of strain-free graphene with varying density of holes.)

	Heating (min)	Charge density (cm <sup>-2</sup> )	Strain ( $\epsilon$ ) <sup>a)</sup>
On SiO <sub>2</sub> /Si	N/A	$3.55 \times 10^{12}$	$\epsilon_C : 0.15 \%$
	0	$3.8 \times 10^{12}$	$\epsilon_T : 0.16 \%$
On Pt(51-18)	10	$6.0 \times 10^{12}$	$\epsilon_C : 0.08 \%$
	20	$9.0 \times 10^{12}$	$\epsilon_C : 0.10 \%$
	30	$1.2 \times 10^{13}$	$\epsilon_C : 0.22 \%$

a)  $\epsilon_C$  : compressive strain,  $\epsilon_T$  : tensile strain

**Table C.1.** Charge density and strain in graphene.

## 국문 초록

# 이중블록공중합체와 마이셀로부터 합성한 정렬된 나노구조 배열의 대면적 그래핀 나노패터닝 응용

김 성 수

화학부 고분자화학 전공

서울대학교 대학원

그래핀이란  $sp^2$  혼성 오비탈로 서로 결합된 탄소 원자들이 벌집 모양의 격자로 한 층에 배열된 평평한 물질을 말하며, 그래핀의 화학적, 물리학적 특성을 최적화하는 것은 신개념의 전자, 화학, 멤브레인 소자에 적용을 위해 매우 중요하다. 한편 그래핀을 나노미터 수준의 구조로 패터닝하게 되면 그래핀 기반의 소자들의 전하 이동 특성이 조절될 수 있음이 알려지게 되면서 그래핀에 나노제작 및 나노패터닝 기술을 적용하는 연구가 널리 진행되었다. 게다가 그래핀은 2차원 평면 물질의 구조적 특성을 가지므로 실리콘 기반의 반도체 공업에서 상용화된 가공 공법의 직접 적용이 가능하기 때문에 전자 빔 및 집속 이온 빔 리소그래피를 포함한 다양한 하향식 공정의 사용이 그래핀 패터닝에 접목될 수 있었다. 이러한 하향식 리소그래피 방법은 나노스케일의 패턴 크기를 정밀하게 조절할 수 있는 장점이 있기 때문에 나노패턴 그래

핀의 다양한 우수한 물성을 발견함은 물론 해당 물성과 패턴 크기와의 관계까지도 정확하게 관찰하는 것이 가능하였다. 그러나 하향식 접근에서 활용되는 공정들은 고비용이고 많은 시간을 필요로 하는 복잡한 기술들이기 때문에 그래핀 패턴 형상의 유연성과 확장성 면에서 어려움이 많았다. 이에 반해 분자의 자기조립을 응용한 상향식 접근을 이용하면 대면적에서 나노구조 및 나노물질들을 효과적으로 제조할 수 있었기 때문에 저비용의 단순하고 쉬운 공정으로도 나노패턴 그래핀을 제조할 수 있다는 점에서 각광받기 시작했다. 여러 가지 상향식 방법들 중에서 이중블록공중합체를 통한 접근법은 다양한 물질들의 나노구조와 나노패턴을 제조할 수 있는 기술이라는 점에서 나노패턴 그래핀을 효과적으로 제조하는 데 응용될 수 있다. 이중블록공중합체는 서로 다른 두 고분자로 이루어져 있으며 자발적으로 조립하여 반복적인 나노구조를 형성하는데 나노구조의 크기와 모양은 공중합체의 분자량과 조성에 따라 조절할 수 있다. 또한 이중블록공중합체가 한쪽 블록만을 선택적으로 녹이는 용매에 용해되는 경우 녹는 블록으로 구성된 코로나와 안 녹는 블록으로 구성된 코어로 이루어진 구형의 마이셀을 얻을 수 있다. 이중블록공중합체와 마이셀은 고체 기판에 코팅되어 나노구조를 가지는 박막을 형성할 수 있는데 이는 식각 과정에 쓰이는 나노스케일의 리소그래피 마스크나 정렬된 무기 나노물질 배열을 제조하는데 필요한 나노템플레이트로 쓰일 수 있다. 그래핀은 2차원의 원자 두께만큼이나 얇고 평평한 물질이기에 어떤 고체 기판 위에 있든지 이중

블록공중합체와 마이셀의 박막을 코팅하기 용이하므로 그래핀이 없는 일반 기판에서 행하는 나노패터닝 공정들을 동일하게 진행할 수 있게 되는 것이다. 본 학위논문에서는 이중블록공중합체 접근법을 통한 대면적의 나노패턴 그래핀을 제조, 분석, 그리고 응용하는 것에 대해 다룬다. 먼저 1장에서 이 연구에 관한 배경 지식과 목표를 소개한 뒤, 이중블록공중합체와 마이셀 박막으로부터 정렬된 다양한 무기 물질의 배열을 제조하는 방법에 대해 2장에서 서술할 것이다. 제조된 나노구조는 나노템플릿, 에칭 마스크, 촉매 식각 구조로서 그래핀 나노패턴에 응용되는데, 공중합체의 분자량을 조절함으로써 제조되는 나노패턴의 크기와 간격을 나노수준에서 제어할 수 있다. 3장에서는 이들을 응용한 환원 산화 그래핀(rGO) 및 그래핀의 나노패터닝을 기술하며 나노입자로 장식된 rGO와 나노닷, 나노리본, 그리고 나노링 형태를 가진 rGO, 구멍 뚫린 그래핀의 배열 제조 실험 결과와 분석 내용을 포함하고 있다. 이중블록공중합체를 이용한 대면적의 그래핀 나노패터닝은 다양한 구조의 그래핀을 쉽고 효과적으로 제조할 수 있다는 장점이 있으므로 앞으로 전자, 화학, 생명, 환경 응용 소자 제작에 널리 활용될 것으로 기대된다.

주요어 : 이중블록공중합체, 마이셀, 자기 조립, 그래핀

학 번 : 2009 - 20290

# Curriculum Vitae

## Sung-Soo Kim

Department of Chemistry, College of Natural Sciences

Seoul National University, Seoul 151-747, Korea

**Telephone:** +82-2-880-9118 / **E-mail:** sskim12@snu.ac.kr

**Date of birth:** 8th September, 1986.

## Field of Interests

Polymer chemistry, self-assembling macromolecules, 2D materials, nanopatterning

## Education

Mar 2009 – Aug 2015

Ph.D. in Polymer Chemistry, Department of Chemistry, Seoul National University.

Dissertation Title: Arrays of Ordered Nanostructures Synthesized from Diblock  
Copolymers and Their Micelles for Large-Area Graphene  
Nanopatterning

Advisor: Prof. Dr. Byeong-Hyeok Sohn

Mar 2005 – Feb 2009

B.S. in Chemistry, Department of Chemistry, Seoul National University.

B.S. in Physics, Department of Physics and Astronomy, Seoul National University.

## Theses

- [1] S.-S. Kim, Arrays of ordered nanostructures synthesized from diblock copolymers and their micelles for large-area graphene nanopatterning. Ph.D. Dissertation, Seoul National University, Seoul, 2015.
- [2] S.-S. Kim, Concentration of  $\text{Ca}^{2+}$  measured by Cameleon based on fluorescence resonance energy transfer (FRET) spectroscopy. B.S. Thesis (Chemistry), Seoul National University, Seoul, 2009.
- [3] S.-S. Kim, Application of polymer nanocomposite to photovoltaic cells. B.S. Thesis (Physics), Seoul National University, Seoul, 2009.

## Honors and Awards

- 2014 Best presenter award, The Polymer Society of Korea.
- 2013 Best poster award, Germany-Korean Polymer Symposium (GKPS).
- 2011 Best poster award, Institute of Electrical and Electronics Engineers (IEEE) Nanotechnology Materials and Device Conference (NMDC).
- 2011 Kwanjeong educational foundation scholarship
- 2009 Graduation with honor (*Summa Cum Laude*), Seoul National University.
- 2006, 2009 Prize for exceptional performance, College of Natural Sciences, Seoul National University.
- 2005–2010 National science & technology scholarship, the Ministry of Education, Science, and Technology.

## Published Papers

- [1] D. Han,\* S.-S. Kim,\* Y.-R. Kim, B.-H. Sohn, T. D. Chung, Surface coverage and size effects on electrochemical oxidation of uniform gold nanoparticles. *Electrochem. Commun.* **2015**, *53*, 11.
- [2] M.-S. Seo, J.-H. Kim, S.-S. Kim, H. Kang, B.-G. Sohn, Transferrable superhydrophobic TiO<sub>2</sub> nanorods on reduced graphene oxide films using block copolymer templates. *Nanotechnology* **2015**, *26*, 165302.
- [3] J.-H. Kim, S.-S. Kim, B.-H. Sohn, ZnO nanorods and nanowalls directly synthesized on flexible substrates with block copolymer templates. *J. Mater. Chem. C* **2015**, *3*, 1507.
- [4] H. Kim, Y. Lim, S. Kim, S.-S. Kim, B.-H. Sohn, Nanoscale arrangement of diblock copolymer micelles with Au nanorods. *Nanotechnology* **2014**, *25*, 455602.
- [5] Y.-J. Kim,\* S.-S. Kim,\* J. B. Park, B.-H. Sohn, G.-C. Yi, Controlled growth of inorganic nanorod arrays using graphene nanodot seed layers. *Nanotechnology* **2014**, *25*, 13609.
- [6] S.-S. Kim,\* Y. R. Kim,\* T. D. Chung, B.-H. Sohn, Tunable decoration of reduced graphene oxide with Au nanoparticles for the oxygen reduction reaction. *Adv. Funct. Mater.* **2014**, *24*, 2764-2771. (inside cover; selected as one of Hottest Articles from the Advanced Materials family)
- [7] Y.-J Kim, H. Tukiman, C. H. Lee, S.-S. Kim, J. Park, B.-H. Sohn, M .Kim, G.-C. Yi, R. Jung, C. Liu, Hydrothermal growth of ZnO microstructures on Ar plasma treated graphite. *Curr. Appl. Phys.* **2013**, *14*, 269-274.
- [8] Y. J. Suh, N. Lu, S. Y. Park, T. H. Lee, S. H. Lee, D. K. Cha, M. G. Lee, J. Huang, S.-S. Kim, B.-H. Sohn, G.-H. Kim, M. J. Ko, J. Kim, M. J. Kim, Three-

dimensional observation of TiO<sub>2</sub> nanostructures by electron tomography. *Micron* **2013**, *46*, 35-42.

- [9] S.-S. Kim, J.-Y. Choi, K. Kim, B.-H. Sohn, Large area tunable arrays of graphene nanodots fabricated using diblock copolymer micelles. *Nanotechnology* **2012**, *23*, 125301.

## **Manuscript in Preparation**

- [1] H. Kang, S.-S. Kim, B.-H. Sohn, Guided arrangement of Au nanorods by diblock copolymer templates in large areas for optical anisotropy. *in preparation*.
- [2] S.-S. Kim,\* M. J. Park,\* J.-H. Kim, G. Ahn, S. Ryu, B. H. Hong, B.-H. Sohn, Strain-assisted nanoscale perforation of large-area graphene by arrayed Pt nanoparticles. *in preparation*.
- [3] S.-S. Kim, B.-H. Sohn, Combination of thin films and micelles of diblock copolymers for the template to fabricate ordered complex nanostructures. *in preparation*.
- [4] S.-S. Kim, B.-H. Sohn, Tunable Pt nanostructures synthesized by diblock copolymers and their micelles to tailor thin film of reduced graphene oxide. *in preparation*.

## **Conference Presentation**

- [1] S.-S. Kim, B.-H. Sohn, Tunable Pt nanostructures synthesized from self-assembled diblock copolymers to tailor reduced graphene oxide films. Korea-Germany International Research Training Group Symposium on Self-Organized Materials for Optoelectronics. Berlin, Germany, Jul 6-8, 2015.

- [2] S.-S. Kim, B.-H. Sohn, Nanopatterning of reduced graphene oxide by Pt nanostructures synthesized from diblock copolymers. Materials Research Society Spring Meetings & Exhibits, San Francisco, CA, Apr 6-10, 2015.
- [3] S.-S. Kim, B.-H. Sohn, Pt nanostructures synthesized from diblock copolymers and their micelles to tailor large-area graphene. Materials Research Society Fall Meetings & Exhibits, Boston, MA, Nov 30-Dec 5, 2015.
- [4] S.-S. Kim, B.-H. Sohn, Diblock copolymers and their micelles to fabricate catalytic Pt nanostructures for graphene etching. Fall Meeting of the Polymer Society of Korea, Jeju, Korea, Oct 6-8, 2014.
- [5] S.-S. Kim, H. Kang, B.-H. Sohn, Reduced graphene oxide films tailored by Pt nanostructures synthesized from diblock copolymers and their micelles. Spring Meeting of the Polymer Society of Korea, Daejeon, Korea, Apr 10-11, 2014.
- [6] S.-S. Kim, M. J. Park, B. H. Hong, B.-H. Sohn, Arrays of Pt nanoparticles synthesized from diblock copolymer micelles for the perforation of graphene films. Korea-Germany International Research Training Group Symposium on Self-Organized Materials for Optoelectronics. Daejeon, Korea, Feb 17-22, 2014.
- [7] S.-S. Kim, M. J. Park, B. H. Hong, B.-H. Sohn, Large-area nanoperforated graphene by arrays of nanoparticles fabricated from diblock copolymer micelles. Materials Research Society Fall Meetings & Exhibits, Boston, MA, Dec 1-6, 2013.
- [8] S.-S. Kim, B.-H. Sohn, Complex arrays of titania nanostructures and metal nanoparticles fabricated by diblock copolymers and their micelles. The 112nd General Meeting of the Korean Chemical Society, Changwon, Korea, Oct 16-18, 2013.
- [9] S.-S. Kim, J.-H. Kim, B.-H. Sohn, Nanopatterning of reduced graphene oxide

- films by arrays of nanoparticles fabricated by diblock copolymer micelles. German-Korean Polymer Symposium, Hamburg, Germany, Aug 26-30, 2013.
- [10] S.-S. Kim, S. Chae, J.-K. Lee, B.-H. Sohn, Transferable graphene films with nanoparticles by diblock copolymer micelles for electrochemical applications. Spring Meeting of the Polymer Society of Korea, Daejeon, Korea, Apr 11-12, 2013.
- [11] S.-S. Kim, Y.-R. Kim, B.-H. Sohn, Graphene films with arrays of nanoparticles by diblock copolymer micelles and their electrochemical properties. Korea-Germany International Research Training Group Symposium on Self-Organized Materials for Optoelectronics. Seoul, Korea, Feb 25-28, 2013.
- [12] S.-S. Kim, Y.-R. Kim, B.-H. Sohn, Nanopatterned and nanoparticle-decorated graphene in large area fabricated by diblock copolymer micelles. Materials Research Society Fall Meetings & Exhibits, Boston, MA, Nov 25-30, 2012.
- [13] S.-S. Kim, B.-H. Sohn, Graphene decorated with arrays of tunable nanoparticles fabricated by diblock copolymer micelles. The 24th International Liquid Crystal Conference, Mainz, Germany, Aug 19-24, 2012.
- [14] S.-S. Kim, Y. Lee, J.-H. Kim, S. Ku, B.-H. Sohn, Fabrication of nanostructured titanium dioxides by nanotemplates of block copolymers. Institute of Electrical and Electronics Engineers Nanotechnology Materials and Device Conference, Jeju, Korea, Oct 18-21, 2011.
- [15] S.-S. Kim, J.-H. Kim, S. Ku, B.-H. Sohn, Tunable and transferable arrays of Au nanoparticles on reduced graphene oxides. Fall Meeting of the Polymer Society of Korea, Gwangju, Korea, Oct 6-7, 2011.
- [16] S.-S. Kim, J.-H. Kim, Y. Lee, B.-H. Sohn, Thin films of diblock copolymers and their micelles for the fabrication of inorganic nanostructures. The 242nd

American Chemical Society National Meeting & Exposition, Denver, CO, Aug 28-Sep 1, 2011.

- [17] S.-S. Kim, J.-H. Kim, S. Chae, B.-H. Sohn, Graphene nanodot arrays by diblock copolymer micelles. Spring Meeting of the Polymer Society of Korea, Daejeon, Korea, Apr 7-8, 2011.
- [18] S.-S. Kim, Y. Lee, B.-H. Sohn, Fabrication of nanostructured inorganic materials by self-assemblies of diblock copolymers. The 241st American Chemical Society National Meeting & Exposition, Anaheim, CA, Mar 27-31, 2011.
- [19] S.-S. Kim, S.-M. Jeon, H. K. Kim, Y. Lee, B.-H. Sohn, Self-assemblies of diblock copolymers for nanostructured carbon and inorganic materials. The 240th American Chemical Society National Meeting & Exposition, Boston, MA, Aug 22-26, 2010.
- [20] S.-S. Kim, B.-H. Sohn, Diblock copolymer micelle lithography for the fabrication of nanostructured carbon materials. Fall Meeting of the Polymer Society of Korea, Daegu, Korea, Oct 7-8, 2010.

## **Patents**

- [1] B.-H. Sohn, C.-S. Han, J. Y. Woo, S.-S. Kim, Fabricating method of graphene decorated with nanoparticles. KR 10-2014-0073787, Jun 17, 2014.
- [2] B.-H. Sohn, C.-S. Han, M.-S. Seo, S.-S. Kim, Transferring method of nanorod. KR 10-2015-0082456, Jun 11, 2015.